

1 SEARCH FOR PRODUCTION OF A HIGGS BOSON AND A SINGLE TOP
2 QUARK IN MULTILEPTON FINAL STATES IN pp COLLISIONS AT $\sqrt{s} = 13$
3 TeV.

4 by

5 Jose Andres Monroy Montañez

6 A DISSERTATION

7 Presented to the Faculty of

8 The Graduate College at the University of Nebraska

In Partial Fulfilment of Requirements

10 For the Degree of Doctor of Philosophy

11 Major: Physics and Astronomy

12 Under the Supervision of Kenneth Bloom and Aaron Dominguez

13 Lincoln, Nebraska

14 July, 2018

15 SEARCH FOR PRODUCTION OF A HIGGS BOSON AND A SINGLE TOP
16 QUARK IN MULTILEPTON FINAL STATES IN pp COLLISIONS AT $\sqrt{s} = 13$
17 TeV.

18 Jose Andres Monroy Montañez, Ph.D.
19 University of Nebraska, 2018

20 Adviser: Kenneth Bloom and Aaron Dominguez

21 Multivariate techniques are used to discriminate the signal from the dominant back-
22 grounds. The analysis yields a 95% confidence level (C.L.) upper limit on the com-
23 bined tH + ttH production cross section times branching ratio of 0.64 pb, with an
24 expected limit of 0.32 pb, for a scenario with $k_t = \pm 1.0$ and $k_V = 1.0$. Values of k_t
25 outside the range of ± 1.25 to ± 1.60 are excluded at 95% C.L., assuming $k_V = 1.0$.

²⁶ Table of Contents

²⁷	Table of Contents	iii
²⁸	List of Figures	viii
²⁹	List of Tables	xiii
³⁰	1 Theoretical approach	1
³¹	1.1 Introduction	1
³²	1.2 Standard model of particle physics	2
³³	1.2.1 Fermions	4
³⁴	1.2.1.1 Leptons	5
³⁵	1.2.1.2 Quarks	7
³⁶	1.2.2 Fundamental interactions	11
³⁷	1.2.3 Gauge invariance.	15
³⁸	1.2.4 Gauge bosons	17
³⁹	1.3 Electroweak unification and the Higgs mechanism	18
⁴⁰	1.3.1 Spontaneous symmetry breaking (SSB)	26
⁴¹	1.3.2 Higgs mechanism	30
⁴²	1.3.3 Masses of the gauge bosons	33
⁴³	1.3.4 Masses of the fermions	34

44	1.3.5	The Higgs field	35
45	1.3.6	Production of Higgs bosons at LHC	36
46	1.3.7	Higgs boson decay channels	40
47	1.4	Experimental status of the anomalous Higgs-fermion coupling	42
48	1.5	Associated production of a Higgs boson and a single top quark	44
49	1.6	CP-mixing in tH processes	49
50	2	The CMS experiment at the LHC	54
51	2.1	Introduction	54
52	2.2	The LHC	55
53	2.3	The CMS experiment	65
54	2.3.1	CMS coordinate system	68
55	2.3.2	Tracking system	70
56	2.3.3	Silicon strip tracker	73
57	2.3.4	Electromagnetic calorimeter	74
58	2.3.5	Hadronic calorimeter	76
59	2.3.6	Superconducting solenoid magnet	77
60	2.3.7	Muon system	79
61	2.3.8	CMS trigger system	80
62	2.3.9	CMS computing	81
63	3	Event generation, simulation and reconstruction	86
64	3.1	Event generation	87
65	3.2	Monte Carlo Event Generators.	90
66	3.3	CMS detector simulation.	92
67	3.4	Event reconstruction.	94
68	3.4.1	Particle-Flow Algorithm.	94

69	3.4.2 Event reconstruction examples	109
70	5 Statistical methods	112
71	5.1 Multivariate analysis	112
72	5.1.1 Decision trees	116
73	5.1.2 Boosted decision trees (BDT).	119
74	5.1.3 Overtraining	121
75	5.1.4 Variable ranking	122
76	5.1.5 BDT output example	122
77	5.2 Statistical inference	123
78	5.2.1 Nuisance parameters	124
79	5.2.2 Maximum likelihood estimation method	125
80	5.3 Upper limits	126
81	5.4 Asymptotic limits	130
82	6 Search for production of a Higgs boson and a single top quark in multilepton final states in pp collisions at $\sqrt{s} = 13$ TeV	132
84	6.1 Introduction	132
85	6.2 tHq signature	135
86	6.3 Background processes	137
87	6.4 Data and MC Samples	139
88	6.4.1 Full 2016 data set	139
89	6.4.2 Triggers	140
90	6.4.3 MC samples	142
91	6.5 Object Identification	145
92	6.5.1 Lepton reconstruction and identification	145
93	6.5.2 Lepton selection efficiency	153

94	6.5.3 Jets and b -jet tagging	155
95	6.5.4 Missing Energy MET	156
96	6.6 Event selection	157
97	6.7 Background modeling and predictions	159
98	6.7.1 $t\bar{t}V$ and diboson backgrounds	159
99	6.7.2 Non-prompt and charge mis-ID backgrounds	162
100	6.8 Pre-selection yields	166
101	6.9 Signal discrimination	168
102	6.9.1 MVA classifiers evaluation	169
103	6.9.2 Discriminating variables	169
104	6.9.3 BDTG classifiers response	174
105	6.9.4 Additional discriminating variables	175
106	6.9.5 Signal extraction procedure	178
107	6.9.6 Binning and selection optimization	180
108	6.10 Forward jet mismodeling	183
109	6.11 Signal model	185
110	6.12 Systematic uncertainties	188
111	6.13 Results	196
112	6.13.1 CL_S and cross section limits	200
113	6.13.2 Best fit	205
114	6.13.3 Effect of the nuisance parameters	206
115	6.14 CP-mixing in tHq	209
116	7 Phase 1 FPix upgrade modules	211
117	7.0.1 The phase 1 FPix upgrade	211
118	7.0.2 FPix module production line	212

119	7.0.3	The Gluing stage	212
120	7.0.4	The Encapsulation stage	212
121	7.0.5	The FPix module production yields	212
122	A Datasets and triggers		214
123	B Aditional plots		218
124	B.1	Pre-selection kinematic variables	218
125	B.2	BDTG input variables for $2lss$ channel	222
126	B.3	Input variables distributions from BDTG classifiers	223
127	B.4	Pulls and impacts	227
128	C Other binning strategies		229
129	D BDTG output variation with κ_V/κ_t		232
130	E tHq-$t\bar{t}H$ overlap		233
131	F Forward jet impact plots		235
132	G Cross sections and Branching ratios scalings		239
133	Bibliography		246
134	References		247

¹³⁵ List of Figures

136	1.1	Standard Model of particle physics.	3
137	1.2	Transformations between quarks	11
138	1.3	Fundamental interactions in nature.	12
139	1.4	SM interactions diagrams	13
140	1.5	Neutral current processes	19
141	1.6	Spontaneous symmetry breaking mechanism	27
142	1.7	SSB Potential form	28
143	1.8	Potential for complex scalar field	29
144	1.9	SSB mechanism for complex scalar field	30
145	1.10	Proton-Proton collision	36
146	1.11	Proton PDFs	37
147	1.12	Higgs boson production mechanism Feynman diagrams	38
148	1.13	Higgs boson production cross section and decay branching ratios	39
149	1.14	κ_t - κ_V plot of the coupling modifiers. ATLAS and CMS combination.	42
150	1.15	Higgs boson production in association with a top quark	45
151	1.16	Cross section for tHq process as a function of κ_t	48
152	1.17	Cross section for tHW process as a function of κ_{Htt}	48
153	1.18	NLO cross section for tX_0 and $t\bar{t}X_0$.	52

154	1.19 NLO cross section for $tWX_0, t\bar{t}X_0$.	53
155	2.1 CERN accelerator complex	55
156	2.2 LHC protons source. First acceleration stage.	56
157	2.3 The LINAC2 accelerating system at CERN.	57
158	2.4 LHC layout and RF cavities module.	58
159	2.5 LHC dipole magnet.	60
160	2.6 Integrated luminosity delivered by LHC and recorded by CMS during 2016	62
161	2.7 LHC interaction points	63
162	2.8 Multiple pp collision bunch crossing at CMS.	65
163	2.9 Layout of the CMS detector	66
164	2.10 CMS detector transverse slice	67
165	2.11 CMS detector coordinate system	69
166	2.12 CMS tracking system schematic view.	70
167	2.13 CMS pixel detector	71
168	2.14 SST Schematic view.	73
169	2.15 CMS ECAL schematic view	75
170	2.16 CMS HCAL schematic view	77
171	2.17 CMS solenoid magnet	78
172	2.18 CMS Muon system schematic view	79
173	2.19 CMS Level-1 trigger architecture	81
174	2.20 WLCG structure	82
175	2.21 Data flow from CMS detector through hardware Tiers	84
176	3.1 Event generation process.	87
177	3.2 Particle flow algorithm.	95
178	3.3 Stable cones identification	102

179	3.4	Jet reconstruction.	104
180	3.5	Jet energy corrections.	106
181	3.6	Secondary vertex in a b-hadron decay.	107
182	3.7	HIG-13-004 Event 1 reconstruction.	109
183	3.8	$e\mu$ event reconstruction.	110
184	3.9	Recorded event reconstruction.	111
185	5.1	Scatter plots-MVA event classification.	114
186	5.2	Scalar test statistical.	115
187	5.3	Decision tree.	116
188	5.4	Decision tree output example.	119
189	5.5	BDT output example.	122
190	5.6	t_r p.d.f. assuming each H_0 and H_1	128
191	5.7	Illustration of the CL_s limit.	129
192	5.8	Example of Brazilian flag plot	130
193	6.1	Analysis strategy workflow	135
194	6.2	tHq event signature	136
195	6.3	$t\bar{t}$ and $t\bar{t}W$ events signature	139
196	6.4	Trigger efficiency for the same-sign $\mu\mu$ category	141
197	6.5	Trigger efficiency for the $e\mu$ category	142
198	6.6	Trigger efficiency for the $3l$ category	143
199	6.7	tHq and tHW cross section in the κ_t - κ_V phase space	143
200	6.8	Tight vs loose lepton selection efficiencies in the $2lss$ channel.	153
201	6.9	Tight vs loose lepton selection efficiencies in the $3l$ channel.	154
202	6.10	Kinematic distributions in the diboson control region.	161
203	6.11	Fake rates	164

204	6.12 Elecron mis-ID probabilities.	165
205	6.13 Discriminating variables for the event pre-selection, $2lss - \mu^\pm\mu^\pm$	167
206	6.14 MVA classifiers performance.	170
207	6.15 BDTG classifier Input variables distributions.	172
208	6.16 BDT input variables. Discrimination against $t\bar{t}$ and $t\bar{t}V$ in $3l$ channel. . .	173
209	6.17 Correlation matrices for the BDT input variables.	174
210	6.18 BDTG classifier response. Default parameters.	175
211	6.19 BDTG classifier output.	176
212	6.20 Additional discriminating variables distributions.	178
213	6.21 2D BDT classifier output planes	179
214	6.22 Binning overlaid on the S/B ratio map on the plane of classifier outputs. .	180
215	6.23 Binning combination scheme.	181
216	6.24 Kinematic distributions for forward jet mismodeling study.	184
217	6.25 Most forward jets η distributions	185
218	6.26 Scaling of the tHq , tHW , and $t\bar{t}H$ production cross section with κ_t/κ_V . .	187
219	6.27 Fake rates closure test.	193
220	6.28 Fake rates closure test in the $3l$ selection.	194
221	6.29 Pre-fit BDT classifier outputs.	196
222	6.30 Pre-fit distributions in the final binning.	197
223	6.31 Post-fit distributions in the final binning.	198
224	6.32 Background-subtracted distributions in the final binning (ITC).	199
225	6.33 Background-subtracted distributions in the final binning (SM)	200
226	6.34 Asymptotic limits on the combined $tH + t\bar{t}H$ $\sigma \times \text{BR}$	202
227	6.35 Asymptotic limits on the combined $tH + t\bar{t}H$ $\sigma \times \text{BR}$, $\kappa_V = 0.5, 1.0, 1.5$. .	203
228	6.36 Observed and a priori expected significance of the fit result.	206
229	6.37 Best fit values of the combined $tH + t\bar{t}H$ $\sigma \times \text{BR}$	207

230	6.38 Post-fit pulls and impacts.	208
231	6.39 Post-fit pulls an impacts for a fit to the Asimov dataset.	209
232	7.1 Expected performance of the previous pixel detector in simulated $t\bar{t}$ events: a) efficiency; b) fake rate. Conventions are the same for both plots.	213
234	B.1 Input variables to the BDT, $3l$ channel.	219
235	B.2 Input variables to the BDT, $2lss - \mu^\pm\mu^\pm$ channel	220
236	B.3 Input variables to the BDT, $2lss - e^\pm\mu^\pm$ channel	221
237	B.4 Input variables to the BDT, $2lss$ channel	222
238	B.5 BDT input variables. Discrimination against $t\bar{t}$ in $2lss$ channel.	223
239	B.6 BDT input variables. Discrimination against $t\bar{t}V$ in $2lss$ channel.	224
240	B.7 BDT input variables. Discrimination against $t\bar{t}$ in $3l$ channel.	225
241	B.8 BDT input variables. Discrimination against $t\bar{t}V$ in $3l$ channel.	226
242	B.9 Additional post-fit pulls and impacts.	227
243	B.10 Additional post-fit pulls an impacts for a fit to the Asimov dataset.	228
244	C.1 Binning by S/B regions for $2lss$ (left) and $3l$ (right).	229
245	C.2 Final bins (corresponding to S/B regions in the 2D plane)	230
246	C.3 Binning into geometric regions using a k -means algorithm.	231
247	C.4 Final bins using a k -means algorithm.	231
248	D.1 BDTG output variation with κ_V/κ_t	232
249	F.1 Post-fit pulls and impacts with p_T cut 25 GeV for the forward jet	236
250	F.2 Post-fit pulls and impacts with p_T cut 30 GeV for the forward jet	237
251	F.3 Post-fit pulls and impacts with p_T cut 25 GeV for the forward jet	238

²⁵² List of Tables

253	1.1	Fermions of the SM.	4
254	1.2	Fermion masses.	5
255	1.3	Lepton properties.	7
256	1.4	Quark properties.	8
257	1.5	Fermion weak isospin and weak hypercharge multiplets.	9
258	1.6	Fundamental interactions features.	14
259	1.7	SM gauge bosons.	18
260	1.8	Higgs boson properties.	36
261	1.9	Predicted branching ratios for a SM Higgs boson with $m_H = 125 \text{ GeV}/c^2$	41
262	1.10	Predicted SM cross sections for tH production at $\sqrt{s} = 13 \text{ TeV}$	46
263	1.11	Predicted enhancement of the tHq and tHW cross sections at LHC	49
264	6.1	Trigger efficiency scale factors and associated uncertainties.	141
265	6.2	MC signal samples.	144
266	6.3	Effective areas, for electrons and muons.	149
267	6.4	Requirements on each of the three muon selections.	152
268	6.5	Criteria for each of the three electron selections.	152
269	6.6	Summary of event pre-selection.	158
270	6.7	Electron charge mis-ID probabilities.	165

271	6.8	Expected and observed yields for 35.9fb^{-1} after the pre-selection.	166
272	6.9	Signal yields split by decay channels of the Higgs boson.	168
273	6.10	BDTG input variables.	171
274	6.11	Configuration used in the final BDTG training.	175
275	6.12	Input variables ranking for BDTG classifiers	177
276	6.13	ROC-integral for all the testing cases.	177
277	6.14	Selection cuts optimization.	181
278	6.15	Limit variation as a function of bin size, $3l$ channel.	182
279	6.16	Limit variation as a function of bin size, $2lss$ channel.	182
280	6.17	Forward jet Data/MC scale factors.	186
281	6.18	κ_t/κ_V ratios.	189
282	6.19	Pre-fit size of systematic uncertainties.	195
283	6.20	Expected and observed upper limits.	201
284	6.21	Expected and observed 95% C.L. cross section upper limits.	204
285	6.22	Expected and observed CL _S limits on the signal strength.	204
286	6.23	Fit results for the ITC and SM scenarios	205
287	6.24	Best-fit signal strengths for a SM-like Higgs signal.	205
288	A.1	Full 2016 dataset.	214
289	A.2	HLT paths	215
290	A.3	κ_V and κ_t combinations.	216
291	A.4	List of background samples used in this analysis (CMSSW 80X).	217
292	E.1	Differences in event selection $tHq-t\bar{t}H$ multilepton analysis.	233
293	E.2	Individual and shared event yields $tHq-t\bar{t}H$ multilepton selections.	234
294	G.1	Scalings of Higgs decay branching ratios vs. κ_t and $\kappa_V = 0.5$	240

295	G.2	Scalings of Higgs decay branching ratios vs. κ_t and $\kappa_V = 1.0$	241
296	G.3	Scalings of Higgs decay branching ratios vs. κ_t and $\kappa_V = 1.5$	242
297	G.4	Scalings of $\sigma \times \text{BR}$ for the signal components and $\kappa_V = 0.5$	243
298	G.5	Scalings of $\sigma \times \text{BR}$ for the signal components and $\kappa_V = 1.0$	244
299	G.6	Scalings of $\sigma \times \text{BR}$ for the signal components and $\kappa_V = 1.5$	245
300	G.7	Cross sections for tHq , tHW and $t\bar{t}H$ as a function of $\cos(\alpha_{CP})$	246

³⁰¹ **Chapter 1**

³⁰² **Theoretical approach**

³⁰³ **1.1 Introduction**

³⁰⁴ The physical description of the universe is a challenge that physicists have faced by
³⁰⁵ making theories that refine existing principles and proposing new ones in an attempt
³⁰⁶ to embrace emerging facts and phenomena.

³⁰⁷ At the end of 1940s Julian Schwinger [1] and Richard P. Feynman [2], based on
³⁰⁸ the work of Sin-Itiro Tomonaga [3], developed an electromagnetic theory consistent
³⁰⁹ with special relativity and quantum mechanics that describes how matter and light
³¹⁰ interact; the so-called *quantum electrodynamics* (QED) was born.

³¹¹ QED has become the blueprint for developing theories that describe the universe.
³¹² It was the first example of a quantum field theory (QFT), which is the theoretical
³¹³ framework for building quantum mechanical models that describes particles and their
³¹⁴ interactions. QFT is composed of a set of mathematical tools that combines classical
³¹⁵ fields, special relativity and quantum mechanics, while keeping the quantum point
³¹⁶ particles and locality ideas.

³¹⁷ This chapter gives an overview of the standard model of particle physics, starting

318 with a description of the particles and their interactions, followed by a description of
 319 the electroweak interaction, the Higgs boson and the associated production of Higgs
 320 boson and a single top quark (tH). The description contained in this chapter is based
 321 on References [4–6].

322 1.2 Standard model of particle physics

323 The *standard model of particle physics (SM)* describes particle physics at the funda-
 324 mental level in terms of a collection of interacting particles and fields. The full picture
 325 of the SM is composed of three fields¹ whose excitations are interpreted as particles
 326 called mediators or force-carriers, a set of fields whose excitations are interpreted as
 327 elementary particles interacting through the exchange of those mediators, and a field
 328 that gives the mass to elementary particles. Figure 1.1 shows a scheme of the SM
 329 particles’ organization. In addition, for each of the particles in the scheme there exists
 330 an antiparticle with the same mass and opposite quantum numbers. The existence of
 331 antiparticles is a prediction of the relativistic quantum mechanics from the solution
 332 of the Dirac equation for which a negative energy solution is also possible. In some
 333 cases a particle is its own anti-particle, like photon or Higgs boson.

334 The mathematical formulation of the SM is based on group theory and the use of
 335 Noether’s theorem [8] which states that for a physical system modeled by a Lagrangian
 336 that is invariant under a group of transformations a conservation law is expected. For
 337 instance, a system described by a time-independent Lagrangian is invariant (symmet-
 338 ric) under time changes (transformations) with the total energy conservation law as
 339 the expected conservation law. In QED, the charge operator (Q) is the generator of

¹ The formal and complete treatment of the SM is out of the scope of this document, however a plenty of textbooks describing it at several levels are available in the literature. The treatment in References [5, 6] is quite comprehensive and detailed. Note that gravitational field is not included in the standard model formulation

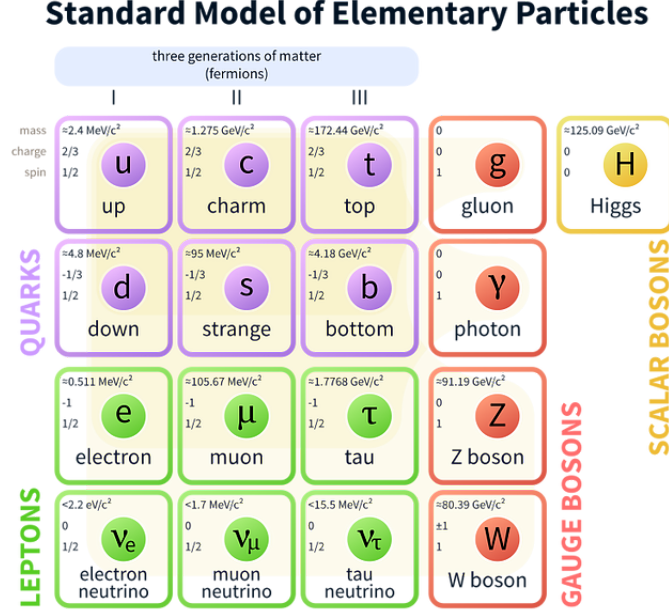


Figure 1.1: Schematic representation of the Standard Model of particle physics. The SM is a theoretical model intended to describe three of the four fundamental forces of the universe in terms of a set of particles and their interactions. [7].

340 the U(1) symmetry which according to the Noether's theorem means that there is a
 341 conserved quantity; this conserved quantity is the electric charge and thus the law
 342 conservation of electric charge is established.

343 In the SM, the symmetry group $SU(3)_C \otimes SU(2)_L \otimes U(1)_Y$ describes three of the
 344 four fundamental interactions in nature (see Section 1.2.2): strong interaction (SI),
 345 weak interaction (WI) and electromagnetic interactions (EI) in terms of symmetries
 346 associated to physical quantities:

- 347 • Strong: $SU(3)_C$ associated to color charge
- 348 • Weak: $SU(2)_L$ associated to weak isospin and chirality
- 349 • Electromagnetic: $U(1)_Y$ associated to weak hypercharge and electric charge
- 350 It will be shown that the electromagnetic and weak interactions are combined in

351 the so-called electroweak interaction where chirality, hypercharge, weak isospin and
 352 electric charge are the central concepts.

353 **1.2.1 Fermions**

354 The basic constituents of the ordinary matter at the lowest level, which form the set
 355 of elementary particles in the SM formulation, are quarks and leptons. All of them
 356 have spin 1/2, therefore they are classified as fermions since they obey Fermi-Dirac
 357 statistics. There are six *flavors* of quarks and three of leptons organized in three
 358 generations, or families, as shown in Table 1.1.

		Generation		
		1st	2nd	3rd
Leptons	Type	Charged	Electron (e)	Moun(μ)
	Neutral	Electron neutrino (ν_e)	Muon neutrino (ν_μ)	Tau neutrino (ν_τ)
Quarks	Up-type	Up (u)	Charm (c)	Top (t)
	Down-type	Down (d)	Strange (s)	Bottom (b)

Table 1.1: Fermions of the SM. There are six flavors of quarks and three of leptons, organized in three generations, or families, composed of two pairs of closely related particles. The close relationship is motivated by the fact that each pair of particles is a member of an $SU(2)_L$ doublet that has an associated invariance under isospin transformations. WI between leptons is limited to the members of the same generation; WI between quarks is not limited but greatly favored, to same generation members.

359

360 There is a mass hierarchy between generations (see Table 1.2), where the higher
 361 generation particles decays to the lower one, which can explain why the ordinary
 362 matter is made of particles from the first generation. In the SM, neutrinos are modeled
 363 as massless particles so they are not subject to this mass hierarchy; however, today it
 364 is known that neutrinos are massive so the hierarchy could be restated. The reason
 365 behind this mass hierarchy is one of the most important open questions in particle
 366 physics, and it becomes more puzzling when noticing that the mass difference between

367 first and second generation fermions is small compared to the mass difference with
 368 respect to the third generation.

Lepton	Mass (MeV/c ²)	Quark	Mass (MeV/c ²)
e	0.51	u	2.2
μ	105.65	c	1.28×10^3
τ	1776.86	t	173.1×10^3
ν_e	Unknown	d	4.7
ν_μ	Unknown	s	96
τ_μ	Unknown	b	4.18×10^3

Table 1.2: Fermion masses [9]. Generations differ by mass in a way that has been interpreted as a mass hierarchy. Approximate values with no uncertainties are used, for comparison purpose.

369

370 Usually, the second and third generation fermions are produced in high energy
 371 processes, like the ones recreated in particle accelerators.

372 **1.2.1.1 Leptons**

373 A lepton is an elementary particle that is not subject to the SI. As seen in Table 1.1,
 374 there are two types of leptons, the charged ones (electron, muon and tau) and the
 375 neutral ones (the three neutrinos). The electric charge (Q) is the property that gives
 376 leptons the ability to participate in the EI. From the classical point of view, Q plays
 377 a central role determining, among others, the strength of the electric field through
 378 which the electromagnetic force is exerted. It is clear that neutrinos are not affected
 379 by EI because they don't carry electric charge.

380 Another feature of the leptons that is fundamental in the mathematical description
 381 of the SM is the chirality, which is closely related to spin and helicity. Helicity
 382 defines the handedness of a particle by relating its spin and momentum such that
 383 if they are parallel then the particle is right-handed; if spin and momentum are

384 antiparallel the particle is said to be left-handed. The study of parity conservation
 385 (or violation) in β -decay has shown that only left-handed electrons/neutrinos or right-
 386 handed positrons/anti-neutrinos are created [10]; the inclusion of that feature in the
 387 theory was achieved by using projection operators for helicity, however, helicity is
 388 frame dependent for massive particles which makes it not Lorentz invariant and then
 389 another related attribute has to be used: *chirality*.

390 Chirality is a purely quantum attribute which makes it not so easy to describe in
 391 graphical terms but it defines how the wave function of a particle transforms under
 392 certain rotations. As with helicity, there are two chiral states, left-handed chiral (L)
 393 and right-handed chiral (R). In the highly relativistic limit where $E \approx p \gg m$ helicity
 394 and chirality converge, becoming exactly the same for massless particles.

395 In the following, when referring to left-handed (right-handed) it will mean left-
 396 handed chiral (right-handed chiral). The fundamental fact about chirality is that
 397 while EI and SI are not sensitive to chirality, in WI left-handed and right-handed
 398 fermions are treated asymmetrically, such that only left-handed fermions and right-
 399 handed anti-fermions are allowed to couple to WI mediators, which is a violation of
 400 parity. The way to translate this statement in a formal mathematical formulation is
 401 based on the isospin symmetry group $SU(2)_L$.

402 Each generation of leptons is seen as a weak isospin doublet.² The left-handed
 403 charged lepton and its associated left-handed neutrino are arranged in doublets of
 404 weak isospin $T=1/2$ while their right-handed partners are singlets:

$$\begin{pmatrix} \nu_l \\ l \end{pmatrix}_L, l_R := \begin{pmatrix} \nu_e \\ e \end{pmatrix}_L, \begin{pmatrix} \nu_\mu \\ \mu \end{pmatrix}_L, \begin{pmatrix} \nu_\tau \\ \tau \end{pmatrix}_L, e_R, \mu_R, \tau_R, \nu_{eR}, \nu_{\mu R}, \nu_{\tau R} \quad (1.1)$$

405 The isospin third component refers to the eigenvalues of the weak isospin operator

² The weak isospin is an analogy of the isospin symmetry in strong interaction where neutron and proton are affected equally by strong force but differ in their charge.

406 which for doublets is $T_3 = \pm 1/2$, while for singlets it is $T_3 = 0$. The physical meaning
 407 of this doublet-singlet arrangement falls in that the WI couples the two particles in
 408 the doublet by exchanging the interaction mediator while the singlet member is not
 409 involved in WI. The main properties of the leptons are summarized in Table 1.3.

410 Although all three flavor neutrinos have been observed, their masses remain un-
 411 known and only some estimations have been made [11]. The main reason is that
 412 the flavor eigenstates are not the same as the mass eigenstates which implies that
 413 when a neutrino is created its mass state is a linear combination of the three mass
 414 eigenstates and experiments can only probe the squared difference of the masses. The
 415 Pontecorvo-Maki-Nakagawa-Sakata (PMNS) mixing matrix encodes the relationship
 416 between flavor and mass eigenstates.

Lepton	$Q(e)$	T_3	L_e	L_μ	L_τ	Lifetime (s)
Electron (e)	-1	-1/2	1	0	0	Stable
Electron neutrino(ν_e)	0	1/2	1	0	0	Unknown
Muon (μ)	-1	-1/2	0	1	0	2.19×10^{-6}
Muon neutrino (ν_μ)	0	1/2	0	1	0	Unknown
Tau (τ)	-1	-1/2	0	0	1	290.3×10^{-15}
Tau neutrino (ν_τ)	0	1/2	0	0	1	Unknown

Table 1.3: Lepton properties [9]. Q: electric charge, T_3 : weak isospin. Only left-handed leptons and right-handed anti-leptons participate in the WI. Anti-particles with inverted T_3 , Q and lepton number complete the leptons set but are not listed. Right-handed leptons and left-handed anti-leptons, neither listed, form weak isospin singlets with $T_3 = 0$ and do not take part in the weak interaction.

417

418 1.2.1.2 Quarks

419 Quarks are the basic constituents of protons and neutrons. The way quarks join to
 420 form bound states, called *hadrons*, is through the SI. Quarks are affected by all the
 421 fundamental interactions which means that they carry all the four types of charges:
 422 color, electric charge, weak isospin and mass.

Flavor	$Q(e)$	I_3	T_3	B	C	S	T	B'	Y	Color
Up (u)	2/3	1/2	1/2	1/3	0	0	0	0	1/3	r,b,g
Charm (c)	2/3	0	1/2	1/3	1	0	0	0	4/3	r,b,g
Top(t)	2/3	0	1/2	1/3	0	0	1	0	4/3	r,b,g
Down(d)	-1/3	-1/2	-1/2	1/3	0	0	0	0	1/3	r,b,g
Strange(s)	-1/3	0	-1/2	1/3	0	-1	0	0	-2/3	r,b,g
Bottom(b)	-1/3	0	-1/2	1/3	0	0	0	-1	-2/3	r,b,g

Table 1.4: Quark properties [9]. Q: electric charge, I_3 : isospin, T_3 : weak isospin, B: baryon number, C: charmness, S: strangeness, T: topness, B' : bottomness, Y: hypercharge. Anti-quarks posses the same mass and spin as quarks but all charges (color, flavor numbers) have opposite sign.

423

424 Table 1.4 summarizes the features of quarks, among which the most remarkable
 425 is their fractional electric charge. Note that fractional charge is not a problem, given
 426 that quarks are not found isolated, but serves to explain how composed particles are
 427 formed out of two or more valence quarks³.

428 Color charge is responsible for the SI between quarks and is the symmetry ($SU(3)_C$)
 429 that defines the formalism to describe SI. There are three colors: red (r), blue (b)
 430 and green (g) and their corresponding three anti-colors; thus each quark carries one
 431 color unit while anti-quarks carries one anti-color unit. As explained in Section 1.2.2,
 432 quarks are not allowed to be isolated due to the color confinement effect, hence, their
 433 features have been studied indirectly by observing their bound states created when

- 434 • one quark with a color charge is attracted by an anti-quark with the correspond-
 435 ing anti-color charge forming a colorless particle called a *meson*.

 436 • three quarks (anti-quarks) with different color (anti-color) charges are attracted
 437 among them forming a colorless particle called a *baryon (anti-baryon)*.

³ Hadrons can contain an indefinite number of virtual quarks and gluons, known as the quark and gluon sea, but only the valence quarks determine hadrons' quantum numbers.

438 In practice, when a quark is left alone isolated a process called *hadronization* occurs
 439 where the quark emits gluons (see Section 1.2.4) which eventually will generate new
 440 quark-antiquark pairs and so on; those quarks will recombine to form hadrons that
 441 will decay into leptons. This proliferation of particles looks like a *jet* coming from
 442 the isolated quark. More details about the hadronization process and jet structure
 443 will be given in chapter3.

444 In the first version of the quark model (1964), M. Gell-Mann [12] and G. Zweig
 445 [13, 14] developed a consistent way to classify hadrons according to their properties.
 446 Only three quarks (u, d, s) were involved in a scheme in which all baryons have baryon
 447 number $B=1$ and therefore quarks have $B=1/3$; non-baryons have $B=0$. Baryon
 448 number is conserved in SI and EI which means that single quarks cannot be created
 449 but in pairs $q - \bar{q}$.

450 The scheme organizes baryons in a two-dimensional space (I_3 - Y); Y (hyper-
 451 charge) and I_3 (isospin) are quantum numbers related by the Gell-Mann-Nishijima
 452 formula [15, 16]:

$$Q = I_3 + \frac{Y}{2} \quad (1.2)$$

453 where $Y = B + S + C + T + B'$ are the quantum numbers listed in Table 1.4.

454 There are six quark flavors organized in three generations (see Table 1.1) fol-
 455 lowing a mass hierarchy which, again, implies that higher generations decay to first
 456 generation quarks.

	Quarks			T_3	Y_W	Leptons			T_3	Y_W
Doublets	$(\frac{u}{d'})_L$	$(\frac{c}{s'})_L$	$(\frac{t}{b'})_L$	$(\frac{1/2}{-1/2})$	$1/3$	$(\nu_e)_L$	$(\nu_\mu)_L$	$(\nu_\tau)_L$	$(\frac{1/2}{-1/2})$	-1
Singlets	u_R	c_R	t_R	0	$4/3$	ν_{eR}	$\nu_{\mu R}$	$\nu_{\tau R}$		
	d'_R	s'_R	b'_R	0	$-2/3$	e_R	μ_R	τ_R	0	-2

Table 1.5: Fermion weak isospin and weak hypercharge multiplets. Weak hypercharge is calculated through the Gell-Mann-Nishijima formula 1.2 but using the weak isospin and charge for quarks.

457

458 Isospin doublets of quarks are also defined (see Table 1.5), and same as for neutrinos,
 459 the WI eigenstates are not the same as the mass eigenstates which means that
 460 members of different quark generations are connected by the WI mediator; thus, up-
 461 type quarks are coupled not to down-type quarks (the mass eigenstates) directly but
 462 to a superposition of down-type quarks (q'_d ; *the weak eigenstates*) via WI according
 463 to:

464

$$\begin{aligned} q'_d &= V_{CKM} q_d \\ \begin{pmatrix} d' \\ s' \\ b' \end{pmatrix} &= \begin{pmatrix} V_{ud} & V_{us} & V_{ub} \\ V_{cd} & V_{cs} & V_{cb} \\ V_{td} & V_{ts} & V_{tb} \end{pmatrix} \begin{pmatrix} d \\ s \\ b \end{pmatrix} \end{aligned} \quad (1.3)$$

465 where V_{CKM} is known as Cabibbo-Kobayashi-Maskawa (CKM) mixing matrix [17,18]
 466 given by

$$\begin{pmatrix} |V_{ud}| & |V_{us}| & |V_{ub}| \\ |V_{cd}| & |V_{cs}| & |V_{cb}| \\ |V_{td}| & |V_{ts}| & |V_{tb}| \end{pmatrix} = \begin{pmatrix} 0.97427 \pm 0.00015 & 0.22534 \pm 0.00065 & 0.00351^{+0.00015}_{-0.00014} \\ 0.22520 \pm 0.00065 & 0.97344 \pm 0.00016 & 0.0412^{+0.0011}_{-0.0005} \\ 0.00867^{+0.00029}_{-0.00031} & 0.0404^{+0.0011}_{-0.0005} & 0.999146^{+0.000021}_{-0.000046} \end{pmatrix}. \quad (1.4)$$

467 The weak decays of quarks are represented in the diagram of Figure 1.2; again
 468 the CKM matrix plays a central role since it contains the probabilities for the differ-
 469 ent quark decay channels, in particular, note that quark decays are greatly favored
 470 between generation members.

471 CKM matrix is a 3×3 unitary matrix parametrized by three mixing angles and
 472 the *CP-mixing phase*; the latter is the parameter responsible for the Charge-Parity

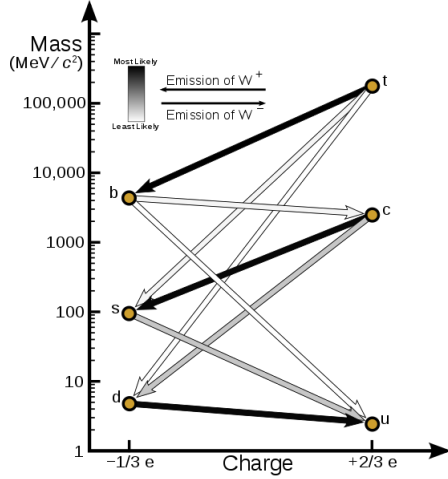


Figure 1.2: Transformations between quarks through the exchange of a WI. Higher generations quarks decay to first generation quarks by emitting a W boson. The arrow color indicates the likelihood of the transition according to the grey scale in the top left side which represent the CKM matrix parameters [19].

473 symmetry violation (CP-violation) in the SM. The fact that the top quark decays
 474 almost all the time to a bottom quark is exploited in this thesis when making the
 475 selection of the signal events by requiring the presence of a jet tagged as a jet coming
 476 from a b quark in the final state.

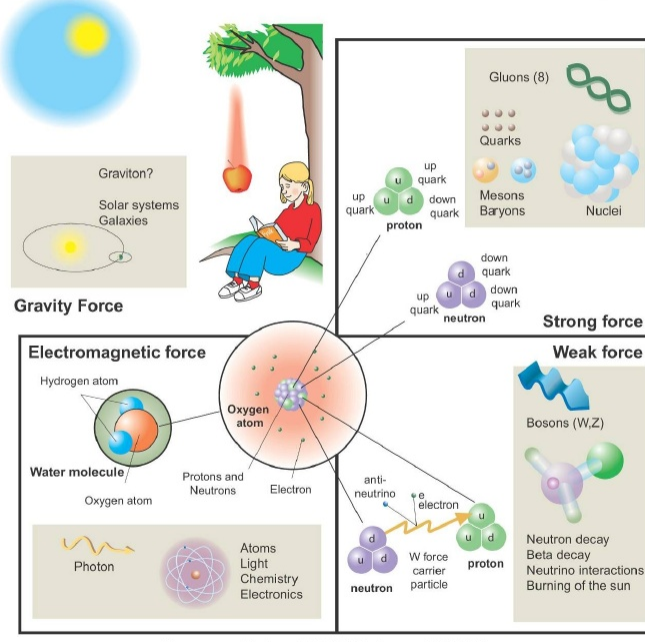
477 1.2.2 Fundamental interactions

478 Even though there are many manifestations of force in nature, like the ones repre-
 479 sented in Figure 1.3, we can classify all of them in four fundamental interactions:

- 480 • *Electromagnetic interaction (EI)* affects particles that are *electrically charged*,
 481 like electrons and protons. Figure 1.4a. shows a graphical representation, known
 482 as *Feynman diagram*, of electron-electron scattering.
- 483 • *Strong interaction (SI)* described by Quantum Chromodynamics (QCD). Hadrons
 484 like the proton and the neutron have internal structure given that they are com-

Fundamental interactions.

Illustration: Typoform



Summer School KPI 15 August 2009

Figure 1.3: Fundamental interactions in nature. Despite the many manifestations of forces in nature, we can track all of them back to one of the fundamental interactions. The most common forces are gravity and electromagnetic given that all of us are subject and experience them in everyday life.

485 posed of two or more valence quarks⁴. Quarks have fractional electric charge
 486 which means that they are subject to electromagnetic interaction and in the case
 487 of the proton they should break apart due to electrostatic repulsion; however,
 488 quarks are held together inside the hadrons against their electrostatic repulsion
 489 by the *Strong Force* through the exchange of *gluons*. The analog to the electric
 490 charge is the *color charge*. Electrons and photons are elementary particles as
 491 quarks but they don't carry color charge, therefore they are not subject to SI. A
 492 Feynman diagram for gluon exchange between quarks is shown in Figure 1.4b.

- 493 • *Weak interaction (WI)* described by the weak theory (WT), is responsible, for
 494 instance, for the radioactive decay in atoms and the deuterium production

⁴ Particles made of four and five quarks are exotic states not so common.

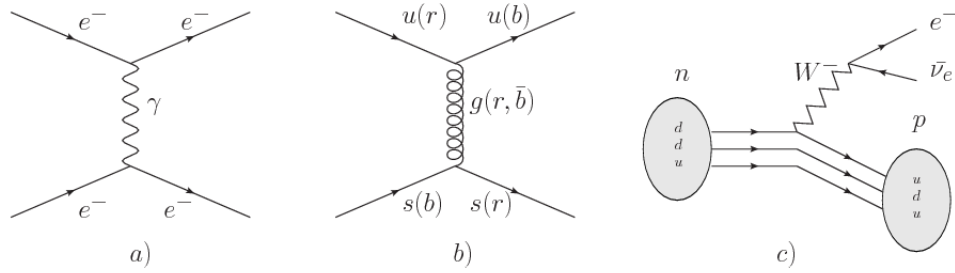


Figure 1.4: Feynman diagrams representing the interactions in SM; a) EI: e - e scattering; b) SI: gluon exchange between quarks ; c) WI: β -decay

within the sun. Quarks and leptons are the particles affected by the weak interaction; they possess a property called *flavor charge* (see 1.2.1) which can be changed by emitting or absorbing one weak force mediator. There are three mediators of the *weak force* known as Z boson in the case of electrically neutral flavor changes and W^\pm bosons in the case of electrically charged flavor changes. The *weak isospin* is the WI analog to electric charge in EI, and color charge in SI, and defines how quarks and leptons are affected by the weak force. Figure 1.4c. shows the Feynman diagram of β -decay where a neutron (n) is transformed in a proton (p) by emitting a W^- particle.

- *Gravitational interaction (GI)* described by General Theory of Relativity (GR). It is responsible for the structure of galaxies and black holes as well as the expansion of the universe. As a classical theory, in the sense that it can be formulated without even appeal to the concept of quantization, it implies that the space-time is a continuum and predictions can be made without limitation to the precision of the measurement tools. The latter represents a direct contradiction of the quantum mechanics principles. Gravity is deterministic while quantum mechanics is probabilistic; despite that, efforts to develop a quantum theory of gravity have predicted the *graviton* as mediator of the gravitational

513 force⁵.

Interaction	Acts on	Relative strength	Range (m)	Mediators
Electromagnetic (QED)	Electrically charged particles	10^{-2}	Infinite	Photon
Strong (QCD)	Quarks and gluons	1	10^{-15}	Gluon
Weak (WI)	Leptons and quarks	10^{-6}	10^{-18}	W^\pm, Z
Gravitational (GI)	Massive particles	10^{-39}	Infinite	Graviton

Table 1.6: Fundamental interactions features [20].

514

515 Table 1.6 summarizes the main features of the fundamental interactions. The
 516 strength of the interactions is represented by the coupling constants which depend
 517 on the energy scale at which the interaction is evaluated, therefore, it is the relative
 518 strength of the fundamental forces that reveals the meaning of strong and weak; in
 519 a context where the relative strength of the SI is 1, the EI is about hundred times
 520 weaker and WI is about million times weaker than the SI. A good description on how
 521 the relative strength and range of the fundamental interactions are calculated can
 522 be found in References [20, 21]. In the everyday life, only EI and GI are explicitly
 523 experienced due to the range of these interactions; i.e., at the human scale distances
 524 only EI and GI have appreciable effects, in contrast to SI which at distances greater
 525 than 10^{-15} m become negligible. Is it important to clarify that the weakness of the
 526 WI is attributed to the fact that its mediators are highly massive which affects the
 527 propagators of the interaction, as a result, the effect of the coupling constant is
 528 reduced.

⁵ Actually a wide variety of theories have been developed in an attempt to describe gravity; some famous examples are string theory and supergravity.

529 **1.2.3 Gauge invariance.**

530 QED was built successfully on the basis of the classical electrodynamics theory (CED)
 531 of Maxwell and Lorentz, following theoretical and experimental requirements imposed
 532 by

- 533 • Lorentz invariance: independence on the reference frame.
- 534 • Locality: interacting fields are evaluated at the same space-time point to avoid
 535 action at a distance.
- 536 • Renormalizability: physical predictions are finite and well defined.
- 537 • Particle spectrum, symmetries and conservation laws already known must emerge
 538 from the theory.
- 539 • Local gauge invariance.

540 The gauge invariance requirement reflects the fact that the fundamental fields
 541 cannot be directly measured but associated fields which are the observables. Electric
 542 (**E**) and magnetic (**B**) fields in CED are associated with the electric scalar potential
 543 V and the vector potential **A**. In particular, **E** can be obtained by measuring the
 544 change in the space of the scalar potential (ΔV); however, two scalar potentials
 545 differing by a constant f correspond to the same electric field. The same happens
 546 in the case of the vector potential **A**; thus, different configurations of the associated
 547 fields result in the same set of values of the observables. The freedom in choosing one
 548 particular configuration is known as *gauge freedom*; the transformation law connecting
 549 two configurations is known as *gauge transformation* and the fact that the observables
 550 are not affected by a gauge transformation is called *gauge invariance*.

551 When the gauge transformation:

$$\begin{aligned} \mathbf{A} &\rightarrow \mathbf{A} - \Delta f \\ V &\rightarrow V - \frac{\partial f}{\partial t} \end{aligned} \tag{1.5}$$

552 is applied to Maxwell equations, they are still satisfied and the fields remain invariant.
 553 Thus, CED is invariant under gauge transformations and is called a *gauge theory*.
 554 The set of all gauge transformations form the *symmetry group* of the theory, which
 555 according to the group theory, has a set of *group generators*. The number of group
 556 generators determine the number of *gauge fields* of the theory.

557 As mentioned in the first lines of Section 1.2, QED has one symmetry group ($U(1)$)
 558 with one group generator (the Q operator) and one gauge field (the electromagnetic
 559 field A^μ). In CED there is not a clear definition, beyond the historical convention,
 560 of which fields are the fundamental and which are the associated, but in QED the
 561 fundamental field is A^μ . When a gauge theory is quantized, the gauge fields are
 562 quantized and their quanta are called *gauge bosons*. The word boson characterizes
 563 particles with integer spin which obey Bose-Einstein statistics.

564 As will be detailed in Section 1.3, interactions between particles in a system can
 565 be obtained by considering first the Lagrangian density of free particles in the sys-
 566 tem, which of course is incomplete because the interaction terms have been left out,
 567 and demanding global phase transformation invariance. Global phase transforma-
 568 tion means that a gauge transformation is performed identically to every point
 569 in the space⁶ and the Lagrangian remains invariant. Then, the global transforma-
 570 tion is promoted to a local phase transformation (this time the gauge transformation
 571 depends on the position in space) and again invariance is required.

⁶ Here space corresponds to the 4-dimensional space i.e. space-time.

572 Due to the space dependence of the local transformation, the Lagrangian density is
 573 not invariant anymore. In order to reinstate the gauge invariance, the gauge covariant
 574 derivative is introduced in the Lagrangian and with it the gauge field responsible for
 575 the interaction between particles in the system. The new Lagrangian density is gauge
 576 invariant, includes the interaction terms needed to account for the interactions and
 577 provides a way to explain the interaction between particles through the exchange of
 578 the gauge boson.

579 This recipe was used to build QED and the theories that aim to explain the
 580 fundamental interactions.

581 1.2.4 Gauge bosons

582 The importance of the gauge bosons comes from the fact that they are the force
 583 mediators or force carriers. The features of the gauge bosons reflect those of the fields
 584 they represent and they are extracted from the Lagrangian density used to describe
 585 the interactions. In Section 1.3, it will be shown how the gauge bosons of the EI and
 586 WI emerge from the electroweak Lagrangian. The SI gauge bosons features are also
 587 extracted from the SI Lagrangian but it is not detailed in this document. The main
 588 features of the SM gauge bosons will be briefly presented below and summarized in
 589 Table 1.7.

- 590 • **Photon.** EI occurs when the photon couples to (is exchanged between) parti-
 591 cles carrying electric charge; however, The photon itself does not carry electric
 592 charge, therefore, there is no coupling between photons. Given that the photon
 593 is massless the EI is of infinite range, i.e., electrically charged particles interact
 594 even if they are located far away one from each other; this also implies that
 595 photons always move with the speed of light.

- 596 • **Gluon.** SI is mediated by gluons which just as photons are massless. They
 597 carry one unit of color charge and one unit of anticolor charge, hence, gluons
 598 can couple to other gluons. As a result, the range of the SI is not infinite
 599 but very short due to the attraction between gluons, giving rise to the *color*
 600 *confinement* which explains why color charged particles cannot be isolated but
 601 live within composite particles, like quarks inside protons.
- 602 • **W, Z.** W^\pm and Z, are massive which explains their short-range. Given that
 603 the WI is the only interaction that can change the flavor of the interacting
 604 particles, the W boson is the responsible for the nuclear transmutation where
 605 a neutron is converted into a proton or vice versa with the involvement of an
 606 electron and a neutrino (see Figure 1.4c). The Z boson is the responsible for the
 607 neutral weak processes like neutrino elastic scattering where no electric charge
 608 but momentum transference is involved. WI gauge bosons carry isospin charge
 609 which makes interaction between them possible.

Interaction	Mediator	Electric charge (e)	Color charge	Weak Isospin	mass (GeV/c ²)
Electromagnetic	Photon (γ)	0	No	0	0
Strong	Gluon (g)	0	Yes -octet	No	0
Weak	W^\pm	± 1	No	± 1	80.385 ± 0.015
	Z	0	No	0	91.188 ± 0.002

Table 1.7: SM gauge bosons main features [9].

610

611 1.3 Electroweak unification and the Higgs 612 mechanism

613 Physicists dream of building a theory that contains all the interactions in one single
 614 interaction, i.e., showing that at some scale in energy all the four fundamental inter-

actions are unified and only one interaction emerges in a *Theory of everything*. The first sign of the feasibility of such unification came from success in the construction of the CED. Einstein spent years trying to reach that full unification, which by 1920 only involved electromagnetism and gravity, with no success; however, a new partial unification was achieved in the 1960's, when S.Glashow [22], A.Salam [23] and S.Weinberg [24] independently proposed that electromagnetic and weak interactions are two manifestations of a more general interaction called *electroweak interaction* (EWI). EWI was developed by following the useful prescription provided by QED and the gauge invariance principles.

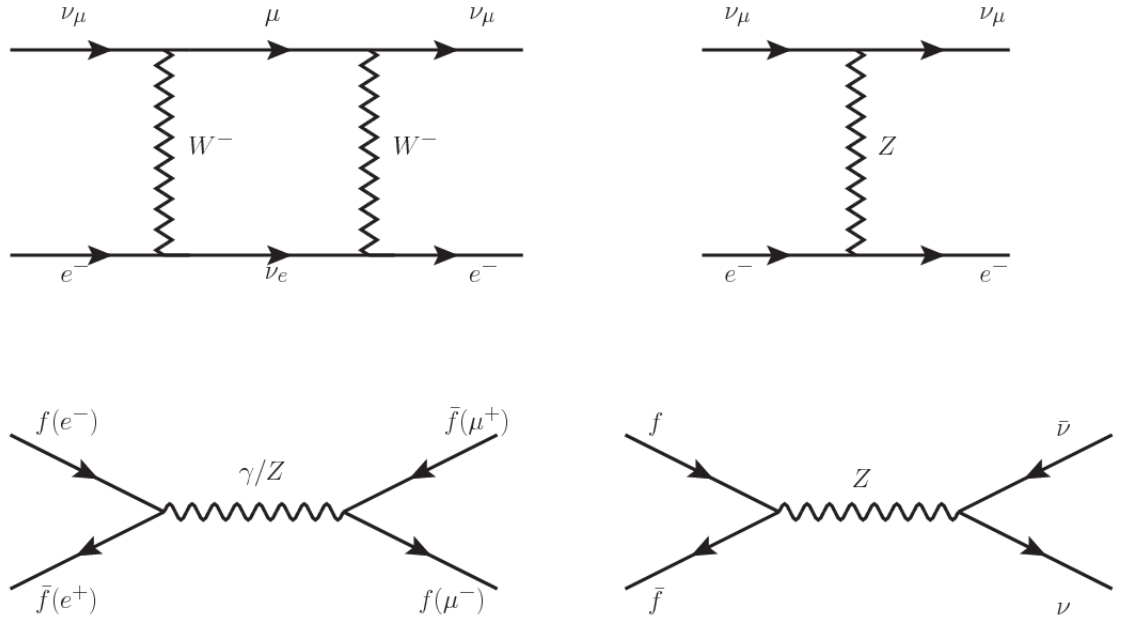


Figure 1.5: Top: $\nu_\mu - e^-$ scattering going through charged currents (left) and neutral currents (right). Bottom: neutral current processes for charged fermions (left) and involving neutrinos (right). While neutral current processes involving only charged fermions can proceed through EI or WI, those involving neutrinos can only proceed via WI.

The *classic* weak theory developed by Fermi, did not have the concept of the W boson but instead it was treated as a point interaction with the dimensionful constant G_F associated with it. It works really well at low energies very far off the W mass

627 shell. When going up in energy, the theory of weak interactions involving the W
 628 boson is capable of explaining the β -decay and in general the processes mediated by
 629 W^\pm bosons. However, there were some processes like the $\nu_\mu - e$ scattering which
 630 would require the exchange of two W bosons (see Figure 1.5 top diagrams) giving
 631 rise to divergent loop integrals and then non-finite predictions. The EWI theory, by
 632 including neutral currents involving fermions via the exchange of a neutral bosons Z,
 633 overcomes those divergences and the predictions become realistic.

634 Neutral weak interaction vertices conserve flavor in the same way as the electro-
 635 magnetic vertices do, but additionally, the Z boson can couple to neutrinos which
 636 implies that processes involving charged fermions can proceed through EI or WI but
 637 processes involving neutrinos can proceed only through WI.

638 The prescription to build a gauge theory of the WI consists of proposing a free
 639 field Lagrangian density that includes the particles involved; next, by requesting
 640 invariance under global phase transformations first and generalizing to local phase
 641 transformations invariance later, the conserved currents are identified and interactions
 642 are generated by introducing gauge fields. Given that the goal is to include the EI
 643 and WI in a single theory, the group symmetry considered should be a combination of
 644 $SU(2)_L$ and $U(1)_{em}$, however the latter cannot be used directly because the EI treats
 645 left and right-handed particles indistinctly in contrast to the former. Fortunately, the
 646 weak hypercharge, which is a combination of the weak isospin and the electric charge
 647 (Eqn. 1.2) is suitable to be used since it is conserved by the EI and WI. Thus, the
 648 symmetry group to be considered is

$$G \equiv SU(2)_L \otimes U(1)_Y \quad (1.6)$$

649 The following treatment applies to any of the fermion generations, but for sim-

650 plicity the first generation of leptons will be considered [5, 6, 25, 26].

651 Given the first generation of leptons

$$\psi_1 = \begin{pmatrix} \nu_e \\ e^- \end{pmatrix}_L, \quad \psi_2 = \nu_{eR}, \quad \psi_3 = e_R^- \quad (1.7)$$

652 the charged fermionic currents are given by

$$J_\mu \equiv J_\mu^+ = \bar{\nu}_{eL} \gamma_\mu e_L, \quad J_\mu^\dagger \equiv J_\mu^- = \bar{e}_L \gamma_\mu \nu_{eL} \quad (1.8)$$

653 and the free Lagrangian is given by

$$\mathcal{L}_0 = \sum_{j=1}^3 i\bar{\psi}_j(x) \gamma^\mu \partial_\mu \psi_j(x). \quad (1.9)$$

654 Mass terms are included directly in the QED free Lagrangians since they preserve
 655 the invariance under the symmetry transformations involved which treat left and right
 656 handed particles similarly, however mass terms of the form

$$m_W^2 W_\mu^\dagger(x) W^\mu(x) + \frac{1}{2} m_Z^2 Z_\mu(x) Z^\mu(x) - m_e \bar{\psi}_e(x) \psi_e(x) \quad (1.10)$$

657 which represent the mass of W^\pm , Z and electrons, are not invariant under G trans-
 658 formations, therefore the gauge fields described by the EWI are in principle massless.

659 Experiments have shown that the EWI gauge fields are not massless [27–30];
 660 however, they have to acquire mass through a mechanism compatible with the gauge
 661 invariance; that mechanism is known as the *Higgs mechanism* and will be considered
 662 later in this Section. The global transformations in the combined symmetry group G
 663 can be written as

$$\begin{aligned}
\psi_1(x) &\xrightarrow{G} \psi'_1(x) \equiv U_Y U_L \psi_1(x), \\
\psi_2(x) &\xrightarrow{G} \psi'_2(x) \equiv U_Y \psi_2(x), \\
\psi_3(x) &\xrightarrow{G} \psi'_3(x) \equiv U_Y \psi_3(x)
\end{aligned} \tag{1.11}$$

664 where U_L represent the $SU(2)_L$ transformation acting only on the weak isospin dou-
 665 blet and U_Y represent the $U(1)_Y$ transformation acting on all the weak isospin mul-
 666 tiplets. Explicitly

$$U_L \equiv \exp\left(i \frac{\sigma_i}{2} \alpha^i\right), \quad U_Y \equiv \exp(i y_i \beta) \quad (i = 1, 2, 3) \tag{1.12}$$

667 with σ_i the Pauli matrices and y_i the weak hypercharges. In order to promote the
 668 transformations from global to local while keeping the invariance, it is required that
 669 $\alpha^i = \alpha^i(x)$, $\beta = \beta(x)$ and the replacement of the ordinary derivatives by the covariant
 670 derivatives

$$\begin{aligned}
D_\mu \psi_1(x) &\equiv \left[\partial_\mu + ig\sigma_i W_\mu^i(x)/2 + ig'y_1 B_\mu(x) \right] \psi_1(x) \\
D_\mu \psi_2(x) &\equiv \left[\partial_\mu + ig'y_2 B_\mu(x) \right] \psi_2(x) \\
D_\mu \psi_3(x) &\equiv \left[\partial_\mu + ig'y_3 B_\mu(x) \right] \psi_3(x)
\end{aligned} \tag{1.13}$$

671 introducing in this way four gauge fields, $W_\mu^i(x)$ and $B_\mu(x)$, in the process. The
 672 covariant derivatives (Eqn. 1.13) are required to transform in the same way as fermion
 673 fields $\psi_i(x)$ themselves, therefore, the gauge fields transform as:

$$\begin{aligned} B_\mu(x) &\xrightarrow{G} B'_\mu(x) \equiv B_\mu(x) - \frac{1}{g'} \partial_\mu \beta(x) \\ W_\mu^i(x) &\xrightarrow{G} W_\mu^{i\prime}(x) \equiv W_\mu^i(x) - \frac{i}{g} \partial_\mu \alpha_i(x) - \varepsilon_{ijk} \alpha_i(x) W_\mu^j(x). \end{aligned} \quad (1.14)$$

674 The G invariant version of the Lagrangian density 1.9 can be written as

$$\mathcal{L}_0 = \sum_{j=1}^3 i \bar{\psi}_j(x) \gamma^\mu D_\mu \psi_j(x) \quad (1.15)$$

675 where free massless fermion and gauge fields and fermion-gauge boson interactions
 676 are included. The EWI Lagrangian density must additionally include kinetic terms
 677 for the gauge fields (\mathcal{L}_G) which are built from the field strengths, according to

$$B_{\mu\nu}(x) \equiv \partial_\mu B_\nu - \partial_\nu B_\mu \quad (1.16)$$

$$W_{\mu\nu}^i(x) \equiv \partial_\mu W_\nu^i(x) - \partial_\nu W_\mu^i(x) - g \varepsilon^{ijk} W_\mu^j W_\nu^k \quad (1.17)$$

678 the last term in Eqn. 1.17 is added in order to hold the gauge invariance; therefore,

$$\mathcal{L}_G = -\frac{1}{4} B_{\mu\nu}(x) B^{\mu\nu}(x) - \frac{1}{4} W_{\mu\nu}^i(x) W_i^{\mu\nu}(x) \quad (1.18)$$

679 which contains not only the free gauge fields contributions, but also the gauge fields
 680 self-interactions and interactions among them.

681 The three weak isospin conserved currents resulting from the $SU(2)_L$ symmetry
 682 are given by

$$J_\mu^i(x) = \frac{1}{2} \bar{\psi}_1(x) \gamma_\mu \sigma^i \psi_1(x) \quad (1.19)$$

683 while the weak hypercharge conserved current resulting from the $U(1)_Y$ symmetry is
 684 given by

$$J_\mu^Y = \sum_{j=1}^3 \bar{\psi}_j(x) \gamma_\mu y_j \psi_j(x) \quad (1.20)$$

685 In order to evaluate the electroweak interactions modeled by an isos triplet field
 686 W_μ^i that couples to isospin currents J_μ^i with strength g and additionally the singlet
 687 field B_μ which couples to the weak hypercharge current J_μ^Y with strength $g'/2$. The
 688 interaction Lagrangian density to be considered is

$$\mathcal{L}_I = -g J^{i\mu}(x) W_\mu^i(x) - \frac{g'}{2} J^{Y\mu}(x) B_\mu(x) \quad (1.21)$$

689 Note that the weak isospin currents are not the same as the charged fermionic cur-
 690 rents that were used to describe the WI (Eqn. 1.8), since the weak isospin eigenstates
 691 are not the same as the mass eigenstates, but they are closely related

$$J_\mu = \frac{1}{2}(J_\mu^1 + iJ_\mu^2), \quad J_\mu^\dagger = \frac{1}{2}(J_\mu^1 - iJ_\mu^2). \quad (1.22)$$

692 The same happens with the gauge fields W_μ^i which are related to the mass eigen-
 693 states W^\pm by

$$W_\mu^+ = \frac{1}{\sqrt{2}}(W_\mu^1 - iW_\mu^2), \quad W_\mu^- = \frac{1}{\sqrt{2}}(W_\mu^1 + iW_\mu^2). \quad (1.23)$$

694 The fact that there are three weak isospin conserved currents is an indication that
 695 in addition to the charged fermionic currents, which couple charged to neutral leptons,
 696 there should be a neutral fermionic current that does not involve electric charge
 697 exchange; therefore, it couples neutral fermions or fermions of the same electric charge.
 698 The third weak isospin current contains a term that is similar to the electromagnetic

699 current (j_μ^{em}), indicating that there is a relation between them and resembling the
 700 Gell-Mann-Nishijima formula 1.2 adapted to electroweak interactions

$$Q = T_3 + \frac{Y_W}{2}. \quad (1.24)$$

701 Just as Q generates the $U(1)_{em}$ symmetry, the weak hypercharge generates the
 702 $U(1)_Y$ symmetry as said before. It is possible to write the relationship in terms of
 703 the currents as

$$j_\mu^{em} = J_\mu^3 + \frac{1}{2} J_\mu^Y. \quad (1.25)$$

704 The neutral gauge fields W_μ^3 and B_μ cannot be directly identified with the Z
 705 and the photon fields since the photon interacts similarly with left and right-handed
 706 fermions; however, they are related through a linear combination given by

$$A_\mu = B_\mu \cos \theta_W + W_\mu^3 \sin \theta_W \quad (1.26)$$

$$Z_\mu = -B_\mu \sin \theta_W + W_\mu^3 \cos \theta_W$$

where θ_W is known as the *Weinberg angle*. The interaction Lagrangian is now given by

$$\begin{aligned} \mathcal{L}_I = & -\frac{g}{\sqrt{2}}(J^\mu W_\mu^+ + J^{\mu\dagger} W_\mu^-) - \left(g \sin \theta_W J_\mu^3 + g' \cos \theta_W \frac{J_\mu^Y}{2}\right) A^\mu \\ & - \left(g \cos \theta_W J_\mu^3 - g' \sin \theta_W \frac{J_\mu^Y}{2}\right) Z^\mu \end{aligned} \quad (1.27)$$

707 the first term is the weak charged current interaction, while the second term is the

708 electromagnetic interaction under the condition

$$g \sin \theta_W = g' \cos \theta_W = e, \quad \frac{g'}{g} = \tan \theta_W \quad (1.28)$$

709 contained in the Eqn.1.25; the third term is the neutral weak current.

710

711 Note that the neutral fields transformation given by the Eqn. 1.26 can be written
 712 in terms of the coupling constants g and g' as:

$$A_\mu = \frac{g' W_\mu^3 + g B_\mu}{\sqrt{g^2 + g'^2}}, \quad Z_\mu = \frac{g W_\mu^3 - g' B_\mu}{\sqrt{g^2 + g'^2}}. \quad (1.29)$$

713 So far, the Lagrangian density describing the non-massive EWI is:

$$\mathcal{L}_{nmEWI} = \mathcal{L}_0 + \mathcal{L}_G \quad (1.30)$$

714 where fermion and gauge fields have been considered massless because their regular
 715 mass terms are manifestly non invariant under G transformations; therefore, masses
 716 have to be generated in a gauge invariant way. The mechanism by which this goal is
 717 achieved is known as the *Higgs mechanism* and is closely connected to the concept of
 718 *spontaneous symmetry breaking*.

719 1.3.1 Spontaneous symmetry breaking (SSB)

720 Figure 1.6 left shows a steel nail (top) which is subject to an external force; the form
 721 of the potential energy is also shown (bottom).

722 Before reaching the critical force value, the system has rotational symmetry with
 723 respect to the nail axis; however, after the critical force value is reached the nail buck-

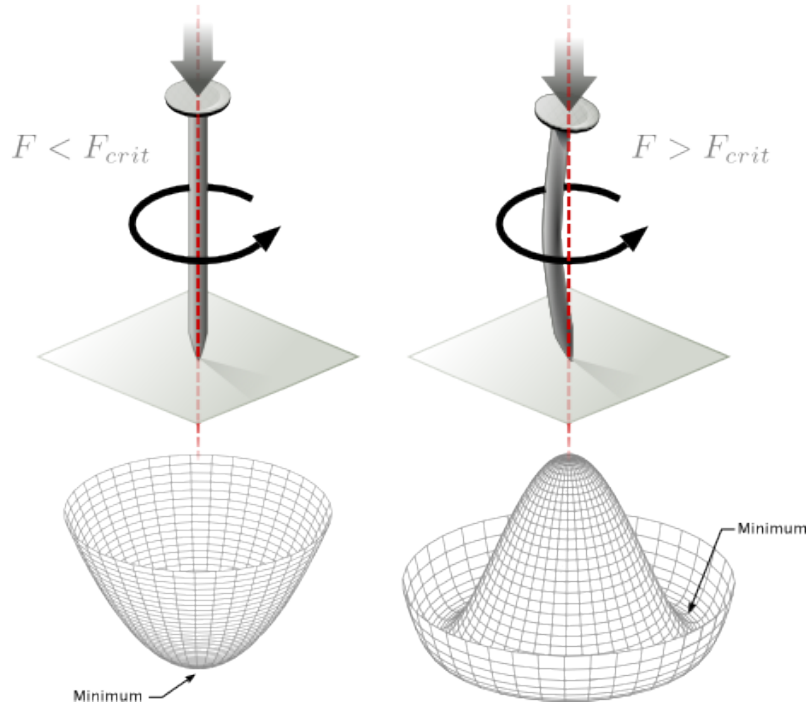


Figure 1.6: Spontaneous symmetry breaking mechanism. The steel nail, subject to an external force (top left), has rotational symmetry with respect to its axis. When the external force overcomes a critical value the nail buckles (top right) choosing a minimal energy state (ground state) and thus *breaking spontaneously the rotational symmetry*. The potential energy (bottom) changes but holds the rotational symmetry; however, an infinite number of asymmetric ground states are generated and circularly distributed in the bottom of the potential [31].

724 les (top right). The form of the potential energy (bottom right) changes appearing a
 725 set of infinity minima but preserving its rotational symmetry. Right before the nail
 726 buckles there is no indication of the direction the nail will bend because any of the
 727 directions are equivalent, but once the nail bends, choosing a direction, an arbitrary
 728 minimal energy state (ground state) is selected and it does not share the system's
 729 rotational symmetry. This mechanism for reaching an asymmetric ground state is
 730 known as *spontaneous symmetry breaking*.

731 The lesson from this analysis is that the way to introduce the SSB mechanism
 732 into a system is by adding the appropriate potential to it.

733 Figure 1.7 shows a plot of the potential $V(\phi)$ in the case of a scalar field ϕ

$$V(\phi) = \mu^2 \phi^\dagger \phi + \lambda (\phi^\dagger \phi)^2 \quad (1.31)$$

734 If $\mu^2 > 0$ the potential has only one minimum at $\phi = 0$ and describes a scalar field
 735 with mass μ . If $\mu^2 < 0$ the potential has a local maximum at $\phi = 0$ and two minima
 736 at $\phi = \pm\sqrt{-\mu^2/\lambda}$ which enables the SSB mechanism to work.

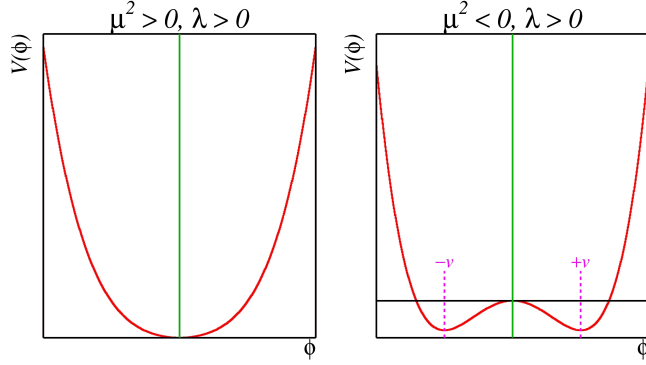


Figure 1.7: Shape of the potential $V(\phi)$ for $\lambda > 0$ and: $\mu^2 > 0$ (left) and $\mu^2 < 0$ (right). The case $\mu^2 < 0$ corresponds to the potential suitable for introducing the SSB mechanism by choosing one of the two ground states which are connected via reflection symmetry. [31].

737 In the case of a complex scalar field $\phi(x)$

$$\phi(x) = \frac{1}{\sqrt{2}}(\phi_1 + i\phi_2) \quad (1.32)$$

738 the Lagrangian (invariant under global $U(1)$ transformations) is given by

$$\mathcal{L} = (\partial_\mu \phi)^\dagger (\partial^\mu \phi) - V(\phi), \quad V(\phi) = \mu^2 \phi^\dagger \phi + \lambda (\phi^\dagger \phi)^2 \quad (1.33)$$

739 where an appropriate potential has been added in order to introduce the SSB.

740 As seen in Figure 1.8, the potential has now an infinite number of minima circularly
 741 distributed along the ξ -direction which makes possible the occurrence of the SSB by
 742 choosing an arbitrary ground state; for instance, $\xi = 0$, i.e. $\phi_1 = v, \phi_2 = 0$

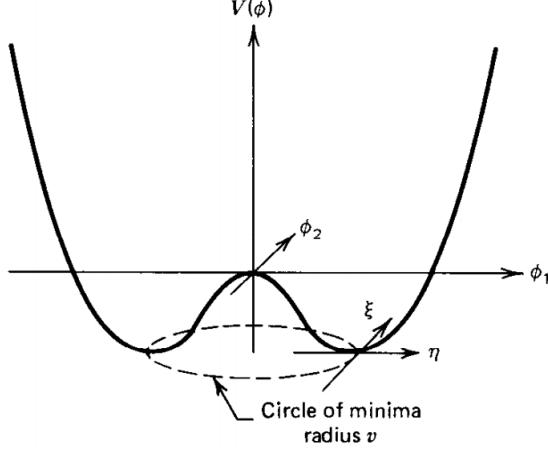


Figure 1.8: Potential for complex scalar field. There is a circle of minima of radius v along the ξ -direction [6].

$$\phi_0 = \frac{v}{\sqrt{2}} \exp(i\xi) \xrightarrow{\text{SSB}} \phi_0 = \frac{v}{\sqrt{2}} \quad (1.34)$$

743 As usual, excitations over the ground state are studied by making an expansion
 744 about it; thus, the excitations can be parametrized as:

$$\phi(x) = \frac{1}{\sqrt{2}}(v + \eta(x) + i\xi(x)) \quad (1.35)$$

745 which when substituted into Eqn. 1.33 produces a Lagrangian in terms of the new
 746 fields η and ξ

$$\mathcal{L}' = \frac{1}{2}(\partial_\mu \xi)^2 + \frac{1}{2}(\partial_\mu \eta)^2 + \mu^2 \eta^2 - V(\phi_0) - \lambda v \eta (\eta^2 + \xi^2) - \frac{\lambda}{4}(\eta^2 + \xi^2)^2 \quad (1.36)$$

747 where the last two terms represent the interactions and self-interaction between the
 748 two fields η and ξ . The particular feature of the SSB mechanism is revealed when
 749 looking to the first three terms of \mathcal{L}' . Before the SSB, only the massless ϕ field is

750 present in the system; after the SSB there are two fields of which the η -field has
 751 acquired mass $m_\eta = \sqrt{-2\mu^2}$ while the ξ -field is still massless (see Figure 1.9).

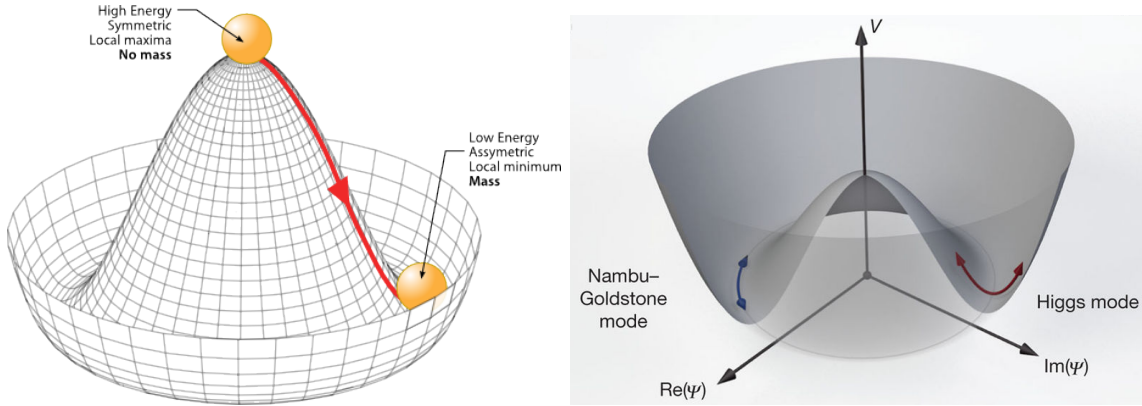


Figure 1.9: SSB mechanism for a complex scalar field [31, 32].

752 Thus, the SSB mechanism serves as a method to generate mass but as a side ef-
 753 fect a massless field is introduced in the system. This fact is known as the Goldstone
 754 theorem and states that a massless scalar field appears in the system for each con-
 755 tinuous symmetry spontaneously broken. Another version of the Goldstone theorem
 756 states that “if a Lagrangian is invariant under a continuous symmetry group G , but
 757 the vacuum is only invariant under a subgroup $H \subset G$, then there must exist as many
 758 massless spin-0 particles (Nambu-Goldstone bosons) as broken generators.” [26] The
 759 Nambu-Goldstone boson can be understood considering that the potential in the ξ -
 760 direction is flat so excitations in that direction are not energy consuming and thus
 761 represent a massless state.

762 1.3.2 Higgs mechanism

763 When the SSB mechanism is introduced in the formulation of the EWI in an attempt
 764 to generate the mass of the so far massless gauge bosons and fermions, an interesting
 765 effect is revealed. In order to keep the G symmetry group invariance and generate

766 the mass of the EW gauge bosons, a G invariant Lagrangian density (\mathcal{L}_S) has to be
 767 added to the non massive EWI Lagrangian (Eqn. 1.30)

$$\mathcal{L}_S = (D_\mu \phi)^\dagger (D^\mu \phi) - \mu^2 \phi^\dagger \phi - \lambda (\phi^\dagger \phi)^2, \quad \lambda > 0, \mu^2 < 0 \quad (1.37)$$

$$D_\mu \phi = \left(i\partial_\mu - g \frac{\sigma_i}{2} W_\mu^i - g' \frac{Y}{2} B_\mu \right) \phi \quad (1.38)$$

768 ϕ has to be an isospin doublet of complex scalar fields so it preserves the G invariance;
 769 thus ϕ can be defined as:

$$\phi = \begin{pmatrix} \phi^+ \\ \phi^0 \end{pmatrix} \equiv \frac{1}{\sqrt{2}} \begin{pmatrix} \phi_1 + i\phi_2 \\ \phi_3 + i\phi_4 \end{pmatrix}. \quad (1.39)$$

770 The minima of the potential are defined by

$$\phi^\dagger \phi = \frac{1}{2} (\phi_1^2 + \phi_2^2 + \phi_3^2 + \phi_4^2) = -\frac{\mu^2}{2\lambda}. \quad (1.40)$$

771 The choice of the ground state is critical. By choosing a ground state, invariant
 772 under $U(1)_{em}$ gauge symmetry, the photon will remain massless and the W^\pm and Z
 773 bosons masses will be generated which is exactly what is needed. In that sense, the
 774 best choice corresponds to a weak isospin doublet with $T_3 = -1/2$, $Y_W = 1$ and $Q = 0$
 775 which defines a ground state with $\phi_1 = \phi_2 = \phi_4$ and $\phi_3 = v$:

$$\phi_0 \equiv \frac{1}{\sqrt{2}} \begin{pmatrix} 0 \\ v \end{pmatrix}, \quad v^2 \equiv -\frac{\mu^2}{\lambda}. \quad (1.41)$$

776 where the vacuum expectation value v is fixed by the Fermi coupling G_F according
 777 to $v = (\sqrt{2}G_F)^{1/2} \approx 246$ GeV.

778 The G symmetry has been broken and three Nambu-Goldstone bosons will appear.

779 The next step is to expand ϕ about the chosen ground state as:

$$\phi(x) = \frac{1}{\sqrt{2}} \exp\left(\frac{i}{v} \sigma_i \theta^i(x)\right) \begin{pmatrix} 0 \\ v + H(x) \end{pmatrix} \approx \frac{1}{\sqrt{2}} \begin{pmatrix} \theta_1(x) + i\theta_2(x) \\ v + H(x) - i\theta_3(x) \end{pmatrix} \quad (1.42)$$

780 to describe fluctuations from the ground state ϕ_0 . The fields $\theta_i(x)$ represent the
 781 Nambu-Goldstone bosons while $H(x)$ is known as *Higgs field*. The fundamental fea-
 782 ture of the parametrization used is that the dependence on the $\theta_i(x)$ fields is factored
 783 out in a global phase that can be eliminated by taking the physical *unitary gauge*
 784 $\theta_i(x) = 0$. Therefore the expansion about the ground state is given by:

$$\phi(x) \frac{1}{\sqrt{2}} \begin{pmatrix} 0 \\ v + H(x) \end{pmatrix} \quad (1.43)$$

785 which when substituted into \mathcal{L}_S (Eqn. 1.37) results in a Lagrangian containing the
 786 now massive three gauge bosons W^\pm, Z , one massless gauge boson (photon) and
 787 the new Higgs field (H). The three degrees of freedom corresponding to the Nambu-
 788 Goldstone bosons are now integrated into the massive gauge bosons as their lon-
 789 gitudinal polarizations which were not available when they were massless particles.
 790 The effect by which vector boson fields acquire mass after an spontaneous symmetry
 791 breaking, but without an explicit gauge invariance breaking is known as the *Higgs*
 792 *mechanism*.

793 The mechanism was proposed by three independent groups: F.Englert and R.Brout
 794 in August 1964 [33], P.Higgs in October 1964 [34] and G.Guralnik, C.Hagen and
 795 T.Kibble in November 1964 [35]; however, its importance was not realized until
 796 S.Glashow [22], A.Salam [23] and S.Weinberg [24], independently, proposed that elec-
 797 tromagnetic and weak interactions are two manifestations of a more general interac-
 798 tion called *electroweak interaction* in 1967.

799 **1.3.3 Masses of the gauge bosons**

800 The masses of the gauge bosons are extracted by evaluating the kinetic part of La-
 801 grangian \mathcal{L}_S in the ground state (known also as the vacuum expectation value), i.e.,

$$\left| \left(\partial_\mu - ig \frac{\sigma_i}{2} W_\mu^i - i \frac{g'}{2} B_\mu \right) \phi_0 \right|^2 = \left(\frac{1}{2} v g \right)^2 W_\mu^+ W^{-\mu} + \frac{1}{8} v^2 (W_\mu^3, B_\mu) \begin{pmatrix} g^2 & -gg' \\ -gg' & g'^2 \end{pmatrix} \begin{pmatrix} W^{3\mu} \\ B^\mu \end{pmatrix} \quad (1.44)$$

802 comparing with the typical mass term for a charged boson $M_W^2 W^+ W^-$

$$M_W = \frac{1}{2} v g. \quad (1.45)$$

The second term in the right side of the Eqn.1.44 comprises the masses of the neutral bosons, but it needs to be written in terms of the gauge fields Z_μ and A_μ in order to be compared to the typical mass terms for neutral bosons, therefore using Eqn. 1.29

$$\begin{aligned} \frac{1}{8} v^2 [g^2 (W_\mu^3)^2 - 2gg' W_\mu^3 B^\mu + g'^2 B_\mu^2] &= \frac{1}{8} v^2 [g W_\mu^3 - g' B_\mu]^2 + 0[g' W_\mu^3 + g B_\mu]^2 \quad (1.46) \\ &= \frac{1}{8} v^2 [\sqrt{g^2 + g'^2} Z_\mu]^2 + 0[\sqrt{g^2 + g'^2} A_\mu]^2 \end{aligned}$$

803 and then

$$M_Z = \frac{1}{2} v \sqrt{g^2 + g'^2}, \quad M_A = 0 \quad (1.47)$$

804 **1.3.4 Masses of the fermions**

805 The lepton mass terms can be generated by introducing a gauge invariant Lagrangian
 806 term describing the Yukawa coupling between the lepton field and the Higgs field

$$\mathcal{L}_{Yl} = -G_l \left[(\bar{\nu}_l, \bar{l})_L \begin{pmatrix} \phi^+ \\ \phi^0 \end{pmatrix} l_R + \bar{l}_R (\phi^-, \bar{\phi}^0) \begin{pmatrix} \nu_l \\ l \end{pmatrix} \right], \quad l = e, \mu, \tau. \quad (1.48)$$

807 After the SSB and replacing the usual field expansion about the ground state
 808 (Eqn.1.41) into \mathcal{L}_{Yl} , the mass term arises

$$\mathcal{L}_{Yl} = -m_l (\bar{l}_L l_R + \bar{l}_R l_L) - \frac{m_l}{v} (\bar{l}_L l_R + \bar{l}_R l_L) H = -m_l \bar{l} l \left(1 + \frac{H}{v} \right) \quad (1.49)$$

809

$$m_l = \frac{G_l}{\sqrt{2}} v \quad (1.50)$$

810 where the additional term represents the lepton-Higgs interaction. The quark masses
 811 are generated in a similar way as lepton masses but for the upper member of the
 812 quark doublet a different Higgs doublet is needed:

$$\phi_c = -i\sigma_2 \phi^* = \begin{pmatrix} -\bar{\phi}^0 \\ \phi^- \end{pmatrix}. \quad (1.51)$$

813 Additionally, given that the quark isospin doublets are not constructed in terms
 814 of the mass eigenstates but in terms of the flavor eigenstates, as shown in Table 1.5,
 815 the coupling parameters will be related to the CKM matrix elements; thus, the quark
 816 Lagrangian is given by:

$$\mathcal{L}_{Yq} = -G_d^{i,j} (\bar{u}_i, \bar{d}'_i)_L \begin{pmatrix} \phi^+ \\ \phi^0 \end{pmatrix} d_{jR} - G_u^{i,j} (\bar{u}_i, \bar{d}'_i)_L \begin{pmatrix} -\bar{\phi}^0 \\ \phi^- \end{pmatrix} u_{jR} + h.c. \quad (1.52)$$

817 with $i, j = 1, 2, 3$. After SSB and expansion about the ground state, the diagonal form

818 of \mathcal{L}_{Yq} is:

$$\mathcal{L}_{Yq} = -m_d^i \bar{d}_i d_i \left(1 + \frac{H}{v}\right) - m_u^i \bar{u}_i u_i \left(1 + \frac{H}{v}\right) \quad (1.53)$$

819 Fermion masses depend on arbitrary couplings G_l and $G_{u,d}$ and are not predicted
820 by the theory.

821 1.3.5 The Higgs field

822 After the characterization of the fermions and gauge bosons as well as their interac-
823 tions, it is necessary to characterize the Higgs field itself. The Lagrangian \mathcal{L}_S in Eqn.
824 1.37 written in terms of the gauge bosons is given by

$$\mathcal{L}_S = \frac{1}{4} \lambda v^4 + \mathcal{L}_H + \mathcal{L}_{HV} \quad (1.54)$$

825

$$\mathcal{L}_H = \frac{1}{2} \partial_\mu H \partial^\mu H - \frac{1}{2} m_H^2 H^2 - \frac{1}{2v} m_H^2 H^3 - \frac{1}{8v^2} m_H^2 H^4 \quad (1.55)$$

826

$$\mathcal{L}_{HV} = m_H^2 W_\mu^+ W^{\mu-} \left(1 + \frac{2}{v} H + \frac{2}{v^2} H^2\right) + \frac{1}{2} m_Z^2 Z_\mu Z^\mu \left(1 + \frac{2}{v} H + \frac{2}{v^2} H^2\right) \quad (1.56)$$

827 The mass of the Higgs boson is deduced as usual from the mass term in the Lagrangian
828 resulting in:

$$m_H = \sqrt{-2\mu^2} = \sqrt{2\lambda}v \quad (1.57)$$

829 however, it is not predicted by the theory either. The experimental measurement of
830 the Higgs boson mass have been performed by the *Compact Muon Solenoid (CMS)*
831 experiment and the *A Toroidal LHC Appartus (ATLAS)* experiments at the *Large
832 Hadron Collider(LHC)*, [36–38], and is presented in Table 1.8.

833

Property	Value
Electric charge	0
Color charge	0
Spin	0
Weak isospin	-1/2
Weak hypercharge	1
Parity	1
Mass (GeV/c^2)	$125.09 \pm 0.21 \text{ (stat.)} \pm 0.11 \text{ (syst.)}$

Table 1.8: Higgs boson properties. Higgs mass is not predicted by the theory and the value here corresponds to the experimental measurement.

1.3.6 Production of Higgs bosons at LHC

At the LHC, Higgs bosons are produced as a result of the collision of two counter-rotating protons beams. A detailed description of the LHC machine will be presented in chapter 2.

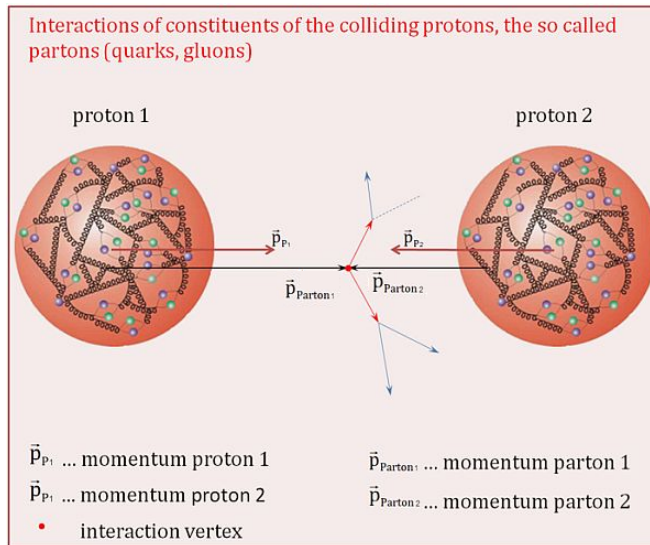


Figure 1.10: Proton-proton collision. Protons are composed of 3 valence quarks, a sea of quarks and gluons; therefore in a proton-proton collision, quarks and gluons are those who collide. [39].

837

838 Protons are composed of quarks and these quarks are bound by gluons; however,
 839 what is commonly called the quark content of the proton makes reference to the
 840 valence quarks. In fact, a proton is not just a rigid entity with three balls in it all
 841 tied up with springs, but the gluons exchanged by the valence quarks tend to split

842 spontaneously into quark-antiquark pairs or more gluons, creating *sea of quarks and*
 843 *gluons* as represented in Figure 1.10.

844 In a proton-proton (pp) collision, the proton's constituents, quarks and gluons, are
 845 those that collide. The pp cross section depends on the momentum of the colliding
 846 particles, reason for which it is needed to know how the momentum is distributed
 847 inside the proton. Quarks and gluons are known as partons, hence, the functions
 848 that describe how the proton momentum is distributed among partons inside it are
 849 called *parton distribution functions (PDFs)*; PDFs are determined from experimental
 850 data obtained in experiments where the internal structure of hadrons is tested, and
 851 depend on the momentum transfer Q and the fraction of momentum x carried by an
 852 specific parton. Figure 1.11 shows the proton PDFs ($xf(x, Q^2)$) for two values of Q .

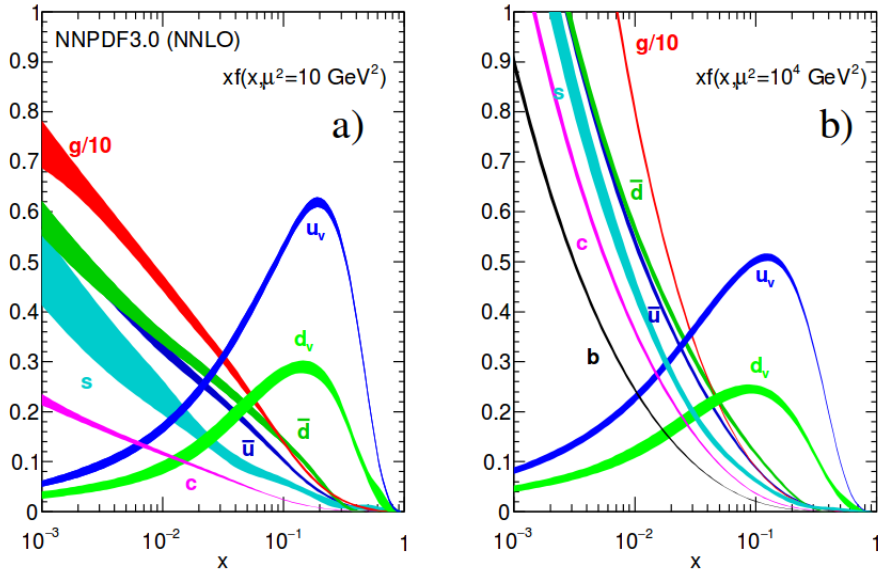


Figure 1.11: Proton PDFs for two values of Q^2 : left. $\mu^2 = Q^2 = 10 \text{ GeV}^2$, right. $\mu^2 = Q^2 = 10^4 \text{ GeV}^2$. u_v and d_v correspond to the u and d valence quarks, $s, c, b, \bar{u}, \bar{d}$ correspond to sea quarks, and g corresponds to gluons. Note that gluons carry a high fraction of the proton's momentum. [9]

853 In physics, a common approach to study complex systems consists of starting
 854 with a simpler version of them, for which a well known description is available, and

adding an additional *perturbation* which represents a small deviation from the known behavior. If the perturbation is small enough, the physical quantities associated with the perturbed system are expressed as a series of corrections to those of the simpler system. The perturbation series corresponds to an expansion in power series of a small parameter, therefore, the more terms are considered in the series (the higher order in the perturbation series), the more precise is the description of the complex system. If the perturbation does not get progressively smaller, the strategy cannot be applied and new methods have to be employed.

High energy systems, like the Higgs production at LHC explored in this thesis, usually can be treated perturbatively with the expansion made in terms of the coupling constants. The overview presented here will be oriented specifically to the Higgs boson production mechanisms in pp collisions at LHC.

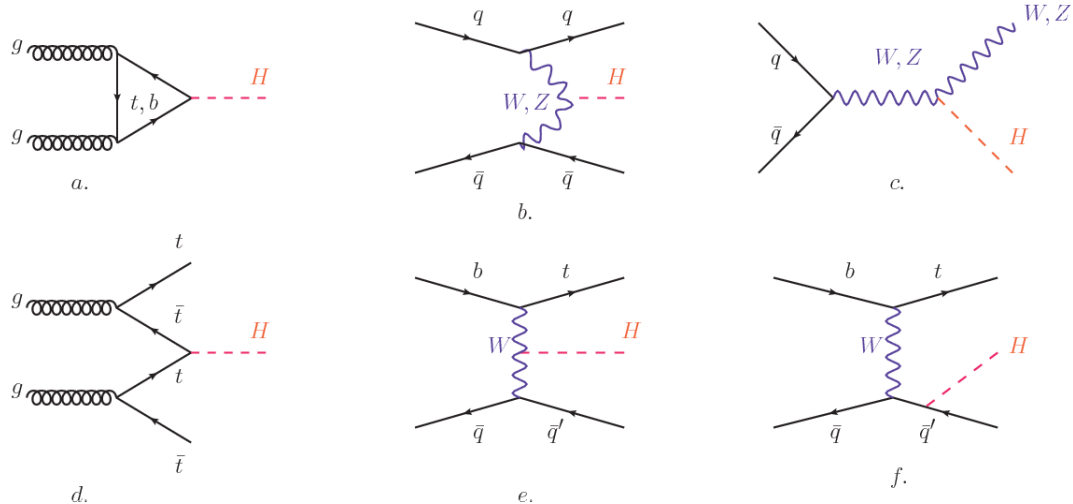


Figure 1.12: Main Higgs boson production mechanism Feynman diagrams. a. gluon-gluon fusion, b. vector boson fusion (VBF), c. Higgs-strahlung, d. Associated production with a top or bottom quark pair, e-f. associated production with a single top quark.

Figure 1.12 shows the Feynman diagrams for the leading order (first order) Higgs production processes at LHC; note that in these diagrams the incoming particles are not the protons themselves but the partons from the protons that actually participate

in the interaction, hence, theorists typically calculate the cross section for the parton interaction, and then convolute that cross section with the information from the PDFs to get a production cross section that is actually measured in experiments. The cross section for Higgs production as a function of the center of mass-energy (\sqrt{s}) for pp collisions is showed in Figure 1.13 left. The tags NLO (next to leading order), NNLO (next to next to leading order) and N3LO (next to next to next to leading order) make reference to the order at which the perturbation series have been considered while the tags QCD and EW correspond to the strong and electroweak coupling constants respectively.

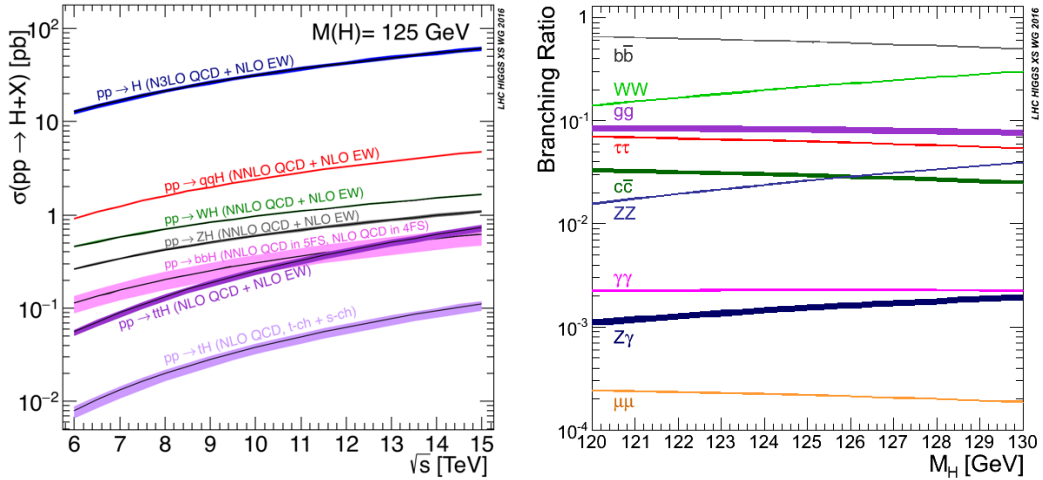


Figure 1.13: Higgs boson production cross sections (left) and decay branching ratios (right) for the main mechanisms. The VBF is indicated as qqH [40].

The main production mechanism is the gluon fusion (Figure 1.12a and $pp \rightarrow H$ in Figure 1.13) given that gluons carry the highest fraction of momentum of the protons in pp colliders (as shown in Figure ??). Since the Higgs boson does not couple to gluons, the mechanism proceeds through the exchange of a virtual top-quark loop. Note that in this process the Higgs boson is produced alone, turning out to be problematic for some Higgs decays, because such absence of anything produced in

885 association with the Higgs represent a trouble for triggering, however, this mechanism
 886 is experimentally clean when combined with the two-photon or the four-lepton decay
 887 channels (see Section 1.3.7).

888 Vector boson fusion (Figure 1.12b and $pp \rightarrow qqH$ in Figure 1.13) has the second
 889 largest production cross section. The scattering of two fermions is mediated by a weak
 890 gauge boson which later emits a Higgs boson. In the final state, the two fermions tend
 891 to be located in the central region of the detector; this kind of features are generally
 892 used as a signature when analyzing the datasets provided by the experiments⁷.

893 In the Higgs-strahlung mechanism (Figure 1.12c and $pp \rightarrow WH, pp \rightarrow ZH$ in
 894 Figure 1.13) two fermions annihilate to form a weak gauge boson. If the initial
 895 fermions have enough energy, the emergent boson might emit a Higgs boson.

896 The associated production with a top or bottom quark pair and the associated
 897 production with a single top quark (Figure 1.12d-f and $pp \rightarrow bbH, pp \rightarrow t\bar{t}H, pp \rightarrow tH$
 898 in Figure 1.13) have a smaller cross section than the main three mechanisms above,
 899 but they provide a good opportunity to test the Higgs-top coupling. The analysis
 900 reported in this thesis is developed using these production mechanisms. A detailed
 901 description of the tH mechanism will be given in Section 1.5.

902 1.3.7 Higgs boson decay channels

903 When a particle can decay through several modes, also known as channels, the prob-
 904 ability of decaying through a given channel is quantified by the *branching ratio (BR)*
 905 of the decay channel; thus, the BR is defined as the ratio of number of decays go-
 906 ing through that given channel to the total number of decays. In regard to the
 907 Higgs boson decay, the BR can be predicted with accuracy once the Higgs mass is
 908 known [41, 42]. In Figure 1.13 right, a plot of the BR as a function of the Higgs mass

⁷ More details about how to identify events of interest in this analysis will be given in chapter 6.

909 is presented; the largest predicted BR corresponds to the $b\bar{b}$ pair decay channel (see
 910 Table 1.9) given that it is the heaviest particle pair whose on-shell⁸ production is
 911 kinematically allowed in the decay.

Decay channel	Branching ratio	Rel. uncertainty
$H \rightarrow b\bar{b}$	5.84×10^{-1}	$+3.2\% - 3.3\%$
$H \rightarrow W^+W^-$	2.14×10^{-1}	$+4.3\% - 4.2\%$
$H \rightarrow \tau^+\tau^-$	6.27×10^{-2}	$+5.7\% - 5.7\%$
$H \rightarrow ZZ$	2.62×10^{-2}	$+4.3\% - 4.1\%$
$H \rightarrow \gamma\gamma$	2.27×10^{-3}	$+5.0\% - 4.9\%$
$H \rightarrow Z\gamma$	1.53×10^{-3}	$+9.0\% - 8.9\%$
$H \rightarrow \mu^+\mu^-$	2.18×10^{-4}	$+6.0\% - 5.9\%$

Table 1.9: Predicted branching ratios and the relative uncertainty for some decay channels of a SM Higgs boson with $m_H = 125\text{GeV}/c^2$ [9]; the uncertainties are driven by theoretical uncertainties for the different Higgs boson partial widths and by parametric uncertainties associated to the strong coupling and the masses of the quarks which are the input parameters. Further details on these calculations can be found in Reference [43]

912

913 Decays to other lepton and quark pairs, like electron, strange, up, and down
 914 quark pairs not listed in the table, are also possible but their likelihood is too small
 915 to measure since they are very lightweight, hence, their interaction with the Higgs
 916 boson is very weak. On other hand, the decay to top quark pairs is heavily suppressed
 917 due to the top quark mass ($\approx 173\text{ GeV}/c^2$).

918 Decays to gluons proceed indirectly through a virtual top quark loop while the
 919 decays to photons proceed through a virtual W boson loop, therefore, their branching
 920 ratio is smaller compared to direct interaction decays. Same is true for the decay to
 921 a photon and a Z boson.

⁸ In general, on-shell or real particles are those which satisfy the energy-momentum relation ($E^2 - |\vec{p}|^2 c^2 = m^2 c^4$); off-shell or virtual particles does not satisfy it which is possible under the uncertainty principle of quantum mechanics. Usually, virtual particles correspond to internal propagators in Feynman diagrams.

922 In the case of decays to pairs of W and Z bosons, the decay proceed with one of
 923 the bosons being on-shell and the other being off-shell. The likelihood of the process
 924 diminish depending on how far off-shell are the virtual particles involved, hence, the
 925 branching ratio for W boson pairs is bigger than for Z boson pairs since Z boson mass
 926 is bigger than W boson mass.

927 Note that the decay to a pair of virtual top quarks is possible, but the probability
 928 is way too small.

929 **1.4 Experimental status of the anomalous
 930 Higgs-fermion coupling**

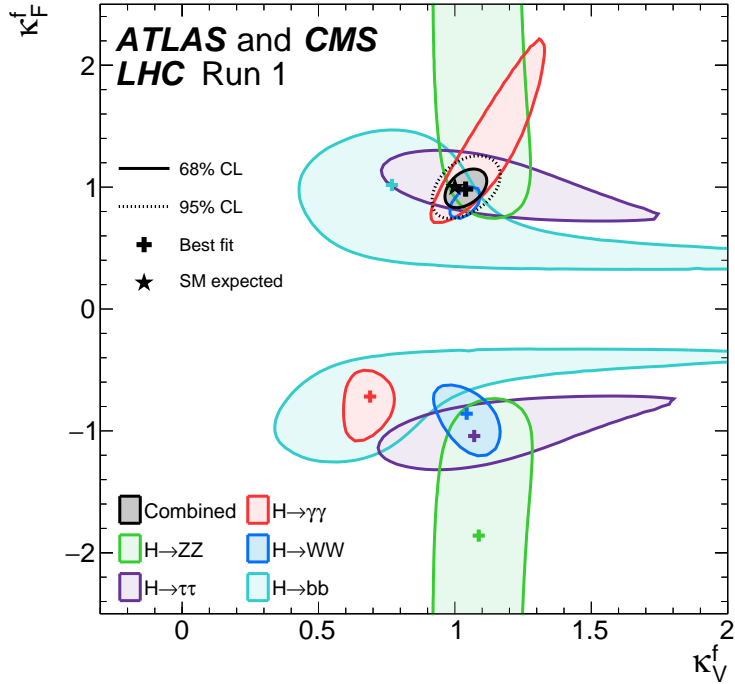


Figure 1.14: Combination of the ATLAS and CMS fits for coupling modifiers $\kappa_t - \kappa_V$; also shown the individual decay channels combination and their global combination. No assumptions have been made on the sign of the coupling modifiers [44].

931 ATLAS and CMS have performed analyses of the anomalous Higgs-fermion cou-
 932 pling by making likelihood scans for the two coupling modifiers, κ_f and κ_V , under
 933 the assumption that $\kappa_Z = \kappa_W \equiv \kappa_V$ and $\kappa_t = \kappa_\tau = \kappa_b \equiv \kappa_f$. Figure 1.14 shows the
 934 result of the combination of ATLAS and CMS fits; also the individual decay channels
 935 combination and the global combination results are shown. Note that from this plot
 936 there is limited information on the sign of the coupling since the only information
 937 available about the sign of the coupling comes from decays rather than production.

938 While all the channels are compatible for positive values of the modifiers, for
 939 negative values of κ_f there is no compatibility. The best fit for individual channels
 940 is compatible with negative values of κ_f except for the $H \rightarrow bb$ channel. The best
 941 fit for the combination yields $\kappa_f \geq 0$, in contrast to the yields from the individual
 942 channels; the reason of this yield resides in the $H \rightarrow \gamma\gamma$ coupling. $H \rightarrow \gamma\gamma$ decay
 943 proceeds through a loop of either top quarks or W bosons, hence, this channel is
 944 sensitive to κ_t thanks to the interference of these two amplitude contributions; under
 945 the assumption that no beyond SM particles take part in the loops, a flipped sign
 946 of κ_t will increase the $H \rightarrow \gamma\gamma$ branching fraction by a factor of ~ 2.4 which is not
 947 supported by measurements; thus, this large asymmetry between the positive and
 948 negative coupling ratios in the $H \rightarrow \gamma\gamma$ channel drives the yield of the global fit and
 949 would mean that the anomalous H-t coupling is excluded as stated in Reference [44],
 950 but there is a caveat, this exclusion holds only if no new particles contribute to the
 951 loop in the main diagram for that decay.

952 Although the $H \rightarrow bb$ channel is expected to be the most sensitive channel and
 953 its best fit value of κ_t is positive, and then the global fit yield is still supported,
 954 the contributions from all the other decay channels, small compared to the $H \rightarrow bb$,
 955 indicate that the anomalous H-t coupling cannot be excluded completely, motivating
 956 to look at tH processes which can help with both, the limited information on the sign

957 of the H-t coupling and the access to information from the Higgs boson production
 958 rather than from its decays.

959 It will be shown in Section 1.5 that the same interference effect enhance the
 960 tH production rate and could reveal evidence of direct production of heavy new par-
 961 ticles as predicted in composite and little Higgs models [45], or new physics related
 962 to Higgs boson mediated flavor changing neutral currents [46] as well as probes the
 963 CP-violating phase of the H-t coupling [47, 48].

964 **1.5 Associated production of a Higgs boson and a 965 single top quark**

966 The production of Higgs boson in association with a top quark has been extensively
 967 studied [47, 49–52]. While measurements of the main Higgs production mechanisms
 968 rates are sensitive to the strength of the Higgs coupling to W boson or top quark,
 969 they are not sensitive to the relative sign between the two couplings. In this thesis,
 970 the Higgs boson production mechanism explored is the associated production with a
 971 single top quark (tH) which offers sensitivity to the relative sign of the Higgs couplings
 972 to W boson and to top quark. The description given here is based on Reference [51]

A process where two incoming particles interact and produce a final state with two particles can proceed in three called channels (see, for instance, Figure 1.15 omitting the red line). The t-channel represents processes where an intermediate particle is emitted by one of the incoming particles and absorbed by the other. The s-channel represents processes where the two incoming particles merge into an intermediate particle which eventually will split into the particles in the final state. The third channel, u-channel, is similar to the t-channel but the two outgoing particles interchange their

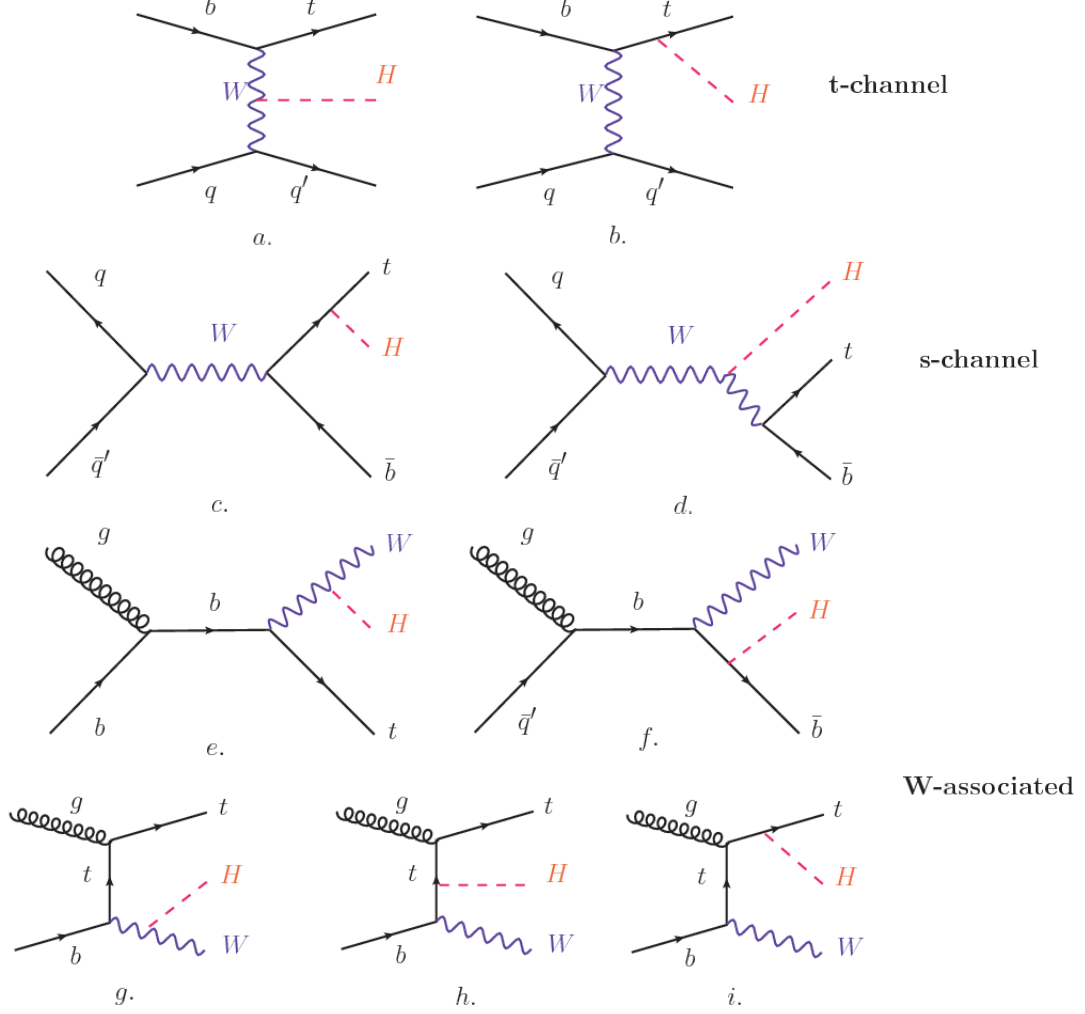


Figure 1.15: Associated Higgs boson production with a top quark mechanism Feynman diagrams. a.,b. t-channel (tHq), c.,d. s-channel (tHb), e-i. W-associated.

roles. These three channels are connected to the so-called Mandelstam variables

$$s = (p_1 + p_2)^2 = (p'_1 + p'_2)^2 \rightarrow \text{square of the center mass-energy.} \quad (1.58)$$

$$t = (p_1 - p'_1)^2 = (p'_2 - p_2)^2 \rightarrow \text{square of the four-momentum transfer.} \quad (1.59)$$

$$u = (p_1 - p'_2)^2 = (p'_1 - p_2)^2 \rightarrow \text{square of the crossed four-momentum transfer.} \quad (1.60)$$

$$s + t + u = m_1^2 + m_2^2 + m'_1{}^2 + m'_2{}^2 \quad (1.61)$$

which relate the momentum, energy and the angles of the incoming and outgoing particles in an scattering process of two particles to two particles. The importance of the Mandelstam variables reside in that they form a minimum set of variables needed to describe the kinematics of this scattering process; they are Lorentz invariant which makes them very useful when doing calculations.

The tH production, where Higgs boson can be radiated either from the top quark or from the W boson, is represented by the leading order Feynman diagrams in Figure 1.15. The cross section for the tH process is calculated, as usual, summing over the contributions from the different Feynman diagrams; therefore it depends on the interference between the contributions. In the SM, the interference for t-channel (tHq process) and W-associated (tHW process) production is destructive [49] resulting in the small cross sections presented in Table 1.10.

tH production channel	Cross section (fb)
t-channel ($pp \rightarrow tHq$)	$70.79^{+2.99}_{-4.80}$
W-associated ($pp \rightarrow tHW$)	$15.61^{+0.83}_{-1.04}$
s-channel($pp \rightarrow tHb$)	$2.87^{+0.09}_{-0.08}$

Table 1.10: Predicted SM cross sections for tH production at $\sqrt{s} = 13$ TeV [53, 54].

985

The s-channel contribution can be neglected. It will be shown that a deviation from the SM destructive interference would result in an enhancement of the tH cross section compared to that in SM, which could be used to get information about the sign of the Higgs-top coupling [51, 52]. In order to describe tH production processes, Feynman diagram 1.15b will be considered; there, the W boson is radiated by a quark in the proton and eventually it will interact with the b quark. In the high energy regime, the effective W approximation [55] is used to describe the process as the

993 emission of an approximately on-shell W and its hard scattering with the b quark;
 994 i.e. $Wb \rightarrow th$. The scattering amplitude for the process is given by

$$\mathcal{A} = \frac{g}{\sqrt{2}} \left[(\kappa_t - \kappa_V) \frac{m_t \sqrt{s}}{m_W v} A \left(\frac{t}{s}, \varphi; \xi_t, \xi_b \right) + \left(\kappa_V \frac{2m_W s}{v t} + (2\kappa_t - \kappa_V) \frac{m_t^2}{m_W v} \right) B \left(\frac{t}{s}, \varphi; \xi_t, \xi_b \right) \right], \quad (1.62)$$

995 where $\kappa_V \equiv g_{HVV}/g_{HVV}^{SM}$ and $\kappa_t \equiv g_{Ht}/g_{Ht}^{SM} = y_t/y_t^{SM}$ are scaling factors that quantify
 996 possible deviations of the couplings from the SM values, Higgs-Vector boson (H-
 997 W) and Higgs-top (H-t) respectively, from the SM couplings; $s = (p_W + p_b)^2$, $t =$
 998 $(p_W - p_H)^2$, φ is the Higgs azimuthal angle around the z axis taken parallel to the
 999 direction of motion of the incoming W; A and B are functions describing the weak
 1000 interaction in terms of the chiral states (ξ_t, ξ_b) of the quarks b and t . Terms that
 1001 vanish in the high energy limit have been neglected as well as the Higgs and b quark
 1002 masses⁹.

1003 The scattering amplitude grows with energy like \sqrt{s} for $\kappa_V \neq \kappa_t$, in contrast to
 1004 the SM ($\kappa_t = \kappa_V = 1$), where the first term in 1.62 cancels out and the amplitude
 1005 is constant for large s ; therefore, a deviation from the SM predictions represents an
 1006 enhancement in the tHq cross section. In particular, for a SM H-W coupling and a
 1007 H-t coupling of inverted sign with respect to the SM ($\kappa_V = -\kappa_t = 1$) the tHq cross
 1008 section is enhanced by a factor greater 10 as seen in the Figure 1.16 taken from
 1009 Reference [51]; Reference [56] has reported similar enhancement results.

1010 A similar analysis is valid for the W-associated channel but, in that case, the in-
 1011 terference is more complicated since there are more than two contributions and an ad-
 1012 ditional interference with the production of Higgs boson and a top pair process($t\bar{t}H$).
 1013 The calculations are made using the so-called Diagram Removal (DR) technique where

⁹ A detailed explanation of the structure and approximations used to derive \mathcal{A} can be found in Reference [51]

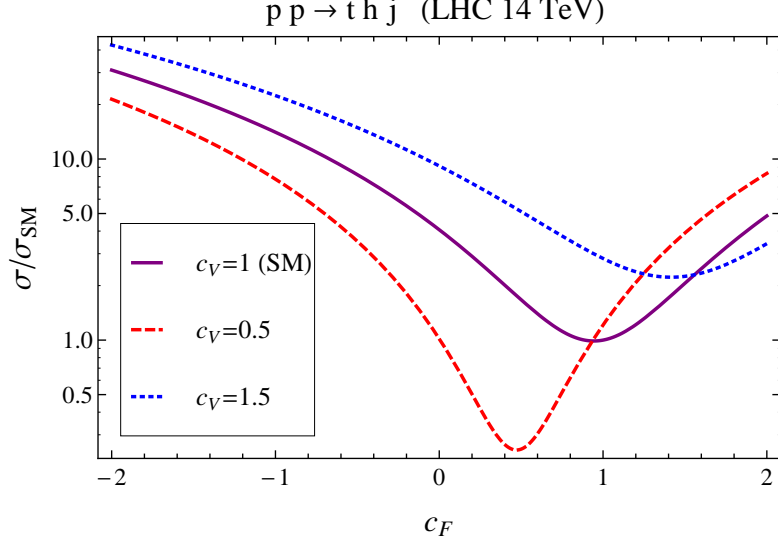


Figure 1.16: Cross section for tHq process as a function of κ_t , normalized to the SM, for three values of κ_V . In the plot c_f refers to the Higgs-fermion coupling which is dominated by the H-t coupling and represented here by κ_t . Solid, dashed and dotted lines correspond to $c_V \rightarrow \kappa_V = 1, 0.5, 1.5$ respectively. Note that for the SM ($\kappa_V = \kappa_t = 1$), the destructive effect of the interference is maximal.

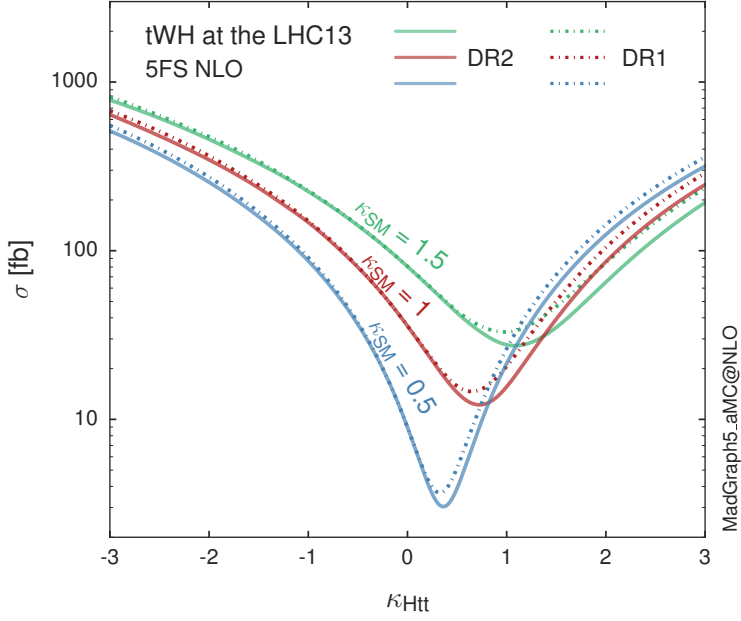


Figure 1.17: Cross section for tHW process as a function of κ_{Htt} , for three values of κ_{SM} at $\sqrt{s} = 13$ TeV. $\kappa_{Htt}^2 = \sigma_{Htt}/\sigma_{Htt}^{SM}$ is a simple re-scaling of the SM Higgs interactions.

interfering diagrams are removed (or added) from the calculations in order to evaluate the impact of the removed contributions. DR1 was defined to neglect $t\bar{t}H$ interference while DR2 was defined to take $t\bar{t}H$ interference into account [48]. As shown in Figure 1.17, the tHW cross section is enhanced from about 15 fb (SM: $\kappa_{Htt} = 1$) to about 150 fb ($\kappa_{Htt} = -1$). Differences between curves for DR1 and DR2 help to gauge the impact of the interference with $t\bar{t}H$. Results of the calculations of the tHq and tHW cross sections at $\sqrt{s} = 13$ TeV can be found in Reference [57] and a summary of the results is presented in Table 1.11.

	\sqrt{s} TeV	$\kappa_t = 1$	$\kappa_t = -1$
$\sigma^{LO}(tHq)(fb)$ [51]	8	≈ 17.4	≈ 252.7
	14	≈ 80.4	≈ 1042
$\sigma^{NLO}(tHq)(fb)$ [51]	8	$18.28^{+0.42}_{-0.38}$	$233.8^{+4.6}_{-0.0}$
	14	$88.2^{+1.7}_{-0.0}$	$982.8^{+28}_{-0.0}$
$\sigma^{LO}(tHq)(fb)$ [56]	14	≈ 71.8	≈ 893
$\sigma^{LO}(tHW)(fb)$ [56]	14	≈ 16.0	≈ 139
$\sigma^{NLO}(tHq)(fb)$ [57]	8	$18.69^{+8.62\%}_{-17.13\%}$	-
	13	$74.25^{+7.48\%}_{-15.35\%}$	$848^{+7.37\%}_{-13.70\%}$
	14	$90.10^{+7.34\%}_{-15.13\%}$	$1011^{+7.24\%}_{-13.39\%}$
$\sigma^{LO}(tHW)(fb)$ [48]	13	$15.77^{+15.91\%}_{-15.76\%}$	-
$\sigma^{NLO}DR1(tHW)(fb)$ [48]	13	$21.72^{+6.52\%}_{-5.24\%}$	≈ 150
$\sigma^{NLO}DR2(tHW)(fb)$ [48]	13	$16.28^{+7.34\%}_{-15.13\%}$	≈ 150

Table 1.11: Predicted enhancement of the tHq and tHW cross sections at LHC for $\kappa_V = 1$ and $\kappa_t = \pm 1$ at LO and NLO; the cross section enhancement of more than a factor of 10 is due to the flipping in the sign of the H-t coupling with respect to the SM one.

1022

1023 1.6 CP-mixing in tH processes

1024 In addition to the sensitivity to sign of the H-t coupling, the tHq and tHW processes
1025 have been proposed as a tool to investigate the possibility of a H-t coupling that does

1026 not conserve CP [47, 48, 58].

1027 In this thesis, the sensitivity of tH processes to CP-mixing is also studied on the
 1028 basis of References [47, 48] using the effective field theory framework where a generic
 1029 particle (X_0) of spin-0 and a general CP violating interaction with the top quark
 1030 (Htt coupling), can couple to scalar and pseudo-scalar fermionic densities. The H-W
 1031 interaction is assumed to be SM-like. The Lagrangian modeling the H-t interaction
 1032 is given by

$$\mathcal{L}_0^t = -\bar{\psi}_t (c_\alpha \kappa_{Htt} g_{Htt} + i s_\alpha \kappa_{Att} g_{Att} \gamma_5) \psi_t X_0, \quad (1.63)$$

1033 where α is the CP-mixing phase, $c_\alpha \equiv \cos \alpha$ and $s_\alpha \equiv \sin \alpha$, κ_{Htt} and κ_{Att} are real
 1034 dimensionless re-scaling parameters¹⁰ used to parametrize the magnitude of the CP-
 1035 violating and CP-conserving parts of the amplitude. The model defines $g_{Htt} =$
 1036 $g_{Att} = m_t/v = y_t/\sqrt{2}$ with $v \sim 246$ GeV the Higgs vacuum expectation value. In
 1037 this parametrization, three special cases can be recovered

1038 • CP-even coupling $\rightarrow \alpha = 0^\circ$

1039 • CP-odd coupling $\rightarrow \alpha = 90^\circ$

1040 • SM coupling $\rightarrow \alpha = 0^\circ$ and $\kappa_{Htt} = 1$

1041 The loop induced X_0 coupling to gluons can also be described in terms of the
 1042 parametrization above, according to

$$\mathcal{L}_0^g = -\frac{1}{4} (c_\alpha \kappa_{Hgg} g_{Hgg} G_{\mu\nu}^a G^{a,\mu\nu} + s_\alpha \kappa_{Agg} g_{Agg} G_{\mu\nu}^a \tilde{G}^{a,\mu\nu}) X_0. \quad (1.64)$$

1043 where $g_{Hgg} = -\alpha_s/3\pi v$ and $g_{Agg} = \alpha_s/2\pi v$ and $G_{\mu\nu}$ is the gluon field strength tensors.

1044 Under the assumption that the top quark dominates the gluon-fusion process at LHC

¹⁰ analog to κ_t and κ_V

1045 energies, $\kappa_{Hgg} \rightarrow \kappa_{Htt}$ and $\kappa_{Agg} \rightarrow \kappa_{Att}$, so that the ratio between the gluon-gluon
 1046 fusion cross section for X_0 and for the SM Higgs prediction can be written as

$$\frac{\sigma_{NLO}^{gg \rightarrow X_0}}{\sigma_{NLO,SM}^{gg \rightarrow H}} = c_\alpha^2 \kappa_{Htt}^2 + s_\alpha^2 \left(\kappa_{Att} \frac{g_{Agg}}{g_{Hgg}} \right)^2. \quad (1.65)$$

1047 If the re-scaling parameters are set to

$$\kappa_{Htt} = 1, \quad \kappa_{Att} = \left| \frac{g_{Hgg}}{g_{Agg}} \right| = \frac{2}{3}. \quad (1.66)$$

1048 the gluon-fusion SM cross section is reproduced for every value of the CP-mixing
 1049 angle α ; therefore, by imposing that condition to the Lagrangian density 1.63, the
 1050 CP-mixing angle is not constrained by current data. Figure 1.18 shows the NLO cross
 1051 sections for t-channel tX_0 (blue) and $t\bar{t}X_0$ (red) associated production processes as a
 1052 function of the CP-mixing angle α . X_0 is a generic spin-0 particle with top quark
 1053 CP-violating coupling. Re-scaling factors κ_{Htt} and κ_{Att} have been set to reproduce
 1054 the SM gluon-fusion cross sections.

1055 It is interesting to notice that the tX_0 cross section is enhanced, by a factor of
 1056 about 10, when a continuous rotation in the scalar-pseudoscalar plane is applied; this
 1057 enhancement is similar to the enhancement produced when the H-t coupling is flipped
 1058 in sign with respect to the SM ($y_t = -y_{t,SM}$ in the plot), as showed in Section 1.5. In
 1059 contrast, the degeneracy in the $t\bar{t}X_0$ cross section is still present given that it depends
 1060 quadratically on the H-t coupling, but more interesting is to notice that $t\bar{t}X_0$ cross
 1061 section is exceeded by tX_0 cross section after $\alpha \sim 60^\circ$.

1062 A similar parametrization can be used to investigate the tHW process sensitivity
 1063 to CP-violating H-t coupling. As said in 1.5, the interference in the W-associated
 1064 channel is more complicated because there are more than two contributions and also
 1065 there is interference with the $t\bar{t}H$ production process.

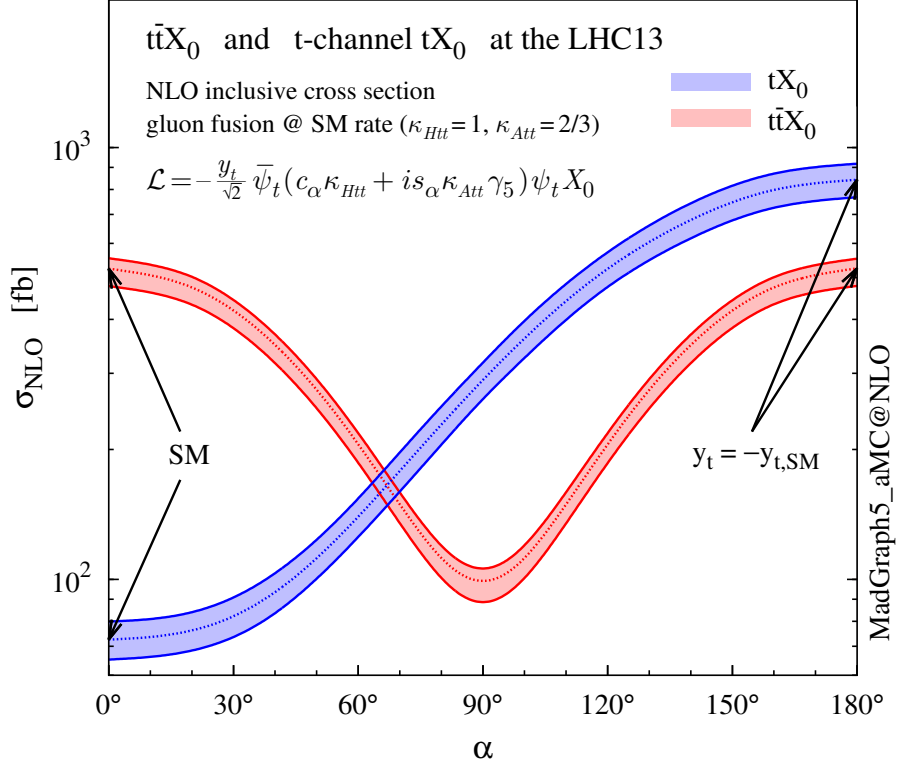


Figure 1.18: NLO cross sections for t-channel tX_0 (blue) and $t\bar{t}X_0$ (red) associated production processes as a function of the CP-mixing angle α . X_0 is a generic spin-0 particle with top quark CP-violating coupling [47].

1066 Figure 1.19 shows the NLO cross sections for t-channel tX_0 (blue), $t\bar{t}X_0$ (red)
 1067 associated production and for the combined $tWX_0 + t\bar{t}X_0 + \text{interference}$ (orange) as
 1068 a function of the CP-mixing angle. It is clear that the effect of the interference in the
 1069 combined case is the lifting of the degeneracy present in the $t\bar{t}X_0$ production. The
 1070 constructive interference enhances the cross section from about 500 fb at SM ($\alpha = 0$)
 1071 to about 600 fb ($\alpha = 180^\circ \rightarrow y_t = -y_{t,SM}$).

1072 An analysis combining tHq and tHW processes will be made in this thesis taking
 1073 advantage of the sensitivity improvement.

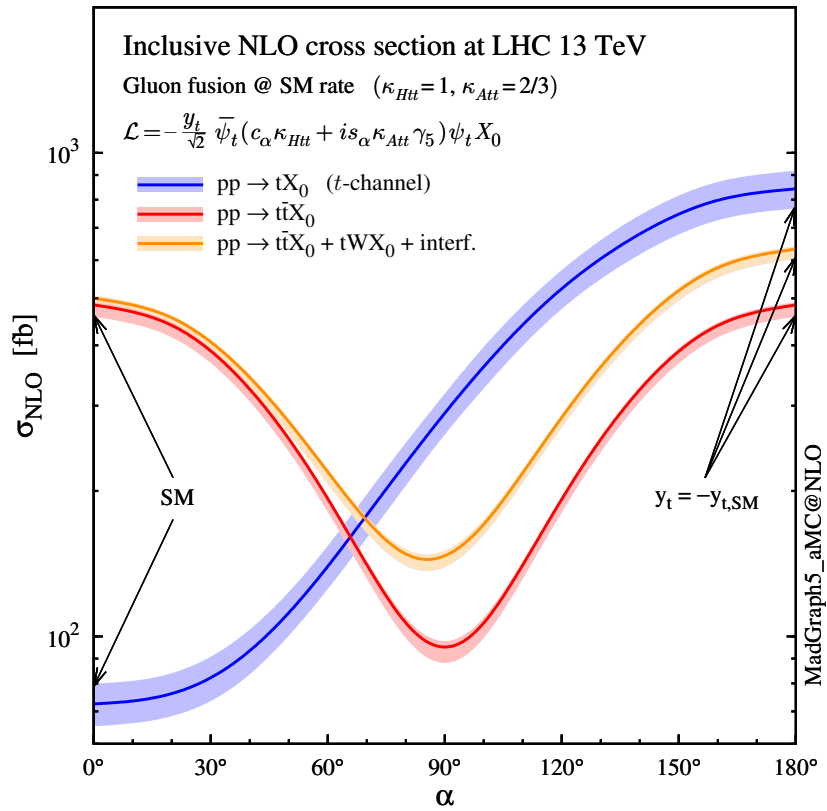


Figure 1.19: NLO cross sections for t-channel tX_0 (blue), $t\bar{t}X_0$ (red) associated production processes and combined $tWX_0 + t\bar{t}X_0$ (including interference) production as a function of the CP-mixing angle α [47].

¹⁰⁷⁴ **Chapter 2**

¹⁰⁷⁵ **The CMS experiment at the LHC**

¹⁰⁷⁶ **2.1 Introduction**

¹⁰⁷⁷ Located on the Swiss-French border, the European Council for Nuclear Research
¹⁰⁷⁸ (CERN) is the largest scientific organization leading particle physics research. About
¹⁰⁷⁹ 13000 people in a broad range of roles including users, students, scientists, engineers,
¹⁰⁸⁰ among others, contribute to the data taking and analysis, with the goal of unveiling
¹⁰⁸¹ the secrets of nature and revealing the fundamental structure of the universe. CERN
¹⁰⁸² is also the home of the Large Hadron Collider (LHC), the largest particle accelerator
¹⁰⁸³ around the world, where protons (or heavy ions) traveling close to the speed of light,
¹⁰⁸⁴ are made to collide. These collisions open a window to investigate how particles (and
¹⁰⁸⁵ their constituents if they are composite) interact with each other, providing clues
¹⁰⁸⁶ about the laws of nature. This chapter presents an overview of the LHC structure
¹⁰⁸⁷ and operation. A detailed description of the CMS detector is offered, given that the
¹⁰⁸⁸ data used in this thesis have been taken with this detector.

1089 2.2 The LHC

1090 With 27 km of circumference, the LHC is currently the most powerful circular accelerator
 1091 in the world. It is installed in the same tunnel where the Large Electron-Positron
 1092 (LEP) collider was located, taking advantage of the existing infrastructure. The LHC
 1093 is part of the CERN's accelerator complex composed of several successive accelerat-
 1094 ing stages before the particles are injected into the LHC ring where they reach their
 1095 maximum energy (see Figure 2.1).

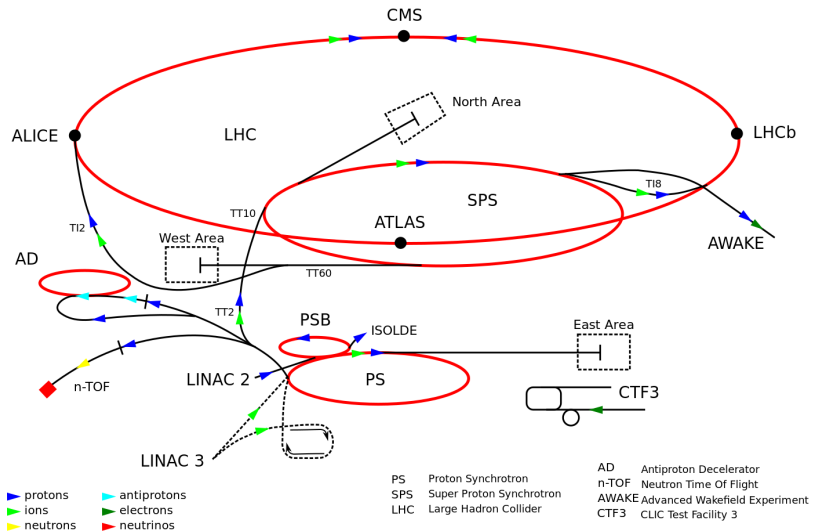


Figure 2.1: CERN accelerator complex. Blue arrows show the path followed by protons along the acceleration process [61].

1096 The LHC runs in three collision modes depending on the particles being acceler-
 1097 ated

- 1098 • Proton-Proton collisions (pp) for multiple physics experiments.
 1099 • Lead-Lead collisions ($Pb-Pb$) for heavy ion experiments.
 1100 • Proton-Lead collisions ($p-Pb$) for quark-gluon plasma experiments.

1101 In this thesis only pp collisions will be considered.

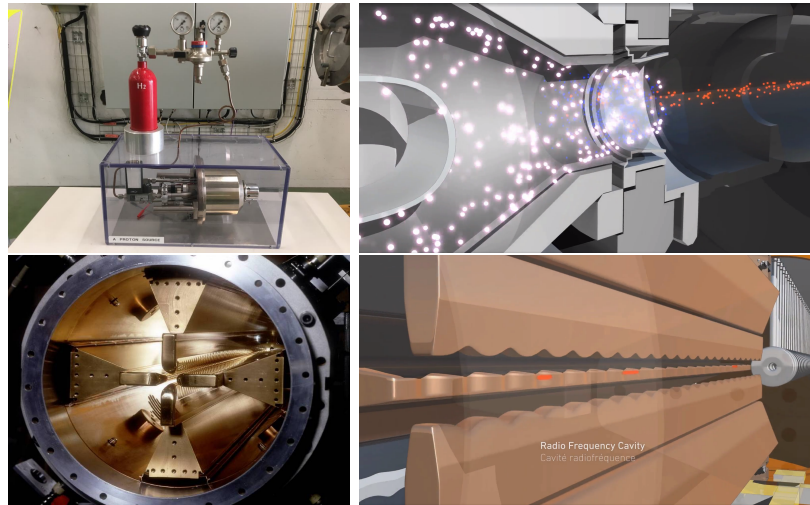


Figure 2.2: LHC protons source and the first acceleration stage. Top: the bottle contains hydrogen gas which is injected into the metal cylinder (white dots) to be broken down into electrons (blue dots) and protons (red dots); Bottom: the obtained protons are directed towards the radio frequency quadrupole which perform the first acceleration, focus the beam and create the bunches of protons. Left images are real pictures while right images are drawings [65, 66].

1102 Collection of protons starts with hydrogen atoms taken from a bottle, containing
 1103 hydrogen gas, and injecting them in a metal cylinder; hydrogen atoms are broken
 1104 down into electrons and protons by an intense electric field (see Figure 2.2 top).
 1105 The resulting protons leave the metal cylinder towards a radio frequency quadrupole
 1106 (RFQ) that focus the beam, accelerates the protons and creates the packets of protons
 1107 called bunches. In the RFQ, an electric field is generated by a RF wave at a frequency
 1108 that matches the resonance frequency of the cavity where the electrodes are contained.
 1109 The beam of protons traveling on the RFQ axis experiences an alternating electric
 1110 field gradient that generates the focusing forces.

1111 In order to accelerate the protons, a longitudinal time-varying electric field com-
 1112 ponent is added to the system; it is done by giving the electrodes a sine-like profile as
 1113 shown in Figure 2.2 bottom. By matching the speed and phase of the protons with
 1114 the longitudinal electric field the bunching is performed; protons synchronized with

1115 the RFQ (synchronous protons) do not feel an accelerating force, but those protons in
 1116 the beam that have more (or less) energy than the synchronous proton (asynchronous
 1117 protons) will feel a decelerating (accelerating) force; therefore, asynchronous protons
 1118 will oscillate around the synchronous ones forming bunches of protons [63]. From the
 1119 RFQ protons emerge with energy 750 keV in bunches of about 1.15×10^{11} protons [64].

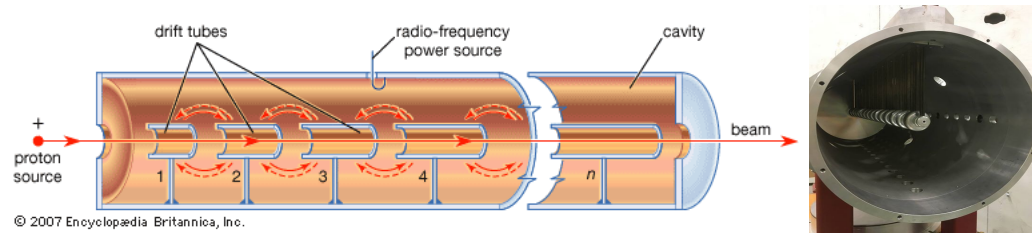


Figure 2.3: Left: drawing of the LINAC2 accelerating system at CERN. Electric fields generated by radio frequency (RF) create acceleration and deceleration zones inside the cavity; deceleration zones are blocked by drift tubes where quadrupole magnets focus the proton beam. Right: picture of a real RF cavity [67].

1120 Proton bunches coming from the RFQ go to the linear accelerator 2 (LINAC2)
 1121 where they are accelerated to reach 50 MeV energy. In the LINAC2 stage, acceleration
 1122 is performed using electric fields generated by radio frequency which create zones
 1123 of acceleration and deceleration as shown in Figure 2.3. In the deceleration zones,
 1124 the electric field is blocked using drift tubes where protons are free to drift while
 1125 quadrupole magnets focus the beam.

1126 The beam coming from LINAC2 is injected into the proton synchrotron booster
 1127 (PSB) to reach 1.4 GeV in energy. The next acceleration is provided at the proton
 1128 synchrotron (PS) up to 26 GeV, followed by the injection into the super proton
 1129 synchrotron (SPS) where protons are accelerated to 450 GeV. Finally, protons are
 1130 injected into the LHC where they are accelerated to the target energy of 6.5 TeV.

1131 PSB, PS, SPS and LHC accelerate protons using the same RF acceleration tech-
 1132 nique described before.

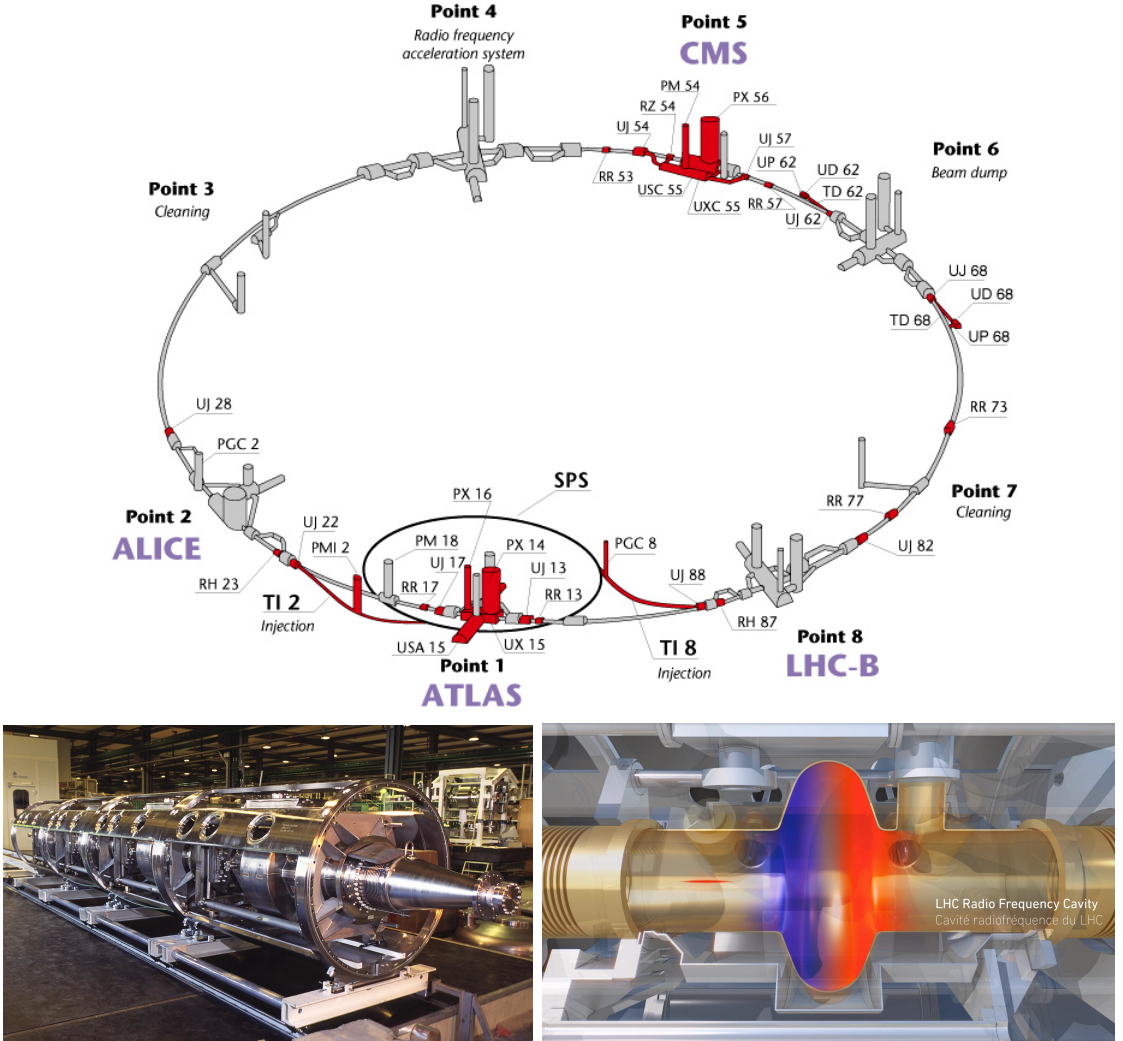


Figure 2.4: Top: LHC layout. The red zones indicate the infrastructure additions to the LEP installations, built to accommodate the ATLAS and CMS experiments which exceed the size of the former experiments located there [62]. Bottom: LHC RF cavities. A module (left picture) accommodates 4 cavities, each like the one in the right drawing, that accelerate protons and preserve the bunch structure of the beam. The color gradient pattern represents the strength of the electric field inside the cavity; red zone corresponds to the maximum of the oscillation electric field while the blue zone corresponds to the minimum. [66, 68]

1133 The LHC has a system of 16 RF cavities located in the so-called point 4, as
 1134 shown in Figure 2.4 top, tuned at a frequency of 400 MHz. The bottom side of
 1135 Figure 2.4 shows a picture of a RF module composed of 4 RF cavities working in a
 1136 superconducting state at 4.5 K; also, a representation of the accelerating electric field

that accelerates the protons in the bunch is shown. The maximum of the oscillating electric field (red region) picks the proton bunches at the entrance of the cavity and keeps accelerating them through the whole cavity. The protons are carefully timed so that in addition to the acceleration effect the bunch structure of the beam is preserved.

While protons are accelerated in one section of the LHC ring, where the RF cavities are located, in the rest of their path they have to be kept in the curved trajectory defined by the LHC ring. Technically, LHC is not a perfect circle; RF, injection, beam dumping, beam cleaning and sections before and after the experimental points where protons collide are all straight sections. In total, there are 8 arcs 2.45 km long each and 8 straight sections 545 m long each. In order to curve the proton's trajectory in the arc sections, superconducting dipole magnets are used.

Inside the LHC ring, there are two proton beams traveling in opposite directions in two separated beam pipes; the beam pipes are kept at ultra-high vacuum ($\sim 10^{-9}$ Pa) to ensure that there are no particles that interact with the proton beams. The superconducting dipole magnets used in LHC are made of a NbTi alloy, capable of transporting currents of about 12000 A when cooled at a temperature below 2K using liquid helium (see Figure 2.5).

Protons in the arc sections of LHC feel a centripetal force exerted by the dipole magnets; the magnitude of magnetic field needed to keep the protons in the LHC curved trayectomy can be found assuming that protons travel at $v \approx c$, using the standard values for proton mass and charge and the LHC radius, as

$$F_m = \frac{mv^2}{r} = qBv \rightarrow B = 8.33T \quad (2.1)$$

which is about 100000 times the Earth's magnetic field. A representation of the

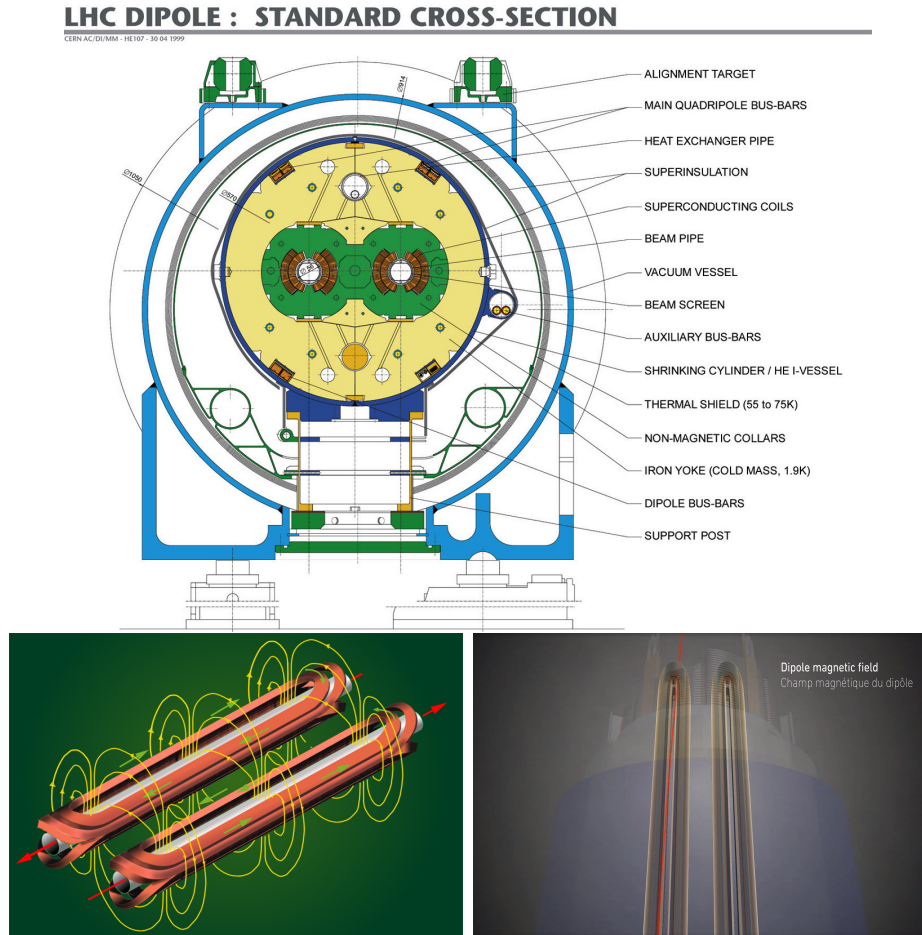


Figure 2.5: Top: LHC dipole magnet transverse view; cooling, shielding and mechanical support are indicated. Bottom left: Magnetic field generated by the dipole magnets; note that the direction of the field inside one beam pipe is opposite with respect to the other beam pipe which guarantee that both proton beams are curved in the same direction towards the center of the ring. The effect of the dipole magnetic field on the proton beam is represented on the bottom right side [66, 69, 70].

1160 magnetic field generated by the dipole magnets is shown on the bottom left side of
 1161 Figure 2.5. The bending effect of the magnetic field on the proton beam is shown on
 1162 the bottom right side of Figure 2.5. Note that the dipole magnets are not curved;
 1163 the arc section of the LHC ring is composed of straight dipole magnets of about 15
 1164 m. In total there are 1232 dipole magnets along the LHC ring.
 1165 In addition to the bending of the beam trajectory, the beam has to be focused. The

focusing is performed by quadrupole magnets installed in a different straight section; in total 858 quadrupole magnets are installed along the LHC ring. Other effects like electromagnetic interaction among bunches, interaction with electron clouds from the beam pipe, the gravitational force on the protons, differences in energy among protons in the same bunch, among others, are corrected using sextupole and other magnetic multipoles.

The two proton beams inside the LHC ring are made of bunches with a cylindrical shape of about 7.5 cm long and about 1 mm in diameter; when bunches are close to the interaction point (IP), the beam is focused up to a diameter of about 16 μm in order to maximize the probability of collisions between protons. The number of collisions per second is proportional to the cross section of the bunches with the *luminosity* (L) as the proportionality factor, thus, the luminosity can be calculated using

$$L = fn \frac{N_1 N_2}{4\pi\sigma_x\sigma_y} \quad (2.2)$$

where f is the revolution frequency, n is the number of bunches per beam, N_1 and N_2 are the numbers of protons per bunch, σ_x and σ_y are the gaussian transverse sizes of the bunches. With the expected parameters, the LHC expected luminosity is about

$$f = \frac{v}{2\pi r_{LHC}} \approx \frac{3 \times 10^8 \text{ m/s}}{27 \text{ km}} \approx 11.1 \text{ kHz},$$

$$n = 2808$$

$$N_1 = N_2 \sim 1.5 \times 10^{11}$$

$$\sigma_x = \sigma_y = 16 \mu\text{m}$$

1181

$$L = 1.28 \times 10^{34} \text{ cm}^{-2} \text{ s}^{-1} = 1.28 \times 10^{-5} \text{ fb}^{-1} \text{ s}^{-1} \quad (2.3)$$

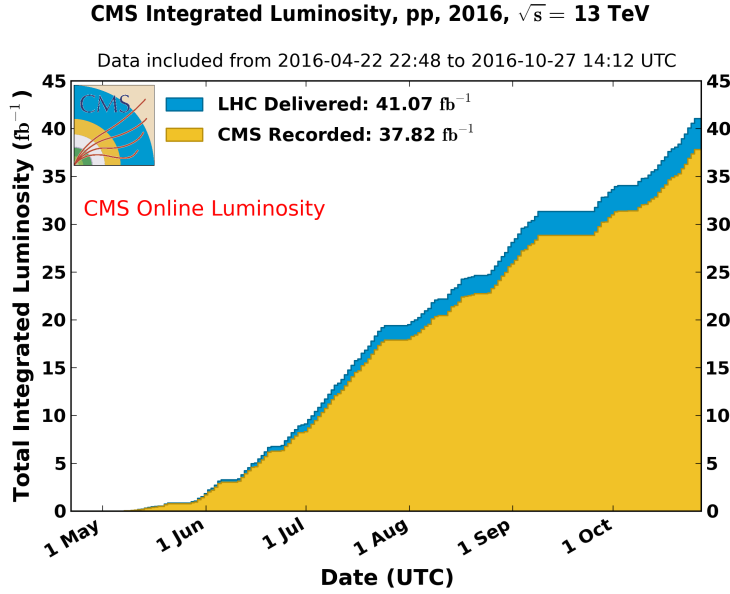


Figure 2.6: Integrated luminosity delivered by LHC and recorded by CMS during 2016. The difference between the delivered and the recorded luminosity is due to fails and issues occurred during the data taking in the CMS experiment [71].

1182 Luminosity is a fundamental aspect of LHC given that the bigger luminosity the
 1183 bigger number of collisions, which means that for processes with a very small cross
 1184 section the number of expected occurrences is increased and so the chances of being
 1185 detected. The integrated luminosity, collected by the CMS experiment during 2016
 1186 is shown in Figure 2.6; the data analyzed in this thesis corresponds to an integrated
 1187 luminosity of 35.9 fb^{-1} at a center of mass-energy $\sqrt{s} = 13 \text{ TeV}$.

1188 One way to increase L is increasing the number of bunches in the beam. Cur-
 1189 rently, the separation between two consecutive bunches in the beam is 7.5 m which
 1190 corresponds to a time separation of 25 ns. In the full LHC ring the allowed number
 1191 of bunches is $n = 27\text{km}/7.5\text{m} = 3600$; however, there are some gaps in the bunch pat-
 1192 tern intended for preparing the dumping and injection of the beam, thus, the proton
 1193 beams are composed of 2808 bunches.

1194 Once the proton beams reach the desired energy, they are brought to cross each

1195 other producing pp collisions. The bunch crossing happens in precise places where
 1196 the four LHC experiments are located, as seen in the top of Figure 2.7. In 2008 pp
 1197 collisions of $\sqrt{s} = 7$ TeV were performed; the energy was increased to 8 TeV in 2012
 1198 and to 13 TeV in 2015.

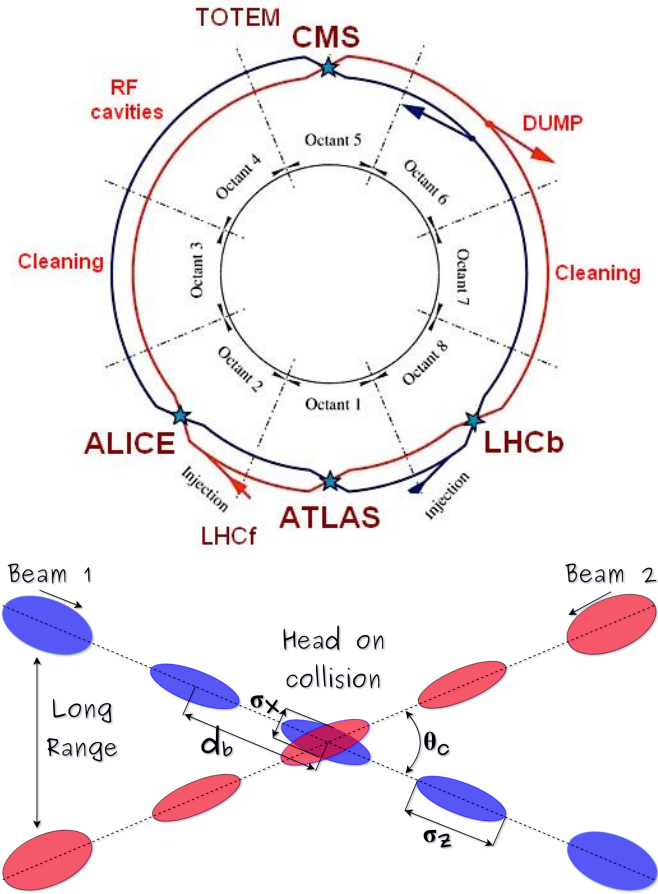


Figure 2.7: Top: LHC interaction points. Bunch crossing occurs where the LHC experiments are located [72]. Sections indicated as cleaning are dedicated to collimate the beam in order to protect the LHC ring from collisions with protons in very spreaded bunches. Bottom: bunch crossing scheme. Since the bunch crossing is not perfectly head-on, the luminosity is reduced in a factor of 17%; adapted from Reference [86].

1199 The CMS and ATLAS experiments are multi-purpose experiments, hence, they
 1200 are enabled to explore physics in any of the LHC collision modes. LHCb experiment
 1201 is optimized to explore bottom quark physics, while ALICE is optimized for heavy

1202 ion collisions searches; TOTEM and LHCf are dedicated to forward physics studies;
 1203 MoEDAL (not indicated in the Figure) is intended for monopole or massive pseudo
 1204 stable particles searches.

1205 At the IP there are two interesting details that need to be addressed. The first
 1206 one is that the bunch crossing does not occur head-on but at a small crossing angle θ_c
 1207 (280 μ rad in CMS and ATLAS) as shown in the bottom side of Figure 2.7, affecting
 1208 the overlapping between bunches; the consequence is a reduction of about 17% in
 1209 the luminosity (represented by a factor not included in eqn. 2.2). The second one
 1210 is the occurrence of multiple pp collisions in the same bunch crossing; this effect is
 1211 called *pileup* (PU). A fairly simple estimation of the PU follows from estimating the
 1212 probability of collision between two protons, one from each of the bunches in the
 1213 course of collision; it depends roughly on the ratio of proton size and the cross section
 1214 of the bunch in the IP, i.e.,

$$P(pp\text{-}collision) \sim \frac{d_{proton}^2}{\sigma_x \sigma_y} = \frac{(1\text{fm})^2}{(16\mu\text{m})^2} \sim 4 \times 10^{-21} \quad (2.4)$$

1215 however, there are $N = 1.15 \times 10^{11}$ protons in a bunch, thus the estimated number of
 1216 collisions in a bunch crossing is

$$PU = N^2 * P(pp\text{-}collision) \sim 50pp \text{ collision per bunch crossing}, \quad (2.5)$$

1217 about 20 of which are inelastic. A multiple pp collision event in a bunch crossing at
 1218 CMS is shown in Figure 2.8.

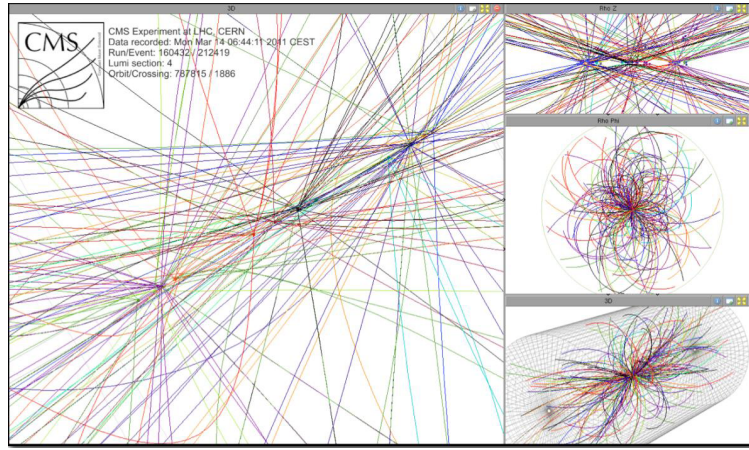


Figure 2.8: Multiple pp collision bunch crossing at CMS. [73].

1219 2.3 The CMS experiment

1220 CMS is a general-purpose detector designed to conduct research in a wide range
 1221 of physics from the standard model to new physics like extra dimensions and dark
 1222 matter. Located at Point 5 in the LHC layout as shown in Figure 2.4, CMS is
 1223 composed of several detection systems distributed in a cylindrical structure; in total,
 1224 CMS weights about 12500 tons in a very compact 21.6 m long and 14.6 m diameter
 1225 cylinder. It was built in 15 separate sections at the ground level and lowered to the
 1226 cavern individually to be assembled. A complete and detailed description of the CMS
 1227 detector and its components is given in Reference [74] on which this section is based.
 1228 Figure 2.9 shows the layout of the CMS detector. The detection system is composed
 1229 of (from the innermost to the outermost)

- 1230 • Pixel detector.
- 1231 • Silicon strip tracker.
- 1232 • Preshower detector.
- 1233 • Electromagnetic calorimeter.

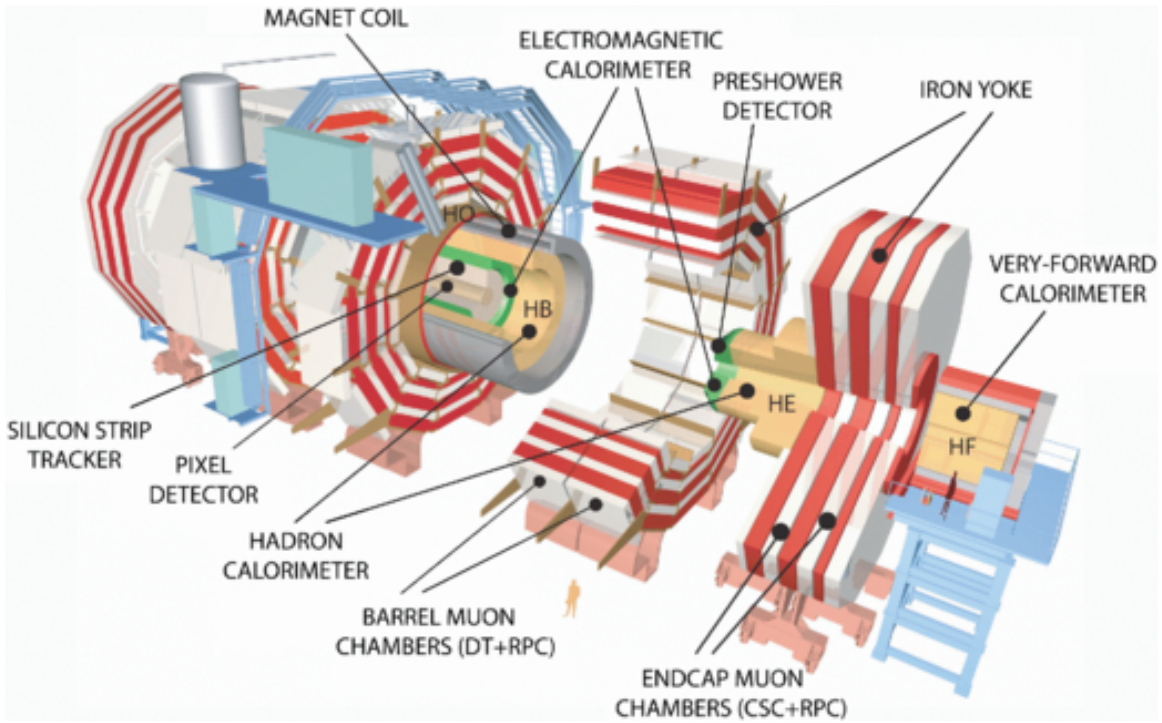


Figure 2.9: Layout of the CMS detector. The several subdetectors are indicated. The central region of the detector is referred as the barrel section while the endcaps are referred as the forward sections. [75].

1234 • Hadronic calorimeter.

1235 • Muon chambers (barrel and endcap)

1236 The central region of the detector is commonly referred as the barrel section while
 1237 the endcaps are referred as the forward sections of the detector; thus, each subdetector
 1238 is composed of a barrel section and a forward section.

1239 When a pp collision happens inside the CMS detector, many different particles are
 1240 produced, but only some of them live long enough to be detected; they are electrons,
 1241 photons, pions, kaons, protons, neutrons and muons; neutrinos are not detected by
 1242 the CMS detector. Thus, the CMS detector was designed to detect those particles and
 1243 measure their properties. Figure 2.10 shows a transverse slice of the CMS detector.
 1244 The silicon tracker (pixel detector + strip tracker) is capable to register the track of

1245 the charged particles traversing it, while calorimeters (electromagnetic and hadronic)
 1246 measure the energy of the particles that are absorbed by their materials. Considering
 1247 the detectable particles, mentioned above, emerging from the IP, a basic description
 1248 of the detection process is as follows.

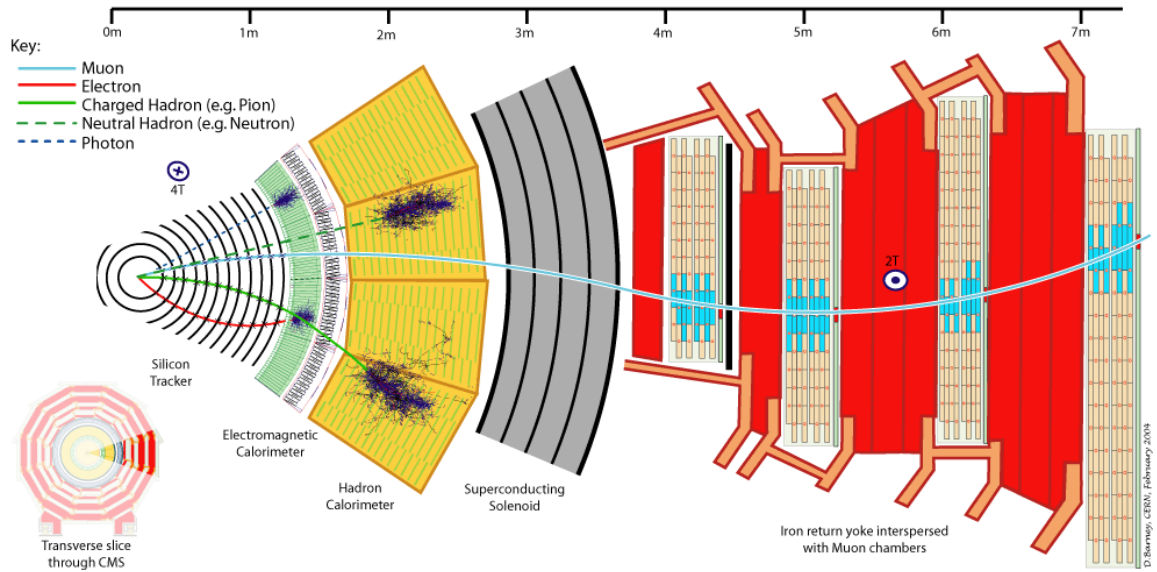


Figure 2.10: CMS detector transverse slice [76].

1249 A muon emerging from the IP, will create a track on the silicon tracker and on
 1250 the muon chambers. The design of the CMS detector is driven by the requirements
 1251 on the identification, momentum resolution and unambiguous charge determination
 1252 of the muons; therefore, a large bending power is provided by the solenoid magnet
 1253 made of superconducting cable capable of generating a 3.8 T magnetic field. The
 1254 muon track is bent twice since the magnetic field inside the solenoid is directed along
 1255 the z -direction but outside its direction is reversed. Muons interact very weakly with
 1256 the calorimeters, therefore, it is not absorbed but escape away from the detector.

1257 An electron emerging from the IP will create a track along the tracker which will
 1258 be bent due to the presence of the magnetic field, later, it will be absorbed in the
 1259 electromagnetic calorimeter where its energy is measured.

1260 A photon will not leave a track because it is neutral, but it will be absorbed in
 1261 the electromagnetic calorimeter.

1262 A neutral hadron, like the neutron, will not leave a track either but it will lose a
 1263 small amount of its energy during its passage through the electromagnetic calorimeter
 1264 and then it will be absorbed in the hadron calorimeter depositing the rest of its energy.

1265 A charged hadron, like the proton or π^\pm , will leave a curved track on the silicon
 1266 tracker, some of its energy in the electromagnetic calorimeter and finally will be
 1267 absorbed in the hadronic calorimeter.

1268 A more detailed description of each detection system will be presented in the
 1269 following sections.

1270 2.3.1 CMS coordinate system

1271 The coordinate system used by CMS is centered on the geometrical center of the
 1272 detector which is the nominal IP as shown in Figure 2.11¹. The z -axis is parallel
 1273 to the beam direction, while the Y -axis pointing vertically upward, and the X -axis
 1274 pointing radially inward toward the center of the LHC.

1275 In addition to the common cartesian and cylindrical coordinate systems, two co-
 1276 ordinates are of particular utility in particle physics: rapidity (y) and pseudorapidity
 1277 (η), defined in connection to the polar angle θ , energy and longitudinal momentum
 1278 component (momentum along the z -axis) according to

$$y = \frac{1}{2} \ln \frac{E + p_z}{E - p_z} \quad \eta = -\ln \left(\tan \frac{\theta}{2} \right) \quad (2.6)$$

1279 Rapidity is related to the angle between the XY -plane and the direction in which
 1280 the products of a collision are emitted; it has the nice property that the difference

¹ Not all the pp interaction occur at the nominal IP because of the bunch lenght, therefore, each pp collision has its own IP location

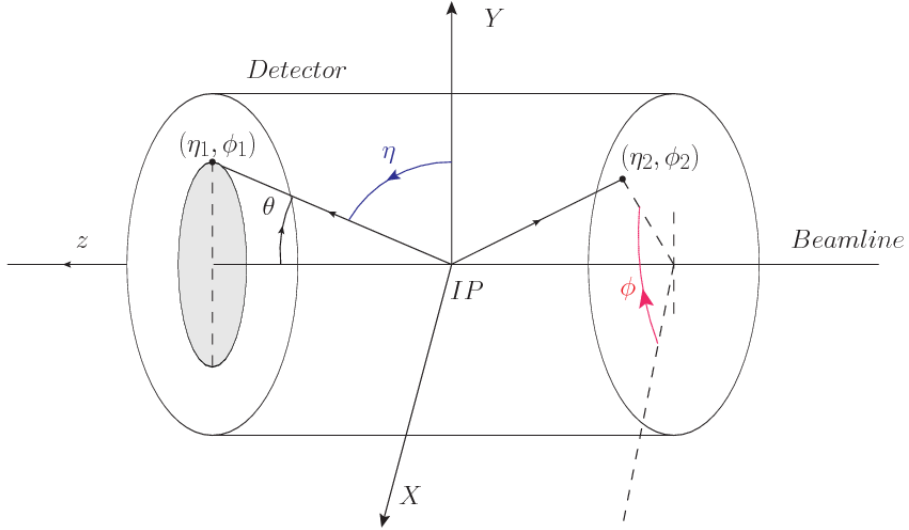


Figure 2.11: CMS detector coordinate system.

1281 between the rapidities of two particles is invariant with respect to Lorentz boosts
 1282 along the z -axis, hence, data analysis becomes more simple when based on rapid-
 1283 ity; however, it is not simple to measure the rapidity of highly relativistic particles,
 1284 as those produced after pp collisions. Under the highly relativistic motion approxi-
 1285 mation, y can be rewritten in terms of the polar angle, concluding that rapidity is
 1286 approximately equal to the pseudorapidity defined above, i.e., $y \approx \eta$. Note that η
 1287 is easier to measure than y given the direct relationship between the former and the
 1288 polar angle.

1289 The angular distance between two objects in the detector (ΔR) is commonly used
 1290 to judge the isolation of those object; it is defined in terms of their coordinates (η_1, ϕ_1) ,
 1291 (η_2, ϕ_2) as

$$\Delta R = \sqrt{(\Delta\eta)^2 - (\Delta\phi)^2} \quad (2.7)$$

1292 2.3.2 Tracking system

1293 The CMS tracking system is designed to provide a precise measurement of the trajectories (*track*) followed by the charged particles created after the pp collisions; also, the
 1294 precise reconstruction of the primary and secondary origins of the tracks (*vertices*) is
 1295 expected in an environment where, each 25 ns, the bunch crossing produces about 20
 1296 inelastic collisions and about 1000 particles.
 1297

1298 Physics requirements guiding the tracking system performance include the precise characterization of events involving gauge bosons, W and Z, and their leptonic
 1299 decays for which an efficient isolated lepton and photon reconstruction is of capital
 1300 importance, given that isolation is required to suppress background events to a level
 1301 that allows observations of interesting processes like Higgs boson decays or beyond
 1302 SM events.

1304 The ability to identify and reconstruct b -jets and B-hadrons within these jets is also
 1305 a fundamental requirement, achieved through the ability to reconstruct accurately
 1306 displaced vertices, given that b -jets are part of the signature of top quark physics, like
 1307 the one treated in this thesis.

1308 An schematic view of the CMS tracking system is shown in Figure 2.12

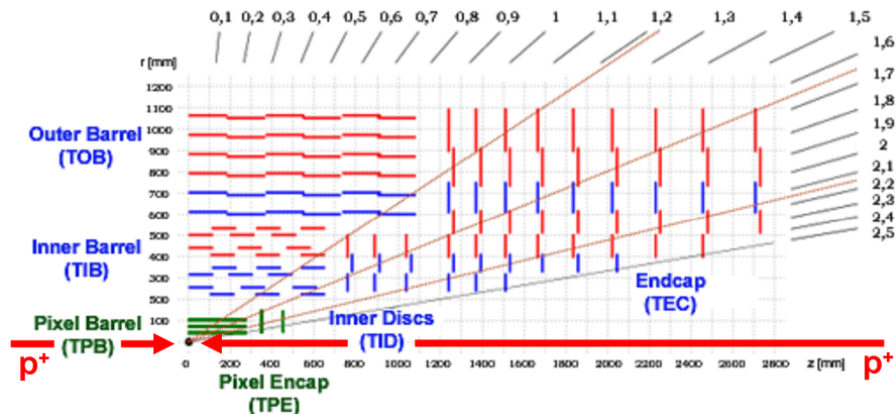


Figure 2.12: CMS tracking system schematic view [78].

1309 In order to satisfy these performance requirements, the tracking system uses two
 1310 different detector subsystems arranged in concentric cylindrical volumes, the pixel
 1311 detector and the silicon strip tracker; the pixel detector is located in the high particle
 1312 density region ($r < 20\text{cm}$) while the silicon strip tracker is located in the medium and
 1313 lower particle density regions $20\text{cm} < r < 116\text{cm}$.

1314 **Pixel detector**

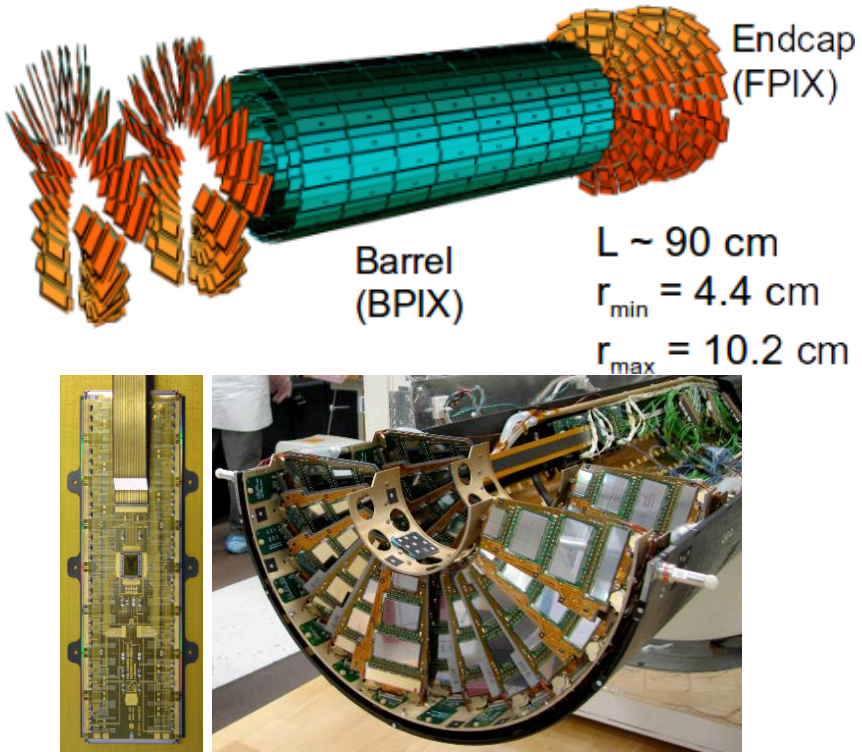


Figure 2.13: CMS pixel detector. Top: schematic view; Bottom: pictures of a barrel(BPIX) module(left) and forward modules(right) [74].

1315 The pixel detector was replaced during the 2016-2017 extended year-end technical
 1316 stop, due to the increasingly challenging operating conditions like the higher particle
 1317 flux and more radiation harsh environment, among others. The new one is responding
 1318 as expected, reinforcing its crucial role in the successful way to fulfill the new LHC

physics objectives after the discovery of the Higgs boson. Since the data sets used in this thesis were produced using the previous version of the pixel detector, it will be the subject of the description in this section. The last chapter of this thesis is dedicated to describe my contribution to the *Forward Pixel Phase 1 upgrade*.

The pixel detector was composed of 1440 silicon pixel detector modules organized in three-barrel layers in the central region (BPix) and two disks in the forward region (FPix) as shown in the top side of Figure 2.13; it was designed to record efficiently and with high precision, up to $20\mu\text{m}$ in the XY -plane and $20\mu\text{m}$ in the z -direction, the first three space-points (*hits*) nearest to the IP region in the range $|\eta| \leq 2.5$. The first barrel layer was located at a radius of 44 mm from the beamline, while the third layer was located at a radius of 102 mm, closer to the strip tracker inner barrel layer (see Section 2.3.3) in order to reduce the rate of fake tracks. The high granularity of the detector is represented in its about 66 Mpixels, each of size $100 \times 150\mu\text{m}^2$. The transverse momentum resolution of tracks can be measured with a resolution of 1-2% for muons of $p_T = 100$ GeV.

A charged particle passing through the pixel sensors produce ionization in them, giving energy for electrons to be removed from the silicon atoms, hence, creating electron-hole pairs. The collection of charges in the pixels generates an electrical signal that is read out by an electronic readout chip (ROC); each pixel has its own electronics which amplifies the signal. Combining the signal from the pixels activated by a traversing particle in the several layers of the detector allows one to reconstruct the particle's trajectory in 3D.

Commonly, the charge produced by traversing of a particle is collected by and shared among several pixels; by interpolating between pixels, the spatial resolution is improved. In the barrel section the charge sharing in the $r\phi$ -plane is due to the Lorentz effect. In the forward pixels the charge sharing is enhanced by arranging the

1345 blades in the turbine-like layout as shown in Figure 2.13 bottom left.

1346 2.3.3 Silicon strip tracker

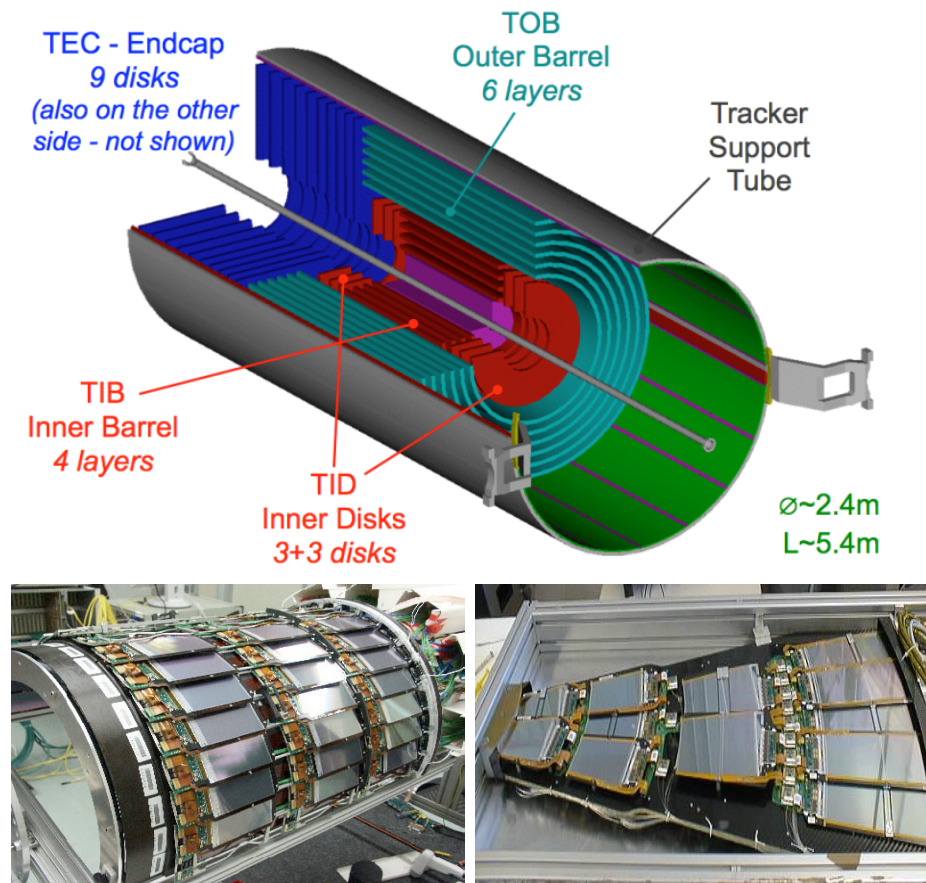


Figure 2.14: Top: CMS Silicon Strip Tracker (SST) schematic view. The SST is composed of the tracker inner barrel (TIB), the tracker inner disks (TID), the tracker outer barrel (TOB) and the tracker endcaps (TEC). Each part is made of silicon strip modules; the modules in blue represent two modules mounted back-to-back and rotated in the plane of the module by a stereo angle of 120 mrad in order to provide a 3-D reconstruction of the hit positions. Bottom: pictures of the TIB (left) and TEC (right) modules [80–82].

1347 The silicon strip tracker (SST) is the second stage in the CMS tracking system.

1348 The top side of Figure 2.14 shows a schematic of the SST. The inner tracker region is

1349 composed of the tracker inner barrel (TIB) and the tracker inner disks (TID) covering

1350 the region $r < 55$ cm and $|z| < 118$ cm. The TIB is composed of 4 layers while the TID

1351 is composed of 3 disks at each end. The silicon sensors in the inner tracker are 320
 1352 μm thick, providing a resolution of about 13-38 μm in the $r\phi$ position measurement.

1353 The modules indicated in blue in the schematic view of Figure 2.14 are two mod-
 1354 ules mounted back-to-back and rotated in the plane of the module by a *stereo* angle
 1355 of 100 mrad; the hits from these two modules, known as *stereo hits*, are combined to
 1356 provide a measurement of the second coordinate (z in the barrel and r on the disks)
 1357 allowing the reconstruction of hit positions in 3-D.

1358 The outer tracker region is composed of the tracker outer barrel (TOB) and the
 1359 tracker endcaps (TEC). The six layers of the TOB offer coverage in the region $r > 55$
 1360 cm and $|z| < 118$ cm, while the 9 disks of the TEC cover the region $124 < |z| < 282$
 1361 cm. The resolution offered by the outer tracker is about 13-38 μm in the $r\phi$ position
 1362 measurement. The inner four TEC disks use silicon sensors 320 μm thick; those in
 1363 the TOB and the outer three TEC disks use silicon sensors of 500 μm thickness. The
 1364 silicon strips run parallel to the z -axis and the distance between strips varies from 80
 1365 μm in the inner TIB layers to 183 μm in the inner TOB layers; in the endcaps the
 1366 wedge-shaped sensors with radial strips, whose pitch range between 81 μm at small
 1367 radii and 205 μm at large radii.

1368 The whole SST has 15148 silicon modules, 9.3 million silicon strips and cover a
 1369 total active area of about 198 m^2 .

1370 **2.3.4 Electromagnetic calorimeter**

1371 The CMS electromagnetic calorimeter (ECAL) is designed to measure the energy of
 1372 electrons and photons. It is composed of 75848 lead tungstate crystals which have a
 1373 short radiation length (0.89 cm) and fast response, since 80% of the light is emitted
 1374 within 25 ns; however, they are combined with Avalanche photodiodes (APDs) as

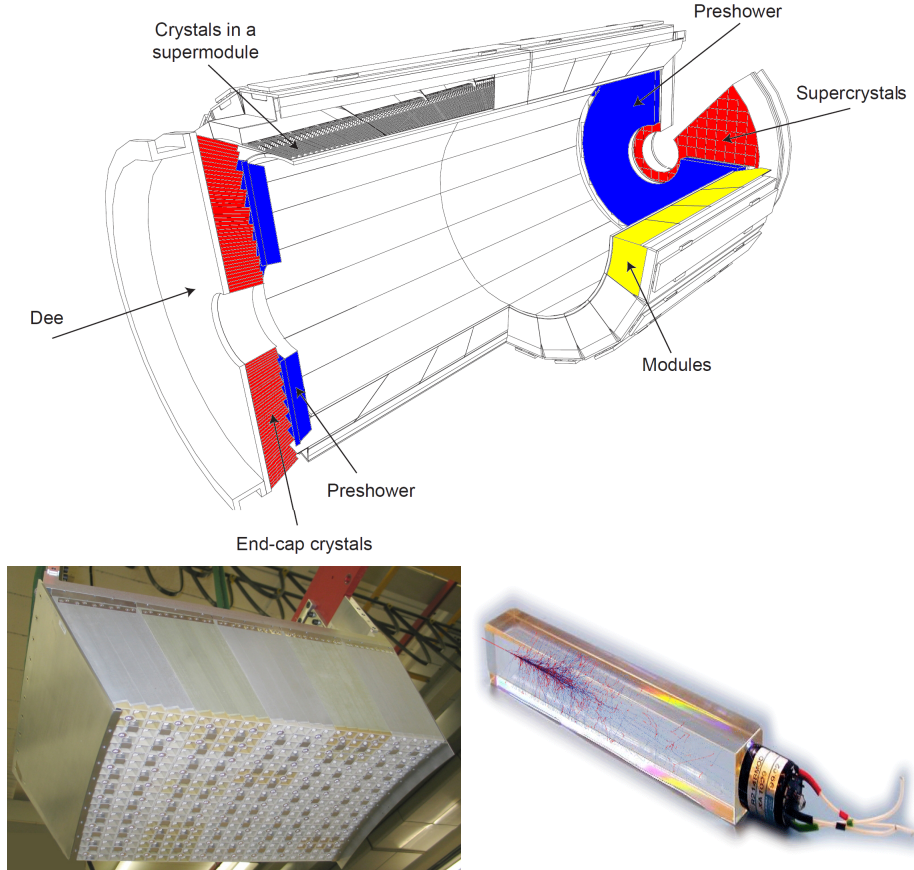


Figure 2.15: Top: CMS ECAL schematic view. Bottom: Module equipped with the crystals (left); ECAL crystal(right) with an artistic representation of an electromagnetic shower [74].

1375 photodetectors given that crystals themselves have a low light yield ($30\gamma/\text{MeV}$). A
 1376 schematic view of the ECAL is shown in Figure 2.15.

1377 Energy is measured when electrons and photons are absorbed by the crystals
 1378 which generates an electromagnetic *shower*, as seen in bottom right picture of the
 1379 Figure 2.15; the shower is seen as a *cluster* of energy which depending on the amount
 1380 of energy deposited can involve several crystals. The ECAL barrel (EB) covers the
 1381 region $|\eta| < 1.479$, using crystals of depth of 23 cm and $2.2 \times 2.2 \text{ cm}^2$ transverse
 1382 section; the ECAL endcap (EE) covers the region $1.479 < |\eta| < 3.0$ using crystals of
 1383 depth 22 cm and transverse section of $2.86 \times 2.86 \text{ cm}^2$; the photodetectors used are

1384 vacuum phototriodes (VPTs). Each EE is divided in two structures called *Dees*.

1385 The preshower detector (ES) is installed in front of the EE and covers the region
 1386 $1.653 < |\eta| < 2.6$. The ES provides a precise measurement of the position of electro-
 1387 magnetic showers, which allows to distinguish electrons and photon signals from π^0
 1388 decay signals. The ES is composed of a layer of lead radiators followed by a layer of
 1389 silicon strip sensors. The lead radiators initiate electromagnetic showers when reached
 1390 by photons and electrons, then, the strip sensors measure the deposited energy and
 1391 the transverse shower profiles. The full ES thickness is 20 cm.

1392 2.3.5 Hadronic calorimeter

1393 Hadrons are not absorbed by the ECAL² but by the hadron calorimeter (HCAL),
 1394 which is made of a combination of alternating brass absorber layers and silicon photo-
 1395 multiplier(SiPM) layers; therefore, particles passing through the scintillator material
 1396 produce showers, as in the ECAL, as a result of the inelastic scattering of the hadrons
 1397 with the detector material. Since the particles are not absorbed in the scintillator,
 1398 their energy is sampled; therefore the total energy is not measured but estimated from
 1399 the energy clusters, which reduces the resolution of the detector. Brass was chosen
 1400 as the absorber material due to its short interaction length ($\lambda_I = 16.42\text{cm}$) and its
 1401 non-magnetivity. Figure 2.16 shows a schematic view of the CMS HCAL.

1402 The HCAL is divided into four sections; the Hadron Barrel (HB), the Hadron
 1403 Outer (HO), the Hadron Endcap (HE) and the Hadron Forward (HF) sections. The
 1404 HB covers the region $0 < |\eta| < 1.4$, while the HE covers the region $1.3 < |\eta| < 3.0$.
 1405 The HF, made of quartz fiber scintillator and steel as absorption material, covers the
 1406 forward region $3.0 < |\eta| < 5.2$. Both the HB and HF are located inside the solenoid.
 1407 The HO is placed outside the magnet as an additional layer of scintillators with the

² Most hadrons are not absorbed, but few low-energy ones might be.

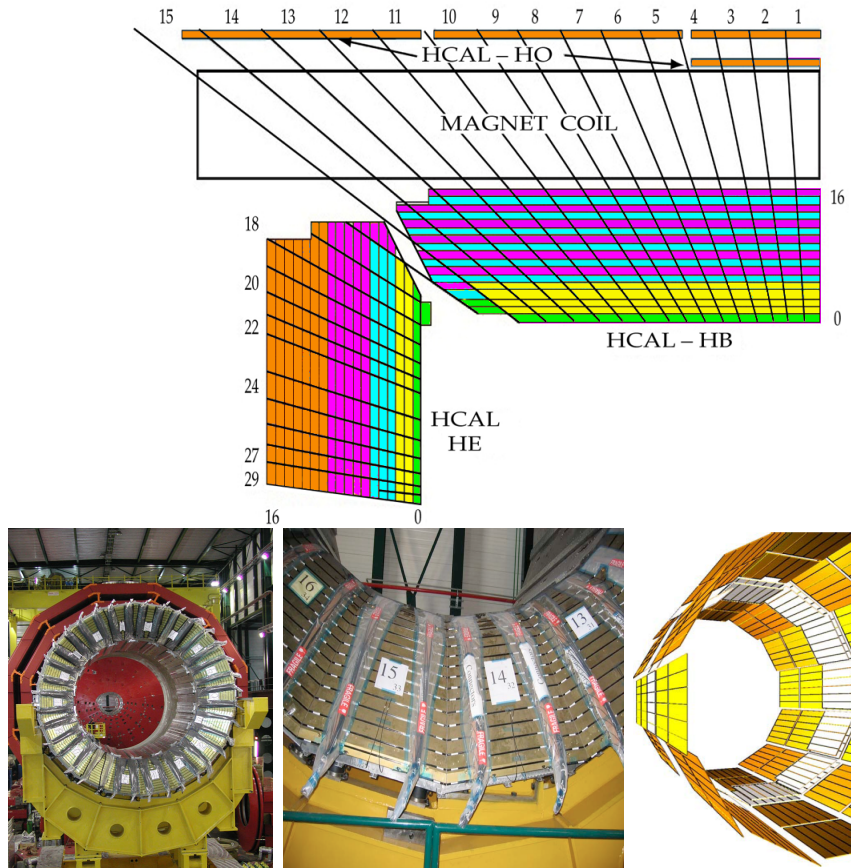


Figure 2.16: Top: CMS HCAL schematic view, the colors indicate the layers that are grouped into the same readout channels. Bottom: picture of a section of the HB; the absorber material is the golden region and scintillators are placed in between the absorber material (left and center). Schematic view of the HO (right). [83,84]

1408 purpose of measure the energy tails of particles passing through the HB and the
 1409 magnet (see Figure 2.16 top and bottom right).

1410 **2.3.6 Superconducting solenoid magnet**

1411 The superconducting magnet installed in the CMS detector is designed to provide
 1412 an intense and highly uniform magnetic field in the central part of the detector.
 1413 In fact, the tracking system takes advantage of the bending power of the magnetic
 1414 field to measure with precision the momentum of the particles that traverse it; the

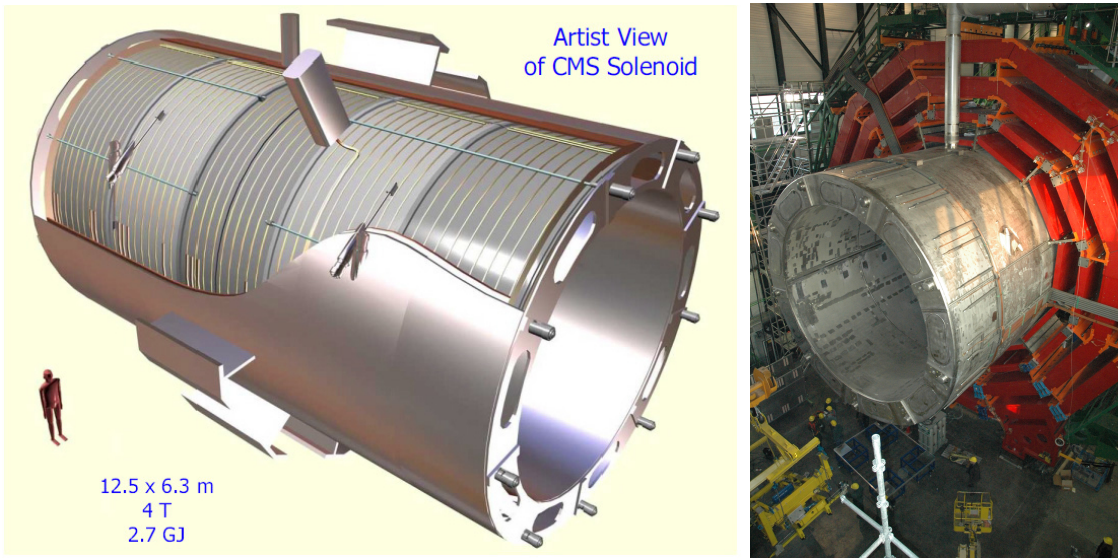


Figure 2.17: Artistic representation of the CMS solenoid magnet(left). The magnet is supported on an iron yoke (right) which also serves as the house of the muon detector and as mechanical support for the whole CMS detector [77].

1415 unambiguous determination of the sign for high momentum muons was a driving
 1416 principle during the design of the magnet. The magnet has a diameter of 6.3 m, a
 1417 length of 12.5 m and a cold mass of 220 t; the generated magnetic field reaches a
 1418 strength of 3.8T. Since it is made of Ni-Tb superconducting cable it has to operate at
 1419 a temperature of 4.7 K by using a helium cryogenic system; the current circulating in
 1420 the cables reaches 18800 A under normal running conditions. The left side of Figure
 1421 2.17 shows an artistic view of the CMS magnet, while the right side shows a transverse
 1422 view of the cold mass where the winding structure is visible.

1423 The yoke (see Figure 2.17), composed of 5 barrel wheels and 6 endcap disks made
 1424 of iron, serves not only as the media for magnetic flux return but also provides housing
 1425 for the muon detector system and structural stability to the full detector.

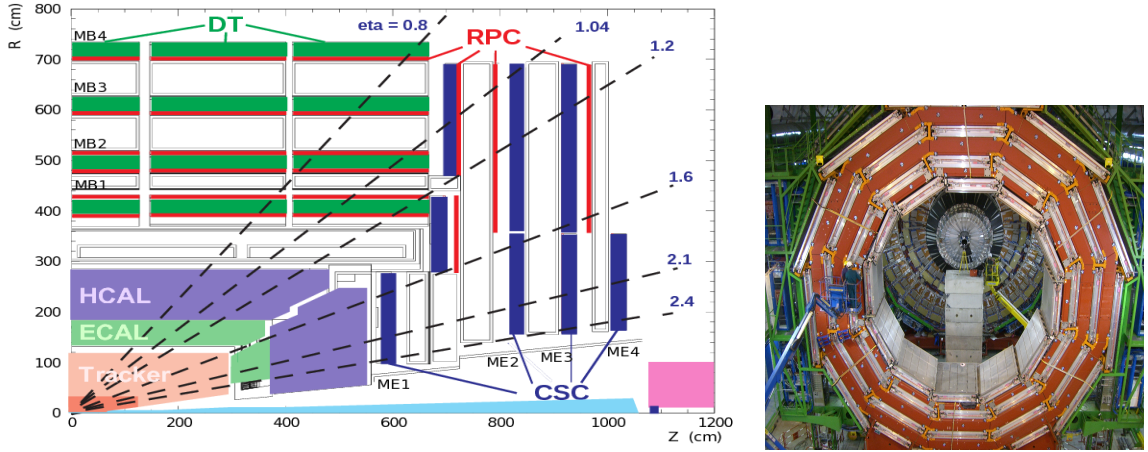


Figure 2.18: Left: CMS muon system schematic view; Right: one of the yoke rings with the muon DTs and RPCs installed; in the back it is possible to see the muon endcap [85].

1426 2.3.7 Muon system

1427 Muons are the only charged particles able to pass through all the CMS detector due
 1428 to their low ionization energy loss; thus, muons can be separated easily from the
 1429 high amount of particles produced in a pp collision. Also, muons are expected to be
 1430 produced in the decay of several new particles; therefore, good detection of muons
 1431 was one of the leading principles when designing the CMS detector.

1432 The CMS muon detection system (muon spectrometer) is embedded in the return
 1433 yoke as seen in Figure 2.18. It is composed of three different detector types, the drift
 1434 tube chambers (DT), cathode strip chambers (CSC), and resistive plate chambers
 1435 (RPC); DT are located in the central region $\eta < 1.2$ arranged in four layers of drift
 1436 chambers filled with an Ar/CO₂ gas mixture.

1437 The muon endcaps are made of CSCs covering the region $\eta < 2.4$ and filled with
 1438 a mixture of Ar/CO₂/CF₄. The reason behind using a different detector type lies on
 1439 the different conditions in the forward region like the higher muon rate and higher
 1440 residual magnetic field compared to the central region.

1441 The third type of detector used in the muon system is a set of four disks of RPCs

1442 working in avalanche mode. The RPCs provide good spatial and time resolutions. The
 1443 track of high- p_T muon candidates is built combining information from the tracking
 1444 system and the signal from up to six RPCs and four DT chambers.

1445 The muon tracks are reconstructed from the hits in the several layers of the muon
 1446 system.

1447 2.3.8 CMS trigger system

1448 CMS expects pp collisions every 25 ns, i.e., an interaction rate of 40 MHz for which
 1449 it is not possible to store the recorded data in full. In order to handle this high event
 1450 rate data, an online event selection, known as triggering, is performed; triggering
 1451 reduces the event rate to 100 Hz for storage and further offline analysis.

1452 The trigger system starts with a reduction of the event rate to 100 kHz in the
 1453 so-called *the level 1 trigger* (L1). L1 is based on dedicated programmable hardware
 1454 like Field Programmable Gate Arrays (FPGAs) and Application Specific Integrated
 1455 Circuits (ASICs), partly located in the detector itself; another portion is located in
 1456 the CMS underground cavern. Hit pattern information from the muon chambers
 1457 and the energy deposits in the calorimeter are used to decide if an event is accepted
 1458 or rejected, according to selection requirements previously defined, which reflect the
 1459 interesting physics processes. Figure 2.19 shows the L1 trigger architecture.

1460 The second stage in the trigger system is called *the high-level trigger* (HLT); events
 1461 accepted by L1 are passed to HLT in order to make an initial reconstruction of them.
 1462 HLT is software based and runs on a dedicated server farm, using selection algorithms
 1463 and high-level object definitions; the event rate at HLT is reduced to 100 Hz. The
 1464 first HLT stage takes information from the muon detectors and the calorimeters to
 1465 make the initial object reconstruction; in the next HLT stage, information from the

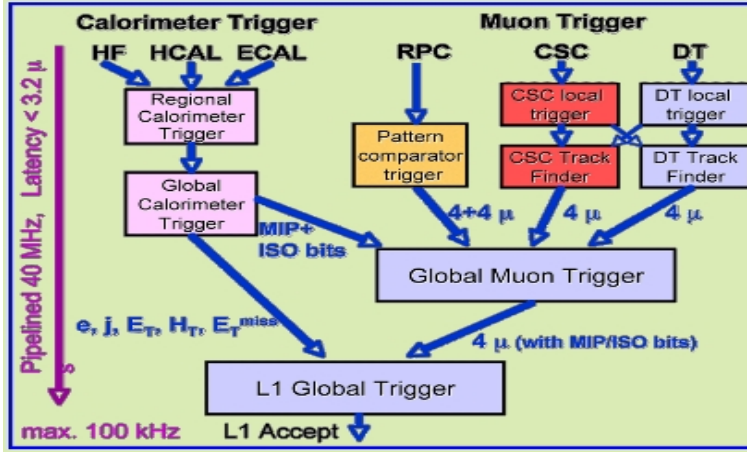


Figure 2.19: CMS Level-1 trigger architecture [86].

pixel and strip detectors is used to do first fast tracking and then full tracking online.
 This initial object reconstruction is used in further steps of the trigger system.

Events and preliminary reconstructed physics objects from HLT are sent to be fully reconstructed at the CERN computing center known also as Tier-0 facility. Again, the pixel detector information provides high-quality seeds for the track reconstruction algorithm offline, primary vertex reconstruction, electron and photon identification, muon reconstruction, τ identification, and b-tagging. After full reconstruction, data sets are made available for offline analyses.

2.3.9 CMS computing

Data coming from the experiment have to be stored and made available for further analysis; in order to cope with all the tasks implied in the offline data processing, like transfer, simulation, reconstruction and reprocessing, among others, a large computing power is required. The CMS computing system is based on the distributed architecture concept, where users of the system and physical computer centers are distributed worldwide and interconnected by high-speed networks.

The worldwide LHC computing grid (WLCG) is the mechanism used to provide

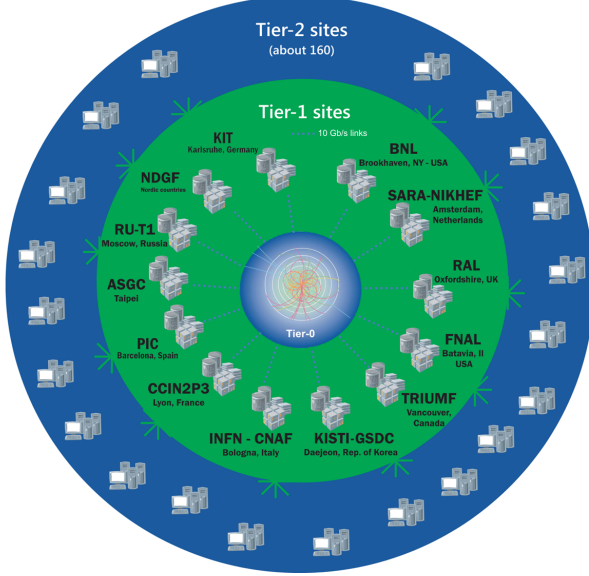


Figure 2.20: WLCG structure. The primary computer centers (Tier-0) are located at CERN (data center) and at the Wigner datacenter in Budapest. Tier-1 is composed of 13 centers and Tier-2 is composed of about 160 centers. [87].

1482 that distributed environment. WLCG is a tiered structure connecting computing
 1483 centers around the world, which provides the necessary storage and computing facil-
 1484 ities. The primary computing centers of the WLCG are located at the CERN and
 1485 the Wigner datacenter in Budapest and are known as Tier-0 as shown in Figure 2.20.
 1486 The main responsibilities for each tier level are [87]

- 1487 • **Tier-0:** initial reconstruction of recorded events and storage of the resulting
 1488 datasets, the distribution of raw data to the Tier-1 centers.
- 1489 • **Tier-1:** provide storage capacity, support for the Grid, safe-keeping of a pro-
 1490 portional share of raw and reconstructed data, large-scale reprocessing and safe-
 1491 keeping of corresponding output, generation of simulated events, distribution
 1492 of data to Tier 2s, safe-keeping of a share of simulated data produced at these
 1493 Tier 2s.
- 1494 • **Tier-2:** store sufficient data and provide adequate computing power for spe-

1495 cific analysis tasks and proportional share of simulated event production and
1496 reconstruction.

1497 Aside from the general computing strategy to manage the huge amount of data
1498 produced by experiments, CMS uses a software framework to perform a variety of
1499 processing, selection and analysis tasks. The central concept of the CMS data model
1500 referred to as *event data model* (EDM) is the *Event*; therefore, an event is the unit
1501 that contains the information from a single bunch crossing, any data derived from
1502 that information like the reconstructed objects, and the details of the derivation.

1503 Events are passed as the input to the *physics modules* that obtain information
1504 from them and create new information; for instance, *event data producers* add new
1505 data into the events, *analyzers* produce an information summary from an event set,
1506 *filters* perform selection and triggering.

1507 CMS uses several event formats with different levels of detail and precision

1508 • **Raw format:** events in this format contain the full recorded information from
1509 the detector as well as trigger decision and other metadata. An extended version
1510 of raw data is used to store information from the CMS Monte Carlo simulation
1511 tools (see Chapter 3). Raw data are stored permanently, occupying about
1512 2MB/event

1513 • **RECO format:** events in this format correspond to raw data that have been
1514 submitted to reconstruction algorithms like primary and secondary vertex re-
1515 construction, particle ID, and track finding. RECO events contain physics ob-
1516 jects and all the information used to reconstruct them; average size is about 0.5
1517 MB/event.

- 1518 • **AOD format:** Analysis Object Data (AOD) is the data format used in the
 1519 physics analyses given that it contains the parameters describing the high-level
 1520 physics objects in addition to enough information to allow a kinematic refitting if
 1521 needed. AOD events are filtered versions of the RECO events to which skimming
 1522 or other filtering have been applied, hence AOD events are subsets of RECO
 1523 events. Requires about 100 kB/event.
- 1524 • **Non-event data** are data needed to interpret and reconstruct events. Some
 1525 of the non-event data used by CMS contains information about the detector
 1526 contraction and condition data like calibrations, alignment, and detector status.

1527 Figure 2.21 shows the data flow scheme between CMS detector and tiers.

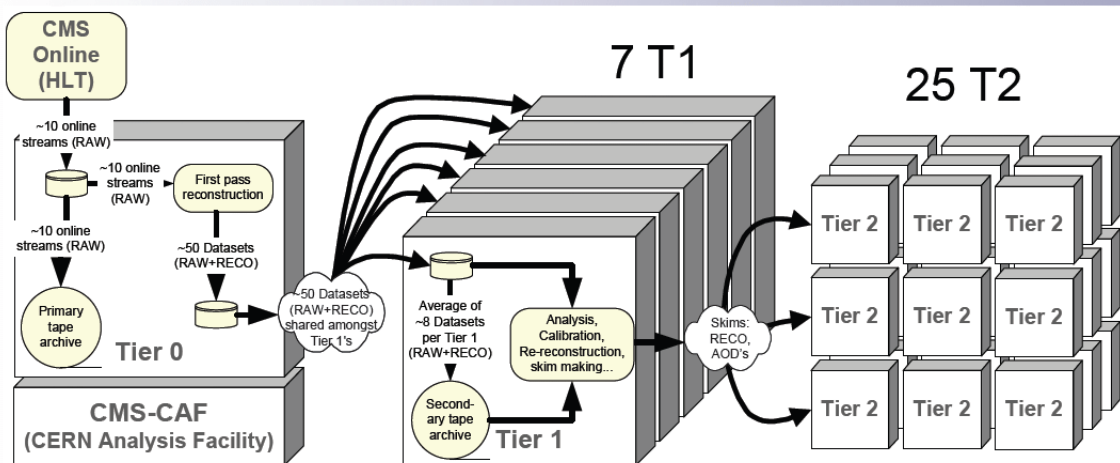


Figure 2.21: Data flow from CMS detector through tiers.

1528 The whole collection of software built as a framework is referred to as *CMSSW*. This
 1529 framework provides the services needed by the simulation, calibration and alignment,
 1530 and reconstruction modules that process event data, so that physicists can perform
 1531 analysis. The CMSSW event processing model is composed of one executable, called
 1532 cmsRun, and several plug-in modules which contains all the tools (calibration, recon-

1533 struction algorithms) needed to process an event. The same executable is used for
1534 both detector data and Monte Carlo simulations [88].

1535 **Chapter 3**

1536 **Event generation, simulation and
1537 reconstruction**

1538 The process of analyzing data recorded by the CMS experiment involves several stages
1539 where the data are processed in order to interpret the information provided by all
1540 the detection systems; in those stages, the particles produced after the pp collision
1541 are identified by reconstructing their trajectories and measuring their features. In
1542 addition, the SM provides a set of predictions that have to be compared with the
1543 experimental results; however, in most of the cases, theoretical predictions are not
1544 directly comparable to experimental results due to the diverse source of uncertainties
1545 introduced by the experimental setup and theoretical approximations, among others.

1546 The strategy to face these conditions consists in using statistical methods imple-
1547 mented in computational algorithms to produce numerical results that can be con-
1548 trasted with the experimental results. These computational algorithms are commonly
1549 known as Monte Carlo (MC) methods and, in the case of particle physics, they are
1550 designed to apply the SM rules and produce predictions about the physical observ-
1551 ables measured in the experiments. Since particle physics is governed by quantum

mechanics principles, predictions are not allowed from single events; therefore, a high number of events are *generated* and predictions are produced in the form of statistical distributions for the observables. Effects of the detector presence are included in the predictions by introducing simulations of the detector itself.

This chapter presents a description of the event generation strategy and the tools used to perform the detector simulation and physics objects reconstruction. A comprehensive review of event generators for LHC physics can be found in Reference [89] on which this chapter is based.

3.1 Event generation

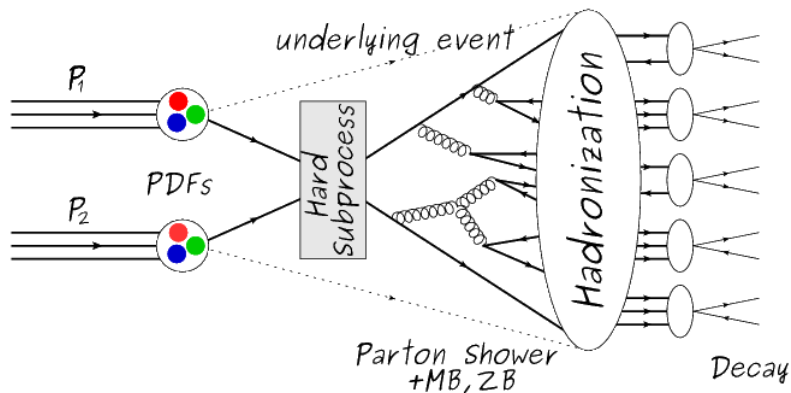


Figure 3.1: Event generation process. The actual interaction is generated in the hard subprocess. The parton shower describes the evolution of the partons from the hard subprocess. Modified from Reference [90].

The event generation is intended to create events that mimic the behavior of actual events produced in collisions; they obey a sequence of steps from the particles collision hard process to the decay process into the final state. Figure 3.1 shows a schematic view of the event generation process; the fact that the full process can be treated as several independent steps is motivated by the QCD factorization theorem.

1566 Generation starts by taking into account the PDFs of the incoming particles.
 1567 Event generators offer the option to chose from several PDF sets depending on the
 1568 particular process under simulation¹; in the following, pp collisions will be consid-
 1569 ered. The *hard subprocess* describes the actual interaction between partons from the
 1570 incoming protons; it is represented by the matrix element connecting the initial and
 1571 final states of the interaction. Normally, the matrix element can be written as a
 1572 sum over Feynman diagrams and consider interferences between terms in the sum-
 1573 mation. During the generation of the hard subprocess, the production cross section
 1574 is calculated.

1575 The order to which the cross section is calculated depends on the order of the Feyn-
 1576 man diagrams involved in the calculation; therefore, radiative corrections are included
 1577 by considering a higher order Feynman diagrams where QCD radiation dominates.
 1578 Currently, cross sections calculated to LO do not offer a satisfactory description of the
 1579 processes, i.e., the results are only reliable for the shape of distributions; therefore,
 1580 NLO calculations have to be performed with the implication that the computing time
 1581 needed is highly increased.

1582 The final parton content of the hard subprocess is subjected to the *parton shower*
 1583 which generates the gluon radiation. Parton shower evolves the partons, i.e., glouns
 1584 split into quark-antiquark pairs and quarks with enough energy radiate gluons giv-
 1585 ing rise to further parton multiplication, following the DGLAP (Dokshitzer-Gribov-
 1586 Lipatov-Altarelli-Parisi) equations. Showering continues until the energy scale is low
 1587 enough to reach the non-perturbative limit.

1588 In the simulation of LHC processes that involve b quarks, like the single top quark
 1589 or Higgs associated production, it is needed to consider that the b quark is heavier
 1590 than the proton; hence, the QCD interaction description is made in two different

¹ Tool in Reference [91] allows to plot different PDF sets under customizable conditions.

1591 schemes [95]

- 1592 • four-flavor (4F) scheme. b quarks appear only in the final state because they
 1593 are heavier than the proton and therefore they can be produced only from the
 1594 splitting of a gluon into pairs or singly in association with a t quark in high
 1595 energy-scale interactions; furthermore, during the simulation, the b -PDFs are set
 1596 to zero. Calculations in this scheme are more complicated due to the presence
 1597 of the second b quark but the full kinematics is considered already at LO and
 1598 therefore the accuracy of the description is better.

- 1599 • five-flavor (5F) scheme. b quarks are considered massless, therefore they can
 1600 appear in both initial and final states since they can now be part of the proton;
 1601 thus, during the simulation b -PDFs are not set to zero. In this scheme, calcula-
 1602 tions are simpler than in the 4F scheme and possible logarithmic divergences
 1603 are absorbed by the PDFs through the DGLAP evolution.

1604 In this thesis, the tHq events are generated using the 4F scheme in order to reduce
 1605 uncertainties, while the tHW events are generated using the 5F scheme to eliminate
 1606 LO interference with $t\bar{t}H$ process [48].

1607 Partons involved in the pp collision are the focus of the simulation, however, the
 1608 rest of the partons inside the incoming protons are also affected because the remnants
 1609 are colored objects; also, multiple parton interactions can occur. The hadronization
 1610 of the remnants and multiple parton interactions are known as *underlying event* and
 1611 it has to be included in the simulation. In addition, multiple pp collisions in the same
 1612 bunch crossing (pile-up mentioned in 2.2) occurs, actually in two forms

- 1613 • *in-time PU* which refers to multiple pp collision in the bunch crossing but that
 1614 are not considered as primary vertices.

1615 • *Out-of-time PU* which refers to overlapping pp collisions from consecutive bunch
 1616 crossings; this can occur due to the time-delays in the detection systems where
 1617 information from one bunch crossing is assigned to the next or previous one.

1618 While the underlying event effects are included in generation using generator-
 1619 specific tools, PU effects are added to the generation by overlaying Minimum-bias (MB)
 1620 and Zero-bias (ZB) events to the generated events. MB events are inelastic events
 1621 selected by using a loose trigger with as little bias as possible, therefore accepting a
 1622 large fraction of the overall inelastic event; ZB events correspond to random events
 1623 recorded by the detector when collisions are likely. MB models in-time PU and ZB
 1624 models out-of-time PU.

1625 The next step in the generation process is called *hadronization*. Since particles
 1626 with a net color charge are not allowed to exits isolated, they have to recombine
 1627 to form bound states. This is precisely the process by which the partons resulting
 1628 from the parton shower arrange themselves as color singlets to form hadrons. At
 1629 this step, the energy-scale is low and the strong coupling constant is large, therefore
 1630 hadronization process is non-perturbative and the evolution of the partons is described
 1631 using phenomenological models. Most of the baryons and mesons produced in the
 1632 hadronization are unstable and hence they will decay in the detector.

1633 The last step in the generation process corresponds to the decay of the unstable
 1634 particles generated during hadronization; it is also simulated in the hadronization
 1635 step, based on the known branching ratios.

1636 **3.2 Monte Carlo Event Generators.**

1637 The event generation described in the previous section has been implemented in
 1638 several software packages for which a brief description is given.

- 1639 • **PYTHIA 8.** It is a program designed to perform the generation of high energy
 1640 physics events which describes the collisions between particles such as electrons
 1641 and protons. Several theories and models are implemented in it, in order to
 1642 describe physical aspects like hard and soft interaction, parton distributions,
 1643 initial and final-state parton showers, multiple parton interactions, beam rem-
 1644 nants, hadronization² and particle decay. Thanks to extensive testing, several
 1645 optimized parametrizations, known as *tunings*, have been defined in order to
 1646 improve the description of actual collisions to a high degree of precision; for
 1647 analysis at $\sqrt{s} = 13$ TeV, the underline event CUETP8M1 tune is employed [97].
 1648 The calculation of the matrix element is performed at LO which is not enough
 1649 for the current required level of precision; therefore, pythia is often used for
 1650 parton shower, hadronization and decays, while other event generators are used
 1651 to generate the matrix element at NLO.
- 1652 • **MadGraph5_aMC@NLO.** MadGraph is a matrix element generator which
 1653 calculates the amplitudes for all contributing Feynman diagrams of a given
 1654 process but does not provide a parton shower while MC@NLO incorporates
 1655 NLO QCD matrix elements consistently into a parton shower framework; thus,
 1656 MadGraph5_aMC@NLO, as a merger of the two event generators MadGraph5
 1657 and aMC@NLO, is an event generator capable to calculate tree-level and NLO
 1658 cross sections and perform the matching of those with the parton shower. It is
 1659 one of the most frequently used matrix element generators; however, it has the
 1660 particular feature of the presence of negative event weights which reduce the
 1661 number of events used to reproduce the properties of the objects generated [98].
- 1662 • **POWHEG.** It is an NLO matrix element generator where the hardest emis-

² based in the Lund string model [96]

1663 sion of color charged particles is generated in such a way that the negative event
 1664 weights issue of MadGraph5_aMC@NLO is overcome; however, the method re-
 1665 quires an interface with p_T -ordered parton shower or a parton shower generator
 1666 where this highest emission can be vetoed in order to avoid double counting of
 1667 this highest-energetic emission. PYTHIA is a commonly matched to POWHEG
 1668 event generator [100].

1669 Events resulting from the whole generation process are known as MC events.

1670 3.3 CMS detector simulation.

1671 After generation, MC events contain the physics of the collisions but they are not
 1672 ready to be compared to the events recorded by the experiment since these recorded
 1673 events correspond to the response of the detection systems to the interaction with
 1674 the particles traversing them. The simulation of the CMS detector has to be applied
 1675 on top of the event generation; it is simulated with a MC toolkit for the simulation
 1676 of particles passing through matter called Geant4 which is also able to simulate the
 1677 electronic signals that would be measured by all detectors inside CMS.

1678 The simulation takes the generated particles contained in the MC events as input,
 1679 makes them pass through the simulated geometry, and models physics processes that
 1680 particles experience during their passage through matter. The full set of results from
 1681 particle-matter interactions corresponds to the simulated hit which contains informa-
 1682 tion about the energy loss, momentum and position. Particles of the input event are
 1683 called *primary*, while the particles originating from GEANT4-modeled interactions of
 1684 a primary particle with matter are called a *secondary*. Simulated hits are the input
 1685 of subsequent modules that emulate the response of the detector readout system and

1686 triggers. The output from the emulated detection systems and triggers is known as
 1687 digitization [101, 102].

1688 The modeling of the CMS detector corresponds to the accurate modeling of the
 1689 interaction among particles, the detector material, and the magnetic field. This
 1690 simulation procedure includes the following standard steps

1691 • Modeling of the Interaction Region.

1692 • Modeling of the particle passage through the hierarchy of volumes that compose
 1693 CMS detector and of the accompanying physics processes.

1694 • Modeling of the effect of multiple interactions per beam crossing and/or the
 1695 effect of events overlay (Pile-Up simulation).

1696 • Modeling of the detector's electronics response, signal shape, noise, calibration
 1697 constants (digitization).

1698 In addition to the full simulation, i.e., a detailed detector simulation, a faster
 1699 simulation (FastSim) have been developed, that may be used where much larger
 1700 statistics are required. In FastSim, detector material effects are parametrized and
 1701 included in the hits; those hits are used as input of the same higher-level algorithms³
 1702 used to analyze the recorded events. In this way, comparisons between fast and full
 1703 simulations can be performed [104].

1704 After the full detector simulation, the output events can be directly compared
 1705 to events actually recorded in the CMS detector. The collection of MC events that
 1706 reproduces the expected physics for a given process is known as MC sample.

³ track fitting, calorimeter clustering, b tagging, electron identification, jet reconstruction and calibration, trigger algorithms which will be considered in the next sections

1707 **3.4 Event reconstruction.**

1708 The CMS experiment use the *particle-flow event reconstruction algorithm (PF)* to do
1709 the reconstruction of particles produced in pp collisions. Next sections will present
1710 a basic description of the *Elements* used by PF (tracker tracks, energy clusters, and
1711 muon tracks), based in the References [105, 106] where more detailed descriptions can
1712 be found.

1713 **3.4.1 Particle-Flow Algorithm.**

1714 Each of the several sub detection systems of the CMS detector is dedicated to identify
1715 an specific type of particles, i.e., photons and electrons are absorbed by the ECAL
1716 and their reconstruction is based on ECAL information; hadrons are reconstructed
1717 from clusters in the HCAL while muons are reconstructed from hits in the muon
1718 chambers. PF is designed to correlate signals from all the detector layers (tracks and
1719 energy clusters) in order to reconstruct and identify each final state particle and its
1720 properties as sketched in Figure 3.2.

1721 For instance, a charged hadron is identified by a geometrical connection, known
1722 as *link*, between one or more calorimeter clusters and a track in the tracker, provided
1723 there are no hits in the muon system; combining several measurements allows a better
1724 determination of the energy and charge sign of the charged hadron.

1725 **Charged-particle track reconstruction.**

1726 The strategy used by PF in order to reconstruct tracks is called *Iterative Tracking*
1727 which occurs in four steps

- 1728 • Seed generation where initial track candidates are found by looking for a combi-
1729 nation of hits in the pixel detector, strip tracker, and muon chambers. In total

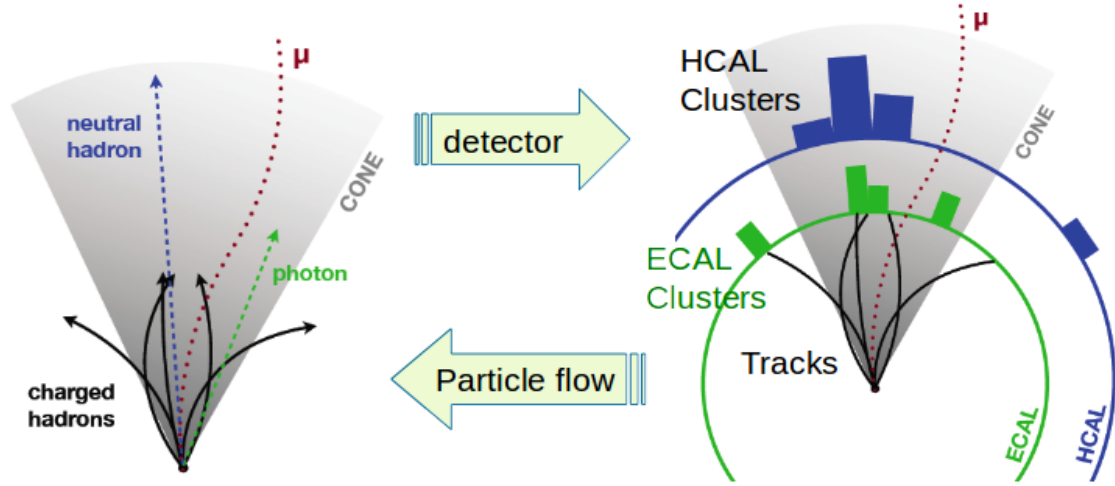


Figure 3.2: Particle flow algorithm. Information from the several CMS detection systems is provided as input to the algorithm which then combine it to identify and reconstruct all the particles in the final state and their properties. Reconstruction of simulated events is also performed by providing information from MC samples, detector and trigger simulation [107].

1730 ten iterations are performed, each one with a different seeding requirement.
 1731 Seeds are used to estimate the trajectory parameters and uncertainties at the
 1732 time of the full track reconstruction. Seeds are also considered track candidates.

- 1733 • Track finding using a tracking software known as Combinatorial Track Finder
 1734 (CTF) [108]. The seed trajectories are extrapolated along the expected flight
 1735 path of a charged particle, in agreement to the trajectory parameters obtained
 1736 in the first step, in an attempt to find additional hits that can be assigned to
 1737 the track candidates.
 - 1738 • Track-fitting where the found tracks are passed as input to a module which
 1739 provides the best estimate of the parameters of each trajectory.
 - 1740 • Track selection where track candidates are submitted to a selection which dis-
 1741 cards those that fail a set of defined quality criteria.
- 1742 Iterations differ in the seeding configuration and the final track selection as elab-

1743 orated in References [105, 106]. In the first iteration, high p_T tracks and tracks pro-
 1744 duced near to the interaction region are identified and those hits are masked thereby
 1745 reducing the combinatorial complexity. Next, iterations search for more complicated
 1746 tracks, like low p_T tracks and tracks from b hadron decays, which tend to be displaced
 1747 from the interaction region.

1748 **Vertex reconstruction.**

1749 During the track reconstruction, an extrapolation toward to the calorimeters is per-
 1750 formed in order to match energy deposits; that extrapolation is performed also toward
 1751 the beamline in order to find the origin of the track known as *vertex*. The vertex re-
 1752 construction is performed by selecting from the available reconstructed tracks, those
 1753 that are consistent with being originated in the interaction region where pp collisions
 1754 are produced. The selection involves a requirement on the number of tracker (pixel
 1755 and strip) hits and the goodness of the track fit.

1756 Selected tracks are clustered using a *deterministic annealing algorithm* (DA)⁴. A
 1757 set of candidate vertices and their associated tracks, resulting from the DA, are then
 1758 fitted with an *adaptive vertex fitter* (AVF) to produce the best estimate of the vertices
 1759 locations.

1760 The p_T of the tracks associated to a reconstructed vertex is added, squared and
 1761 used to organize the vertices; the vertex with the highest squared sum is designated
 1762 as the *primary vertex* (*PV*) while the rest are designated as PU vertices.

1763 **Calorimeter clustering.**

1764 After traversing the CMS tracker system, electrons, photons and hadrons deposit their
 1765 energy in the ECAL and HCAL cells. The PF clustering algorithm aims to provide

⁴ DA algorithm and AVF are described in detail in References [110, 111]

1766 a high detection efficiency even for low-energy particles and an efficient distinction
 1767 between close energy deposits. The clustering runs independently in the ECAL barrel
 1768 and endcaps, HCAL barrel and endcaps, and the two preshower layers, following two
 1769 steps

- 1770 • cells with an energy larger than a given seed threshold and larger than the energy
 1771 of the neighboring cells are identified as cluster seeds. The neighbor cells are
 1772 those that either share a side with the cluster seed candidate, or the eight closest
 1773 cells including cells that only share a corner with the seed candidate.
- 1774 • cells with at least a corner in common with a cell already in the cluster seed
 1775 and with an energy above a cell threshold are grouped into topological clusters.

1776 Clusters formed in this way are known as *particle-flow clusters*. With this cluster-
 1777 ing strategy, it is possible to detect and measure the energy and direction of photons
 1778 and neutral hadrons as well as differentiate these neutral particles from the charged
 1779 hadron energy deposits. In cases involving charged hadrons for which the track pa-
 1780 rameters are not determined accurately, for instance, low-quality and high- p_T tracks,
 1781 clustering helps in the energy measurements.

1782 Electron track reconstruction.

1783 Although the charged-particle track reconstruction described above works for elec-
 1784 trons, they lose a significant fraction of their energy via bremsstrahlung photon radi-
 1785 ation before reaching the ECAL; thus, the reconstruction performance depends on the
 1786 ability to measure also the radiated energy. The reconstruction strategy, in this case,
 1787 requires information from the tracking system and from the ECAL. Bremsstrahlung
 1788 photons are emitted at similar η values to that of the electron but at different values
 1789 of ϕ ; therefore, the radiated energy can be recovered by grouping ECAL clusters in a

1790 η window over a range of ϕ around the electron direction. The group is called ECAL
 1791 supercluster.

1792 Electron candidates from the track-seeding and ECAL super clustering are merged
 1793 into a single collection which is submitted to a full electron tracking fit with a
 1794 Gaussian-sum filter (GSF) [109]. The electron track and its associated ECAL su-
 1795 percluster form a *particle-flow electron*.

1796 Muon track reconstruction.

1797 Given that the CMS detector is equipped with a muon spectrometer capable to iden-
 1798 tify and measure the momentum of the muons traversing it, the muon reconstruction
 1799 is not specific to PF; therefore, three different muon types are defined

- 1800 ● *Standalone muon.* A clustering on the DTs or CSCs hits is performed to form
 1801 track segments; those segments are used as seeds for the reconstruction in the
 1802 muon spectrometer. All DTs, CSCs, and RPCs hits along the muon trajectory
 1803 are combined and fitted to form the full track. The fitting output is called a
 1804 *standalone-muon track*.
- 1805 ● *Tracker muon.* Each track in the inner tracker with p_T larger than 0.5 GeV and
 1806 a total momentum p larger than 2.5 GeV is extrapolated to the muon system.
 1807 A *tracker muon track* corresponds to a extrapolated track that matches at least
 1808 one muon segment.
- 1809 ● *Global muon.* When tracks in the inner tracker (inner tracks) and standalone-
 1810 muon tracks are matched and turn out being compatibles, their hits are com-
 1811 bined and fitted to form a *global-muon track*.

1812 Global muons sharing the same inner track with tracker muons are merged into
 1813 a single candidate. PF muon identification uses the muon energy deposits in ECAL,
 1814 HCAL, and HO associated with the muon track to improve the muon identification.

1815 **Particle identification and reconstruction.**

1816 PF elements are connected by a linker algorithm that tests the connection between any
 1817 pair of elements; if they are found to be linked, a geometrical distance that quantifies
 1818 the quality of the link is assigned. Two elements may be linked indirectly through
 1819 common elements. Linked elements form *PF blocks* and each PF block may contain
 1820 elements originating in one or more particles. Links can be established between
 1821 tracks, between calorimeter clusters, and between tracks and calorimeter clusters.
 1822 The identification and reconstruction start with a PF block and proceed as follows

1823 • Muons. An *isolated global muon* is identified by evaluating the presence of
 1824 inner track and energy deposits close to the global muon track in the (η, ϕ)
 1825 plane, i.e., in a particular point of the global muon track, inner tracks and
 1826 energy deposits are sought within a radius of $\Delta R = 0.3$ (see eqn. 2.7) from the
 1827 muon track; if they exist and the p_T of the found track added to the E_T of the
 1828 found energy deposit does not exceed 10% of the muon p_T then the global muon
 1829 is an isolated global muon. This isolation condition is stringent enough to reject
 1830 hadrons misidentified as muons.

1831 *Non-isolated global muons* are identified using additional selection requirements
 1832 on the number of track segments in the muon system and energy deposits along
 1833 the muon track. Muons inside jets are identified with more stringent criteria
 1834 in isolation and momentum as described in Reference [112]. The PF elements
 1835 associated with an identified muon are masked from the PF block.

- 1836 ● Electrons are identified and reconstructed as described above plus some addi-
 1837 tional requirements on fourteen variables like the amount of energy radiated,
 1838 the distance between the extrapolated track position at the ECAL and the po-
 1839 sition of the associated ECAL supercluster, among others, which are combined
 1840 in an specialized multivariate analysis strategy that improves the electron iden-
 1841 tification. Tracks and clusters used to identify and reconstruct electrons are
 1842 masked in the PF block.
- 1843 ● Isolated photons are identified from ECAL superclusters with E_T larger than 10
 1844 GeV, for which the energy deposited at a distance of 0.15, from the supercluster
 1845 position on the (η, ϕ) plane, does not exceed 10% of the supercluster energy;
 1846 note that this is an isolation requirement. In addition, there must not be links
 1847 to tracks. Clusters involved in the identification and reconstruction are masked
 1848 in the PF block.
- 1849 ● Bremsstrahlung photons and prompt photons tend to convert to electron-positron
 1850 pairs inside the tracker, therefore, a dedicated finder algorithm is used to link
 1851 tracks that seem to originate from a photon conversion; in case those two tracks
 1852 are compatible with the direction of a bremsstrahlung photon, they are also
 1853 linked to the original electron track. Photon conversion tracks are also masked
 1854 in the PF block.
- 1855 ● The remaining elements in the PF block are used to identify hadrons. In the
 1856 region $|\eta| \leq 2.5$, neutral hadrons are identified with HCAL clusters not linked
 1857 to any track while photons from neutral pion decays are identified with ECAL
 1858 clusters without links to tracks. In the region $|\eta| > 2.5$ ECAL clusters linked to
 1859 HCAL clusters are identified with a charged or neutral hadron shower; ECAL
 1860 clusters with no links are identified with photons. HCAL clusters not used yet,

1861 are linked to one or more unlinked tracks and to an unlinked ECAL in order to
 1862 reconstruct charged-hadrons or a combination of photons and neutral hadrons
 1863 according to certain conditions on the calibrated calorimetric energy.

- 1864 • Charged-particle tracks may be liked together when they converge to a *sec-*
 1865 *ondary vertex (SV)* displaced from the IP where the PV and PU vertices are
 1866 reconstructed; at least three tracks are needed in that case, of which at most
 1867 one has to be an incoming track with hits in tracker region between a PV and
 1868 the SV.

1869 The linker algorithm, as well as the whole PF algorithm, has been validated and
 1870 commissioned; results from that validation are presented in the Reference [105].

1871 **Jet reconstruction.**

1872 Quarks and gluons may be produced in the pp collisions, therefore, their hadronization
 1873 will be seen in the detector as a shower of hadrons and their decay products in the
 1874 form of a *jet*. Two classes of clustering algorithms have been developed based in
 1875 their jet definition [113]:

- 1876 • Iterative cone algorithms (IC). Jets are defined in terms of circles of fixed radius
 1877 R in the $\eta\text{-}\phi$ plane, known as *stable cones*, for which the sum of the momenta
 1878 of all the particles within the cone points in the same direction as the center
 1879 of the circle. The seed of the iteration is the hardest non-isolated particle in
 1880 the event, then, the resulting momentum direction is assigned as the new cone
 1881 direction and a new iteration starts; iteration process stops when the cone if
 1882 found to be stable.

1883 • Sequential recombination algorithms. The distance between non-isolated par-
 1884 ticles is calculated; if that distance is below a threshold, these particles are
 1885 recombined into a new object. The sequence is repeated until the separation
 1886 between the recombined object and any other particle is above certain thresh-
 1887 old; the recombined object is called a jet and the algorithm starts again with
 1888 the remaining particles.

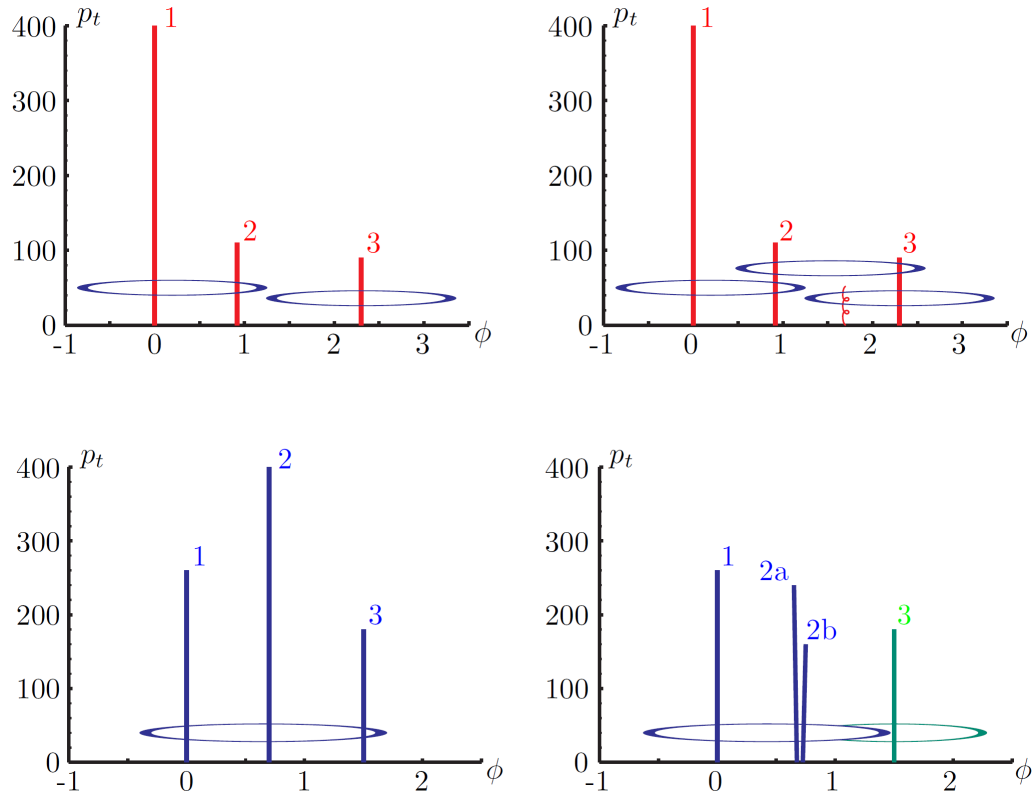


Figure 3.3: Stable cones identification using IC algorithms [113].

1889 Two conditions are of particular importance for the clustering algorithms, *infrared*
 1890 and *collinear (IRC) safety*. In order to explain the concept of infrared (IR) safety,
 1891 consider an event with three hard particles as shown in the top left side of Figure 3.3,
 1892 two stable cones are found and then two jets are identified; if a soft gluon is added, as
 1893 shown in the top right side of Figure 3.3, three stable cones are found and the three

1894 hard particles are now clustered into a single jet. If the addition of soft particles
 1895 change the outcome of the clustering, then it is said that the algorithm is IR unsafe.
 1896 Soft radiation is highly likely in perturbative QCD, which dominates the physics of
 1897 the jets, and then IR unsafe effect leads to divergences [113].

1898 The concept of collinear safety can also be explained considering a three hard
 1899 particles event, as shown in the bottom left side of Figure 3.3, where one stable cone
 1900 containing all three particles is found and one jet is identified; if the hardest particle
 1901 is split into two collinear particles (2a and 2b) in the bottom right side of Figure 3.3,
 1902 then the clustering results in a different jet identification and the algorithm is said
 1903 to be collinear unsafe. The collinear unsafe effect leads to divergences in jet cross
 1904 section calculations [114].

1905 It has been determined that IC algorithms are IRC unsafe, and therefore, they
 1906 have to be replaced by algorithms that not only provide the finite perturbative results
 1907 from theoretical computations, but also that are not highly dependent on underlying
 1908 event and pileup effects which leads to significant corrections [113].

1909 The sequential recombination algorithms arise as the IRC safe alternative used by
 1910 the CMS experiment; in particular the anti- k_t algorithm which is a generalization of
 1911 the previously existing k_t [115] and Cambridge/Aachen [116] jet clustering algorithms.

1912 The anti- k_t algorithm is used to perform the jet reconstruction by clustering those
 1913 PF particles within a cone (see Figure 3.4); previously, isolated electrons, isolated
 1914 muons, and charged particles associated with other interaction vertices are excluded
 1915 from the clustering.

1916 The anti- k_t algorithm proceeds in a sequential recombination of PF particles; the
 1917 distance between particles i and j (d_{ij}) and the distance between particles and the
 1918 beam are defined as

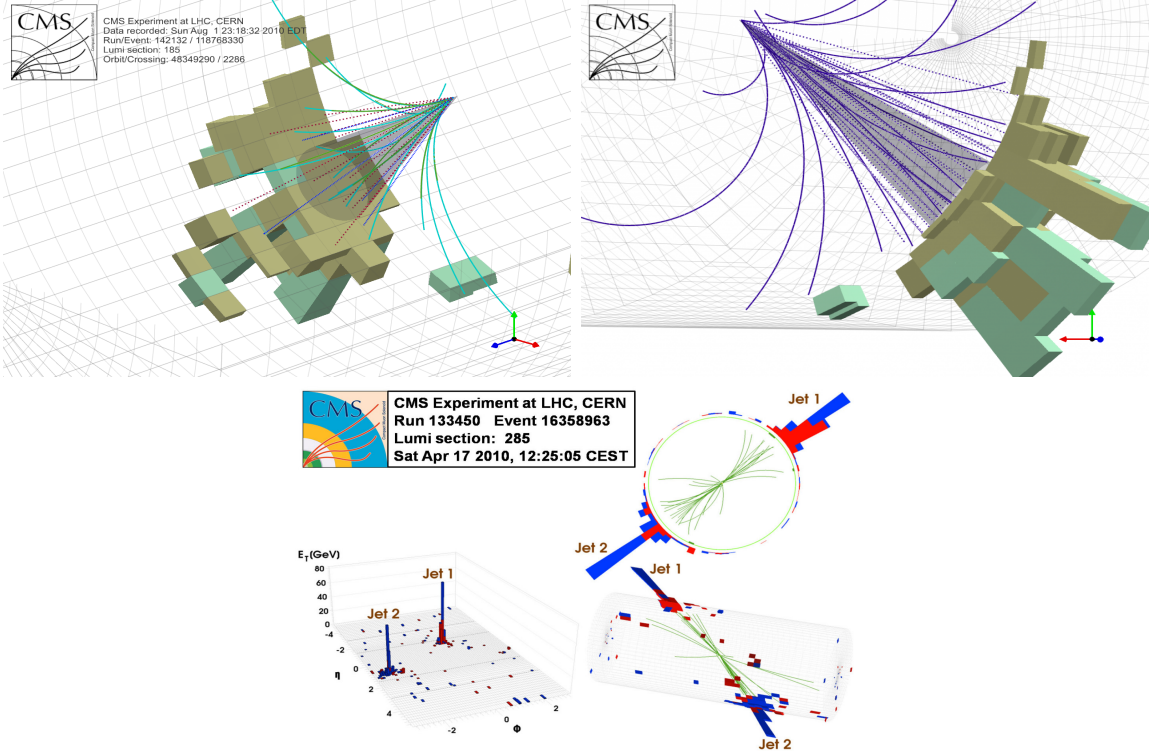


Figure 3.4: Jet reconstruction performed by the anti- k_t algorithm. Top: Two different views of a CMS recorded event are presented. Continuous lines correspond to tracks left by charged particles in the tracker while dotted lines are the imaginary paths followed by neutral particles. The green cubes represent the ECAL cells while the blue ones represent the HCAL cells; in both cases, the height of the cube represent the amount of energy deposited in the cells [117]. Bottom: Reconstruction of a recorded event with two jets [118].

$$d_{ij} = \min\left(\frac{1}{k_{ti}^2}, \frac{1}{k_{tj}^2}\right) \frac{\Delta_{ij}^2}{R^2}$$

$$d_{iB} = \frac{1}{k_{ti}^2} \quad (3.1)$$

1919 where $\Delta_{ij}^2 = (y_i - y_j)^2 + (\phi_i - \phi_j)^2$, k_{ti}, y_i and ϕ_i are the transverse momentum, ra-
1920 pidity and azimuth of particle i respectively and R is the called jet radius. For all
1921 the remaining PF particles, after removing the isolated ones, d_{ij} and d_{iB} are calcu-

1922 lated⁵ and the smallest is identified; if it is a d_{ij} , particles i and j are replaced with
 1923 a new object whose momentum is the vectorial sum of the combined particles. If the
 1924 smallest distance is a d_{iB} the clustering process ends, the object i (which at this stage
 1925 should be a combination of several PF particles) is declared as a *Particle-flow-jet* (PF
 1926 jet) and all the associated PF particles are removed from the detector. The clustering
 1927 process is repeated until no PF particles remain. R is a free parameter that can be
 1928 adjusted according to the specific analysis conditions; usually, two values are used,
 1929 $R=0.4$ and $R=0.5$, giving the name to the so-called AK4-jet and AK5-jet respectively.

1930 An advantage of the anti- k_t algorithm over other clustering algorithms is the reg-
 1931 ularity of the boundaries of the resulting jets. For all known IRC safe algorithms,
 1932 soft radiation can introduce irregularities in the boundaries of the final jets; however,
 1933 anti- k_t algorithm is soft-resilient, meaning that jets shape is not affected by soft radi-
 1934 ation, which is a valuable property considering that knowing the typical shape of jets
 1935 makes experimental calibration of jets more simple. In addition, that soft-resilience
 1936 is expected to simplify certain theoretical calculations and reduce the momentum-
 1937 resolution loss caused by underlying-event (UE) and pileup contamination [114].

1938 The effect of the UE and pileup contamination over a jet identification, can be
 1939 seen as if soft events are added to the jet; for instance, if a soft event representing UE
 1940 or pileup is added to an event for which a set of jets J have been identified, and the
 1941 clustering is rerun on that new extended event, the outcome will be different in two
 1942 aspects: jets will contain some additional soft energy and the distribution of particles
 1943 in jets may have change; that effect is called *back-reaction*. The back-reaction effect in
 1944 the anti- k_t algorithm is suppressed not by the amount of momentum added to the jet
 1945 but by the jet transverse momentum $p_{T,J}$, which means that this strong suppression
 1946 leads to a smaller correction due to EU and pileup effect [114].

⁵ Notice that this is a combinatorial calculation.

1947 **Jet energy Corrections**

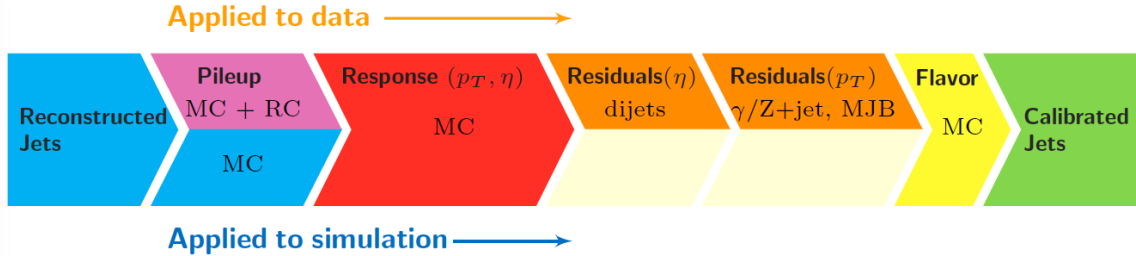


Figure 3.5: Jet energy correction diagram. Correction levels are applied sequentially in the indicated fixed order [120].

1948 Even though jets can be reconstructed efficiently, there are some effects that are
 1949 not included in the reconstruction and that lead to discrepancies between the re-
 1950 constructed results and the predicted results; in order to overcome these discrep-
 1951 ancies, a factorized model has been designed in the form of jet energy corrections
 1952 (JEC) [119, 120] applied sequentially as shown in the diagram of Figure 3.5.

1953 At each level, the jet four-momentum is multiplied by a scaling factor based on
 1954 jet properties, i.e., η , flavor, etc.

- 1955 • Level 1 correction removes the energy coming from pile-up. The scale factor is
 1956 determined using a MC sample of QCD dijet (2 jets) events with and without
 1957 pileup overlay; it is parametrized in terms of the offset energy density ρ , jet
 1958 area A , jet η and jet p_T . Different corrections are applied to data and MC due
 1959 to the detector simulation.
- 1960 • MC-truth correction accounts for differences between the reconstructed jet en-
 1961 ergy and the MC particle-level energy. The correction is determined on a QCD
 1962 dijet MC sample and is parametrized in terms of the jet p_T and η .
- 1963 • Residuals correct remaining small differences within jet response in data and
 1964 MC. The Residuals η -dependent correction compares jets of similar p_T in the

1965 barrel reference region. The Residuals p_T -dependent correct the jet absolute
 1966 scale (JES vs p_T).

- 1967 • Jet-flavor corrections are derived in the same way as MC-truth corrections but
 1968 using QCD pure flavor samples.

1969 ***b*-tagging of jets.**

1970 A particular feature of the hadrons containing bottom quarks (*b*-hadrons) is that
 1971 their lifetime is long enough to travel some distance before decaying, but it is not as
 1972 long as those of light quark hadrons; therefore, when looking at the hadrons produced
 1973 in pp collisions, *b*-hadrons decay typically inside the tracker rather than reaching the
 1974 calorimeters as some light-hadrons do. As a result, a *b*-hadron decay gives rise to a
 1975 displaced vertex (secondary vertex) with respect to the primary vertex as shown in
 1976 Figure 3.6; the SV displacement is in the order of a few millimeters. A jet resulting
 1977 from the decay of a *b*-hadron is called *b* jet; other jets are called light jets.

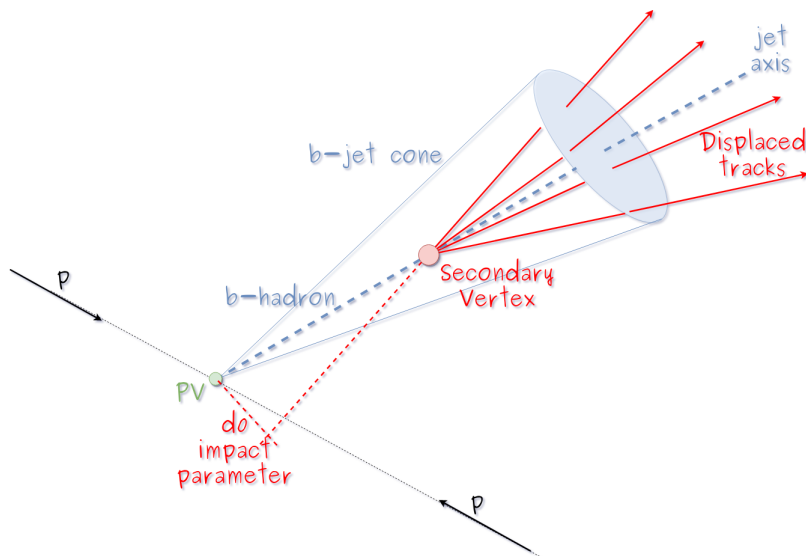


Figure 3.6: Secondary vertex in a *b*-hadron decay.

1978 Several methods to identify *b*-jets (*b*-tagging) have been developed; the method

1979 used in this thesis is known as *Combined Secondary Vertex* algorithm in its second
 1980 version (CSVv2) [121]. By using information of the impact parameter, the recon-
 1981 structed secondary vertices, and the jet kinematics as input in a multivariate analysis
 1982 that combines the discrimination power of each variable in one global discrimina-
 1983 tor variable, three working points (references): loose, medium and tight, are defined
 1984 which quantify the probabilities of mistag jets from light quarks as jets from b quarks;
 1985 10, 1 and 0.1 % respectively. Although the mistagging probability decreases with the
 1986 working point strength, the efficiency to correctly tag b -jets also decreases as 83, 69
 1987 and 49 % for the respective working point; therefore, a balance needs to be achieved
 1988 according to the specific requirements of the analysis.

1989 **Missing transverse energy.**

1990 The fact that proton bunches carry momentum along the z -axis implies that for
 1991 each event it is expected that the momentum in the transverse plane is balanced.
 1992 Imbalances are quantified by the missing transverse energy (MET) and are attributed
 1993 to several sources including particles escaping undetected through the beam pipe,
 1994 neutrinos produced in weak interactions processes which do not interact with the
 1995 detector and thus escaping without leaving a sign, or even undiscovered particles
 1996 predicted by models beyond the SM.

1997 The PF algorithm assigns the negative sum of the momenta of all reconstructed
 1998 PF particles to the *particle-flow MET* according to

$$\vec{E}_T = - \sum_i \vec{p}_{T,i} \quad (3.2)$$

1999 JEC are propagated to the calculation of the \vec{E}_T as described in the Reference [122].

2000 3.4.2 Event reconstruction examples

2001 Figures 3.7-3.9 show the results of the reconstruction performed on 3 recorded events.

2002 Descriptions are taken directly from the source.

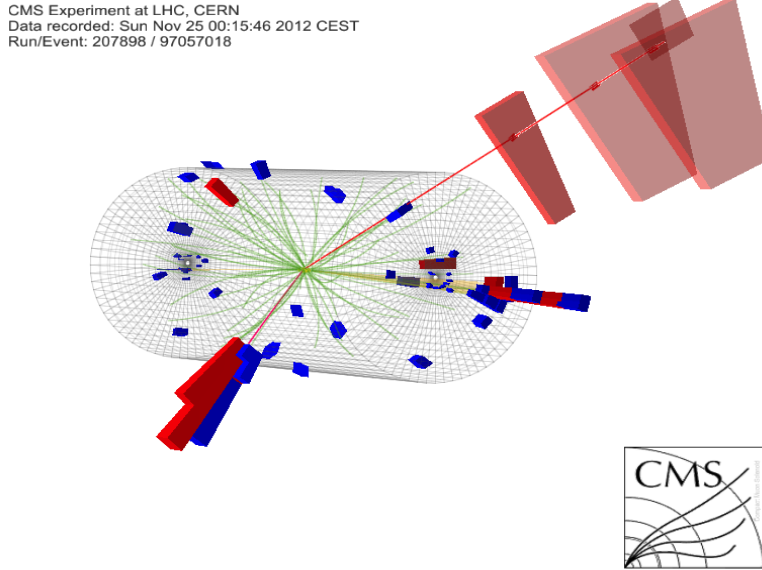


Figure 3.7: HIG-13-004 Event 1 reconstruction results; “HIG-13-004 Event 1: Event recorded with the CMS detector in 2012 at a proton-proton center-of-mass energy of 8 TeV. The event shows characteristics expected from the decay of the SM Higgs boson to a pair of τ leptons. Such an event is characterized by the production of two forward-going jets, seen here in opposite endcaps. One of the τ decays to a muon (red lines on the right) and neutrinos, while the other τ decays into a charged hadron and a neutrino.” [123].

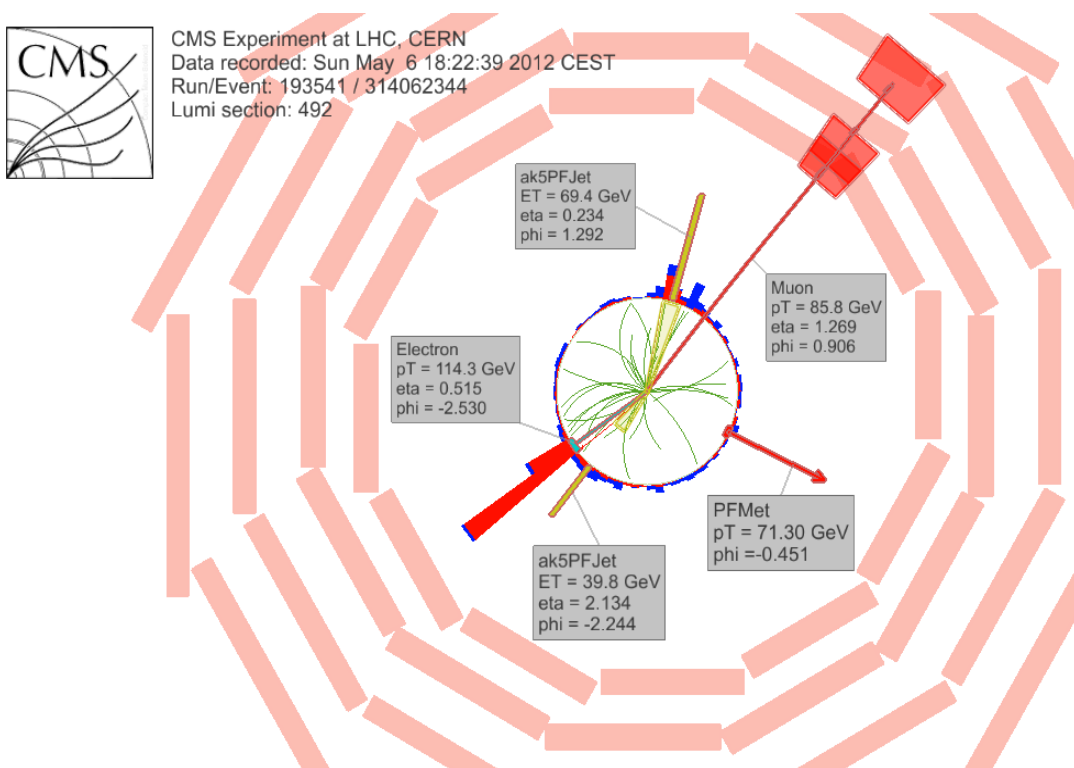


Figure 3.8: $e\mu$ event reconstruction results; “An $e\mu$ event candidate selected in 8 TeV data, as seen from the direction of the proton beams. The kinematics of the main objects used in the event selection are highlighted: two isolated leptons and two particle-flow jets. The reconstructed missing transverse energy is also displayed for reference” [124].

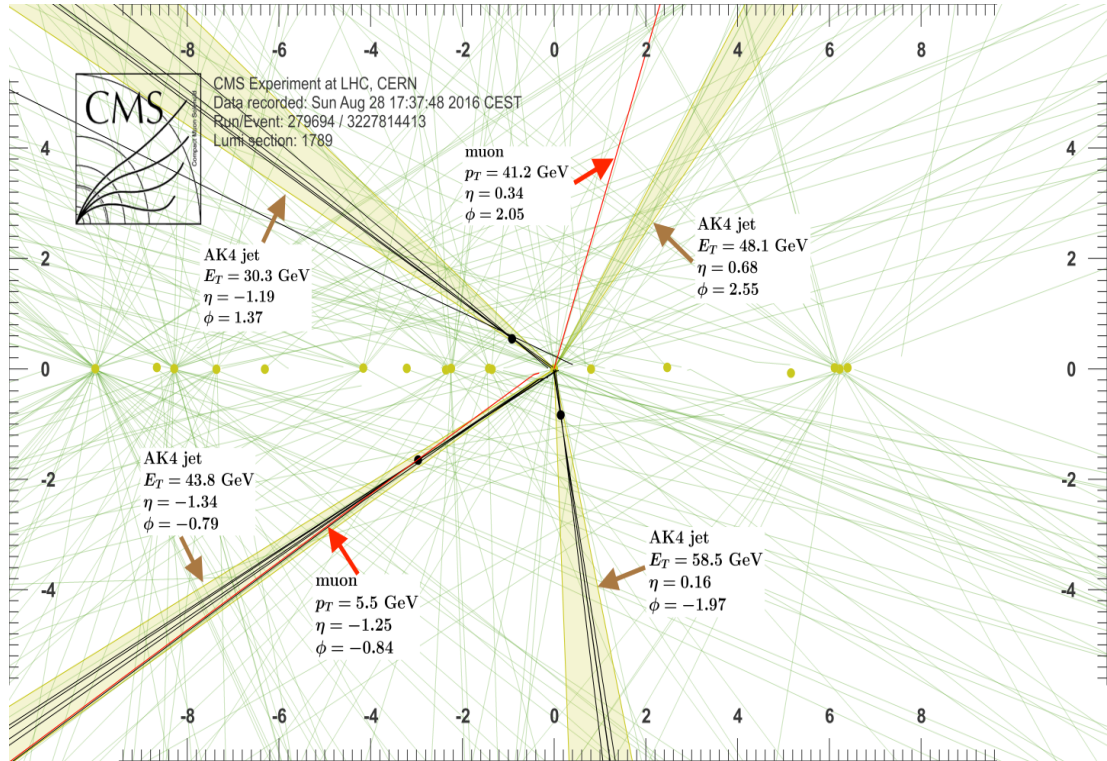


Figure 3.9: Recorded event reconstruction results; “Recorded event (ρ - z projection) with three jets with $p_T > 30$ GeV with one displaced muon track in 2016 data collected at 13 TeV. Each of the three jets has a displaced reconstructed vertex. The jet with $p_T(j) = 43.8$ GeV, $\eta(j) = -1.34$, $\phi(j) = -0.79$ contains muon with $p_T(\mu) = 5.5$ GeV, $\eta(\mu) = -1.25$, $\phi(\mu) = -0.84$. Event contains reconstructed isolated muon with $p_T(\mu) = 41.2$ GeV, $\eta(\mu) = 0.34$, $\phi(\mu) = 2.05$ and MET with $p_T = 72.5$ GeV, $\phi = -0.32$. Jet candidates for a b -jet from top quark leptonic and hadronic decays are tagged by CSVv2T algorithm. One of the other two jets is tagged by CharmT algorithm. Tracks with $p_T > 0.5$ GeV are shown. The number of reconstructed primary vertices is 18. Reconstructed $m_T(W)$ is 101.8 GeV. Beam spot position correction is applied. Reconstructed primary vertices are shown in yellow color, while reconstructed displaced vertices and associated tracks are presented in black color. Dimensions are given in cm” [125].

2003 **Chapter 5**

2004 **Statistical methods**

2005 In the course of analyzing the data sets provided by the CMS experiment and used in
2006 this thesis, several statistical tools have been employed; in this chapter, a description
2007 of these tools will be presented, starting with the general statement of the multivariate
2008 analysis methods, followed by the particularities of the Boosted Decision Trees (BDT)
2009 method and its application to the classification problem. Statistical inference methods
2010 used will also be presented. This chapter is based mainly on References [126–128].

2011 **5.1 Multivariate analysis**

2012 Multivariate data analysis (MVA) makes use of the statistical techniques developed to
2013 analyze more than one variable at once, taking into account all the correlations among
2014 variables. MVA is employed in a variety of fields like consumer and market research,
2015 quality control and process optimization. Using MVA it is possible to identify the
2016 dominant patterns in a data sample, like groups, outliers and trends, and determine
2017 to which group a set of values belong; in the particle physics context, MVA methods
2018 are used to perform the selection of certain type of events from a large data set.

2019 Processes with small cross section, such as the tHq process ($\sigma_{SM}(\sqrt{s} = 13\text{TeV}) =$
 2020 70.96 fb), are hard to detect in the presence of the processes with larger cross sections,
 2021 $\sigma_{SM}^{t\bar{t}}(\sqrt{s} = 13\text{TeV}) = 823.44$ fb for instance; therefore, only a small fraction of the data
 2022 contains events of interest (signal), the major part is signal-like events, which mimic
 2023 signal characteristics but belong to different processes, so they are a background to
 2024 the process of interest. This implies that it is not possible to say with certainty
 2025 that a given event is a signal or a background and statistical methods should be
 2026 involved. In that sense, the challenge can be formulated as one where a set of events
 2027 have to be classified according to certain special features; these features correspond
 2028 to the measurements of several parameters like energy or momentum, organized in a
 2029 set of *input variables*. The measurements for each event can be written in a vector
 2030 $\mathbf{x} = (x_1, \dots, x_n)$ for which

- 2031 • $f(\mathbf{x}|s)$ is the probability density (*likelihood function*) that \mathbf{x} is the set of mea-
 2032 sured values given that the event is a signal event (signal hypothesis).
- 2033 • $f(\mathbf{x}|b)$ is the probability density (*likelihood function*) that \mathbf{x} is the set of mea-
 2034 sured values given that the event is a background event (background hypothe-
 2035 sis).

2036 Figure 5.1 shows three ways to perform a classification of events for which mea-
 2037 surements of two properties, i.e., two input variables x_1 and x_2 , have been performed;
 2038 blue circles represent signal events while red triangles represent background events.
 2039 The classification on the left is *cut-based* requiring $x_1 < c_1$ and $x_2 < c_2$; usually the
 2040 cut values (c_1 and c_2) are chosen according to some knowledge about the event pro-
 2041 cess. In the middle plot, the classification is performed using a linear function of
 2042 the input variables, hence the boundary is a straight line, while in the right plot the

2043 the relationship between input variables is not linear thus the boundary is not linear
 2044 either.

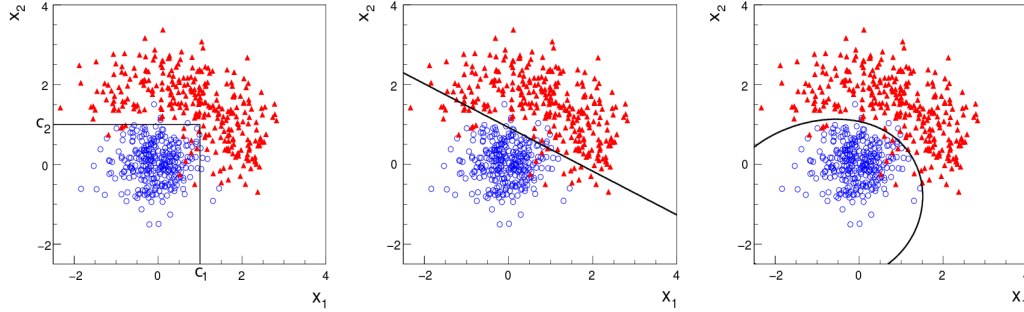


Figure 5.1: Scatter plots-MVA event classification. Distribution of two input variables x_1 and x_2 measured for a set of events; blue circles represent signal events and red triangles represent background events. The classification is based on cuts (left), linear boundary (center), and nonlinear boundary (right) [126]

2045 In general, the boundary can be parametrized in terms of the input variables such
 2046 that the cut is set on the parametrization instead of on the variables, i.e., $y(\mathbf{x}) = y_{cut}$
 2047 with y_{cut} being a constant; thus, the acceptance or rejection of an event is based on
 2048 which side of the boundary the event is located. If $y(\mathbf{x})$, usually called *test statistic*,
 2049 has functional form, it can be used to determine the probability distribution functions
 2050 $p(y|s)$ and $p(y|b)$ and then perform a test statistic with a single cut on the scalar
 2051 variable y .

2052 Figure 5.2 shows an example of what would be the probability distribution func-
 2053 tions under the signal and background hypotheses for a scalar test statistic with a cut
 2054 on the classifier y . Note that the tails of the distributions indicate that some signal
 2055 events fall in the rejection region and some background events fall on the acceptance
 2056 region; therefore, it is convenient to define the *efficiency* with which events of a given
 2057 type are accepted. The signal and background efficiencies are given by

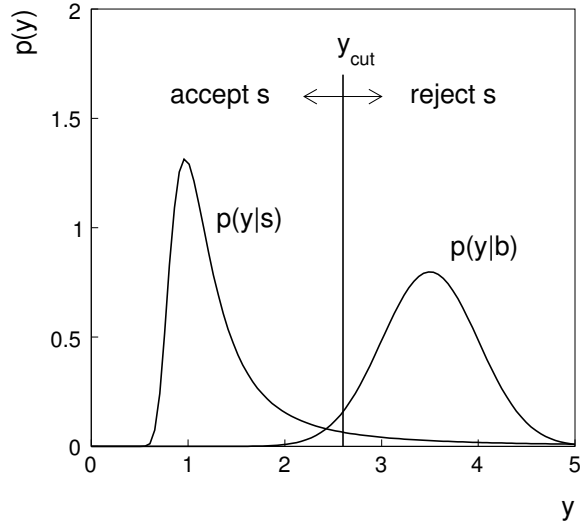


Figure 5.2: Distributions of the scalar test statistic $y(\mathbf{x})$ under the signal and background hypotheses. [126]

$$\varepsilon_s = P(\text{accept event}|s) = \int_A f(\mathbf{x}|s) d\mathbf{x} = \int_{-\infty}^{y_{cut}} p(y|s) dy , \quad (5.1)$$

$$\varepsilon_b = P(\text{accept event}|b) = \int_A f(\mathbf{x}|b) d\mathbf{x} = \int_{-\infty}^{y_{cut}} p(y|b) dy , \quad (5.2)$$

2058 where A is the acceptance region. If the background hypothesis is the *null hypothesis*
 2059 (H_0), the signal hypothesis would be *alternative hypothesis* (H_1); in this context, the
 2060 background efficiency corresponds to the significance level of the test (α) and describes
 2061 the misidentification probability, while the signal efficiency corresponds to the power
 2062 of the test ($1-\beta$)¹ and describes the probability of rejecting the background hypothesis
 2063 if the signal hypothesis is true. What is sought in an analysis is to maximize the power
 2064 of the test relative to the significance level, i.e., set a selection with the largest possible
 2065 selection efficiency and the smallest possible misidentification probability.

¹ β is the fraction of signal events that fall out of the acceptance region

2066 **5.1.1 Decision trees**

2067 For this thesis, the implementation of the MVA strategy, described above, is per-
 2068 formed through decision trees by using the TMVA software package [127] included
 2069 in the ROOT analysis framework [129]. In a simple picture, a decision tree classifies
 2070 events according to their input variables values by setting a cut on each input variable
 2071 and checking which events are on which side of the cut, just as proposed in the MVA
 2072 strategy, but in addition, as a machine learning algorithm, decision trees offer the
 2073 possibility to be trained and then perform the classification efficiently.

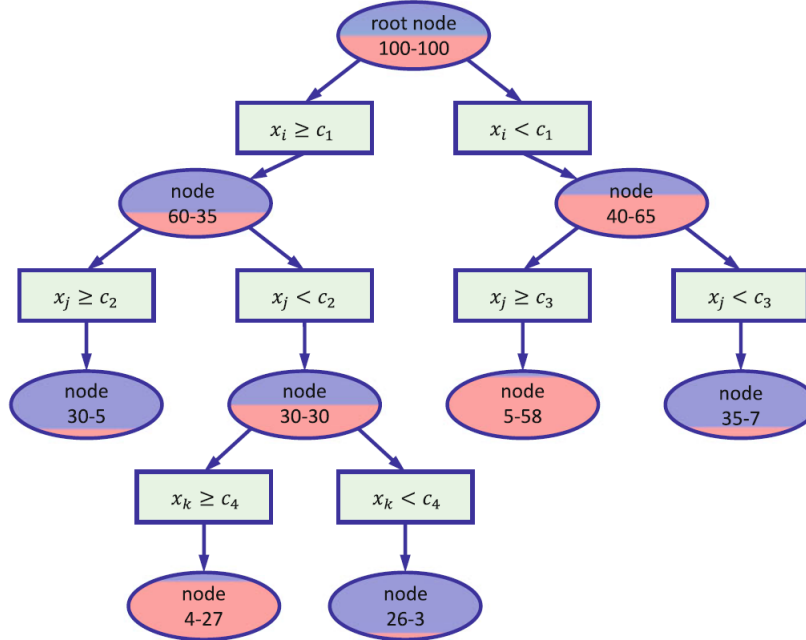


Figure 5.3: Example of a decision tree. Each node is fed with a MC sample mixing signal and background events (left-right numbers); nodes colors represent the relative number of signal/background events [128].

2074 The training or growing of a decision tree is the process where the rules for clas-
 2075 sifying events are defined; this process is represented in Figure 5.3 and consists of
 2076 several steps:

- 2077 • take MC samples of signal and background events and split them into two parts

2078 each; the first parts will be used in the decision tree training, while the second
 2079 parts will be used for testing the final classifier obtained from the training.
 2080 Each event has associated a set of input variables $\mathbf{x} = (x_1, \dots, x_n)$ which serve
 2081 to distinguish between signal and background events. The training sample is
 2082 taken in at the *root node*.

- 2083 • Pick one variable, say x_i .
- 2084 • Pick one value of x_i , each event has its own value of x_i , and split the training
 2085 sample into two subsamples B_1 and B_2 ; B_1 contains events for which $x_i < c_1$
 2086 while B_2 contains the rest of the training events;
- 2087 • scan all possible values of x_i and find the splitting value that provides the *best*
 2088 classification², i.e., B_1 is mostly made of signal events while B_2 is mostly made
 2089 of background events.
- 2090 • It is possible that variables other than the picked one produce a better classi-
 2091 fication, hence, all the variables have to be evaluated. Pick the next variable,
 2092 say x_j , and repeat the scan over its possible values.
- 2093 • At the end, all the variables and their values will have been scanned, the *best*
 2094 variable and splitting value will have been identified, say x_1, c_1 , and there will
 2095 be two nodes fed with the subsamples B_1 and B_2 .

2096 Nodes are further split by repeating the decision process until a given number of
 2097 final nodes is obtained, nodes are largely dominated by either signal or background
 2098 events, or nodes have too few events to continue. Final nodes are called *leaves* and
 2099 they are classified as signal or background leaves according to the class of the majority
 2100 of events in them. Each *branch* in the tree corresponds to a sequence of cuts.

² Quality of the classification will be treated in the next paragraph.

2101 The quality of the classification at each node is evaluated through a separation
 2102 criteria; there are several of them but the *Gini Index* (G) is the one used in the
 2103 decision trees trained for the analysis in this thesis. G is written in terms of the
 2104 purity (P), i.e., the fraction of signal events in the samples after the separation is
 2105 made; it is given by

$$G = P(1 - P) \quad (5.3)$$

2106 note that $P=0.5$ at the root node while $G=0$ for pure leaves. For a node A split into
 2107 two nodes B_1 and B_2 the G gain is

$$\Delta G = G(A) - G(B_1) - G(B_2). \quad (5.4)$$

2108 The *best* classification corresponds to that for which the gain of G is maximized;
 2109 hence, the scanning over all the variables in an event and their values is of great
 2110 importance.

2111 In order to provide a numerical output for the classification, events in a sig-
 2112 nal(background) leaf are assigned an score of 1(-1) each, defining in this way the
 2113 decision tree *classifier/weak learner* as

$$f(\mathbf{x}) = \begin{cases} 1 & \mathbf{x} \text{ in signal region,} \\ -1 & \mathbf{x} \text{ in background region.} \end{cases}$$

2114 Figure 5.4 shows an example of the classification of a sample of events, containing
 2115 two variables, performed by a decision tree.

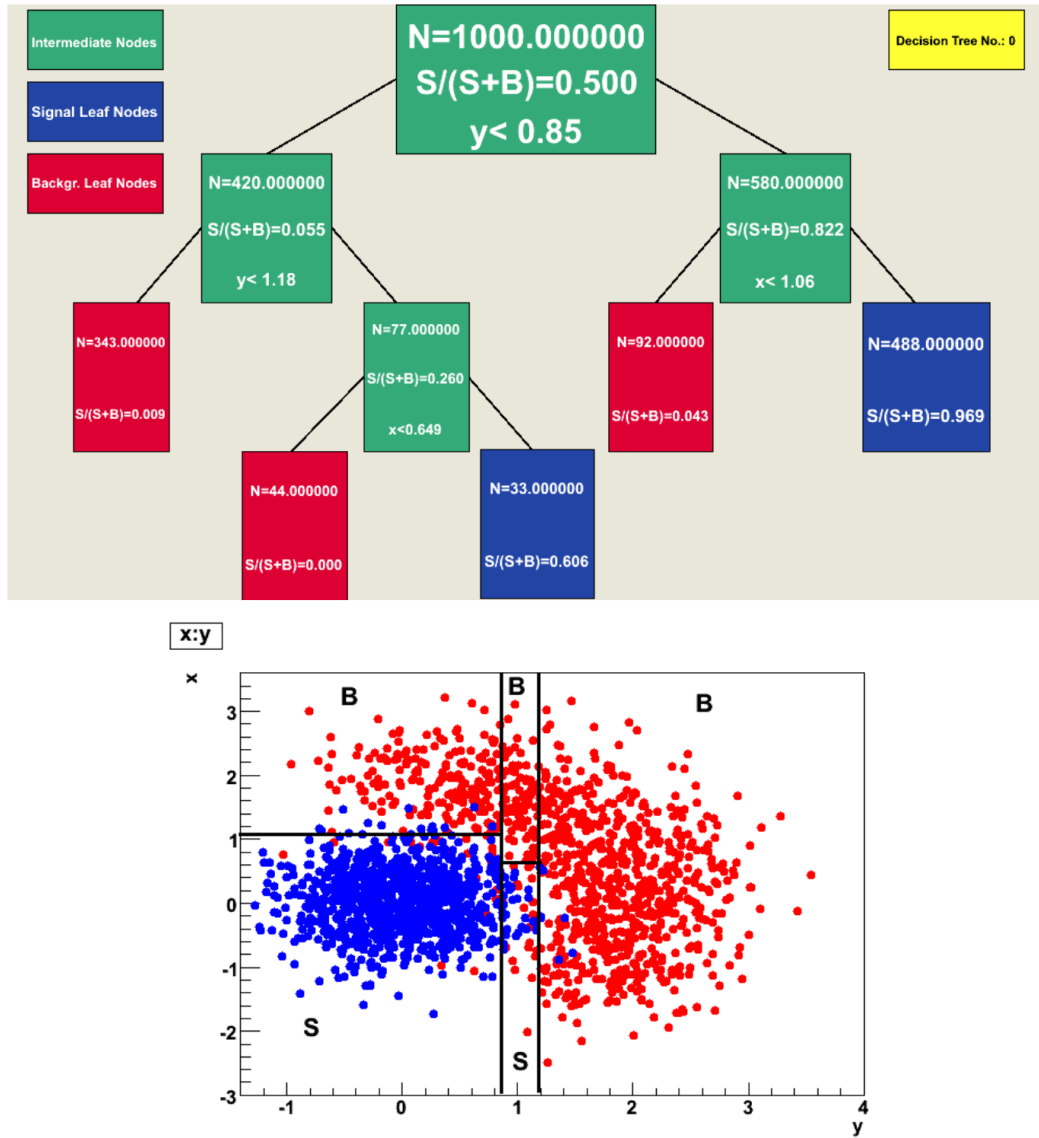


Figure 5.4: Example of a decision tree output. Each leaf, blue for signal events and red for background events, is represented by a region in the variables phase space [130].

2116 5.1.2 Boosted decision trees (BDT).

2117 Event misclassification occurs when a training event ends up in the wrong leaf, i.e., a
 2118 signal event ends up in a background leaf or a background event ends up in a signal
 2119 leaf. A way to correct it is to assign a weight to the misclassified events and train
 2120 a second tree using the reweighted events; the event reweighting is performed by a

boosting algorithm in such a way that when used in the training of a new decision tree the *boosted events* get correctly classified. The process is repeated iteratively adding a new tree to the forest and creating a set of classifiers, which are combined to create the next classifier; the final classifier offers more stability³ and has a smaller misclassification rate than any individual ones. The resulting tree collection is known as a *boosted decision tree (BDT)*.

Thus, purity of the sample is generalized to

$$P = \frac{\sum_s w_s}{\sum_s w_s + \sum_b w_b} \quad (5.5)$$

where w_s and w_b are the weights of the signal and background events respectively; the Gini index is also generalized

$$G = \left(\sum_i^n w_i \right) P(1 - P) \quad (5.6)$$

with n the number of events in the node. The final score of an event, after passing through the forest, is calculated as the renormalized sum of all the individual (possibly weighted) scores; thus, high(low) score implies that the event is most likely signal(background).

The boosting procedure, implemented in the *Gradient boosting* algorithm used in this thesis, produces a classifier $F(\mathbf{x})$ which is the weighted sum of the individual classifiers obtained after each iteration, i.e.,

$$F(\mathbf{x}) = \sum_{m=1}^M \beta_m f(\mathbf{x}; a_m) \quad (5.7)$$

where M is the number of trees in the forest. The *loss function* $L(F, y)$ represents the

³ Decision trees suffer from sensitivity to statistical fluctuations in the training sample which may lead to very different results with a small change in the training samples.

2138 deviation between the classifier $F(\mathbf{x})$ response and the true value y obtained from the
 2139 training sample (1 for signal events and -1 for background event), according to

$$L(F, y) = \ln(1 + e^{-2F(\mathbf{x})y}) \quad (5.8)$$

2140 thus, the reweighting is employed to ensure the minimization of the loss function; a
 2141 more detailed description of the minimization procedure can be found in Reference
 2142 [131]. The final classifier output is later used as a final discrimination variable, labeled
 2143 as *BDT output/response*.

2144 5.1.3 Overtraining

2145 Decision trees offer the possibility to have as many nodes as desired in order to
 2146 reduce the misclassification to zero (in theory); however, when a classifier is too much
 2147 adjusted to a particular training sample, the classifier's response to a slightly different
 2148 sample may leads to a completely different classification results; this effect is known
 2149 as *overtraining*.

2150 An alternative to reduce the overtraining in BDTs consists in pruning the tree
 2151 by removing statistically insignificant nodes after the tree growing is completed but
 2152 this option is not available for BDTs with gradient boosting in the TMVA-toolkit,
 2153 therefore, the overtraining has to be reduced by tuning the algorithm, number of
 2154 nodes, minimum number of events in the leaves, etc. The overtraining can be evaluated
 2155 by comparing the responses of the classifier when running over the training and
 2156 test samples.

2157 5.1.4 Variable ranking

2158 BDTs have a couple of particular advantages related to the input variables; they are
 2159 relatively insensitive to the number of input variables used in the vector \mathbf{x} . The
 2160 ranking of the BDT input variables is determined by counting the number of times a
 2161 variable is used to split decision tree nodes; in addition, the separation gain-squared
 2162 achieved in the splitting and the number of events in the node are accounted by
 2163 applying a weighting to that number. Thus, those variables with small or no power
 2164 to separate signal and background events are rarely chosen to split the nodes, i.e., are
 2165 effectively ignored.

2166 In addition, variables correlations play an important role for some MVA methods
 2167 like the Fisher discriminant algorithm in which the first step consist of performing a
 2168 linear transformation to a phase space where the correlations between variables are
 2169 removed; in the case of BDT algorithm, correlations do not affect the performance.

2170 5.1.5 BDT output example

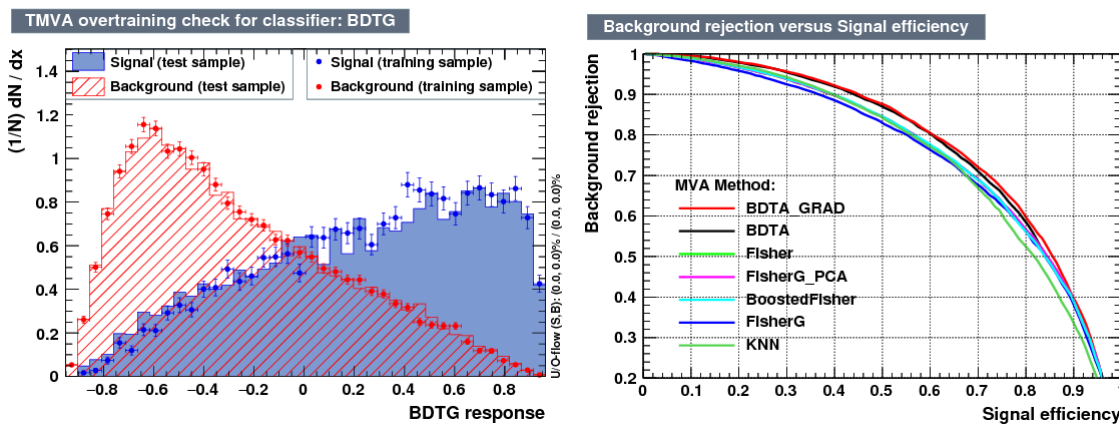


Figure 5.5: Left: Output distributions for the gradient boosted decision tree (BDTG) classifier using a sample of signal ($pp \rightarrow tHq$) and background ($pp \rightarrow tt$) events. Right: Background rejection vs signal efficiency (ROC curves) for various MVA classifiers running over the same sample used to produce the plot on the left.

2171 The left side of figure 5.5 shows the BDT output distributions for signal ($pp \rightarrow$
 2172 tHq) and background ($pp \rightarrow t\bar{t}$) events; this plot is the equivalent to the one showed
 2173 in Figure 5.2. A forest with 800 trees, maximum depth per tree = 3, and gradient
 2174 boosting have been used as training parameters. The BDTG classifier offers a good
 2175 separation power. There is a small overtraining in the signal distribution, while the
 2176 background distribution is very well predicted which might indicate that the sample
 2177 is composed of more background than signal events.

2178 The right side of figure 5.5 shows the background rejection vs signal efficiency
 2179 curves for several combinations of MVA classifiers-boosting algorithms running over
 2180 the same MC sample; these curves are known as ROC curves and give an indication
 2181 of the performance of the classifier. In this particular example, the best performance
 2182 is achieved with the BDTG classifier (BDTA_GRAD), which motivate its use in this
 2183 thesis.

2184 **5.2 Statistical inference**

2185 Once events are classified, the next step consists of finding the parameters that define
 2186 the likelihood functions $f(\mathbf{x}|s)$, $f(\mathbf{x}|b)$ for signal and background events respectively.
 2187 In general, likelihood functions depend not only on the measurements but also on
 2188 parameters (θ_m) that define their shapes; the process of estimating these *unknown*
 2189 parameters and their uncertainties from the experimental data is called *inference*.

2190 The statistical inference tools used in this analysis are implemented in the RooFit
 2191 toolkit [132] and COMBINE package [133] included in the CMSSW software frame-
 2192 work.

2193 **5.2.1 Nuisance parameters**

2194 The unknown parameter vector θ is made of two types of parameters: those pa-
 2195 rameters that provide information about the physical observables of interest for the
 2196 experiment or *parameters of interest*, and the *nuisance parameters* that are not of
 2197 a direct interest for the experiment but that need to be included in the analysis in
 2198 order to achieve a satisfactory description of the data; they represent effects of the
 2199 detector response like the finite resolutions of the detection systems, miscalibrations,
 2200 and in general any source of uncertainty introduced in the analysis.

2201 Nuisance parameters can be estimated from experimental data; for instance, data
 2202 samples from a test beam are usually employed for calibration purposes. In cases
 2203 where experimental samples are not availables, the estimation of nuisance parameters
 2204 makes use of dedicated simulation programs to provide the required samples.

2205 The estimation of the unknown parameters involves certain deviations from their
 2206 true values, hence, the measurement of the nuisance parameter is written in terms
 2207 of an estimated value, also called central value, $\hat{\theta}$ and its uncertainty $\delta\theta$ using the
 2208 notation

$$\theta = \hat{\theta} \pm \delta\theta \quad (5.9)$$

2209 where the interval $[\hat{\theta} - \delta\theta, \hat{\theta} + \delta\theta]$ is called *confidence interval*; it is usually interpreted,
 2210 in the limit of infinite number of experiments, as the interval where the true value
 2211 of the unknown parameter θ is contained with a probability of 0.6827 (if no other
 2212 convention is stated); this interval represents the area under a Gaussian distribution
 2213 in the interval $\pm 1\sigma$.

2214 Conventionally, uncertainties are split into two classes: *systematic*, associated with
 2215 the systematic effects, and *statistical*, related only to fluctuations in data and having

2216 statistical nature.

2217 5.2.2 Maximum likelihood estimation method

2218 The estimation of the unknown parameters that are in best agreement with the ob-
 2219 served data is performed through a function of the data sample that returns the
 2220 estimate of those parameters; that function is called an *estimator*. Estimators are
 2221 usually constructed using mathematical expressions encoded in computer programs.

2222 In this thesis, the estimator used is the likelihood function $f(\mathbf{x}|\boldsymbol{\theta})$ ⁴ which depends
 2223 on a set of measured variables \mathbf{x} and a set of unknown parameters $\boldsymbol{\theta}$. The likelihood
 2224 function for N events in a sample is the combination of all the individual likelihood
 2225 functions, i.e.,

$$L(\boldsymbol{\theta}) = \prod_{i=1}^N f(\mathbf{x}^i|\boldsymbol{\theta}) = \prod_{i=1}^N f(x_1^i, \dots, x_n^i; \theta_1, \dots, \theta_m) \quad (5.10)$$

2226 and the estimation method used is the *Maximum Likelihood Estimation* method
 2227 (MLE); it is based on the combined likelihood function defined by eqn. 5.10 and
 2228 the procedure seeks for the parameter set that corresponds to the maximum value of
 2229 the combined likelihood function, i.e., the *maximum likelihood estimator* of the un-
 2230 known parameter vector $\boldsymbol{\theta}$ is the function that produces the vector of *best estimators*
 2231 $\hat{\boldsymbol{\theta}}$ for which the likelihood function $L(\boldsymbol{\theta})$ evaluated at the measured \mathbf{x} is maximum.

2232 Usually, the logarithm of the likelihood function is used in numerical algorithm
 2233 implementations in order to avoid underflow the numerical precision of the computers
 2234 due to the product of small likelihoods. In addition, it is common to minimize the
 2235 negative logarithm of the likelihood function, therefore, the negative log-likelihood

⁴ analogue to the likelihood functions described in previous sections

2236 function is

$$F(\boldsymbol{\theta}) = -\ln L(\boldsymbol{\theta}) = -\sum_{i=1}^N f(\mathbf{x}^i | \boldsymbol{\theta}). \quad (5.11)$$

2237 The minimization process is performed by the software MINUIT [134] imple-
 2238 mented in the ROOT analysis framework. In case of data samples with large number
 2239 of measurements, the computational resources necessary to calculate the likelihood
 2240 function are too big; therefore, the parameter estimation is performed using binned
 2241 distributions of the variables of interest for which the *binned likelihood function* is
 2242 given by

$$L(\mathbf{x}|r, \boldsymbol{\theta}) = \prod_{i=1} \frac{(r \cdot s_i(\boldsymbol{\theta}) + b_i(\boldsymbol{\theta}))^{n_i}}{n_i!} e^{-r \cdot s_i(\boldsymbol{\theta}) - b_i(\boldsymbol{\theta})} \prod_{j=1} \frac{1}{\sqrt{2\pi}\sigma_{\theta_j}^2} e^{-(\theta_j - \theta_{0,j})^2 / 2\sigma_{\theta_j}^2}, \quad (5.12)$$

2243 with s_i and b_i the expected number of signal and background yields for the bin i , n_i is
 2244 the observed number of events in the bin i and $r = \sigma/\sigma_{SM}$ is the signal strength. Note
 2245 that the number of entries per bin follows a Poisson distribution. The effect of the
 2246 nuisance parameters have been included in the likelihood function through Gaussian
 2247 distributions that models the nuisance. The three parameters, r , s_i and b_i are jointly
 2248 fitted to estimate the value of r .

2249 5.3 Upper limits

2250 In this analysis, two hypotheses are considered; the background only hypothesis
 2251 ($H_0(b)$) and the signal plus background hypothesis ($H_1(s+b)$), i.e., the sample of
 2252 events is composed of background only events ($r=0$) or it is a mixture of signal plus
 2253 background events ($r=1$). The exclusion of one hypothesis against the other means
 2254 that the observed data sample better agrees with H_0 or rather with H_1 . In order
 2255 to discriminate these hypotheses, a test statistic is constructed on the basis of the

2256 likelihood function evaluated for each of the hypothesis.

2257 The *Neyman-Pearson* lemma [135] states that the test statistic that provides the
 2258 maximum power for H_1 for a given significance level (background misidentification
 2259 probability α), is given by the ratio of the likelihood functions $L(\mathbf{x}|H_1)$ and $L(\mathbf{x}|H_0)$;
 2260 however, in order to use that definition it is necessary to know the true likelihood
 2261 functions, which in practice is not always possible. Approximate functions obtained
 2262 by numerical methods, like the BDT method described above, have to be used, so
 2263 that the *profile likelihood* test statistic is defined by

$$\lambda(\mathbf{r}) = \frac{L(\mathbf{x}|r, \hat{\boldsymbol{\theta}}(r))}{L(\mathbf{x}|\hat{r}, \hat{\boldsymbol{\theta}})}, \quad (5.13)$$

2264 where, \hat{r} and $\hat{\boldsymbol{\theta}}$ maximize the likelihood function, and $\hat{\boldsymbol{\theta}}$ maximizes the likelihood
 2265 function for a given value of the signal strength modifier r . In practice, the test
 2266 statistic t_r

$$t_r = -2\ln\lambda(r) \quad (5.14)$$

2267 is used to evaluate the presence of signal in the sample, since the minimum of t_r at
 2268 $r = \hat{r}$ suggests the presence of signal with signal strength \hat{r} . The uncertainty interval
 2269 for r is determined by the values of r for which $t_r = +1$.

2270 The expected probability density function (p.d.f) $f(t_r|r, \boldsymbol{\theta})$ of the test statistic t_r
 2271 can be obtained numerically by generating MC samples where one hypothesis, $H_0(b)$
 2272 or $H_1(s+b)$, is assumed; thus, MC samples contain the possible values of t_r obtained
 2273 from *pseudo-experiments* as shown in Figure 5.6. The probability that t_r takes a value
 2274 equal or greater than the observed value ($t_{r,obs}$) when a signal with a signal modifier
 2275 r is present in the data sample, is called the *p-value* of the observation; it can be
 2276 calculated using

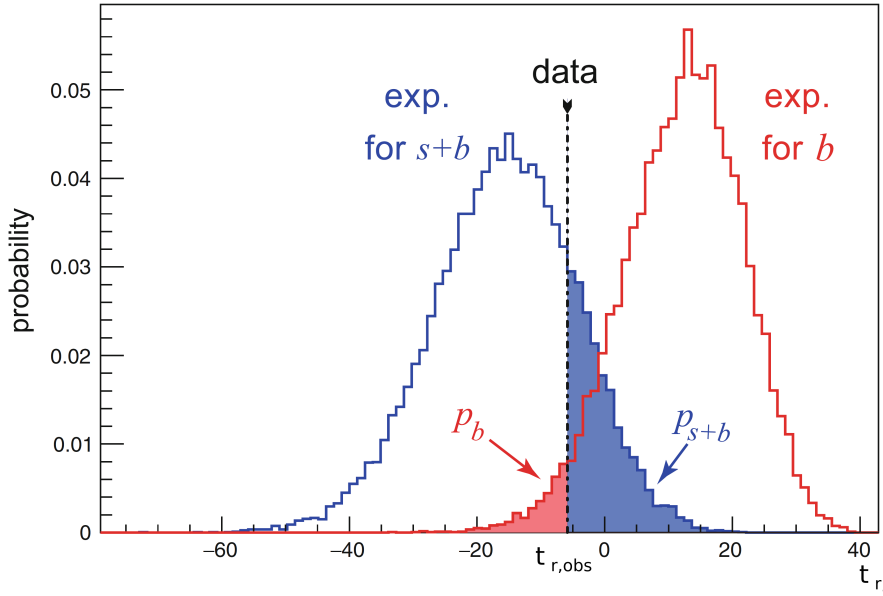


Figure 5.6: t_r p.d.f. from MC pseudo experiments assuming H_0 (red) and H_1 (blue). The black dashed line shows the value of the test statistic as measured from data. Adapted from Reference [128].

$$p_r = \int_{t_{r,obs}}^{\infty} f(t'_r | r, \boldsymbol{\theta}) dt'_r, \quad (5.15)$$

thus, $p_r < 0.05$ means that, for that particular value of r , H_1 could be excluded at 95% Confidence Level (CL). The corresponding background-only p-value is given by

$$1 - p_b = \int_{t_{r,obs}}^{\infty} f(t'_r | 0, \boldsymbol{\theta}) dt'_r, \quad (5.16)$$

If the t_r p.d.f.s for both hypotheses are well separated, as shown in the top side of Figure 5.7, the experiment is sensitive to the presence of signal in the sample. If the signal presence is small, both p.d.f.s will be largely overlapped (bottom of Figure ??) and either the signal hypothesis could be rejected with not enough justification because the experiment is not sensitive to the signal or a fluctuation of the background could be misinterpreted as presence of signal with the corresponding rejection of the

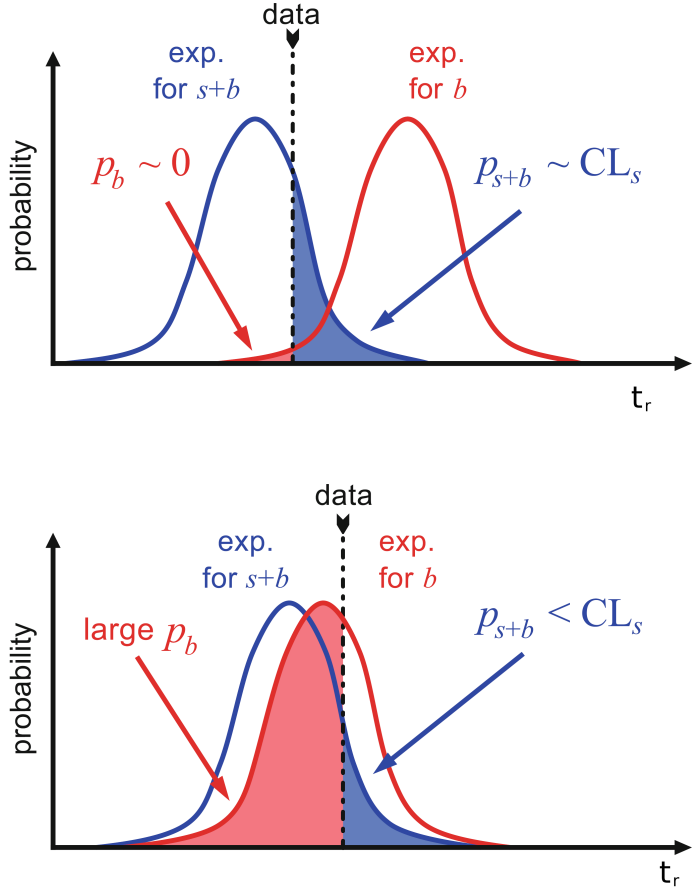


Figure 5.7: CL_s limit illustration. When the test statistic p.d.f. for the two hypotheses H_0 and H_1 are well separated (top) and when they are largely overlapped (bottom). Adapted from Reference [128].

2285 background-only hypothesis. These issues are corrected by using the modified p-
2286 value [136]

$$p'_r = \frac{p_r}{1 - p_b} \equiv CL_s. \quad (5.17)$$

2287 If H_1 is true, then p_b is small, $CL_s \simeq p_r$ and H_0 is rejected; if there is large
2288 overlap and a statistical fluctuation causes that p_b is large, then both numerator and
2289 denominator in Eqn. 5.17 become small but CL_s would allow the rejection of H_1
2290 even if there is poor sensitivity to signal.

2291 The upper limit of the parameter of interest r^{up} is determined by excluding the
 2292 range of values of r for which $CL_s(r, \theta)$ is lower than the confidence level desired,
 2293 normally 90% or 95%, e.g, scanning over r and finding the value for which $p_r'^{up} =$
 2294 0.05. The expected upper limit can be calculated using pseudo-experiments based on
 2295 the background-only hypothesis and obtaining a distribution for r_{ps}^{up} ; the median of
 2296 that distribution corresponds to the expected upper limit, while the $\pm 1\sigma$ and $\pm 2\sigma$
 2297 deviations correspond to the values of the distribution that defines the 68% and 95%
 2298 of the area under the distribution centered in the median. It is usual to present all
 2299 the information about the expected and observed limits in the so-called *Brazilian-flag*
 2300 *plot* as the one showed in Figure 5.8. The solid line represent the observed CL_s

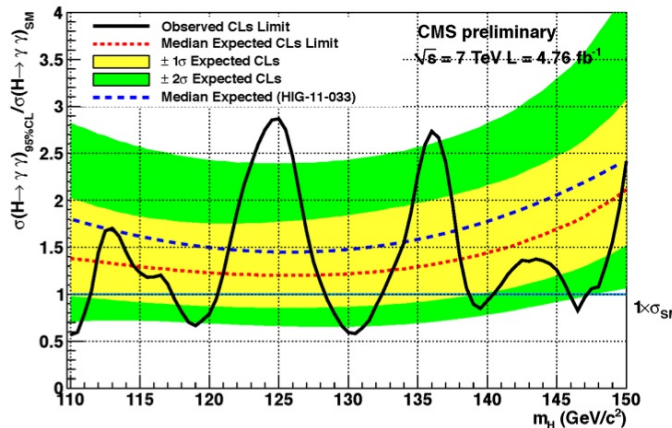


Figure 5.8: Brazilian flag plot of CMS experiment limits for Higgs boson decaying to photons [137].

2301 5.4 Asymptotic limits

2302 As said before, the complexity of the likelihood functions, the construction of test
 2303 statistics, and the calculation of the limits and their uncertainties is not always man-
 2304 ageable and requires extensive computational resources; in order to overcome those
 2305 issues, asymptotic approximations for likelihood-based test statistics, like the ones

2306 described in previous sections, have been developed [138, 139] using Wilks' theorem.
2307 Asymptotic approximations replace the construction of the test statistics p.d.f.s using
2308 MC pseudo-experiments, with the approximate calculation of the test statistics p.d.f.s
2309 by employing the so-called *Asimov dataset*.

2310 The Asimov dataset is defined as the dataset that produce the true values of the
2311 nuisance parameters when it is used to evaluate the estimators for all the parameters;
2312 it is obtained by setting the values of the variables in the dataset to their expected
2313 values [139].

2314 Limits calculated by using the asymptotic approximation and the Asimov dataset
2315 are know as *asymptotic limits*.

²³¹⁶ **Chapter 6**

²³¹⁷ **Search for production of a Higgs**

²³¹⁸ **boson and a single top quark in**

²³¹⁹ **multilepton final states in pp**

²³²⁰ **collisions at $\sqrt{s} = 13$ TeV**

²³²¹ **6.1 Introduction**

²³²² The Higgs boson discovery, supported on experimental observations and theoretical
²³²³ predictions made about the SM, gives the clue of the way in that elementary parti-
²³²⁴ cles acquire mass through the Higgs mechanism; therefore, knowing the Higgs mass,
²³²⁵ the Higgs-vector boson and Higgs-fermion couplings can be tested. In order to test
²³²⁶ the Higgs-top coupling, several measurements have been performed, as stated in the
²³²⁷ chapter 1, but they are limited in sensitivity to measure the square of the coupling.

²³²⁸ The production of a Higgs boson in association with a single top quark (tH) not
²³²⁹ only offers access to the sign of the coupling, but also, to the CP phase of the Higgs

2330 couplings.

2331 This chapter presents the search for the associated production of a Higgs boson
 2332 and a single top quark (tHq) events, focusing on leptonic signatures provided by the
 2333 Higgs decay modes to WW , ZZ , and $\tau\tau$; the 13 TeV dataset produced in 2016, with
 2334 an integrated luminosity of 35.9fb^{-1} , is used.

2335 As shown in Section 1.5, the SM cross section of tHq process is affected by a
 2336 destructive interference between two contributions (see Figure 1.15), where the Higgs
 2337 couples to either the W boson or the top quark; however, if the sign of the Higgs-
 2338 top coupling is flipped with respect to the SM prediction, a large enhancement of
 2339 the cross section occurs, making this analysis sensitive to such deviation. A second
 2340 process, where the Higgs boson and top quark are accompanied by a W boson (tHW)
 2341 has similar behavior, albeit with a weaker interference pattern and lower contribution
 2342 to the cross section, therefore, a combination of both processes would increase the
 2343 sensitivity to the sign of the coupling; in this analysis both contributions are combined
 2344 and referred to as tH channel. A third contribution comes from $t\bar{t}H$ process. The
 2345 purpose of this analysis is to investigate the exclusion of the presence of the $tH+$
 2346 $t\bar{t}H$ processes in the SM under the assumption of the anomalous Higgs-top coupling
 2347 modifier ($\kappa_t = -1$). The analysis exploits signatures with two leptons of the same sign
 2348 ($2lss$) channel and three leptons ($3l$) channel in the final state.

2349 Constraints on the sign of the Higgs-top coupling (y_t) have been derived from the
 2350 decay rate of Higgs boson to photon pairs [50] and from the cross section for associated
 2351 production of Higgs and Z bosons via gluon fusion [141], with recent results disfavoring
 2352 negative signs of the coupling [44, 59, 142], although the negative sign coupling have
 2353 not been completely excluded.

2354 The analysis presented here, expands previous analyses performed at 8 TeV [143,
 2355 144] and searches for associated production of $t\bar{t}$ pair and a Higgs boson in the mul-

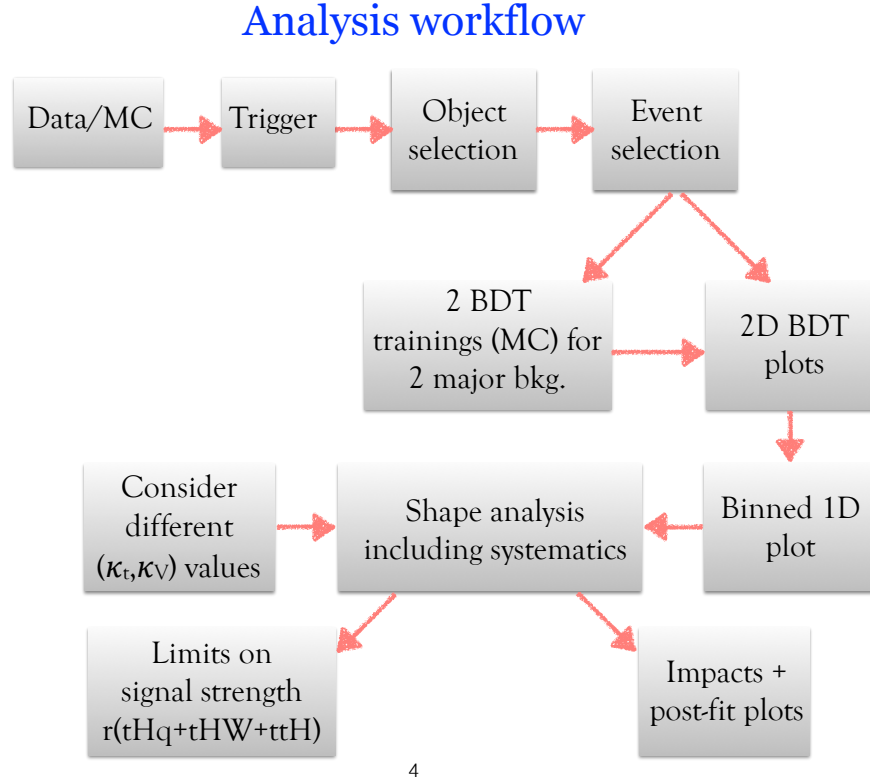
2356 tilepton final state channel [145]; it also complements searches in $H \rightarrow b\bar{b}$ [146].

2357 The first sections present the characteristic tHq signature as well as the expected
 2358 backgrounds. The MC samples, data sets, and the physics object definitions are then
 2359 described; after, the background predictions, the signal extraction, the statistical
 2360 treatment of the selected events and the discussion of the systematic uncertainties
 2361 are described. The final section presents the results for the exclusion limits as a
 2362 function of the ratio of κ_t and the dimensionless modifier of the Higgs-vector boson
 2363 coupling κ_V .

2364 The analysis is designed to efficiently identify and select prompt leptons from on-
 2365 shell W and Z boson decays and to reject non-prompt leptons from b quark decays
 2366 and spurious lepton signatures from hadronic jets. Events are then selected in the
 2367 $2lss$ and $3l$ channels, and are required to contain hadronic jets, some of which must
 2368 be consistent with b quark hadronization. Finally, the signal yield is extracted by
 2369 simultaneously fitting the output of two dedicated multivariate discriminants, trained
 2370 to separate the tHq signal from the two dominant backgrounds, in all categories. The
 2371 fit result is then used to set an upper limit on the combined $t\bar{t}H + tH$ production
 2372 cross section, as a function of the relative coupling strengths of Higgs-top quark and
 2373 Higgs-Vector boson. Figure 6.1 shows an schematic overview of the analysis strategy
 2374 workflow.

2375 With respect to the 8 TeV analysis, the object selections have been adjusted for
 2376 the updated LHC running conditions at 13 TeV, the lepton identification has been
 2377 improved, and more powerful multivariate analysis techniques are used for the signal
 2378 extraction.

2379 The analysis has been made public by CMS as a Physics Analysis Summary [147]
 2380 combining the result for the three lepton and two lepton same-sign channels; the
 2381 content present in this chapter is based on that document and on References [145,149]



4

Figure 6.1: A schematic overview of the analysis workflow. Based on sets of optimized physics object definitions and selection criteria, signal and background events in a data sample are discriminated. The discrimination is performed by a BDT, previously trained using MC samples of the dominant backgrounds, using discriminant variables based on the b -jet multiplicity, the activity in the forward region of the detector, and the kinematic properties of leptons. The CL_s limits on the combined $t\bar{t}H + tH$ production cross section, as a function of the relative coupling strengths are calculated.

unless other Reference is stated. Currently, an effort to turn the analysis into a paper combining the multilepton and $H \rightarrow b\bar{b}$ is ongoing.

6.2 tHq signature

In order to select events of tHq process, its features are translated into a set of selection rules; Figure 6.2 shows the Feynman diagram and a schematic view of the

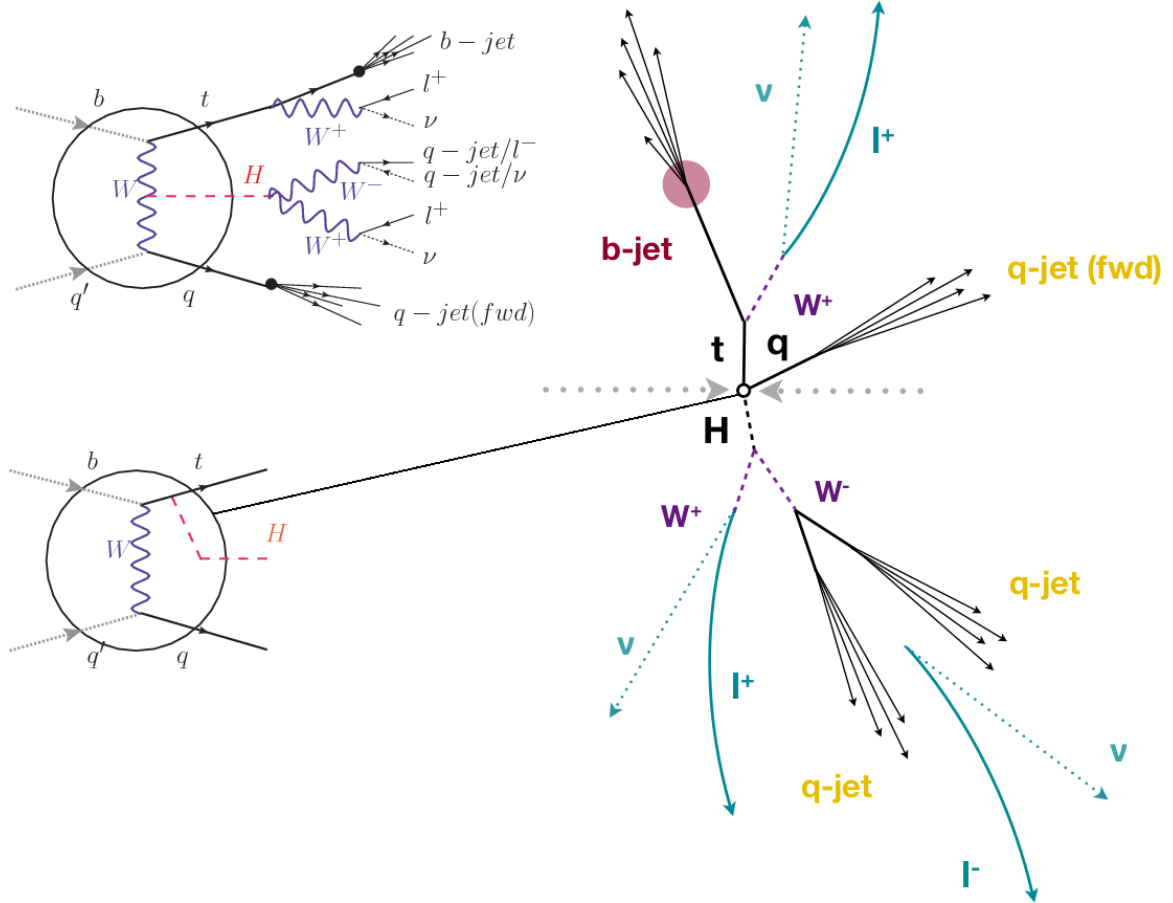


Figure 6.2: tHq event signature. Left: Feynman diagram including the whole evolution up to the final state for the case of the Higgs boson emitted by the W boson (top); Feynman diagram for the case where the Higgs boson is emitted by the top quark. Right: Schematic view as it would be seen in the detector; the circle in the Feynman diagrams on the left corresponds to the circle in the center of the schematic view as indicated by the line connecting them. In the $2lss$ channel, one of the W bosons from the Higgs boson decays to two light-quark jets while in the $3l$ channel both W bosons decay to leptons.

2387 tHq process from the pp collision to the final state configuration. A single top quark
 2388 is produced accompanied by a light quark, denoted as q ; this light quark is produced
 2389 predominantly in the forward region of the detector. The Higgs boson can be either
 2390 emitted by the exchanged W boson or directly by the singly produced top quark.

2391 Due to their high masses/short lifetimes, top quark and Higgs boson decay after
 2392 their production within the detector. The Higgs boson is required to decay into a W

2393 boson pair¹. The top quark almost always decays into a bottom quark and a W boson,
 2394 as encoded in the CMK matrix. The W bosons are required to decay leptonically
 2395 either all the three in the $3l$ channel or the pair with equal electrical charge in the
 2396 $2lss$ channel case; τ leptons are not reconstructed separately and only their leptonic
 2397 decays into either electrons or muons are considered in this analysis.

2398 In summary, the signal process is characterized by a the final state with

- 2399 • one light-flavored forward jet,
 - 2400 • one central b-jet,
 - 2401 • $2lss$ channel → two leptons of the same sign, two neutrinos and two light (often
 2402 soft) jets,
 - 2403 • $3l$ channel → three leptons, three neutrinos and no central light-flavored jets,
- 2404 The presence of neutrinos is inferred from the presence of MET.

2405 6.3 Background processes

2406 The background processes are those that can mimic the signal signature or at least
 2407 can be reconstructed as signal as a result of certain circumstances. The backgrounds
 2408 can be classified as

- 2409 • irreducible backgrounds: where genuine prompt leptons are produced in on-
 2410 shell W and Z boson decays; they can be reliably estimated directly from MC
 2411 simulated events, using higher-order cross sections or data control regions for
 2412 the overall normalization.

¹ ZZ and $\tau\tau$ decays are also include in the analysis but they are not separately reconstructed

2413 • reducible backgrounds: where at least one of the leptons is *non-prompt*, i.e.,
 2414 produced within a hadronic jet; genuine leptons from heavy flavor decays and
 2415 misreconstructed jets, also known as *mis-ID leptons* are considered non-prompt
 2416 leptons or or *fake leptons* as well as electrons from photon conversions. These
 2417 non-prompt leptons leave tracks and hits in the detection systems as would a
 2418 prompt lepton, but evaluation the correlation of those hits with nearby jets
 2419 could be a way of removing them. The misassignment of electron charge in
 2420 processes like $t\bar{t}$ or Drell-Yan, represents an additional source of background,
 2421 but it is relevant only for the $2lss$ channel. Reducible backgrounds are not well
 2422 predicted by simulation, hence, they are estimated using data-driven methods.

2423 The main sources of background events for tHq process are $t\bar{t}$ process and $t\bar{t}V(V =$
 2424 W, Z, γ) processes. Figure 6.3 shows the signature for $t\bar{t}$ and $t\bar{t}W$ processes.

2425 The largest contribution to irreducible backgrounds comes from $t\bar{t}W$ and $t\bar{t}Z$ pro-
 2426 cesses for which the number of ($b-$)jets (($b-$)jet multiplicity) is higher than that
 2427 of the signal events, while for other contributing background events, WZ , ZZ , and
 2428 rare SM processes like $W^\pm W^\pm qq$, $t\bar{t}t\bar{t}$, tZq , tZW , WWW , WWZ , WZZ , ZZZ ,
 2429 the ($b-$)jet multiplicity is lower compared to that of the signal events. None of the
 2430 irreducible backgrounds present activity in the forward region of the detector.

2431 On the side of the reducible backgrounds, the largest contribution comes from the
 2432 $t\bar{t}$ events which have a very similar signature to the signal events but does no present
 2433 activity in the forward region of the detector either; A particular feature of the $t\bar{t}$
 2434 events is their charge-symmetry, which is different from the characteristics of signal
 2435 events.

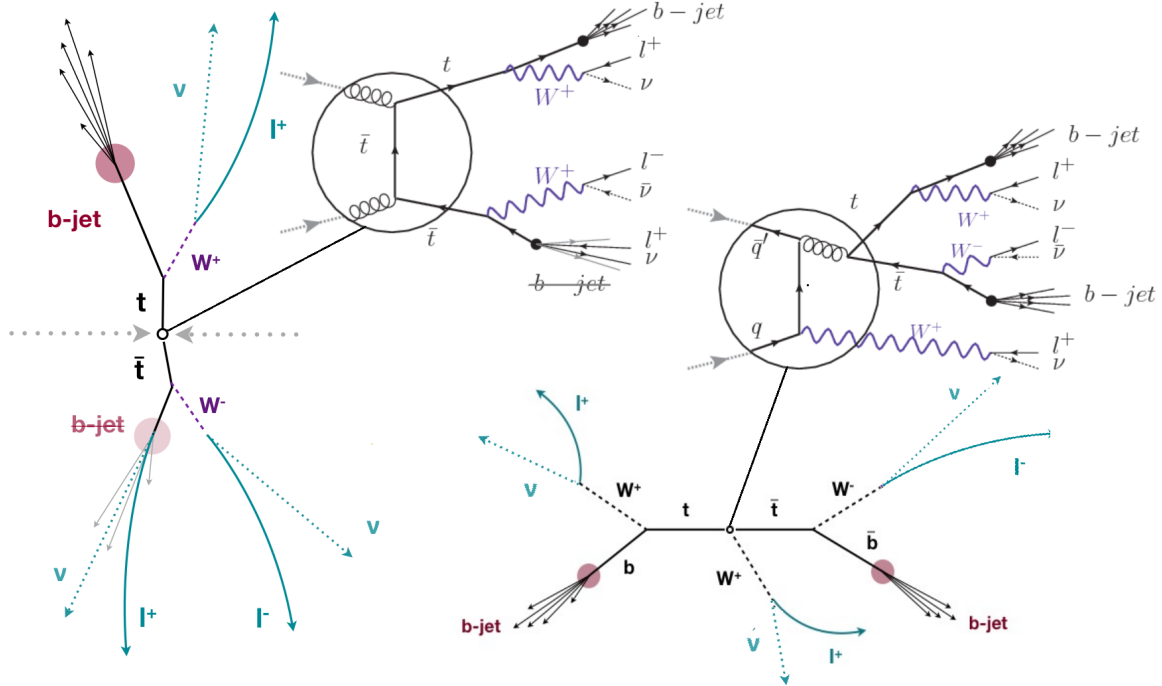


Figure 6.3: $t\bar{t}$ (left) and $t\bar{t}W$ (right) events signature as they would be seen in the detector; the Feynman diagrams including the whole evolution up to the final state are also showed. The $t\bar{t}$ process signature is very similar to that of the signal process with one fake lepton and no forward activity. The $t\bar{t}W$ process presents a higher b-jet multiplicity compared to the signal process, a prompt lepton and no forward activity.

2436 6.4 Data and MC Samples

2437 6.4.1 Full 2016 data set

2438 The data set used in this analysis was collected by the CMS experiment during 2016,
 2439 while running at $\sqrt{s} = 13$ TeV, and corresponds to a total integrated luminosity
 2440 of 35.9 fb^{-1} . Only periods when the CMS magnet was on were considered when
 2441 selecting the data samples; that corresponds to the 23Sep2016 (Run B to G) and
 2442 PromptReco (Run H) versions of the datasets.

2443 Multilepton final states with either two same-sign leptons or three leptons tar-
 2444 get the case where the Higgs boson decays to a pair of W bosons, τ leptons, or Z
 2445 bosons, and where the top quark decays leptonically, hence, the SingleElectron,

2446 SingleMuon, DoubleEG, MuonEG, DoubleMuon dataset (see Table A.1) compose the
 2447 full dataset. The certified luminosity sections are selected using the golden JSON file
 2448 defined by the CMS experiment [148].

2449 6.4.2 Triggers

2450 The events considered are those online-reconstructed events triggered by one, two, or
 2451 three leptons. Single-lepton triggers are included in order to boost the acceptance
 2452 of events where the p_T of the sub-leading lepton falls below the threshold of the
 2453 double-lepton triggers. The trigger efficiency is increased by including double-lepton
 2454 triggers in the $3l$ category, and single-lepton triggers in all categories; it is possible
 2455 given the logical “or” of the trigger decisions of all the individual triggers in a given
 2456 category. Table A.2 shows the lowest-threshold non-prescaled triggers present in the
 2457 High-Level Trigger (HLT) menus for both Monte-Carlo and data in 2016.

2458 Trigger efficiency scale factors

2459 Trigger efficiency describes the ability of events to pass the trigger requirements. It
 2460 is measured in simulated events using generator information given that there is no
 2461 trigger bias with the MC sample. Measuring the trigger efficiency in data requires a
 2462 more elaborated procedure; first, select a set of events collected by a trigger that is
 2463 uncorrelated with the lepton triggers such that the selected events form an unbiased
 2464 sample. In this analysis, that uncorrelated trigger is a MET trigger. Second step
 2465 is looking for candidate events with exactly two good leptons (exactly three good
 2466 leptons for the $3l$ channel). Finally, measure the efficiency for the candidate events to
 2467 pass the logical “or” of triggers being considered in a given event category as defined
 2468 in Table A.2.

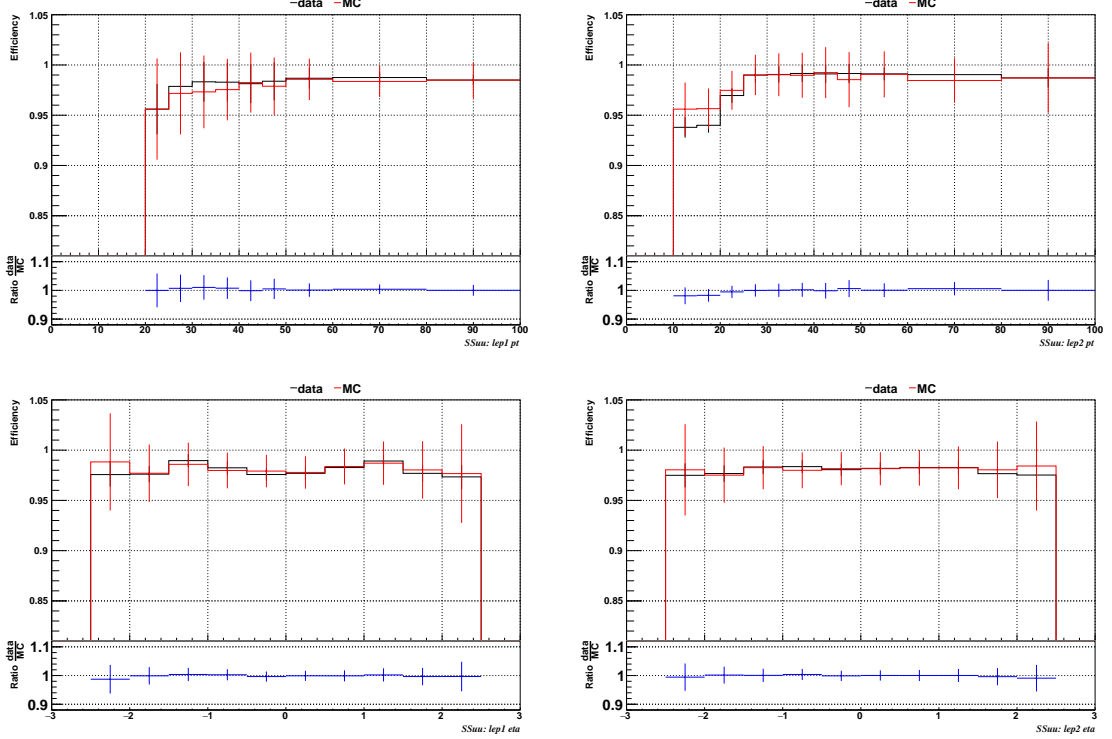


Figure 6.4: Comparison between data and MC trigger efficiencies in the same-sign $\mu\mu$ category, as a function of the p_T (top) and η (bottom) of the leading lepton (left) and the sub-leading lepton (right) [149].

Category	Scale Factor
ee	1.01 ± 0.02
e μ	1.01 ± 0.01
$\mu\mu$	1.00 ± 0.01
3l	1.00 ± 0.03

Table 6.1: Trigger efficiency scale factors and associated uncertainties, shown here rounded to the nearest percent.

2469 Comparisons between the data and MC efficiencies for each category, showed in
 2470 Figures 6.4, 6.5, and 6.6, reveal that they are in good agreement; the difference is
 2471 corrected by applying scale factors derived from the ratio between both efficiencies.
 2472 Applied flat scale factors in each category are shown in Table 6.1; they have been
 2473 inherited from Reference [149].

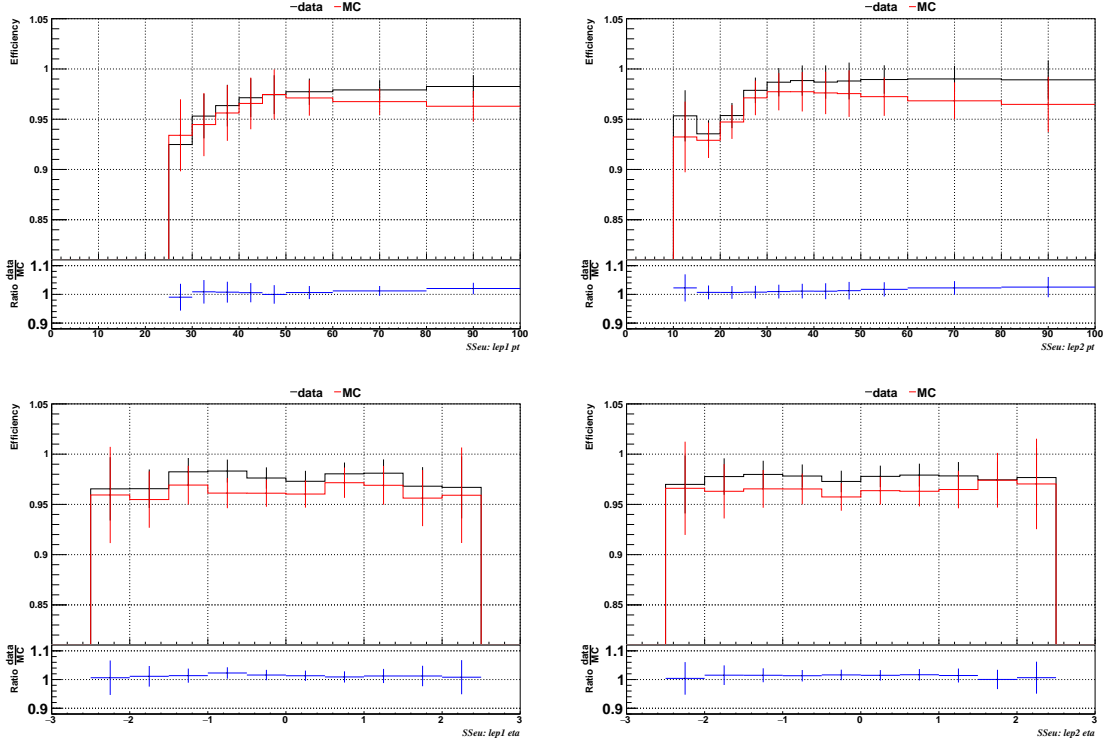


Figure 6.5: Comparison between data and MC trigger efficiencies in the same-sign $e\mu$ category as a function of the p_T (top) and η (bottom) of the leading lepton (left) and the sub-leading lepton (right) [149].

2474 6.4.3 MC samples

2475 Current event generators allow the adjustment of the kinematics of the generated
 2476 events, based on an event-wise reweighting; in this way, several generation parameters
 2477 phase spaces can be explored according to the experimental interests. The signal
 2478 samples used in this analysis were generated in such a way that not only the case κ_t
 2479 $=-1$, but an extended range of κ_t and κ_V values may be investigated.

2480 tHq and tHW cross section in the κ_t - κ_V phase space are shown in Figure 6.7. As
 2481 said in section 3.1, the tHq sample was generated using the 4F scheme which provides
 2482 a better description of the additional b quark from the initial gluon splitting, while the
 2483 tHW sample was generated using the 5F scheme in order to remove its interference

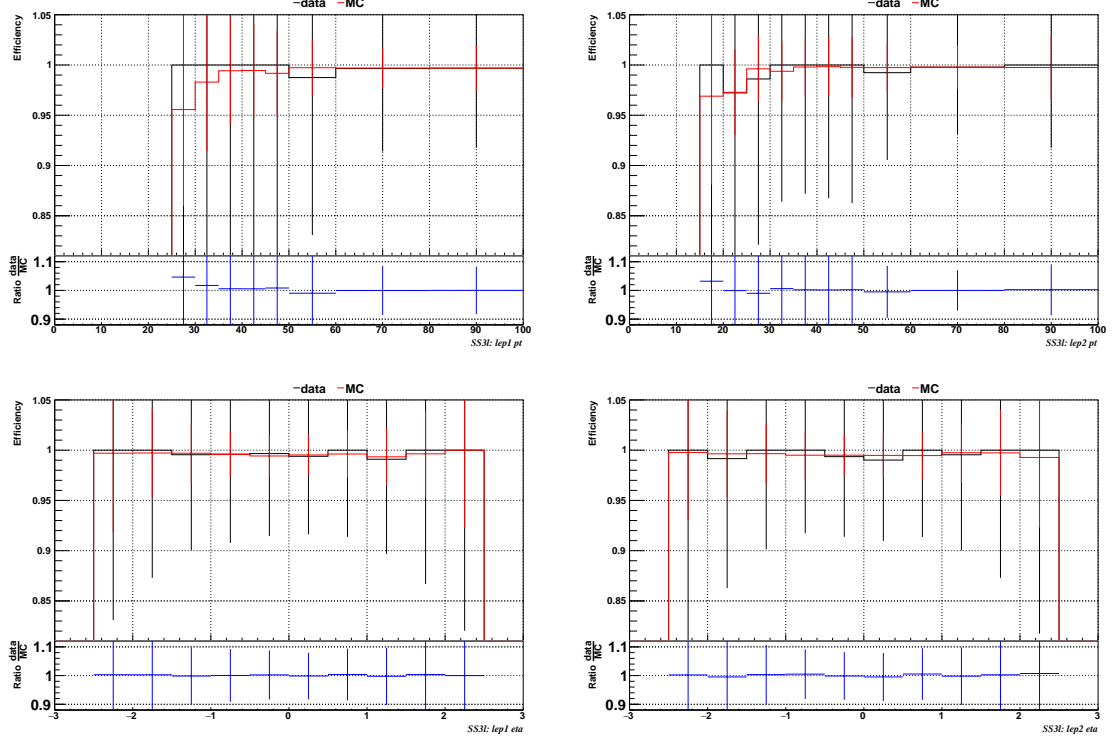


Figure 6.6: Comparison between data and MC trigger efficiencies in the $3l$ category, as a function of the p_T (top) and η (bottom) of the leading lepton (left) and the sub-leading lepton (right) [149].

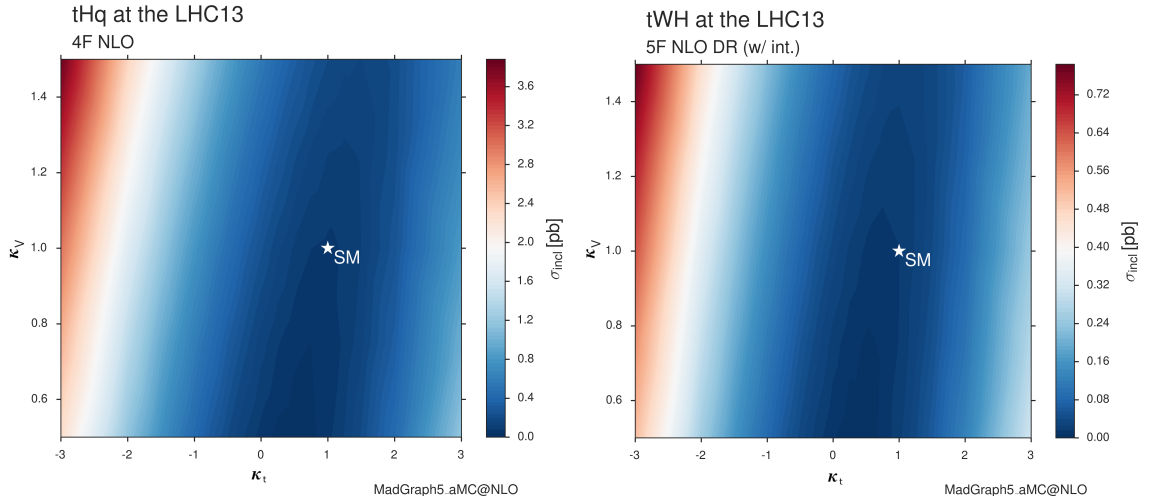


Figure 6.7: tHq and tHW cross section in the κ_t - κ_V phase space [150].

2484 with $t\bar{t}H$ at LO.

2485 **MC signal samples**

2486 The two signal samples, tHq and tHW , correspond to the RunIISummer16MiniAODv2
 2487 campaign produced with CMSSW_80X; they were produced with MG5_aMC@NLO
 2488 (version 5.2.2.3), in LO mode at $\sqrt{s} = 13$ TeV, and are normalized to NLO cross sec-
 2489 tions (see Table 6.2). The Higgs boson is assumed to be SM-like except for the values
 2490 of its couplings to the top quark and W boson. Each sample was generated with a set
 2491 of event weights corresponding to 51 different values of (κ_t, κ_V) couplings, accessible
 2492 in terms of LHE event weights as shown in Table A.3; however, the main interest is
 2493 the $(\kappa_t = -1, \kappa_V = 1)$ case.

Sample	σ [pb]	BF
/THQ_Hincl_13TeV-madgraph-pythia8_TuneCUETP8M1/	0.7927	0.324
/THW_Hincl_13TeV-madgraph-pythia8_TuneCUETP8M1/	0.1472	1.0
/tTHJetToNonbb_M125_13TeV_amcatnloFXFX_madspin_pythia8_mWCutfix/	0.2151	1.0

Table 6.2: MC signal samples used in this analysis; cross section and branching fraction are also listed [150].

2494 The $t\bar{t}H$ sample was produced using AMC@NLO interfaced to PYTHIA 8 for
 2495 the parton shower, and is scaled to NLO cross sections. The $t\bar{t}H$ cross section depends
 2496 quadratically on κ_t ; however, in contrast to the tHq and tHW samples, the scaling
 2497 is not performed during the sample generation process but in the analysis code since
 2498 it was decided to include the $t\bar{t}H$ process as a part of the signal in the course of the
 2499 analysis.

2500 **MC background samples**

2501 Several MC generators were used to generate the samples of the background processes.
 2502 The dominant background sources ($t\bar{t}$, $t\bar{t}W$, $t\bar{t}Z$) were produced using AMC@NLO

2503 interfaced to PYTHIA8, and are scaled to NLO cross sections. Other minor back-
 2504 ground processes are simulated using POWHEG interfaced to PYTHIA, or bare
 2505 PYTHIA as stated in the sample names in Table A.4. Pileup interactions are in-
 2506 cluded in the simulation in order to reflect the observed multiplicity in data; the
 2507 simulated events are weighted according to the actual pileup in data, estimated from
 2508 the measured bunch-to-bunch instantaneous luminosity and the total inelastic cross
 2509 section, 69.2 mb. All events are finally passed through a full simulation of the CMS
 2510 detector using GEANT4, and reconstructed using the same algorithms as used for
 2511 the data.

2512 **6.5 Object Identification**

2513 In this section, the specific definitions of the physical objects in terms of the recon-
 2514 struction parameters are presented; thus, the provided details summarize and com-
 2515 plement the descriptions presented in previous chapters. The object reconstruction
 2516 and selection strategy used in this thesis are inherited from the analyses in Refer-
 2517 ences [145, 149].

2518 **6.5.1 Lepton reconstruction and identification**

2519 Two types of leptons are defined in this analysis: *signal leptons* are those coming from
 2520 W, Z and τ decays which usually are isolated from other particles; *background leptons*
 2521 are defined as leptons produced in b -jet hadron decays, light-jets misidentification,
 2522 and photon conversions.

2523 The process of reconstruction and identification of electron and muon candidates
 2524 was described in chapter 3, hence, the identification variables used in order to retain

2525 the highest possible efficiency for signal leptons while maximizing the rejection of
 2526 background leptons are listed and described in the following sections ².

2527 The identification variables include not only observables related directly to the re-
 2528 constructed leptons themselves, but also to the clustered energy deposits and charged
 2529 particles in a cone around the lepton direction (jet-related variables); an initial loose
 2530 preselection of leptons candidates is performed and then an MVA discriminator, re-
 2531 fered to as *lepton MVA* discriminator, is used to distinguish signal leptons from
 2532 background leptons.

2533 Muons

2534 The Physics Objects Groups (POG) at CMS, are in charge of studying and defining
 2535 the set of selection criteria applied on the course of reconstruction and identification
 2536 of particles. These selection criteria are implemented in the CMS framework in the
 2537 form of several object identification working points according to the strength of the
 2538 requirements.

2539 The muon candidates are reconstructed by combining information from the tracker
 2540 system and the muon detection system of CMS detector and the POG defined three
 2541 working points for muon identification *MuonID* [153];

- 2542 • *POG Loose Muon ID* is a particle identified as a muon by the PF event re-
 2543 construction and also reconstructed either as a global-muon or as an arbitrated
 2544 tracker-muon. This identification criteria is designed to be highly efficient for
 2545 prompt muons and for muons from heavy and light quark decays; it can be com-
 2546 plemented by applying impact parameter cuts in analyses with prompt muon
 2547 signals.

² The studies performed to optimize the identification are far from the scope of this thesis,
 therefore, only general descriptions are provided

- 2548 • *POG Medium Muon ID* is a Loose muon with additional track-quality and
 2549 muon-quality (spatial matching between the individual measurements in the
 2550 tracker and the muon system) requirements. This identification criteria is de-
 2551 signed to be highly efficient in the separation of the muons coming from decay
 2552 in flight of heavy quarks and muons coming from B meson decays as well as
 2553 prompt muons. An additional category *MVA Prompt ID* is defined in this iden-
 2554 tification criteria directed to discriminated muons from B mesons and prompt
 2555 muons (from W,Z and τ decays). The Medium ID provides the same fake rate as
 2556 the Tight Muon ID but a higher efficiency on prompt and B-decays muons. [154]

 2557 • *POG Tight Muon ID* is a global muon with additional muon-quality require-
 2558 ments Tight Muon ID selects a subset of the PF muons.

2559 Only muons within the muon system acceptance $|\eta| < 2.4$ and minimum p_T of 5
 2560 GeV are considered.

2561 **Electrons**

2562 Electrons are reconstructed using information from the tracker and from the electro-
 2563 magnetic calorimeter and identified by an MVA algorithm (*MVA eID* discriminant)
 2564 using the shape of the calorimetric shower variables like the shape in η and ϕ , the clus-
 2565 ter circularity, widths along η and ϕ ; track-cluster matching variables like E_{tot}/p_{in} ,
 2566 E_{Ele}/p_{out} , $\Delta\eta_{in}$, $\Delta\eta_{out}$, $\Delta\phi_{in}$, $1/E - 1/p$; and track quality variables like χ^2 of the
 2567 GSF tracks, the number of hits used by the GSF filter [155].

2568 A loose selection based on η -dependent cuts on this discriminant is used to prese-
 2569 lect electron candidates, the full shape of the discriminant is used in the lepton MVA
 2570 selection to separate signal leptons from background leptons (described in Section
 2571 6.5.1).

2572 In order to reject electrons from photon conversions, electron candidates with
 2573 missing hits in the pixel tracker layers or matched to a conversion secondary vertex
 2574 are discarded. Electrons are selected for the analysis if they have $p_T > 7$ GeV and
 2575 are located within the tracker system acceptance region ($|\eta| < 2.5$).

2576 **Lepton vertexing and pile-up rejection**

2577 The impact parameter in the transverse plane d_0 , impact parameter along the z -
 2578 axis d_z , and the impact parameter significance in the detector space SIP_{3D} , are
 2579 considered to perform the identification and rejection of pile-up, misreconstructed
 2580 tracks, and background leptons from b-hadron decays; pile-up and misreconstructed
 2581 track mitigation is achieved by imposing loose cuts on the impact parameter variables.
 2582 The full shape of those variables is used in a lepton MVA classifier to achieve the best
 2583 separation between the signal and the background leptons.

2584 **Lepton isolation**

2585 PF is able to recognize leptons from two different sources: on one side, leptons from
 2586 the decays of heavy particles, such as W and Z bosons, which are normally isolated in
 2587 space from the hadronic activity in the event; on the other side, leptons from decays
 2588 of hadrons and jets misidentified as leptons, which are not isolated as the former. For
 2589 highly boosted systems, like the lepton and the b -jet generated in the semileptonic
 2590 decay of a boosted top, the decay products tend to be more closer and sometimes they
 2591 even overlap; thus, the PF standard definition of isolation in terms of the separation
 2592 ΔR between lepton candidates (l) and other PF objects (i) in the η - ϕ plane,

$$\Delta R = \sqrt{(\eta^l - \eta^i)^2 + (\phi^l - \phi^i)^2} < 0.3 \quad (6.1)$$

which considers all the neutral, charged hadrons and photons in a cone around the leptons, is refocused to the local isolation of the leptons through the mini-isolation I_{mini} [156] defined as the sum of particle flow candidates p_T within a cone around the lepton, corrected for the effects of pileup and divided by the lepton p_T

$$I_{mini} = \frac{\sum_R p_T(h^\pm) - \max\left(0, \sum_R p_T(h^0) + p_T(\gamma) - \rho \mathcal{A}\left(\frac{R}{0.3}\right)^2\right)}{p_T(l)} \quad (6.2)$$

where ρ is the pileup energy density, h^\pm, h^0, γ, l , represent the charged hadron, neutral hadrons, photons, and the lepton, respectively. The radius R of the cone depends on the p_T of the lepton according to

$$R = \frac{10\text{GeV}}{\min(\max(p_T(l), 50\text{GeV}), 200\text{GeV})}, \quad (6.3)$$

The p_T dependence of the cone size allows for greater signal efficiency. Setting a cut on I_{mini} below a given threshold ensures that the lepton is locally isolated, even in boosted systems. The effect of pileup is mitigated using the so-called effective area correction \mathcal{A} listed in Table 6.3.

$ \eta $ range	$\mathcal{A}(e)$ neutral/charged	$\mathcal{A}(\mu)$ neutral/charged
0.0 - 0.8	0.1607 / 0.0188	0.1322 / 0.0191
0.8 - 1.3	0.1579 / 0.0188	0.1137 / 0.0170
1.3 - 2.0	0.1120 / 0.0135	0.0883 / 0.0146
2.0 - 2.2	0.1228 / 0.0135	0.0865 / 0.0111
2.2 - 2.5	0.2156 / 0.0105	0.1214 / 0.0091

Table 6.3: Effective areas, for electrons and muons used to mitigate the effect of pileup by using the so-called effective area correction.

A loose cut on I_{mini} is applied to pre-select the muon and electron candidates; however, the full shape is used in the lepton MVA discriminator when performing the signal lepton selection.

2607 **Jet-related variables**

2608 In order to reject misidentified leptons from b -jets, mostly coming from $t\bar{t}$ +jets,
 2609 Drell-Yan+jets, and W+jets events, the vertexing and isolation described in previous
 2610 sections are complemented with additional variables related to the closest recon-
 2611 structed jet to the lepton, i.e., the PF jets reconstructed³ around the leptons with
 2612 $\Delta R = \sqrt{(\eta^l - \eta^{jet})^2 + (\phi^l - \phi^{jet})^2} < 0.5$. The identification variables used in the lep-
 2613 ton MVA discriminator are the ratio p_T^l/p_T^{jet} , the CSV b-tagging discriminator value
 2614 of the jet, the number of charged tracks of the jet, and the relative p_T given by

$$p_T^{rel} = \frac{(\vec{p}_{jet} - \vec{p}_l) \cdot \vec{p}_l}{\|\vec{p}_{jet} - \vec{p}_l\|}. \quad (6.4)$$

2615 **LeptonMVA discriminator**

2616 Electrons and muons passing the basic selection process described above are referred
 2617 to as *loose leptons*. Additional discrimination between signal leptons and background
 2618 leptons is crucial considering that the rate of $t\bar{t}$ production is much larger than the
 2619 signal, hence, an overwhelming background from $t\bar{t}$ production is present. To maxi-
 2620 mally exploit the available information in each event to that end, the dedicated lepton
 2621 MVA discriminator, based on a boosted decision tree (BDT) algorithm, has been built
 2622 so that all the identification variables can be used together.

2623 The lepton MVA discriminator training is performed using simulated signal Loose
 2624 leptons from the $t\bar{t}H$ MC sample and fake leptons from the $t\bar{t}$ +jets MC sample,
 2625 separately for muons and electrons. The input variables used include vertexing, iso-
 2626 lation and jet-related variables, the p_T and η of the lepton, the electron MVA eID
 2627 discriminator and the muon segment-compatibility variables. An additional require-
 2628 ment known as *tight-charge* requirement, is imposed by comparing two independent

³ Charged hadrons from PU vertices are not removed prior to the jet clustering.

measurement of the charge, one from the ECAL supercluster and the other from the tracker; thus, the consistency in the measurements of the electron charge is ensured so that events with a wrong electron charge assignment are rejected; this variable is particularly used in the $2lss$ channel to suppress opposite-sign events for which the charge of one of the leptons has been mismeasured. The tight-charge requirement for muons is represented by the requirement of a consistently well measured track transverse momentum given by $\Delta p_T/p_T < 0.2$. Leptons are selected for the final analysis if they pass a given threshold of the BDT output, and are referred to as *tight leptons* in the following.

The validation of the lepton MVA algorithm and the lepton identification variables is performed using data in various control regions; the details about that validation are not discussed here but can be found in Reference [149].

Selection definitions

Electron and muon object identification is defined in three different sets of selections criteria; the *Loose*, *Fakeable Object*, and *Tight* selection. These three levels of selection are designed to serve for event level vetoes, the fake rate estimation application region (see Section 6.7.2), and the final signal selection, respectively. The p_T of fakeable objects is defined as $0.85 \times p_T(\text{jet})$, where the jet is the one associated to the lepton object. This mitigates the dependence of the fake rate on the momentum of the fakeable object and thereby improves the precision of the method.

Tables 6.4 and 6.5 list the full criteria for the different selections of muons and electrons.

In addition to the previously defined requirements for jets, they are required to be separated from any lepton candidates passing the fakeable object selections by $\Delta R > 0.4$.

Cut	Loose	Fakeable object	Tight
$ \eta < 2.4$	✓	✓	✓
p_T	$> 5\text{GeV}$	$> 15\text{GeV}$	$> 15\text{GeV}$
$ d_{xy} < 0.05 \text{ (cm)}$	✓	✓	✓
$ d_z < 0.1 \text{ (cm)}$	✓	✓	✓
$\text{SIP}_{3D} < 8$	✓	✓	✓
$I_{\text{mini}} < 0.4$	✓	✓	✓
is Loose Muon	✓	✓	✓
jet CSV	—	< 0.8484	< 0.8484
is Medium Muon	—	—	✓
tight-charge	—	—	✓
lepMVA > 0.90	—	—	✓

Table 6.4: Requirements on each of the three muon selections. In the cases where the cut values change between the selections, those values are listed in the table. Otherwise, whether the cut is applied is indicated.

Cut	Loose	Fakeable Object	Tight
$ \eta < 2.5$	✓	✓	✓
p_T	$> 7\text{GeV}$	$> 15\text{GeV}$	$> 15\text{GeV}$
$ d_{xy} < 0.05 \text{ (cm)}$	✓	✓	✓
$ d_z < 0.1 \text{ (cm)}$	✓	✓	✓
$\text{SIP}_{3D} < 8$	✓	✓	✓
$I_{\text{mini}} < 0.4$	✓	✓	✓
MVA eID $> (0.0, 0.0, 0.7)$	✓	✓	✓
$\sigma_{in\eta} < (0.011, 0.011, 0.030)$	—	✓	✓
H/E $< (0.10, 0.10, 0.07)$	—	✓	✓
$\Delta\eta_{in} < (0.01, 0.01, 0.008)$	—	✓	✓
$\Delta\phi_{in} < (0.04, 0.04, 0.07)$	—	✓	✓
$-0.05 < 1/E - 1/p < (0.010, 0.010, 0.005)$	—	✓	✓
p_T^{ratio}	—	$> 0.5^\dagger / -$	—
jet CSV	—	$< 0.3^\dagger / < 0.8484$	< 0.8484
tight-charge	—	—	✓
conversion rejection	—	—	✓
Number of missing hits	< 2	$= 0$	$= 0$
lepton MVA > 0.90	—	—	✓

Table 6.5: Criteria for each of the three electron selections. In cases where the cut values change between selections, those values are listed in the table. Otherwise, whether the cut is applied is indicated. In some cases, the cut values change for different η ranges. These ranges are $0 < |\eta| < 0.8$, $0.8 < |\eta| < 1.479$, and $1.479 < |\eta| < 2.5$ and the respective cut values are given in the form (value₁, value₂, value₃). For the two p_T^{ratio} and CSV rows, the cuts marked with a \dagger are applied to leptons that fail the lepton MVA cut, while the loose cut value is applied to those that pass the lepton MVA cut.

2654 6.5.2 Lepton selection efficiency

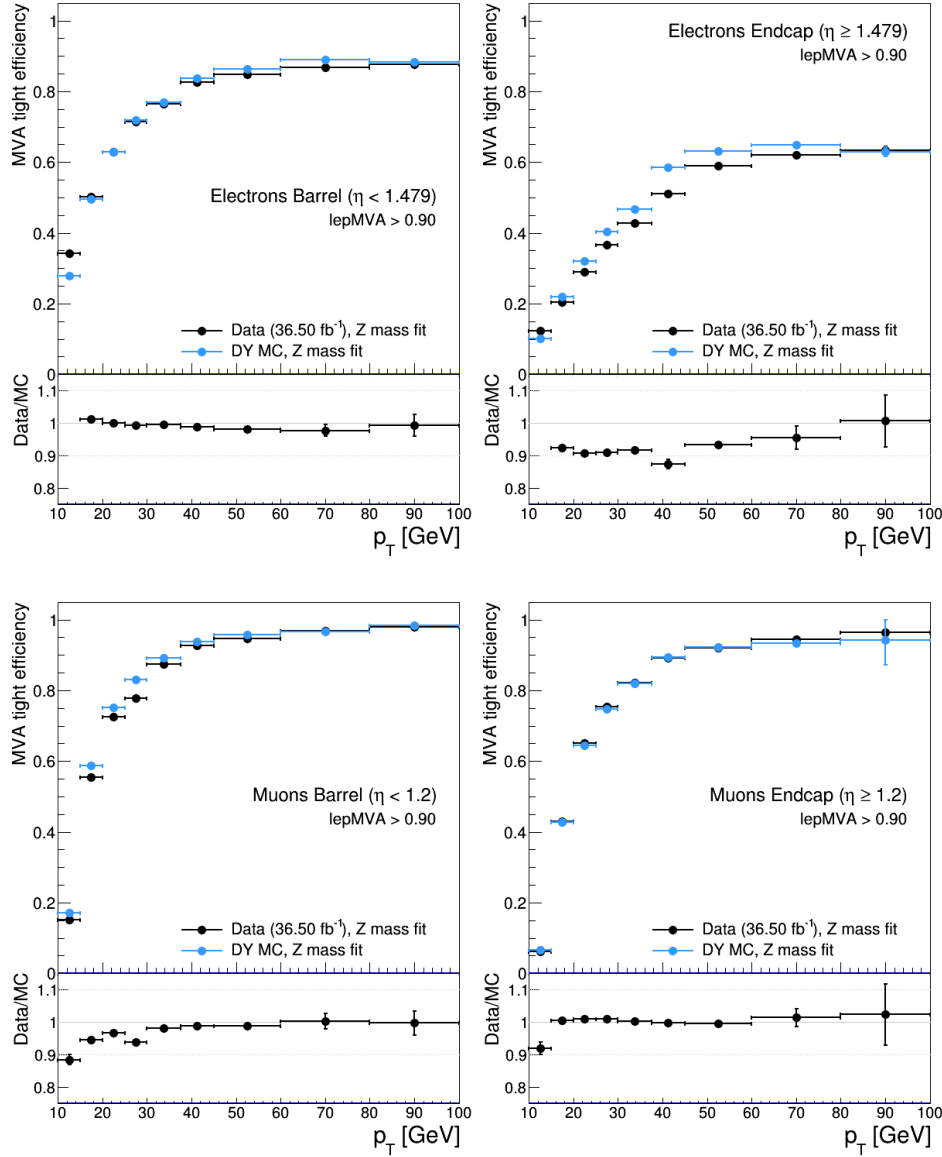


Figure 6.8: Tight vs loose selection efficiencies for electrons (top), and muons (bottom), for the $2lss$ definition, i.e., including the tight-charge requirement.

2655 Efficiencies of reconstruction and selecting loose leptons are measured both for
 2656 muons and electrons using a tag and probe method on both data and MC, using
 2657 $Z \rightarrow \ell^+ \ell^-$ [157]. The scale factors are derived from the ratio of efficiencies $\varepsilon_i(p_T, \eta)$

2658 measured for a given lepton in data/MC, according to

$$\rho(p_T, \eta) = \frac{\varepsilon_{data}(p_T, \eta)}{\varepsilon_{MC}(p_T, \eta)}. \quad (6.5)$$

2659 The scale factor for each event is used to correct the weight of the event in the

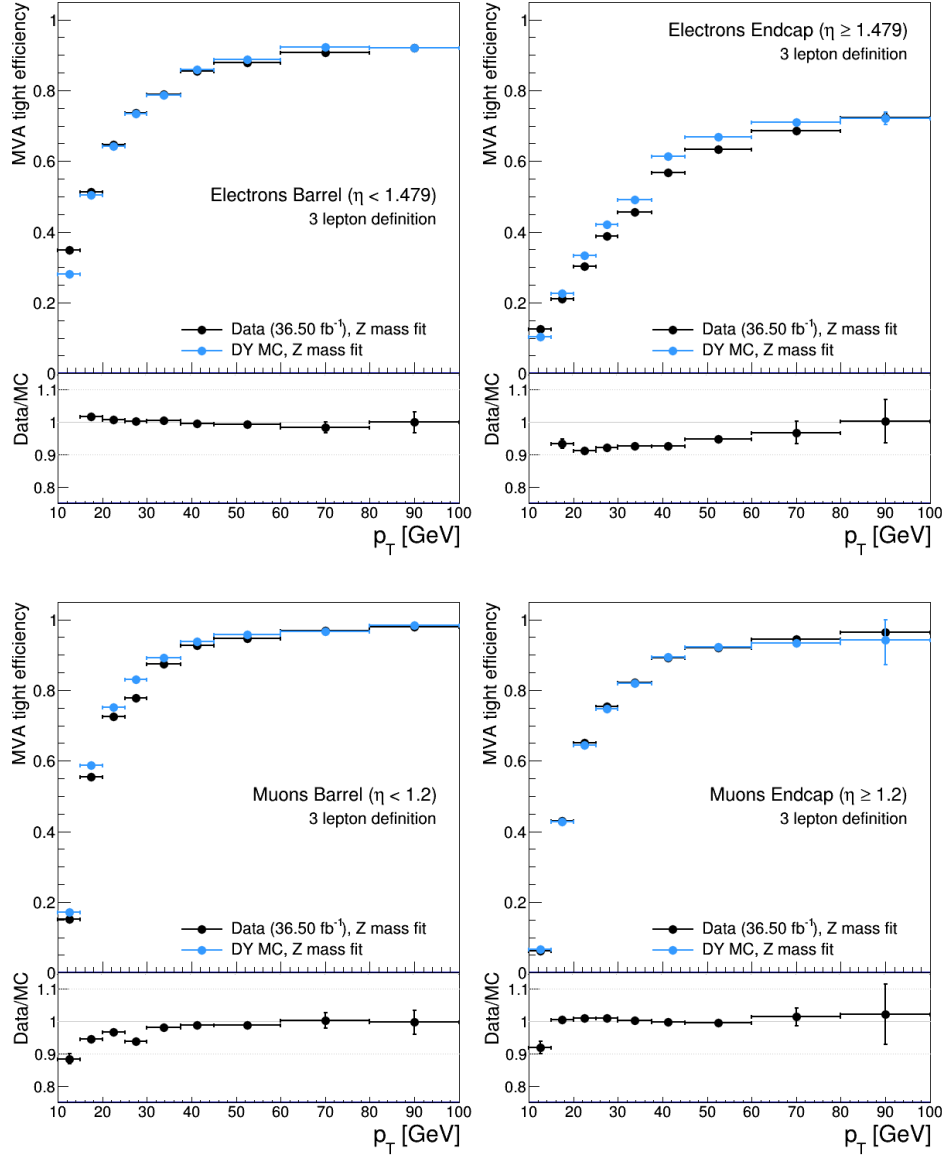


Figure 6.9: Tight vs loose selection efficiencies for electrons (top), and muons (bottom), for the $3l$ channel not including the tight-charge requirement.

2660 full sample; therefore, the full simulation correction is given by the product of all
 2661 the individual scale factors. The scale factors used in this thesis are inherited from
 2662 Reference [149] which in turns inherited them from leptonic SUSY analyses using
 2663 equivalent lepton selections.

2664 The efficiency of applying the tight selection as defined in Tables 6.4 and 6.5, on
 2665 the loose leptons is determined by using a tag and probe method on a sample of Drell-
 2666 Yan enriched events. Figures 6.8 and 6.9 show the efficiencies for the $2lss$ channel and
 2667 $3l$ channel respectively. Efficiencies in the $2lss$ channel have been produced including
 2668 the tight-charge requirement, while for the $3l$ channel it is not included. Number
 2669 of passed and failed probes are determined from a fit to the invariant mass of the
 2670 dilepton system. Simulation is corrected using these scale factors; note that they
 2671 depend on η and p_T .

2672 **6.5.3 Jets and b -jet tagging**

2673 In this analysis, jets are reconstructed by clustering PF candidates using the anti- k_t
 2674 algorithm with parameter distance $\Delta R = 0.4$; those charged hadrons that are not
 2675 consistent with the selected primary vertex are discarded from the clustering. The
 2676 jet energy is then corrected for the varying response of the detector as a function of
 2677 transverse momentum p_T and pseudorapidity η . Jets are selected for being used in the
 2678 analysis only if they have $p_T > 25$ GeV and are separated from any selected leptons
 2679 by $\Delta R > 0.4$.

2680 Jets coming from the primary vertex and jets coming from pile-up vertices are
 2681 distinguished using a MVA discriminator based on the differences in the jet shapes,
 2682 in the relative multiplicity of charged and neutral components, and in the different
 2683 fraction of transverse momentum which is carried by the most energetic components.

2684 Jet tracks are also required to be compatible with the primary vertex.

2685 Jets originated from the hadronization of a b quark are selected using a MVA
 2686 likelihood discriminant which uses track-based lifetime information and reconstructed
 2687 secondary vertices (CSV algorithm). Only jets within the CMS tracker acceptance
 2688 ($\eta < 2.4$) are identified with this tool. Data samples are used to measure the efficiency
 2689 of the b -jet tagging and the probability to misidentify jets from light quarks or gluons;
 2690 in both cases the measurements are parametrized as a function of the jet p_T and η
 2691 and later used to correct differences between the data and MC simulation in the b
 2692 tagging performance, by applying per-jet weights to the simulation, dependent on
 2693 the jet p_T , η , b tagging discriminator, and flavor (from the MC generation/simulation
 2694 truth information) [151]. The per-event weight is taken as the product of the per-jet
 2695 weights, including those of the jets associated to the leptons. The weights are derived
 2696 on $t\bar{t}$ and Z+jets events.

2697 Two working points are defined, based on the CSV algorithm output: *loose* work-
 2698 ing point ($\text{CSV} > 0.46$) with a b signal tagging efficiency of about 83%, and *medium*
 2699 working point ($\text{CSV} > 0.80$) with b -tagging efficiency of about 69% [152]. Tagging of
 2700 jets from charm quarks have efficiencies of about 40% and 18% for loose and medium
 2701 working points respectively. Separate scale factors are applied to jets originating from
 2702 bottom/charm quarks and from light quarks in simulated events to match the tagging
 2703 efficiencies measured in the data.

2704 6.5.4 Missing Energy MET

2705 As stated in Section 3.4.1, the MET vector is calculated as the negative of the vector
 2706 sum of transverse momenta of all PF candidates in the event and its magnitude is
 2707 referred to as E_T^{miss} . Due to pile-up interactions, the performance in determining

2708 MET is degraded; in order to correct for that, the energy from the selected jets and
 2709 leptons that compose the event is assigned to the variable H_T^{miss} . It is calculated in
 2710 the same way as E_T^{miss} and although it has worse resolution than E_T^{miss} , it is more
 2711 robust in the sense that it does not rely on the soft part of the event. The event
 2712 selection uses a linear discriminator based on the two variables given by

$$E_T^{miss, LD} = 0.00397 * E_T^{miss} + 0.00265 * H_T^{miss} \quad (6.6)$$

2713 taking advantage of the fact that the correlation between E_T^{miss} and H_T^{miss} is less
 2714 for events with instrumental missing energy than for events with real missing energy.
 2715 The working point $E_T^{miss, LD} > 0.2$ was chosen to ensure a good signal efficiency while
 2716 keeping an efficient background rejection.

2717 6.6 Event selection

2718 Events are selected considering the features of the signal process and the decay sig-
 2719 nature as described in Section 6.2. At the trigger level, events are selected to contain
 2720 either one, two, or three leptons with minimal p_T thresholds:

- 2721 • single-lepton trigger → 24 GeV for muons and at 27 GeV for electrons
- 2722 • double-lepton triggers → leading and sub-leading leptons: 17 and 8 GeV for
 2723 muons and 23 and 12 GeV for electrons.
- 2724 • three-lepton triggers → threshold on the third hardest lepton in the event: 5
 2725 and 9 GeV for muons and electrons, respectively.

2726 The offline event selection level targets the specific topology of the tHq signal
 2727 with $H \rightarrow WW$ and $t \rightarrow Wb \rightarrow l\nu b$; therefore, the resulting state is composed of three

2728 W bosons, one b quark, and a light spectator quark at high rapidity. The selection
 2729 criteria for the two channels exploited in this analysis are summarized in Table 6.6.
 2730 This selection includes contributions from $H \rightarrow \tau\tau$ and $H \rightarrow ZZ$ as well.

Same-sign $\ell\ell$ channel $e^\pm\mu^\pm, \mu^\pm\mu^\pm$	$\ell\ell\ell$ channel
Have fired one of the corresponding trigger paths	
No loose leptons with $m_{\ell\ell} < 12\text{GeV}$	
One or more b tagged jets (CSV medium) $ \eta < 2.4$	
One or more non-tagged jets: central $\rightarrow p_T > 25\text{ GeV}, \eta < 2.4$	
	forward $\rightarrow p_T > 40\text{ GeV}, \eta > 2.4$
$E_T^{miss}_{LD} > 0.2$	
Exactly two tight same-sign leptons	Exactly three tight leptons
Lepton $p_T > 25/15\text{GeV}$	Lepton $p_T > 25/15/15\text{GeV}$
Electrons are triple-charge consistent.	No OSSF lepton pair with $ m_{\ell\ell} - m_Z < 15\text{GeV}$
Muon p_T resolution: $\Delta p_T/p_T < 0.2$.	
No ee pair with $ m_{ee} - m_Z < 10\text{GeV}$	

Table 6.6: Summary of event pre-selection.

2731 In the $2lss$ channel, events with additional tight leptons are vetoed as well as those
 2732 for which a loose lepton pair has an invariant mass below 12 GeV. A threshold in p_T of
 2733 the leading and sub-leading leptons is also required. Events where the two electrons
 2734 have invariant mass within 10 GeV of the Z boson mass (Z -veto) are discarded in
 2735 order to reject events from DY+jets production with charge misidentified electrons.
 2736 In addition, contribution from the associated production of two W bosons of equal
 2737 charge and two light jets $W^\pm W^\pm qq$ and from same-sign W boson pairs can also be
 2738 produced in double parton scattering (DPS) processes, where each of the colliding
 2739 protons gives two partons, resulting in two hard interactions.

2740 In the $3l$ lepton channel, leptons are required to have respectively $p_T > 25\text{GeV}, >$
 2741 $> 15\text{ GeV}$, and $> 15\text{ GeV}$. Events with an opposite-sign same-flavor lepton combination
 2742 (OSSF) with invariant mass within 15 GeV of the Z boson mass are discarded in order
 2743 to reject events from $WZ + \text{jets}$ production.

2744 6.7 Background modeling and predictions

2745 The dominant background contribution is expected to arise from top quark produc-
2746 tion processes, either $t\bar{t}$ pair production or in $t\bar{t}$ associated production with a W/Z.
2747 Processes with production of single top quarks also contribute, mainly in the associ-
2748 ated production with a Z boson (tZq) or when produced with both a W and a Z boson
2749 (tZW). Background contamination from diboson processes is strongly suppressed by
2750 imposing the Z-veto, vetoing additional leptons and requiring b -jets in the event.

2751 The selection criteria in Table 6.6 represent a relatively loose selection that allows
2752 to maintain a large signal efficiency while suppressing the main backgrounds; thus
2753 that selection is called *pre-selection*. The events obtained from the pre-selection are
2754 then used to extract the signal contribution in a second analysis step, using BDT dis-
2755 criminators against the main backgrounds of $t\bar{t}W/t\bar{t}Z$ and non-prompt leptons from
2756 $t\bar{t}$. The shape of the discriminator variables is then fit to the observed data distribu-
2757 tion to estimate the signal and background yields, simultaneously for all channels.

2758 Irreducible backgrounds are reliably estimated from MC simulated events; there-
2759 fore, in this analysis all backgrounds involving prompt leptons are estimated in this
2760 way. Reducible backgrounds, like non-prompt lepton backgrounds, are not well pre-
2761 dicted by simulation, hence, they are estimated using data-driven methods.

2762 6.7.1 $t\bar{t}V$ and diboson backgrounds

2763 Backgrounds from $t\bar{t}W$ and $t\bar{t}Z$ processes are estimated using simulated events, cor-
2764 rected for data/MC differences and inefficiencies (trigger and lepton selection) in the
2765 same way as signal events. Their production cross sections are calculated at NLO of
2766 QCD and EWK, considering theoretical uncertainties from unknown higher orders of
2767 12% for $t\bar{t}W$ and 10% for $t\bar{t}Z$. Additional uncertainties arise from the knowledge of

2768 PDFs and α_s of about 4% each for $t\bar{t}W$ and $t\bar{t}Z$.

2769 The diboson contribution is also estimated from simulated events; however, the
 2770 overall normalization of this process is obtained from a dedicated control region.
 2771 The motivation behind that strategy is that even though the measured inclusive
 2772 cross section for diboson processes (WZ, ZZ) is in good agreement with the NLO
 2773 calculations [149], that agreement is perturbed when leptonic Z decays and hadronic
 2774 jets in the final state are required; those requirements are precisely the ones that
 2775 make the diboson production a background for the tHq signal. Thus, by using a
 2776 dedicated control region dominated by WZ production⁴, the overall normalization is
 2777 constrained.

2778 The control region is defined by the presence of at least three leptons, of which
 2779 one opposite-sign pair must be compatible with a Z boson decay, i.e., invert the Z -
 2780 veto which makes the control region orthogonal to signal region; the b-jet tagging
 2781 requirements is also inverted with respect to the signal region, i.e., require two not
 2782 b -jets. A scale factor is extracted from the predicted distribution of WZ events in the
 2783 control region, and the observed data, while keeping other processes fixed; this factor
 2784 is used to scale the diboson prediction in the signal selection region. More details
 2785 about the procedure used can be found in Reference [149] from where the scale factor
 2786 is taken.

2787 In order to test the usability of the diboson background scale factor in this analysis,
 2788 a Z -enriched control region⁵ was defined by inverting the Z -veto and requiring exactly
 2789 three tight leptons with $p_T > 25/15/15$ GeV, one or more jets passing the CSVv2 loose
 2790 working point and less than four central jets. Figure 6.10 shows the distribution of
 2791 three variables in the diboson control region; the good agreement between MC and

⁴ ZZ background is strongly reduced by the cut on MET.

⁵ This control region is different to the one used to find the scale factor.

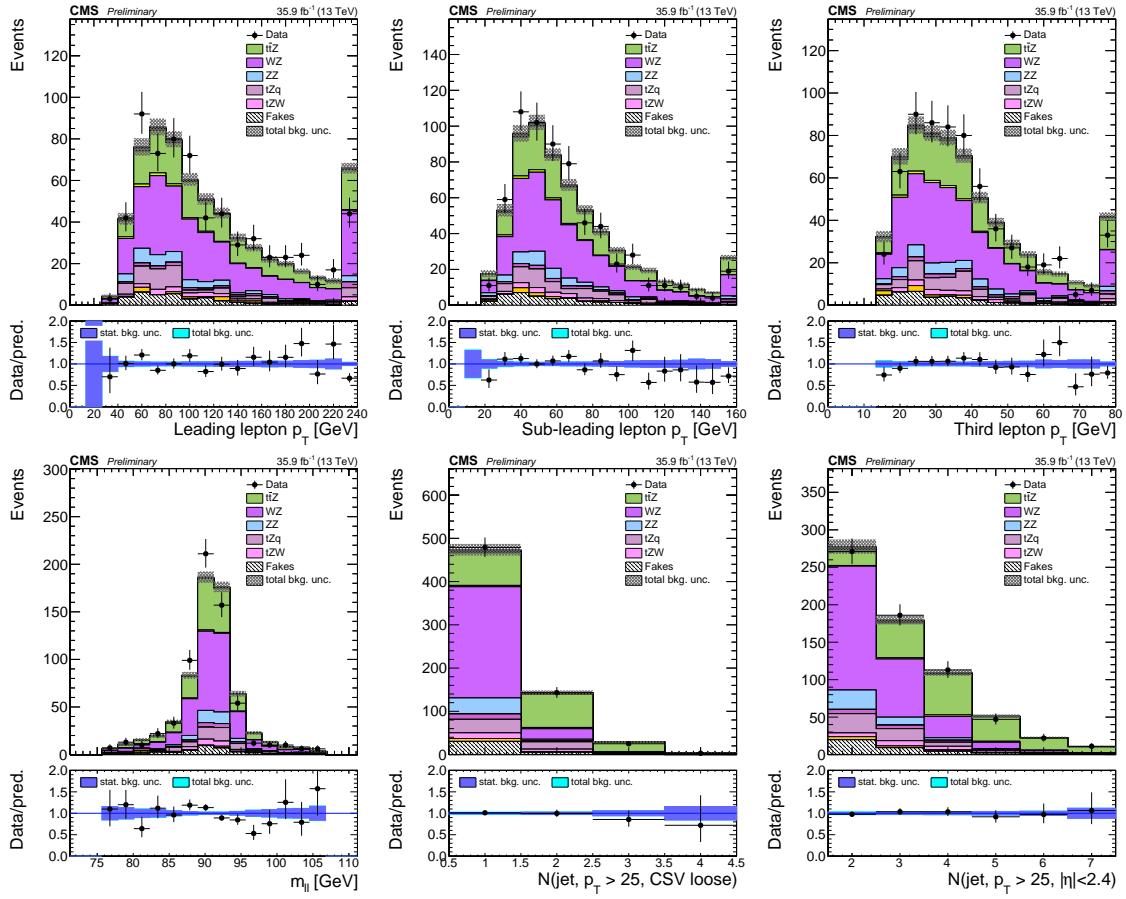


Figure 6.10: Kinematic distributions in the diboson control region.

2792 data motivates the adoption of the diboson background scale factor.

2793 Most of the diboson events passing the signal selection contain jets from light
 2794 quarks and gluons that are incorrectly tagged as b -jets; it makes the estimate mainly
 2795 sensitive to the experimental uncertainty in the mis-tag rate rather than the theore-
 2796 tical uncertainty in the jet flavor composition. The overall uncertainty assigned to
 2797 the diboson prediction is estimated from the statistical uncertainty due to the limited
 2798 sample size in the control region (30%), the residual background in the control region
 2799 (20%), the uncertainties on the b -tagging rate (10-40%), and from the knowledge of
 2800 PDFs and the theoretical uncertainties of the extrapolation (up to 10%).

2801 **6.7.2 Non-prompt and charge mis-ID backgrounds**

2802 The non-prompt lepton background contribution to the final selection is estimated
 2803 using the fake factor method. The main idea of the method is to define a control
 2804 region of events enriched in the background to estimate and determine a factor that
 2805 relates (extrapolates) these events to those in the signal region. The method is data-
 2806 driven in the sense that the control sample is selected from data, and the extrapolation
 2807 factor is measured from data.

2808 In the signal region of this analysis, non-prompt leptons are predominantly pro-
 2809 duced in $t\bar{t}$ events, with a much smaller contribution, from Drell-Yan production;
 2810 therefore, the control region also known as *application region*, is defined by modifying
 2811 the event selection criteria in such a way that most of the events after selection are
 2812 $t\bar{t}$ events and thus the misidentification rate is increased. The application regions
 2813 for electrons and muons are defined by the *fakeable* object definitions in Tables 6.4
 2814 and 6.5. Since the *fakeable* definition is a loosened version of the tight definition, in
 2815 the context of fake rates, the *fakeable* definition becomes the loose selection.

2816 The ratio between the number of events that pass both, the loose and tight se-
 2817 lections, and the number of events that pass the loose selection but fail the tight
 2818 one, corresponds to the *loose-to-tight ratio or fake factor/rate (f)*. The measurement
 2819 of the fake factor is made using two background dominated data samples, collected
 2820 with dedicated triggers, as a function of p_T and $|\eta|$ and separately for muons and
 2821 electrons:

- 2822 • A sample dominated by QCD multijet events, collected using single lepton trig-
 2823 gers at relatively high p_T thresholds. It is used to extract ratios for lepton
 2824 candidates with p_T above 30 GeV.
- 2825 • A sample dominated by Z + jets events, where the two high p_T leptons resulting

2826 from the Z decay are used to trigger the events without biasing the p_T spectrum
 2827 of a third lepton at low transverse momentum. It is used to determine the ratios
 2828 for low p_T leptons.

2829 Processes like $W + \text{jets}$, $Z + \text{jets}$, WZ and ZZ produce prompt leptons that
 2830 contaminate the samples; thus, they are suppressed by vetoing additional leptons in
 2831 the selection, and the residual contamination is then subtracted using the transverse
 2832 mass as a discriminating variable.

2833 The extrapolation from the application region to the signal region is performed
 2834 by weighting the events in the application region using the fake factor according to
 2835 the following rules:

- 2836 • events with one lepton failing the tight criteria are weighted with the factor
 2837 $\frac{f}{(1-f)}$ for the estimate to the signal region.
- 2838 • events with two leptons (i,j) failing the tight criteria are weighted with the factor
 2839 $-\frac{f_i f_j}{(1-f_i)(1-f_j)}$ for the estimate to the signal region.
- 2840 • events with three leptons (i,j,k) failing the tight criteria are weighted with the
 2841 factor $\frac{f_i f_j f_k}{(1-f_i)(1-f_j)(1-f_k)}$ for the estimate to the signal region.

2842 Figure 6.11 shows the fake rates for electrons and muons used in this analysis
 2843 which were taken from the studies in Reference [149].

2844 The resulting prediction of the event yield in the signal selection carries an uncer-
 2845 tainty of 30-50% which is composed of the statistical uncertainty in the measurement
 2846 of the fake rates due to prescaling of lepton triggers, the uncertainty in the subtraction
 2847 of residual prompt leptons from the control region, and from testing the closure of the
 2848 method in simulated background events; hence, it is one of the dominant limitations
 2849 on the performance of multilepton analyses in general and this analysis in particular.

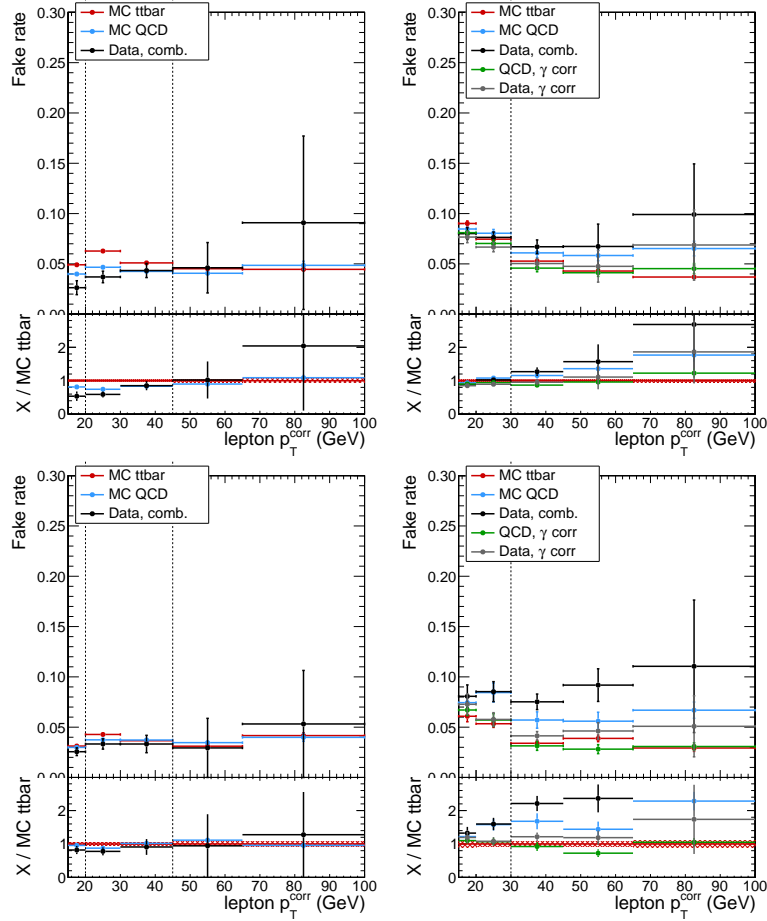


Figure 6.11: Fake rate measurement in events in data for muons (left column) and electrons (right column). Predictions from simulated events in the measurement region (blue) and from non-prompt leptons in $t\bar{t}$ (red) are included for comparison. Top row is for $|\eta| < 2.5$ and bottom row for $|\eta| > 2.5$.

Finally, an additional source of background arises in the $2lss$ channel from events with an originally opposite-sign lepton pair for which the charge of one of the leptons is misidentified (*charge mis-ID*); usually this happens because of the conversion of hard bremsstrahlung photons emitted from the initial lepton, hence, it is more likely to happen for electrons than for muons.

The charge mis-ID background is estimated from the yield of opposite-sign event in the signal region by measuring the charge mis-ID probability in same-sign and opposite-sign events compatible with a Z boson decay, in several bins of p_T and η ,

and weighting events with opposite-sign leptons in the signal selection.

Data	$10 \leq p_T < 25$ GeV	$25 \leq p_T < 50$ GeV	$50 \text{ GeV} \leq p_T$
$0 \leq \eta < 1.48$	0.0442 ± 0.0011	0.0179 ± 0.0004	0.0262 ± 0.0020
$1.48 \leq \eta < 2.5$	0.1329 ± 0.0066	0.1898 ± 0.0014	0.3067 ± 0.0113
MC			
$0 \leq \eta < 1.48$	0.0378 ± 0.0016	0.0222 ± 0.0003	0.0233 ± 0.0015
$1.48 \leq \eta < 2.5$	0.0956 ± 0.0044	0.2108 ± 0.0027	0.3157 ± 0.0018

Table 6.7: Electron charge mis-ID probabilities (in percent), determined in data (top) and Drell-Yan MC (bottom) [149].

The charge mis-ID probability is found to be negligible for this analysis for muons, whereas for electrons it ranges from about 0.02% in the barrel section ($|\eta| < 1.48$) up to about 0.35% in the detector endcaps ($1.48 < |\eta| < 2.5$). as shown in Table 6.7 and Figure 6.12.

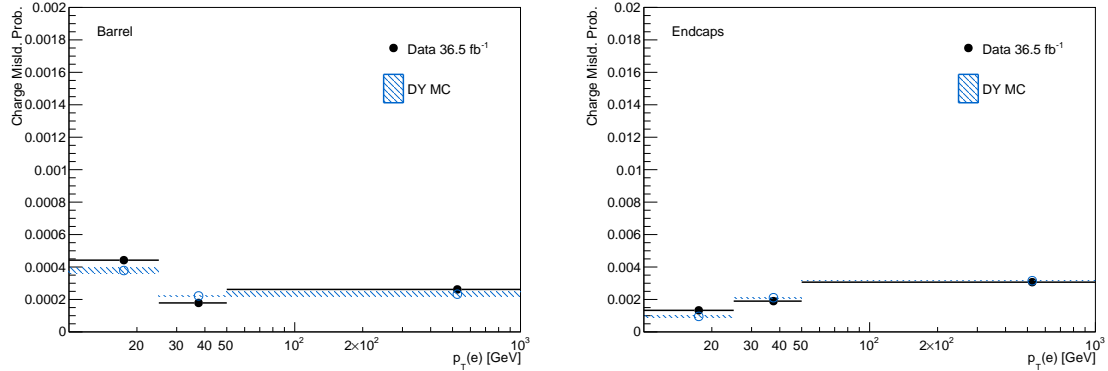


Figure 6.12: Electron charge mis-ID probabilities as a function of p_T for $|\eta| < 2.5$ (left) and $|\eta| < 2.5$ (right) [149].

The contribution from charge mis-ID electrons in signal selection of this analysis comes mainly from $t\bar{t}$ and Drell-Yan events. The systematic uncertainty of the normalization of the charge mis-ID estimate is evaluated at about 30%, arising from a slight disagreement of the mis-ID probability between data and simulation. Given that it only affects the $e\mu$ channel, its impact on the final sensitivity is very limited.

2868 6.8 Pre-selection yields

2869 The expected and observed event yields of the pre-selection are shown in Table 6.8;
 2870 Figure 6.13 shows the distributions of some relevant kinematic variables, normalized
 2871 to the cross section of the respective processes and to the integrated luminosity. The
 2872 remaining variables distributions are shown in Appendix B.1.

	3ℓ	$\mu^\pm \mu^\pm$	$e^\pm \mu^\pm$
$t\bar{t}W$	22.50 ± 0.35	68.03 ± 0.61	97.00 ± 0.71
$t\bar{t}Z/\gamma^*$	32.80 ± 1.79	25.89 ± 1.12	64.82 ± 2.42
WZ	8.22 ± 0.86	15.07 ± 1.19	26.25 ± 1.57
ZZ	1.62 ± 0.33	1.16 ± 0.29	2.86 ± 0.45
$W^\pm W^\pm qq$	–	3.96 ± 0.52	6.99 ± 0.69
$W^\pm W^\pm(\text{DPS})$	–	2.48 ± 0.42	4.17 ± 0.54
VVV	0.42 ± 0.16	2.99 ± 0.34	4.85 ± 0.43
ttt	1.84 ± 0.44	2.32 ± 0.45	4.06 ± 0.57
tZq	3.92 ± 1.48	5.77 ± 2.24	10.73 ± 3.03
tZW	1.70 ± 0.12	2.13 ± 0.13	3.91 ± 0.18
γ conversions	7.43 ± 1.94	–	23.81 ± 6.04
Non-prompt	25.61 ± 1.26	80.94 ± 2.02	135.34 ± 2.83
Charge mis-ID	–	–	58.50 ± 0.31
All backgrounds	106.05 ± 3.45	210.74 ± 3.61	443.30 ± 8.01
tHq ($\kappa_t = -1.0$)	7.48 ± 0.14	18.48 ± 0.22	27.41 ± 0.27
tHW ($\kappa_V = -1.0$)	7.38 ± 0.16	7.72 ± 0.17	11.23 ± 0.20
$t\bar{t}H$	18.29 ± 0.41	24.18 ± 0.48	35.21 ± 0.58
Data ($35.9 fb^{-1}$)	127	280	525

Table 6.8: Expected and observed yields for $35.9 fb^{-1}$ after the pre-selection in all final states. Uncertainties are statistical only.

2873 For the tH and $t\bar{t}H$ processes, the largest contribution comes from Higgs decays
 2874 to WW (about 75%), followed by $\tau\tau$ (about 20%) and ZZ (about 5%). Other Higgs
 2875 production modes contribute negligible event yields (< 5% of the $tH+t\bar{t}H$ yield) as
 2876 shown in Table 6.9.

2877 A significant fraction of selected data events (about 50% in the dilepton channels,
 2878 and about 80% in the trilepton channel) also passes the selection used in the dedicated

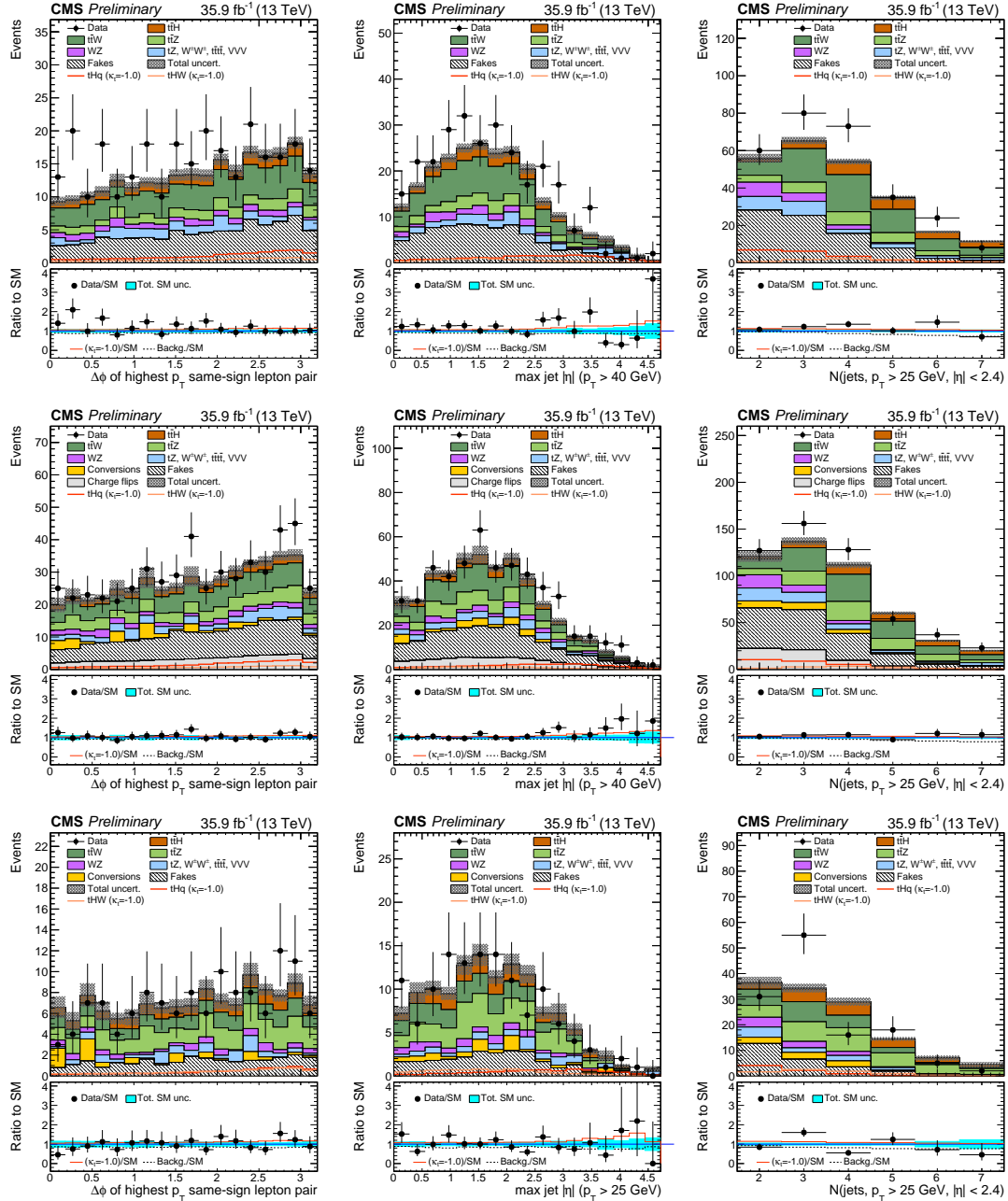


Figure 6.13: Distributions of discriminating variables for the event pre-selection for the same-sign $\mu^{\pm}\mu^{\pm}$ channel (top row), the same-sign $e^{\pm}\mu^{\pm}$ channel (middle row) and three lepton channel (bottom row), normalized to 35.9 fb^{-1} , before fitting the signal discriminant to the observed data. Uncertainties are statistical and unconstrained (pre-fit) normalization systematics. The shape of the two tH signals for $\kappa_t = -1.0$ is shown, normalized to their respective cross sections for $\kappa_t = -1.0, \kappa_V = 1.0$.

	3ℓ	$\mu^\pm\mu^\pm$	
tHq (Inclusive)	6.57	100.0%	17.38 100.0%
$tHq(H \rightarrow WW)$	4.84	73.9%	13.33 76.9%
$tHq(H \rightarrow \tau\tau)$	1.04	15.9%	3.62 20.6%
$tHq(H \rightarrow ZZ)$	0.48	7.2%	0.37 2.2%
$tHq(H \rightarrow \mu\mu)$	0.21	3.0%	0.04 0.2%
$tHq(H \rightarrow \gamma\gamma)$	< 0.01	0.1%	0.02 0.1%
$tHq(H \rightarrow bb)$	< 0.01	< 0.1%	0.01 < 0.1%
tHW (Inclusive)	7.32	100.0%	7.62 100.0%
$tHW(H \rightarrow WW)$	5.50	76.9%	5.60 74.1%
$tHW(H \rightarrow \tau\tau)$	1.40	20.6%	1.81 23.1%
$tHW(H \rightarrow ZZ)$	0.31	2.2%	0.21 2.7%
$tHW(H \rightarrow \mu\mu)$	0.12	0.2%	0.01 0.1%
$tHW(H \rightarrow \gamma\gamma)$	< 0.01	< 0.1%	< 0.01 < 0.1%
$tHW(H \rightarrow bb)$	< 0.01	< 0.1%	< 0.01 < 0.1%

Table 6.9: Signal yields split by decay channels of the Higgs boson. Forward jet p_T cut at 25 GeV.

2879 search for $t\bar{t}H$ in multilepton channels [149]. This is particularly important when
 2880 considering a possible combination of the measurements from both studies. More
 2881 details about the overlap between these two analyses are presented in Appendix E.

2882 6.9 Signal discrimination

2883 The production cross section for the signal processes tHq , tHW , and $t\bar{t}H$ is only
 2884 about 600 fb (the enhancement provided by inverted couplings, $\kappa_t = -1$ almost double
 2885 it), resulting in a small signal to background ratio even for a tight selection. A
 2886 multivariate method is hence employed to train discriminators to separate tH signal
 2887 events from the dominant background events.

2888 **6.9.1 MVA classifiers evaluation**

2889 Several MVA classifier algorithms were evaluated in order to determine the most
 2890 appropriate method for this analysis⁶. The comparison is based on the performance
 2891 of the classifiers, encoded in the plot of the background rejection as a function of the
 2892 signal efficiency (ROC curve). The top row of Figure 6.14 shows the ROC curves for
 2893 evaluated methods; two separated training were performed in the $3l$ channel: against
 2894 $t\bar{t}$ (right) and $t\bar{t}V$ (left) processes.

2895 In both cases, the gradient boosted decision tree *BDTG* (*BDTA_GRAD* in the
 2896 plot) classifier offers the best results, followed by the adaptive BDT classifier (*BDTA*);
 2897 the several Fisher classifiers tested, which differ in their parameters and/or boosting
 2898 method, they offer similar performance among them, while the k-Nearest Neighbour
 2899 (kNN) classifier performance is below the rest of the classifiers. The corresponding
 2900 ROC curves and in the $2lss$ channel for trainings against $t\bar{t}V$ (left) and $t\bar{t}$ (right)
 2901 processes are shown in the bottom row of Figure 6.14; the BDTG performance is
 2902 similar to that in the $3l$ channel.

2903 **6.9.2 Discriminating variables**

2904 The classifier chosen to separate the tHq signal from the main backgrounds is the
 2905 *BDTG* classifier, trained on simulated signal and background events. The samples
 2906 used in the training are the tHq sample in Table 6.2, the samples in the third section
 2907 of Table A.4 and the samples marked with an * in the same table.

2908 As explained in Section 5.1.1, a set of discriminating variables are given as input to
 2909 the *BDTG* which combines the individual discrimination power of each input variable

⁶ The choice of the tested algorithms was based on the recommendations provided by the official TMVA user guide, the experience from previous analyses and considering the expertise of the members of the tHq and $t\bar{t}H$ analyses groups. Only the BDT classifier is described in this thesis and a detailed description of all available methods can be found in Reference [127]

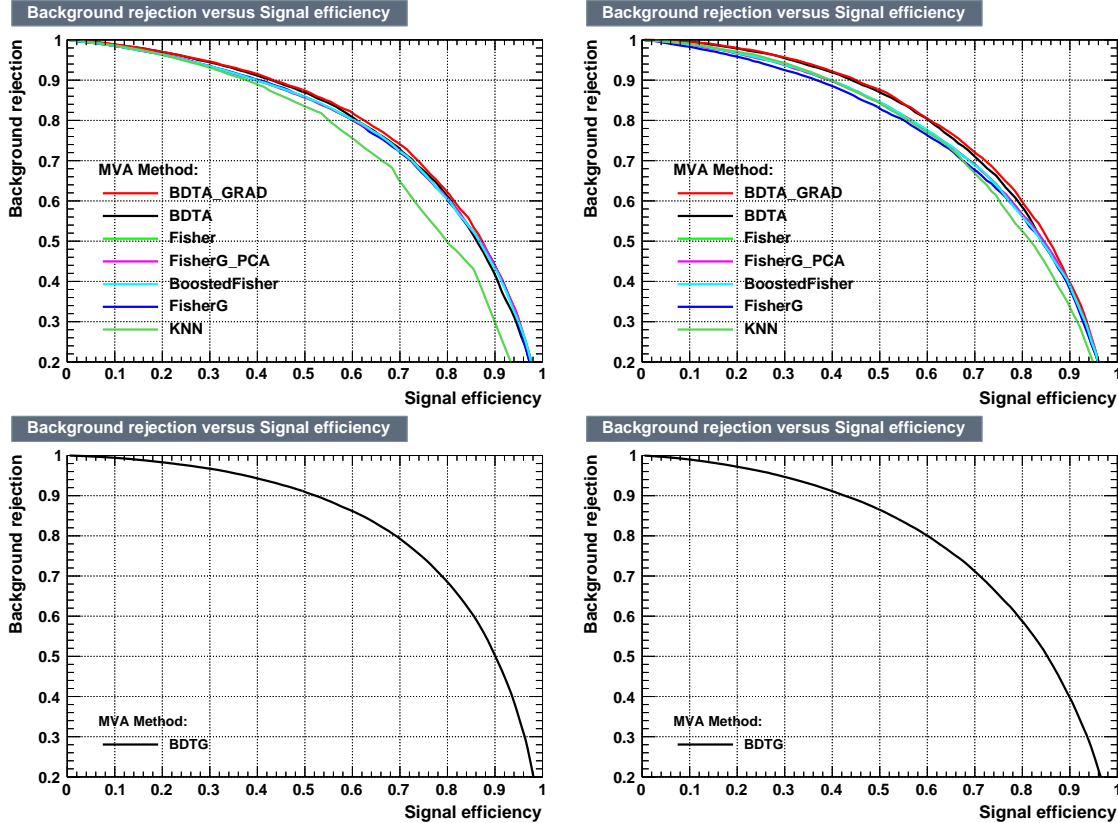


Figure 6.14: Top: Background rejection vs signal efficiency (ROC curves) for various MVA classifiers in the $3l$ channel for training against $t\bar{t}V$ (left) and $t\bar{t}$ (right). Bottom: background rejection vs signal efficiency (ROC curve) in the $2lss$ channel for a single discriminator: BDTG, against $t\bar{t}V$ (left) and $t\bar{t}$ (right).

2910 to produce a discriminator with the maximum discrimination power. Table 6.10 lists
 2911 the input variables used in the BDTG trainings for this analysis. The same set of
 2912 input variables was used to produce the plots for MVA classifiers evaluation.

2913 Plots in Figure 6.15 shows the BDTG input variables distributions for the signal
 2914 and background samples, in the $3l$ channels.

2915 All the input variables have some discrimination power, however, that power is
 2916 bigger for some of them; for instance, the third lepton p_T plot (top left in Figure 6.15)
 2917 shows some discrimination power against WZ and VVV backgrounds for which there
 2918 is a peak around 30 GeV while tHq peak around 18 GeV; although the discrimination

Variable name	Description
nJet25	Number of jets with $p_T > 25$ GeV, $ \eta < 2.4$
nJetEta1	Number of jets with $ \eta > 1.0$, non-CSV-loose
MaxEtaJet25	Max. $ \eta $ of any (non-CSV-loose) jet with $p_T > 25$ GeV
deltaFwdJetClosestLep	$\Delta\eta$ forward light jet and closest lepton
deltaFwdJetBJet	$\Delta\eta$ forward light jet and hardest CSV loose jet
deltaFwdJet2BJet	$\Delta\eta$ forward light jet and second hardest CSV loose jet
Lep3Pt/Lep2Pt	p_T of the 3 rd lepton (2 nd for ss2l)
totCharge	Sum of lepton charges
minDRll	Min ΔR any two leptons
dphiHighestPtSSPair	$\Delta\phi$ of highest p_T same-sign lepton pair

Table 6.10: BDTG input variables. First section lists variables related to jet multiplicities; second section lists variables related to forward jet activity, and third section lists variables related to lepton kinematics.

2919 power does not cover all the backgrounds, it counts for the final discriminator. A
 2920 similar situation can be seen in the plot for the number of jets (row three, column two);
 2921 $t\bar{t}W$, $t\bar{t}Z$ and $t\bar{t}H$ processes tend to have more jets compared to the tHq process. The
 2922 discrimination power is more evident in other plots like in the plot of the maximum
 2923 $|\eta|$ of the jets in the event (row two, column three). The same or equivalent input
 2924 variables are found to be performing well for both $3l$ and $2lss$ channels. Figure B.4
 2925 shows the corresponding input variables distribution plots for the $2lss$ channel.

2926 Discrimination power from BDTG classifier

2927 The Discrimination power of the input variables can also be evaluated from the BDTG
 2928 training, exclusively for the training samples, i.e., dominant backgrounds ($t\bar{t}$ and $t\bar{t}V$);
 2929 the training samples are submitted to the selection cuts on Table 6.6.

2930 Figure 6.16 shows the comparison between input variables for the two trainings
 2931 in the $3l$ channel; it reveals that some variables show opposite behavior for the two
 2932 background sources, which results in potentially screening the discrimination power
 2933 if they were to be used in a single discriminant, i.e., if the training would join $t\bar{t}$ and

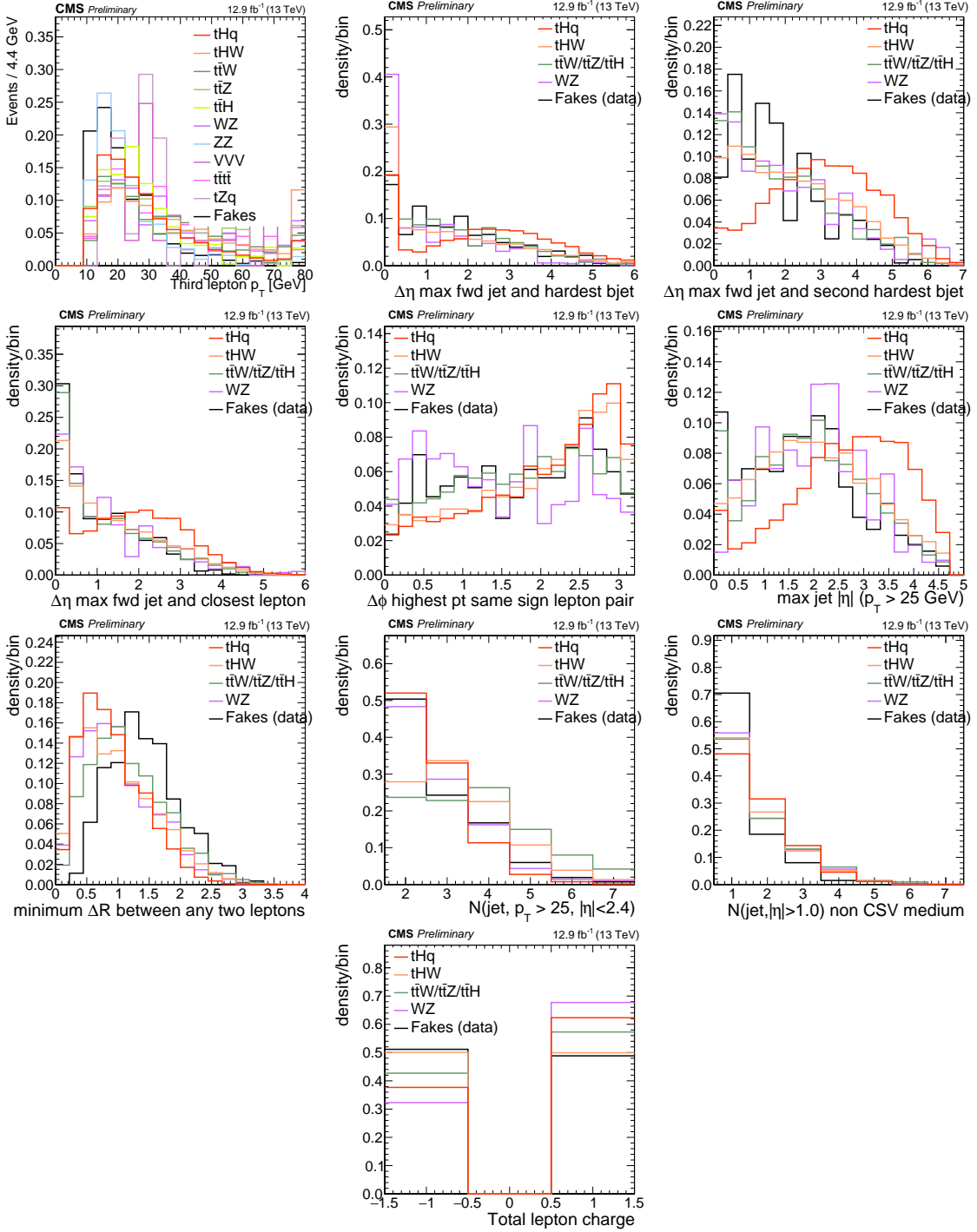


Figure 6.15: Distributions of the BDTG classifier input variables (not normalized) for signal discrimination in the $3l$ channel.

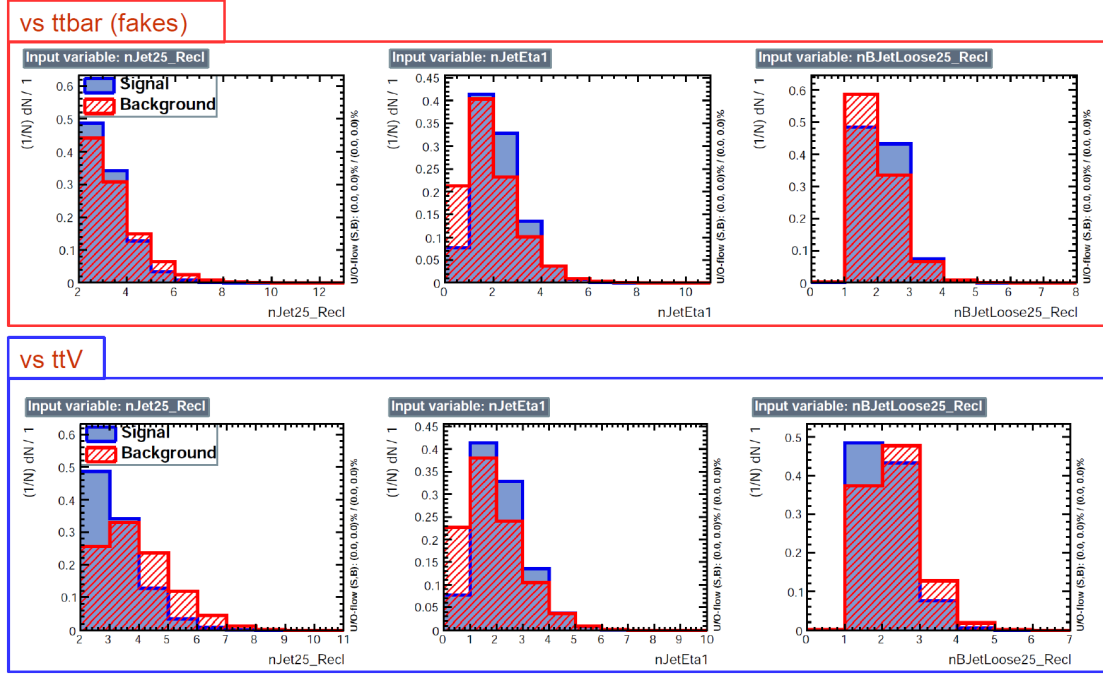


Figure 6.16: BDT input variables as seen by BDTG classifier for the $3l$ channel, tHq signal(blue) discriminated against $t\bar{t}V$ background (red).

2934 $t\bar{t}V$. For some other variables the distributions are similar in both background cases.

2935 In contrast to the distributions in Figure 6.15 only the dominant backgrounds are
2936 included; however, the discrimination power agrees among plots.

2937 Figures in the Appendix B.5, B.6, B.7, and B.8 show the input variables
2938 distributions for the $2lss$ and $3l$ channel as seen by the BDTG classifier.

2939 Input variables correlations

2940 From Table 6.10, it is clear that the input variables are correlated to some extent.
2941 These correlations play an important role for some MVA methods like the Fisher
2942 discriminant method in which the first step consist of performing a linear transfor-
2943 mation to an phase space where the correlations between variables are removed. In
2944 the case of BDT, correlations do not affect the performance. Figure 6.17 shows the

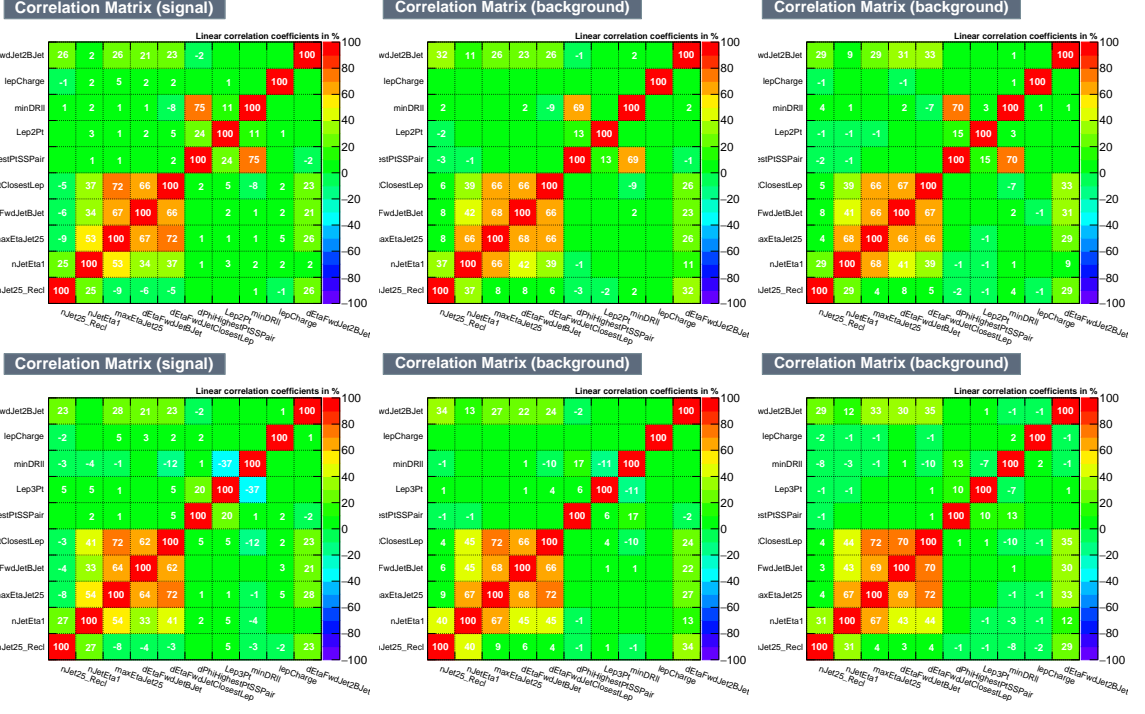


Figure 6.17: Signal (left), $t\bar{t}$ background (middle), and $t\bar{t}V$ background (right.) correlation matrices for the input variables in the BDTG classifier for the $2lss$ (top) and $3l$ (bottom) channels.

2945 linear correlation coefficients for signal and background for the two training cases (the
 2946 signal values are identical by construction). As expected, strong correlations appears
 2947 for variables related to the forward jet activity.

2948 6.9.3 BDTG classifiers response

2949 After the training stage, the BDTG classifier is tested to ensure its ability to discrim-
 2950 inate between simulated signal and background events. The BDTG classifier output
 2951 distributions for signal and backgrounds in the $3l$ channel are shown in Figure 6.18.
 2952 As expected, a good discrimination power is obtained using default discriminator
 2953 parameter values; some overtraining is also visible.

2954 In order to explore further optimization in the BDTG performance, several changes

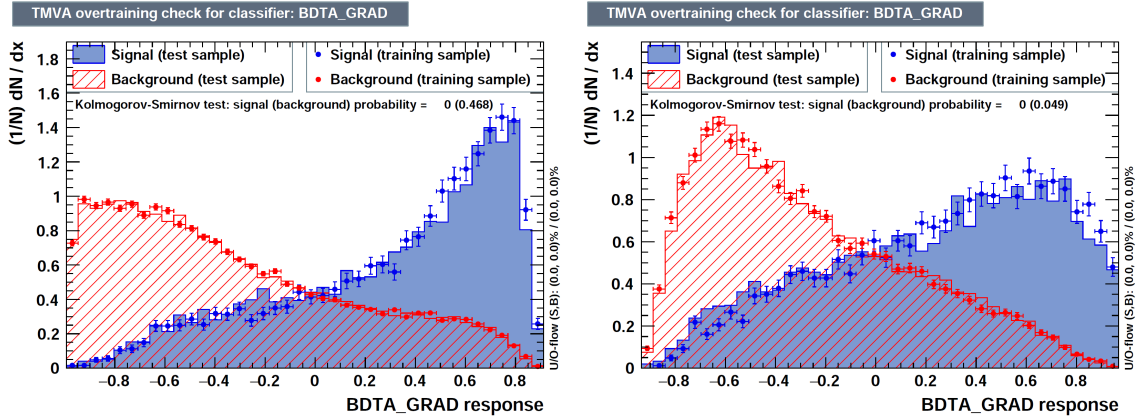


Figure 6.18: BDTG classifier output for trainings against $t\bar{t}V$ (left) and $t\bar{t}$ (right). Default BDTG parameters have been used.

from the default BDTG parameters were tested; Table 6.11 list the set of parameters found to be most discriminant with minimal overtraining as shown in Figure 6.19.

TMVA.Types.kBDT		
Option	Default	Used
NTrees	200	800
BoostType	AdaBoost	Grad
Shrinkage	1	0.1
nCuts	20	50
MaxDepth	3	

Table 6.11: Configuration used in the final BDTG training. Parameters not listed were not tested.

The ranking of the input variables by their importance in the classification process is shown in Table 6.12; for both trainings the rankings show almost the same five variables in the first places.

6.9.4 Additional discriminating variables

Given that the forward jet in background processes could be originated from pileup, two additional discriminating variables accounting for that were tested. These additional variables describe the forward jet momentum (`fwdJetPt25`) and the forward

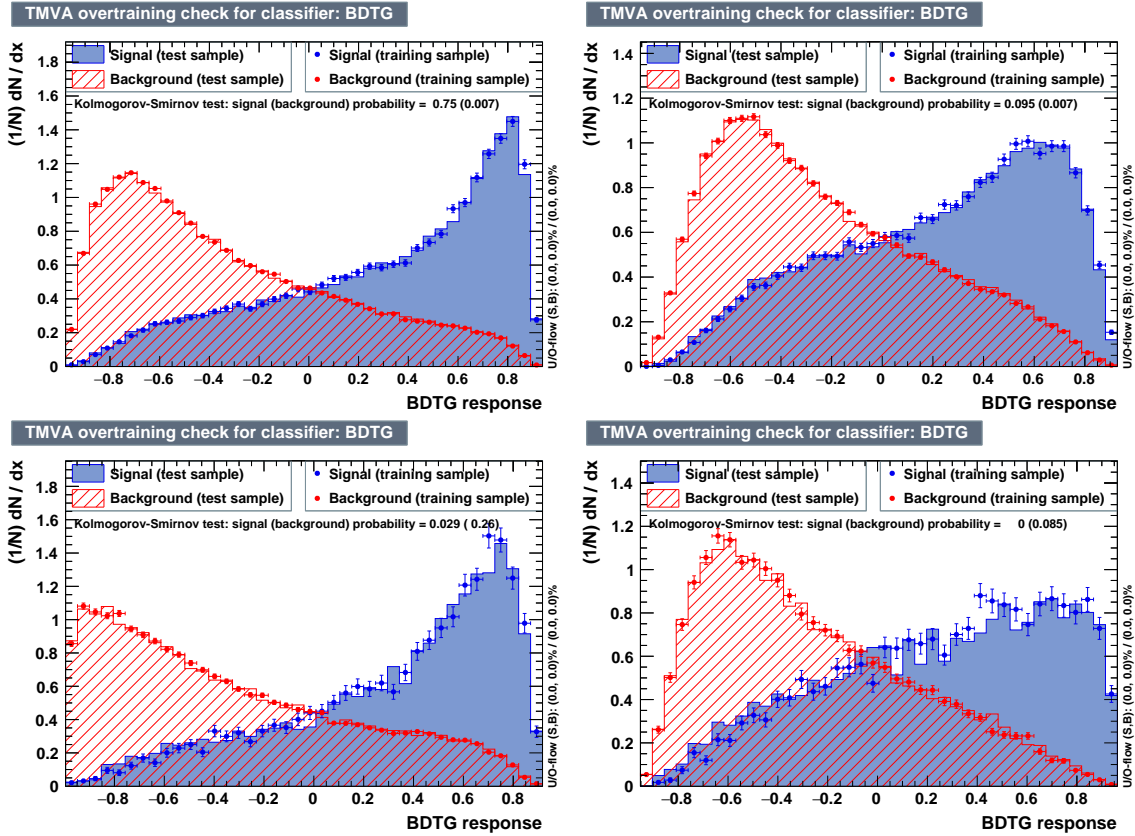


Figure 6.19: BDTG classifiers output for training against $t\bar{t}V$ (left) and $t\bar{t}$ (right) for $2lss$ channel(top) and $3l$ channel (bottom) .

2964 jet identification (fwdJetPUID); their distributions in the $3l$ channel are shown in
 2965 Figure 6.20. The forward jet identification distribution shows that for both, signal
 2966 and background, jets are mostly originated in the primary vertex.

2967 The testing was performed by including in the BDTG input one variable at a
 2968 time, so the discrimination power of each variable can be evaluated individually, and
 2969 then both simultaneously. fwdJetPUID was ranked the last place in importance (11)
 2970 in both training ($t\bar{t}V$ and $t\bar{t}$) while fwdJetPt25 was ranked 3 in the $t\bar{t}V$ training and
 2971 7 in the $t\bar{t}$ training. When training using 12 variables, fwdJetPt25 was ranked 5 and
 2972 7 in the $t\bar{t}V$ and $t\bar{t}$ trainings respectively, while fwdJetPUID was ranked 12 in both
 2973 cases.

Rank	$t\bar{t}$ training	$t\bar{t}V$ training
	Variable	Variable
1	minDRll	dEtaFwdJetBJet
2	dEtaFwdJetClosestLep	Lep3Pt
3	dEtaFwdJetBJet	maxEtaJet25
4	dPhiHighestPtSSPair	dEtaFwdJet2BJet
5	Lep3Pt	dEtaFwdJetClosestLep
6	maxEtaJet25	minDRll
7	dEtaFwdJet2BJet	dPhiHighestPtSSPair
8	nJetEta1	nJet25_Recl
9	nJet25_Recl	nJetEta1
10	lepCharge	lepCharge
1	dEtaFwdJetClosestLep	maxEtaJet25
2	minDRll	dEtaFwdJet2BJet
3	maxEtaJet25	dEtaFwdJetBJet
4	dPhiHighestPtSSPair	Lep2Pt
5	Lep2Pt	dEtaFwdJetClosestLep
6	dEtaFwdJetBJet	minDRll
7	dEtaFwdJet2BJet	nJet25_Recl
8	nJetEta1	dPhiHighestPtSSPair
9	nJet25	nJetEta1
10	lepCharge	lepCharge

Table 6.12: Input variables ranking for BDTG classifiers for the trainings in the $2lss$ channel (first section) and $3l$ channel (second section). For both trainings the rankings show almost the same five variables in the first places.

2974 The improvement in the discrimination performance provided by the additional
 2975 variables is about 1%, so it was decided not to include them in the procedure. Table
 2976 6.13 shows the ROC-integral for all the testing cases performed.

	ROC-integral	
	$t\bar{t}V$	$t\bar{t}$
base 10 var	0.848	0.777
+ fwdJetPUID	0.849	0.777
+ fwdJetPt25	0.856	0.787
12 var	0.856	0.787

Table 6.13: ROC-integral for all the testing cases performed in the evaluation of the additional variables discriminating power. The improvement in the discrimination performance provided by the additional variables is about 1% .

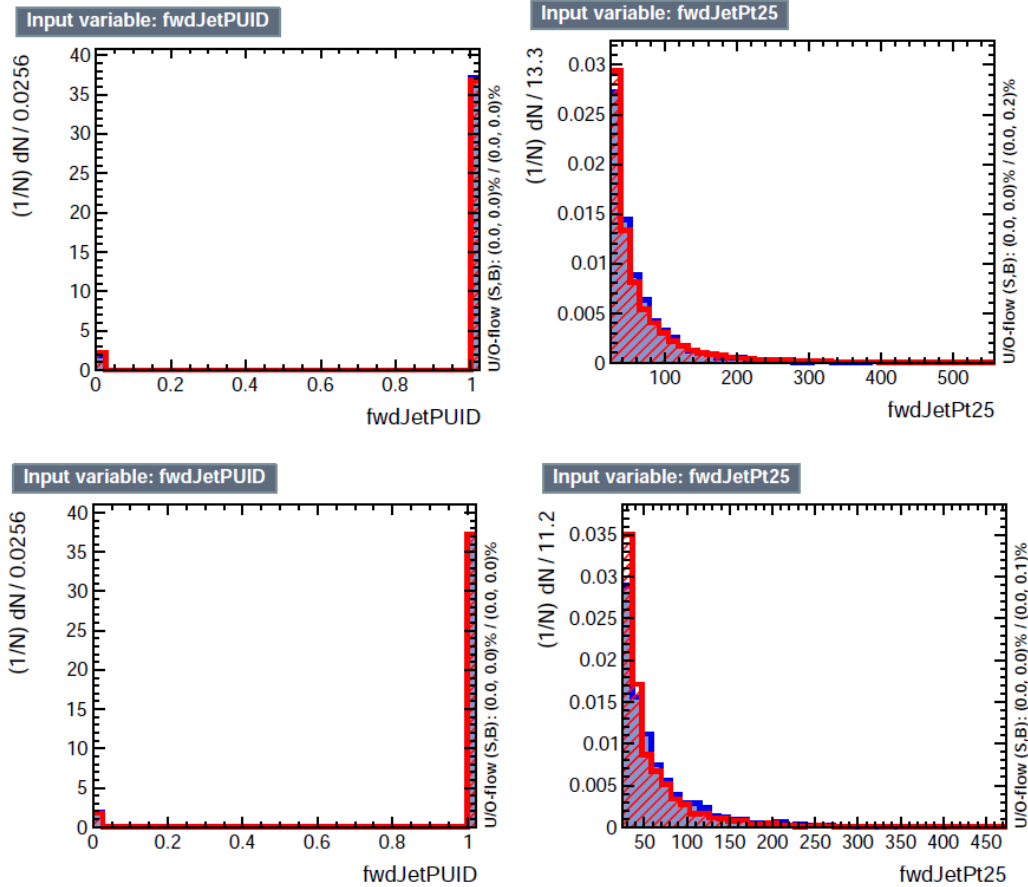


Figure 6.20: Additional discriminating variables distributions for $t\bar{t}V$ training (top row) and $t\bar{t}$ training (bottom row) in the $3l$ channel. The origin of the jets in the forward jet identification distribution is tagged as 0 for *pileup jets* while *primary vertex jets* are tagged as 1.

2977 6.9.5 Signal extraction procedure

2978 Once the two BDTG classifiers, introduced in the previous section, are trained against
 2979 the dominant backgrounds in each channel, they are used to classify the events in the
 2980 samples; their outputs are then used to evaluate the signal cross section limits in a
 2981 fit to the classifier shape. Figure 6.21 shows the expected output distributions in a
 2982 2D plane of one training vs. the other, i.e., $t\bar{t}V$ vs. $t\bar{t}$. Top row shows the 2D planes
 2983 for tHq and tHW signals, while the bottom left plot shows the corresponding 2D

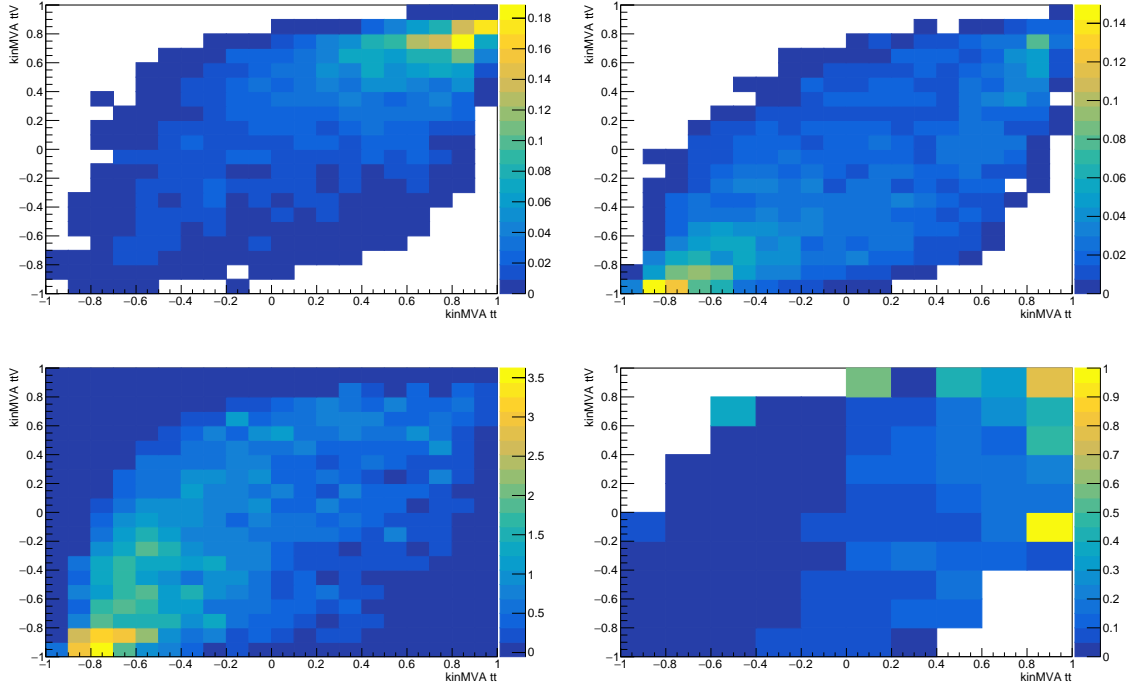


Figure 6.21: BDT classifier output planes (training vs $t\bar{t}$ on x-axis and vs $t\bar{t}V$ on y-axis) for the tHq and tHW signals (top row), and for the combined backgrounds (bottom left). Bottom right: S/B ratio (combining tHq and tHW) in the same plane. Plots are for $3l$ channel.

2984 plane for the combined backgrounds, which are evaluated as in the final background
 2985 prediction, i.e., these are not the samples used in the BDTG training and this includes
 2986 data-driven backgrounds. The signal (combining of tHq and tHW) to background
 2987 ratio (S/B) is showed in the bottom right plot of Figure 6.21.

2988 Each event is now classified into one of ten 2D-bins according to its position in the
 2989 plane, as shown in Figure 6.22. The number of bins is chosen such that no bins are
 2990 entirely empty for any process. The bin boundary positions and number of bins have
 2991 been studied and optimized with respect to the expected limit on the signal strength
 2992 (see Sec. 6.9.6).

2993 From this event categorization, a 1D histogram of expected distribution is pro-
 2994 duced for each signal and background process, and fit to the observed data (or the

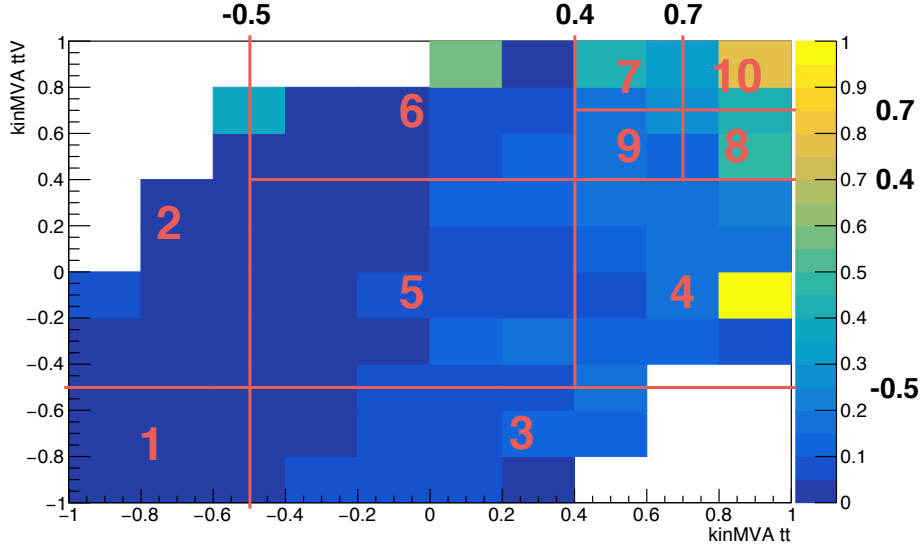


Figure 6.22: Binning overlaid on the S/B ratio map on the plane of classifier outputs.

2995 Asimov dataset for expected limits).

2996 6.9.6 Binning and selection optimization

2997 The effect of the choice of pre-selection cuts and the number of bins of the 1D his-
 2998 togram on the cross section limit is evaluated by varying the most important cuts and
 2999 re-calculating the limit in each case. In this analysis, the optimization was performed
 3000 in the $3l$ channel, by evaluating the upper limits on the $tHq + tHW$ expected signal
 3001 strength only (without $t\bar{t}H$ component), always evaluated at $\kappa_t = -1.0$, $\kappa_V = 1.0$.

3002 Table 6.14 shows several explored variations, compared with a baseline; the base-
 3003 line is similar to the selection reported in Table 6.6 but only a loose CSV jet and a Z
 3004 veto of ± 10 GeV are required.

3005 The optimal limit is found when requiring a slightly tighter selection with respect
 3006 to the baseline. The optimal selection is reported in Table 6.6.

3007 The signal strength limit also depends on the chosen binning in the 2D plane as
 3008 the S/B ratio varies across the plane, hence, several sizes and binning combinations

Selection	Variation	Expected limit
Baseline		< 2.93
Loose CSV tags	$\geq 1 \rightarrow \geq 2$	< 3.81
Medium CSV tags	$\geq 0 \rightarrow \geq 1$	< 2.76
Light forward jet η	$\geq 0 \rightarrow \geq 1$	< 2.94
Light forward jet η	$\geq 0 \rightarrow \geq 1.5$	< 3.00
MET > 30 GeV		< 2.91
Z veto ($ m_{\ell\ell} - m_Z $)	$> 10 \text{ GeV} \rightarrow > 15 \text{ GeV}$	< 2.79
One medium CSV + 15 GeV Z veto	combined	< 2.62

Table 6.14: Signal strength limit variation as a function of tighter cuts. The baseline selection corresponds to a looser selection compared to the one reported in Table 6.6 where only a CSV-loose b -jet is required, and the Z veto is loosened to ± 10 GeV. The optimal selection determined here corresponds to the baseline plus the two variations in the last row.

were tested in order to improve the limit. Figure 6.23 shows some of the binning combinations tested; in the default combination all the bins have the same size, while the best limit was found for a set of 10 bins. The bin borders and the resulting limits are shown in Table 6.15.

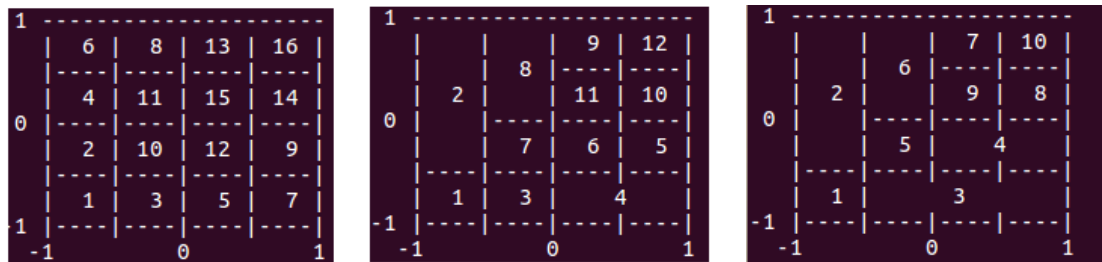


Figure 6.23: Binning combination scheme.

Combining the optimization of binning and using the tighter pre-selection cuts, the expected limit in the $3l$ channel alone reaches $r < 2.59$.

A similar binning optimization was made for $2lss$ channel, including other binning combinations. First, the $3l$ channel binning was used to estimate the expected limit, then, bin borders were varied to obtain the best possible expected limit. The bin

Number of bins	Bin borders						Expected limit
	x_1	x_2	x_3	y_1	y_2	y_3	
16 (default)	-0.5	0.0	0.5	-0.5	0.0	0.5	< 2.91
16	-0.5	0.3	0.7	-0.5	0.3	0.7	< 2.83
10	-0.5	0.0	0.5	-0.5	0.0	0.5	< 2.93
10	-0.5	0.0	0.7	-0.5	0.0	0.7	< 2.86
10	-0.5	0.0	0.7	-0.5	0.0	0.5	< 2.84
10	-0.5	0.0	0.5	-0.5	0.0	0.7	< 2.87
10	-0.5	0.4	0.7	-0.5	0.4	0.7	< 2.81

Table 6.15: Limit variation as a function of bin size. The final bin borders used in the $3l$ channel are indicated in bold.

3018 borders and the resulting signal strength limits for the same-sign dimuon channel are
 3019 shown in Table 6.16.

Number of bins	Bin borders						Expected limit
	x_1	x_2	x_3	y_1	y_2	y_3	
16	-0.5	0.4	0.7	-0.5	0.4	0.7	< 1.72
12	-0.5	0.4	0.7	-0.5	0.4	0.7	< 1.72
12	-0.3	0.4	0.7	-0.5	0.4	0.7	< 1.71
12	-0.3	0.3	0.7	-0.5	0.4	0.7	< 1.71
12	-0.3	0.3	0.7	-0.4	0.4	0.7	< 1.70
12	-0.3	0.3	0.7	-0.3	0.4	0.7	< 1.70
12	-0.3	0.3	0.7	-0.3	0.2	0.7	< 1.68
12	-0.3	0.3	0.7	-0.3	0.1	0.7	< 1.70
12	-0.3	0.3	0.7	-0.3	0.2	0.6	< 1.70
10	-0.5	0.4	0.7	-0.5	0.4	0.7	< 1.75
10	-0.3	0.3	0.7	-0.3	0.2	0.6	< 1.69

Table 6.16: Limit variation as a function of bin size in the same-sign dimuon channel. (In bold: the final bin borders used in the $2lss$ channel.)

3020 The expected limit was found to be **r<1.69** for optimized bin borders in 10 bins
 3021 and optimized pre-selection cuts.

3022 Two additional binning strategies were tested, however, the obtained limits are
 3023 degraded; they are documented in Appendix C.

3024 6.10 Forward jet mismodeling

3025 As said in previous section, among the features of the tHq signature that serves as a
 3026 powerful discriminating variable is the presence of a forward jet; unfortunately, its η
 3027 distribution is poorly modeled in simulation. To estimate the effect of a mismodeled
 3028 forward jet distribution, a reweighting of the events in simulation based on the nor-
 3029 malized data/MC ratio in a control region is performed; as a result, an alternative
 3030 shape of the BDT output distributions that reflects a hypothetical perfect data/MC
 3031 agreement is derived.

3032 Using a sample of dileptonic $t\bar{t}$ events, the control region is defined by requiring
 3033 two opposite-sign tight leptons in the $e\mu$ channel, with at least two jets and at least
 3034 one medium CSV tagged jet. (Otherwise the selection is identical to the same-sign
 3035 $e^\pm\mu^\pm$ channel selection). Some distributions related to the forward jet for MC and
 3036 data are shown in Figure 6.24.

3037 The disagreement of the η distribution of forward jets for a p_T cut of 25 GeV is
 3038 well visible especially at higher values of $|\eta|$. The multiplicity for central jets is poorly
 3039 described by the MadgraphMLM sample used here; consistent with other observations
 3040 of the same sample. The $t\bar{t}$ background in this analysis is modeled with a data-driven
 3041 method and these disagreements do not directly affect the $t\bar{t}$ contribution in the
 3042 analysis. They do however reflect the expected agreement in these distributions for
 3043 the irreducible backgrounds and the signal.

3044 The effect of higher p_T cuts on the forward jet has been studied for three values:
 3045 25, 30 and 40 GeV. In order to take into account the data/MC disagreement in the
 3046 high η regions, the events are weighted accordingly to the data/MC ratio of the
 3047 unity normalized control plots shown in Figure 6.25. The data/MC agreement in the
 3048 forward jet η distribution improves significantly at higher jet p_T s.

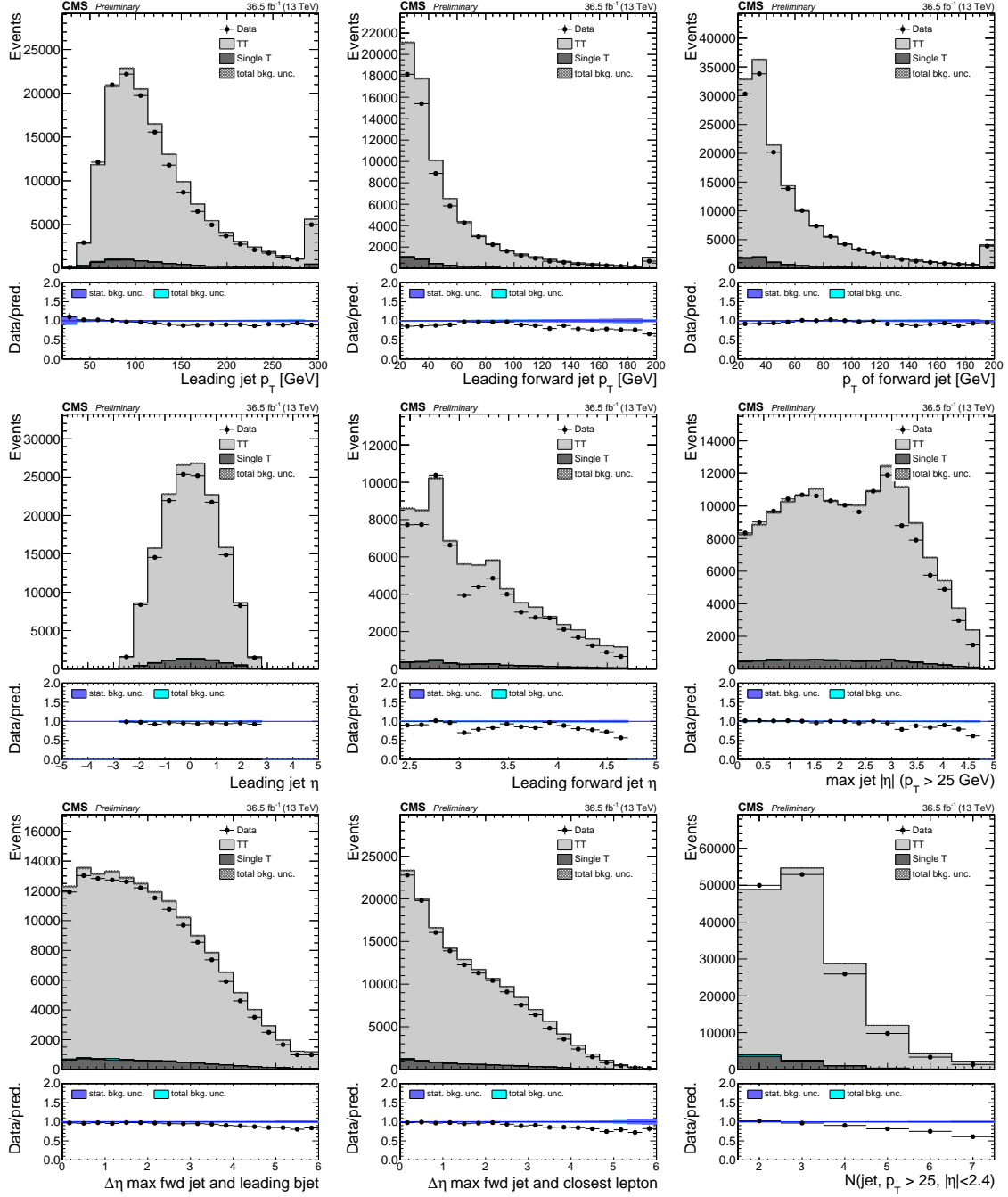


Figure 6.24: Kinematic distributions in the $t\bar{t}$ -enriched opposite-sign $e\mu$ selection. Top row, left to right: leading central ($\eta < 2.4$) jet p_T , leading forward ($\eta > 2.4$) jet p_T , p_T of non-CSV-loose jet with highest η (“light forward jet”). Middle row: η distribution of those same jets. Bottom row: $\Delta\eta$ between light forward jet and leading CSV-loose tagged jet; $\Delta\eta$ between light forward jet and closest lepton; number of central jets.

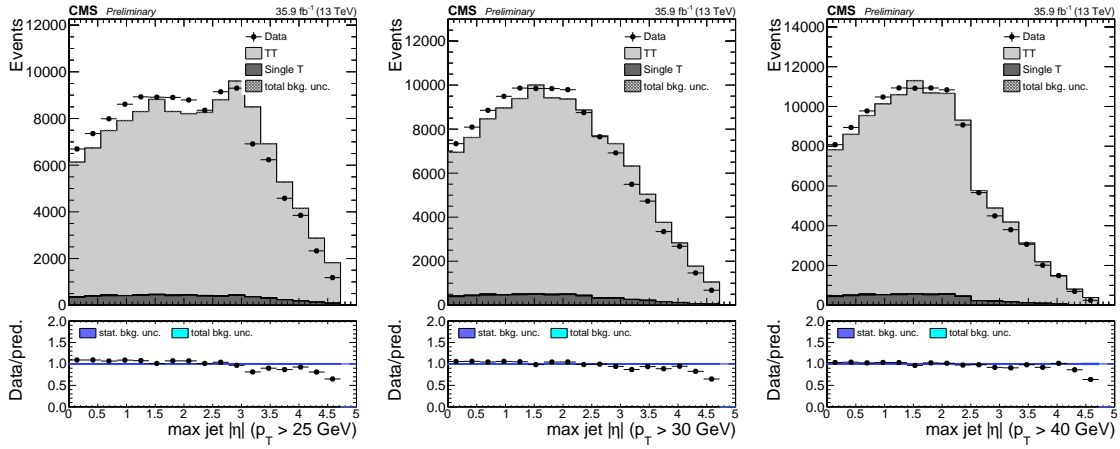


Figure 6.25: Pseudorapidity distributions of the most forward, non-CSV-loose tagged jet in the $t\bar{t}$ -enriched opposite-sign $e\mu$ selection for the three p_T cut values studied.

3049 Table 6.17 shows the scale factors obtained for the three p_T values. The expected
 3050 limit on cross section in the $3l$ was used to determine the most appropriate forward
 3051 jet p_T cut; higher p_T cut improves from 1.54 at 25 GeV to 1.51 at 30 GeV and 1.50
 3052 at 40 GeV. The impact of the data/MC disagreement for forward jet η is observed
 3053 to reduce with higher p_T cuts. Figures F.1, F.2 and F.3 show this reduction in the
 3054 impact of the forward jet η nuisance in the fit.

3055 6.11 Signal model

3056 It is worth to remind that the main goal of this analysis is to test the compatibility
 3057 of points in the parameter space of Higgs-to-vector boson and Higgs-to-top quark
 3058 couplings. This is achieved by using simulated tHq , tHW , and $t\bar{t}H$ signal events
 3059 which are weighted to reflect the impact of the couplings on kinematic distributions,
 3060 and together with different predictions of the respective production cross sections and
 3061 branching ratios, to produce limits on the cross section for different values of κ_V and
 3062 κ_t . See Section 6.4.3 and Table A.3 for the set of κ_t and κ_V values generated. The
 3063 slight shape-dependence of the BDTG classifier outputs as a function of the couplings

η range	$p_T > 25$ GeV	$p_T > 30$ GeV	$p_T > 40$ GeV
0 – 0.278	1.0925	1.0566	1.0326
0.278 – 0.556	1.0920	1.0617	1.0407
0.556 – 0.833	1.0675	1.0459	1.0244
0.833 – 1.111	1.0888	1.0593	1.0340
1.111 – 1.389	1.0759	1.0508	1.0322
1.389 – 1.667	1.0109	0.9847	0.9661
1.667 – 1.944	1.0727	1.0448	1.0239
1.944 – 2.222	1.0715	1.0457	1.0169
2.222 – 2.500	1.0112	0.9871	0.9746
2.500 – 2.778	1.0387	0.9942	0.9816
2.778 – 3.056	0.9687	0.9427	0.9200
3.056 – 3.333	0.8137	0.8695	0.9092
3.333 – 3.611	0.9010	0.9387	0.9807
3.611 – 3.889	0.8685	0.8887	0.9213
3.889 – 4.167	0.9277	0.9466	1.0135
4.167 – 4.444	0.8111	0.8278	0.8637
4.444 – 4.722	0.6497	0.6485	0.6367
4.722 – 5.000	1.0000	1.0000	1.0000
Exp. limit ($\ell\ell\ell$)	$r < 1.54$	$r < 1.51$	$r < 1.50$

Table 6.17: Data/MC scale factors for η distribution of most forward, non-tagged jet with three different p_T cuts, see Figure 6.25.

3064 is showed in Appendix D.

3065 In addition to the (κ_t, κ_V) dependence of the tHq and tHW production cross
 3066 sections, due to interferences, the cross section of $t\bar{t}H$ depends quadratically on κ_t
 3067 according to [158]:

$$\sigma(tHq) = (2.633\kappa_t^2 + 3.578\kappa_V^2 - 5.211\kappa_t\kappa_V) * \sigma_{SM}(tHq), \quad (6.7)$$

$$\sigma(tHW) = (2.909\kappa_t^2 + 2.310\kappa_V^2 - 4.220\kappa_t\kappa_V) * \sigma_{SM}(tHW), \quad (6.8)$$

$$\sigma(t\bar{t}H) = \kappa_t^2 * \sigma_{SM}(t\bar{t}H). \quad (6.9)$$

3068 The Higgs branching fractions to vector bosons depend on κ_V , and the overall

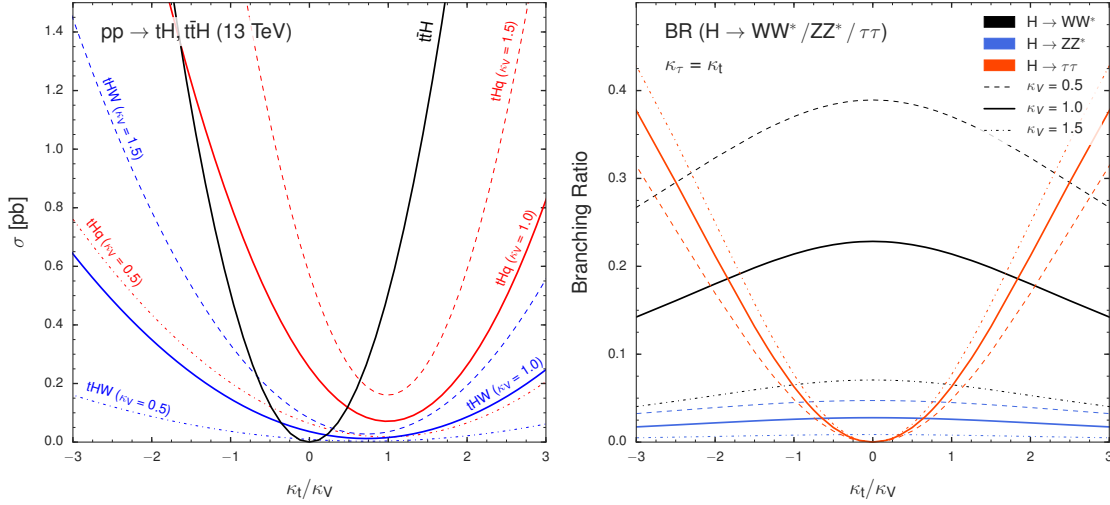


Figure 6.26: Scaling of the tHq , tHW , and $t\bar{t}H$ production cross sections (left) and of the $H \rightarrow WW^*$, $H \rightarrow \tau\tau$, and $H \rightarrow ZZ^*$ branching ratios (right), as a function of κ_t/κ_V , for three different values of κ_V .

3069 Higgs decay width depend both on κ_t and κ_V when considering resolved top quark
 3070 loops in the $H \rightarrow \gamma\gamma$, $H \rightarrow Z\gamma$, and $H \rightarrow gg$ decays. The relative contributions from
 3071 $H \rightarrow WW$, $H \rightarrow ZZ$, and $H \rightarrow \tau\tau$ also changes with changing κ_V .

3072 If the Higgs-to-tau coupling modifier (κ_τ) is assumed to be equal to κ_t , the relative
 3073 fractions of WW , ZZ , and $\tau\tau$ in the event selection will only depend on the ratio of
 3074 κ_t/κ_V ; thus, any limit set at any given value of κ_t/κ_V is valid for all values of κ_t and
 3075 κ_V with that ratio, and could then be compared with theoretical predictions of cross
 3076 sections at different values of either modifier. Figure 6.26 shows the tHq , tHW and
 3077 $t\bar{t}H$ cross sections(left) and the Higgs boson branching ratios $H \rightarrow WW$, $H \rightarrow ZZ$,
 3078 and $H \rightarrow \tau\tau$ (right) as a function of the κ_t/κ_V ratio.

3079 Thus, this analysis sets an upper limit on the combined cross section times branch-
 3080 ing ratio of tHq , tHW , and $t\bar{t}H$ as a function of the ratio κ_t/κ_V .

3081 Similar interpretation can be made if instead of reporting the limits as a function
 3082 of the κ_t/κ_V ratio, they are reported as a function of the relative strength of Higgs-top
 3083 and Higgs-vector-boson couplings, multiplied by the relative sign

$$f_t = \text{sign}\left(\frac{\kappa_t}{\kappa_V}\right) \times \frac{\kappa_t^2}{\kappa_t^2 + \kappa_V^2}. \quad (6.10)$$

3084 this parameter covers the full space between -1.0 and 1.0 , with the SM at 0.5 .
 3085 Absolute values of 1.0 or 0.0 would correspond to purely Higgs-top and purely Higgs-
 3086 V couplings, respectively.

3087 Table 6.18 shows the points in the κ_t/κ_V and f_t parameter space that are mapped
 3088 by the 51 individual κ_t and κ_V points.

3089 The overall Higgs decay width (modified by both κ_t and κ_V) becomes irrelevant
 3090 if limits are quoted as absolute cross sections rather than multiples of the expected
 3091 cross section (which depends on it).

3092 The 1D histograms of events as categorized in regions of the 2D BDTG plane are
 3093 then used in a maximum likelihood fit of signal and background shapes, where the
 3094 tHq , tHW , and $t\bar{t}H$ signals are floating with a common signal strength modifier r ,
 3095 producing a 95% C.L. upper limit the observed cross section of $tHq + tHW + t\bar{t}H$.

3096 This procedure is done separately for each point (κ_t, κ_V) where the cross sections
 3097 and branching fractions are scaled accordingly in each point. Limits at fixed values
 3098 of κ_t/κ_V are by construction identical. Tables G.1–G.3 and G.4–G.6 in Appendix G
 3099 show the scalings of cross section times branching fraction, as well as branching
 3100 fractions alone for each of the Higgs decay modes and each of the signal components.

3101 6.12 Systematic uncertainties

3102 The uncertainties present in this analysis can be either of statistical nature given
 3103 the size of the samples and the probabilistic nature of the processes, or of system-
 3104 atic nature. The systematic uncertainties are associated to theoretical uncertainties
 3105 originating in the limited knowledge of the processes, and also to experimental uncer-

f_t	κ_t/κ_V	$\kappa_V = 0.5$	$\kappa_V = 1.0$	$\kappa_V = 1.5$
-0.973	-6.000	-3.00		
-0.941	-4.000	-2.00		
-0.900	-3.000	-1.50	-3.00	
-0.862	-2.500	-1.25		
-0.800	-2.000	-1.00	-2.00	-3.00
-0.692	-1.500	-0.75	-1.50	
-0.640	-1.333			-2.00
-0.610	-1.250		-1.25	
-0.500	-1.000	-0.50	-1.00	-1.50
-0.410	-0.833			-1.25
-0.360	-0.750		-0.75	
-0.308	-0.667			-1.00
-0.200	-0.500	-0.25	-0.50	-0.75
-0.100	-0.333			-0.50
-0.059	-0.250		-0.25	
-0.027	-0.167			-0.25
0.000	0.000	0.00	0.00	0.00
0.027	0.167			0.25
0.059	0.250		0.25	
0.100	0.333			0.50
0.200	0.500	0.25	0.50	0.75
0.308	0.667			1.00
0.360	0.750		0.75	
0.410	0.833			1.25
0.500	1.000	0.50	1.00	1.50
0.610	1.250		1.25	
0.640	1.333			2.00
0.692	1.500	0.75	1.50	
0.800	2.000	1.00	2.00	3.00
0.862	2.500	1.25		
0.900	3.000	1.50	3.00	
0.941	4.000	2.00		
0.973	6.000	3.00		

Table 6.18: The 33 distinct values of κ_t/κ_V and f_t as mapped by the 51 κ_t and κ_V points.

3106 tainties originating for instance from the limited resolution of the detectors. In this
 3107 section, the contributions to the systematic uncertainties from all the sources in this
 3108 analysis are considered.

3109 Rate uncertainties associated to the application of scaling factors for the affected
3110 processes, and shape uncertainties which affect not only the normalization but also
3111 the shape of certain distributions, compose the systematic uncertainties. The latter
3112 can affect the analysis during the event selection; therefore, these systematic shape
3113 uncertainties are applied to the simulation samples.

3114 **Experimental uncertainties.**

3115 • *Luminosity.* The measurement of the luminosity delivered by the LHC is af-
3116 fected by experimental conditions like pileup and the number of protons per
3117 bunch. Due to variations in the LHC running parameters an uncertainty of
3118 2.6% is applied.

3119 • *Lepton efficiencies.* Systematic uncertainties in the signal selection efficiency
3120 arise from correction factors applied to the simulated events in order to better
3121 match the measured detector performance; also from theoretical uncertainties in
3122 the modeling of the signal process. Data/MC differences in the trigger efficiency
3123 accounted with scale factors applied to correct for them, lepton reconstruction
3124 and identification performance, and lepton selection efficiency carry a combined
3125 uncertainty of about 5% per lepton.

3126 • *Jets related uncertainties.* Jet energy corrections affect the uncertainty in the
3127 signal selection efficiency it is evaluated by varying the correction factors within
3128 their uncertainties and propagating the effects to the final results by recalculat-
3129 ing the kinematic quantities. The effects of the jet energy scale uncertainties,
3130 b -tagging efficiency and forward jet mismodeling are evaluated using dedicated
3131 shape templates derived from a variation of the jet energy scale within its uncer-
3132 tainty and from varying the b -tagging forward jet data/MC scale factors within
3133 their uncertainty.

3134 **Theory uncertainties**

3135 The uncertainties from unknown higher orders of tHq and tHW production are
 3136 estimated from a change in the Q^2 scale of double and half the initial value, evaluated
 3137 for each point of κ_t and κ_V . The $t\bar{t}H$ signal component has an uncertainty of about
 3138 $+5.8/-9.2\%$ from Q^2 scale variations and a further 3.6% from the knowledge of PDFs
 3139 and α_s [57]. Uncertainties related to the choice of PDF set and its scale are estimated
 3140 to be about 3.7% for tHq and about 4.0% for tHW .

3141 The theoretical uncertainties from unknown higher orders for $t\bar{t}W$ and $t\bar{t}Z$ are 12%
 3142 and 10% respectively; additional uncertainties from the knowledge of PDFs and α_s
 3143 of about 4% each for $t\bar{t}W$ and $t\bar{t}Z$ are estimated.

3144 **Backgrounds**

3145 Besides the theory uncertainties on $t\bar{t}W$ and $t\bar{t}Z$, uncertainties of the smaller irre-
 3146 ducible backgrounds and the charge mis-identification estimate are covered with flat
 3147 normalization uncertainties. The WZ contribution due to the scale factor is derived
 3148 during the background estimation using the control region.

3149 The dominant uncertainty is associated to the estimate of the non-prompt lepton
 3150 contribution using a fake rate method; the main normalization uncertainty comes from
 3151 limited statistics in the data control region, and the subtraction of residual prompt
 3152 lepton contribution as stated in section 6.7.2. Shape variations resembling data/MC
 3153 differences and deviations in closure test are evaluated as shape uncertainties.

3154 **Fake rate closure uncertainties**

3155 In order to determine the systematic uncertainties associated to the fake rates,
 3156 the BDTG classifier output shapes from a pure MC estimation of fake leptons (in
 3157 $t\bar{t}$) and from the application of fake-rates as measured in QCD MC, applied in $t\bar{t}$
 3158 MC events, are compared. The difference in the resulting normalization and output
 3159 shapes, for both trainings vs. $t\bar{t}$ and vs. $t\bar{t}V$, are estimated and propagated to the

3160 fit as normalization and shape variations; Figures 6.27 and 6.28 show the results of
3161 these closure tests.

3162 Table 6.19 list all the systematic uncertainties currently considered in the analysis.

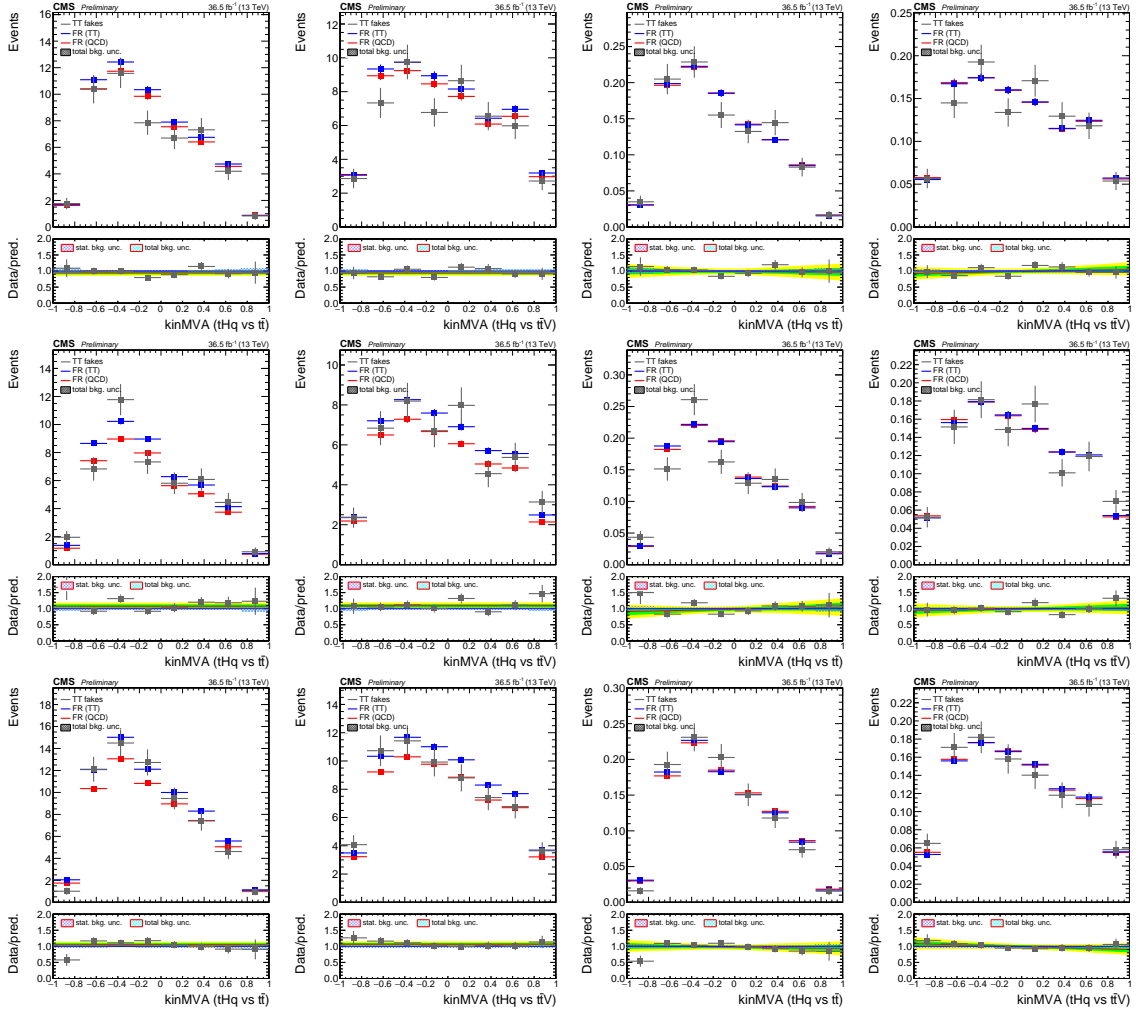


Figure 6.27: BDT outputs comparing $t\bar{t}$ MC to a fake-rate prediction using fake rates measured in QCD MC. Agreement in normalization is estimated from the plots in the two left columns, shape disagreement is estimated from the (normalized) plots in the two right columns. From top to bottom rows: same-sign $e^\pm \mu^\mp$ selection with electron fakes, same-sign $e^\pm \mu^\mp$ selection with muon fakes, same-sign $\mu^\pm \mu^\pm$ selection.

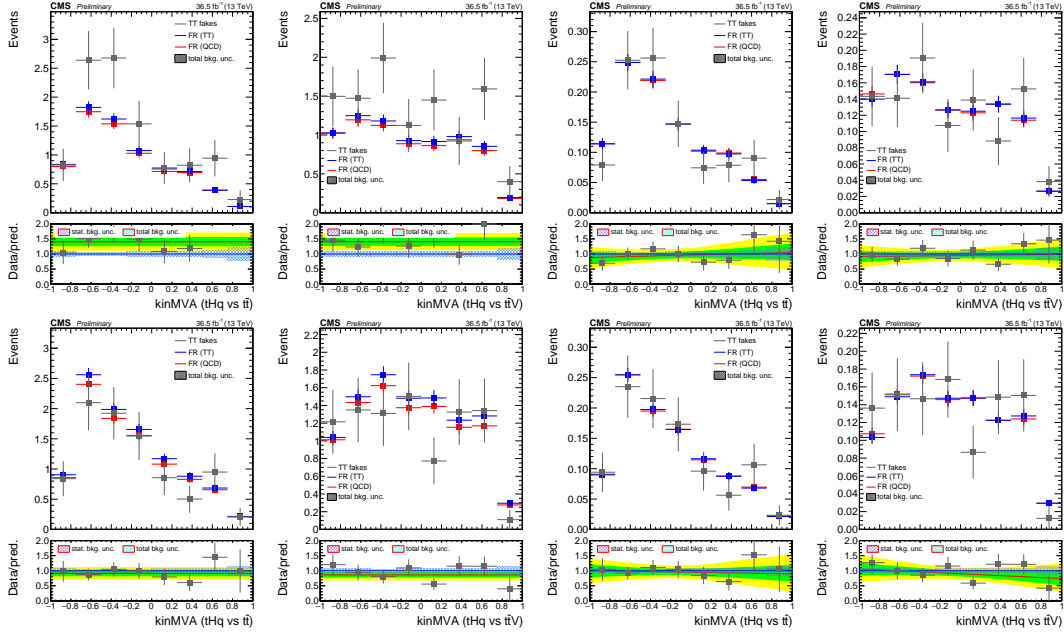


Figure 6.28: BDT outputs comparing $t\bar{t}$ MC to a fake-rate prediction using fake rates measured in QCD MC. Agreement in normalization is estimated from the plots in the two left columns, shape disagreement is estimated from the (normalized) plots in the two right columns. From top to bottom rows: three lepton selection with electron fakes, three lepton selection with muon fakes.

Source	Channel	Size
Experimental uncertainties		
Luminosity	all	1.026
Loose lepton efficiency		1.02 per lepton
Tight lepton efficiency		1.03 per lepton
Trigger efficiency	$\mu^\pm \mu^\pm$ $e^\pm \mu^\pm$ $\ell\ell\ell$	1.01 1.01 1.03
Jet energy scale	all	templates
Forward jet modeling	all	templates, see Table 6.17
_tagging efficiency	all	templates
Theory uncertainties		
Q^2 scale (tHq)	all	0.92–1.06 (depending on κ_t, κ_V)
Q^2 scale (tHW)	all	0.93–1.05 (depending on κ_t, κ_V)
Q^2 scale ($t\bar{t}H$)	all	0.915/1.058
Q^2 scale ($t\bar{t}W$)	all	1.12
Q^2 scale ($t\bar{t}Z$)	all	1.11
pdf ($t\bar{t}H$)	all	1.036
pdf gg ($t\bar{t}Z$)	all	0.966
pdf $q\bar{q}$ ($t\bar{t}W$)	all	1.04
pdf qg (tHq)	all	1.037
pdf qg (tHW)	all	1.040
Higgs branching fractions		
param_alphaS	all	1.012
param_mB	all	0.981
HiggsDecayWidthTHU_hqq	all	0.988
HiggsDecayWidthTHU_hvv	all	1.004
HiggsDecayWidthTHU_hll	all	1.019
Backgrounds		
WZ control region statistics	$\ell\ell\ell$	1.10
WZ control region backgrounds	$\ell\ell\ell$	1.20
WZ modeling	$\ell\ell\ell$	1.07
$WZ + 2\text{jet}$ background	$\mu^\pm \mu^\pm, e^\pm \mu^\pm$	1.50
Rare SM processes	all	1.50
Charge flips	$e^\pm \mu^\pm$	1.30
Fake rate estimate		
Electron FR measurement		templates
Muon FR measurement		templates
Electron closure	$e^\pm \mu^\pm$	0.94 norm., (0.98 ($t\bar{t}$))/1.07 ($t\bar{t}V$)) shape var.
	$\ell\ell\ell$	1.40 norm., (1.09 ($t\bar{t}$))/1.05 ($t\bar{t}V$)) shape var.
Muon closure	$\mu^\pm \mu^\pm$	1.07 norm., (0.97 ($t\bar{t}$))/0.91 ($t\bar{t}V$)) shape var.
	$e^\pm \mu^\pm$	1.09 norm., (1.06 ($t\bar{t}$))/1.03 ($t\bar{t}V$)) shape var.
	$\ell\ell\ell$	1.09 norm., (0.95 ($t\bar{t}$))/0.83 ($t\bar{t}V$)) shape var.

Table 6.19: Pre-fit size of systematic uncertainties.

3163 6.13 Results

3164 As a result of applying the event pre-selection on the dataset, 127 events are observed
 3165 in the $3l$ channel, 280 in the $2lss \mu^\pm \mu^\pm$ channel and 525 in the $2lss e^\pm \mu^\pm$ channel
 3166 as shown in Table 6.8. These events are then classified into one of ten categories,
 3167 depending on the output of the two BDTG classifiers and according to the optimized
 binning strategy.

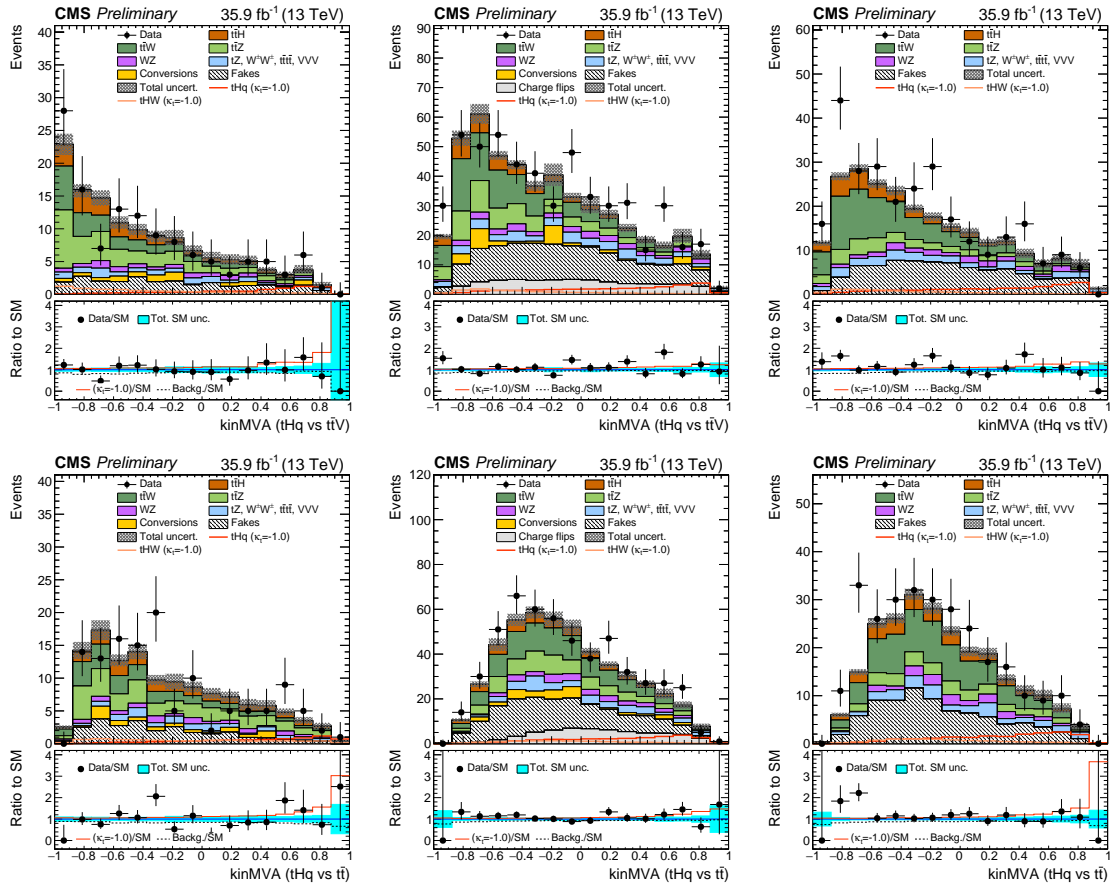


Figure 6.29: Pre-fit BDT classifier outputs, for the three-lepton channel (left), $e^\pm \mu^\pm$ (center), and $\mu^\pm \mu^\pm$ (right), for 35.9 fb^{-1} , for training against $t\bar{t}V$ (top row) and against $t\bar{t}$ (bottom row). In the box below each distribution, the ratio of the observed and predicted event yields is shown. The shape of the two tH signals for $\kappa_t = -1.0$ is shown, normalized to their respective cross sections for $\kappa_t = -1.0, \kappa_V = 1.0$. The grey band represents the unconstrained (pre-fit) statistical and systematical uncertainties.

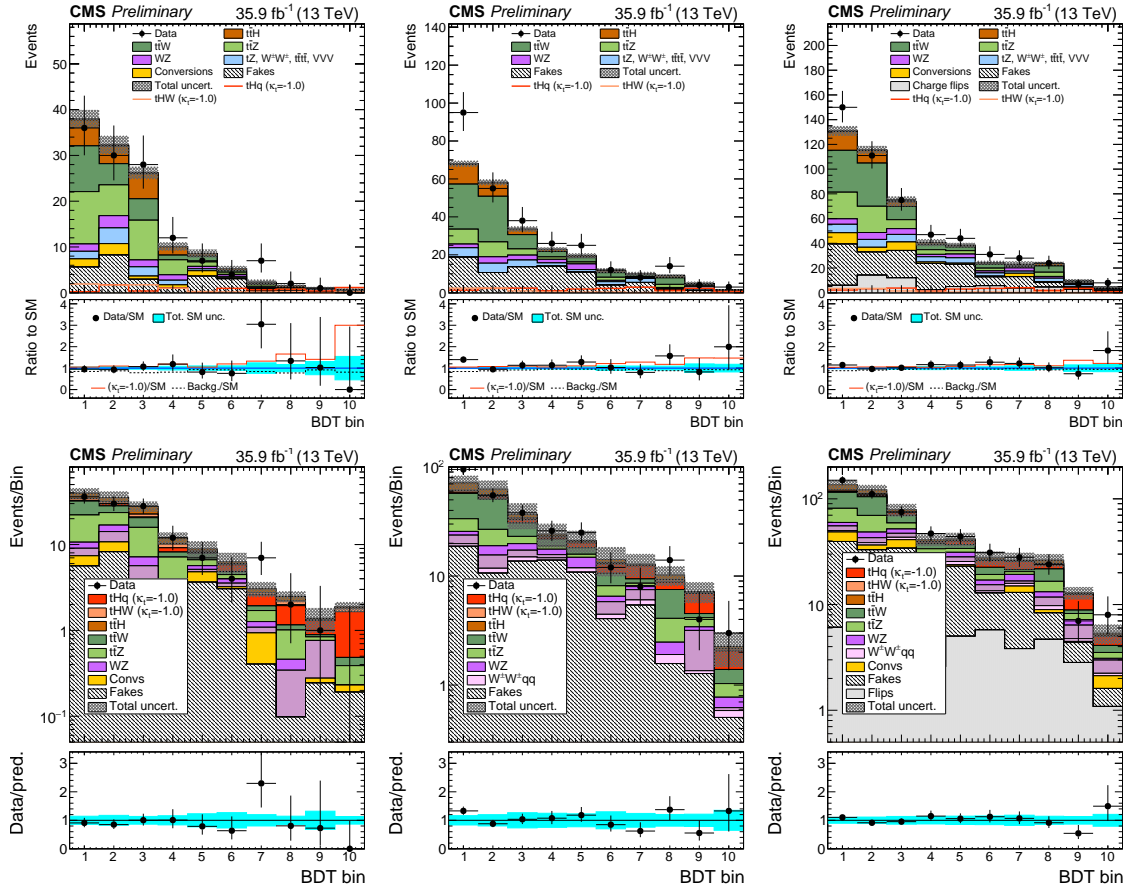


Figure 6.30: Expected (pre-fit) distributions in the final binning used for the signal extraction, for (from left to right) the three lepton channel, the $\mu^{\pm}\mu^{\pm}$ channel, and the $e^{\pm}\mu^{\pm}$ channel. Linear scale (top row), and logarithmic scale (bottom row).

3169 The pre-fit distributions of BDTG outputs are shown in Figure 6.29, while the
 3170 pre-fit distributions in the final binning used in the signal extraction are shown in
 3171 Figure 6.30.

3172 The expected signal and background shapes for the distribution in the 1D his-
 3173 togram (with ten bins) are fit to the observed data in a maximum likelihood fit, for
 3174 all three channels simultaneously and separately for the signal shapes for each of the
 3175 33 κ_t/κ_V coupling configuration points.

3176 The tH and $t\bar{H}$ production cross sections and the Higgs decay branching ratios are
 3177 modified in each point with the Higgs-top (κ_t) and Higgs-vector boson (κ_V) coupling

strength and the Higgs-tau coupling strength modifier (κ_τ) is assumed to be equal to κ_t ; the rest of the parameters are assumed to be at the SM predicted values. The combined signal shape is then uniquely defined by the ratio of κ_t/κ_V . In the fit, the signal components, tH and $t\bar{t}H$, are floated with a common signal strength modifier (defined as the ratio to the expected cross section) to produce a 95% confidence level (C.L) upper limit on the observed $tH + t\bar{t}H$ cross section times the combined branching ratio of $H \rightarrow WW^* + ZZ^* + \tau\tau$.

The post-fit categorized BDTG output distributions obtained in the maximum likelihood fit to extract the limits, are shown in Figure 6.31.

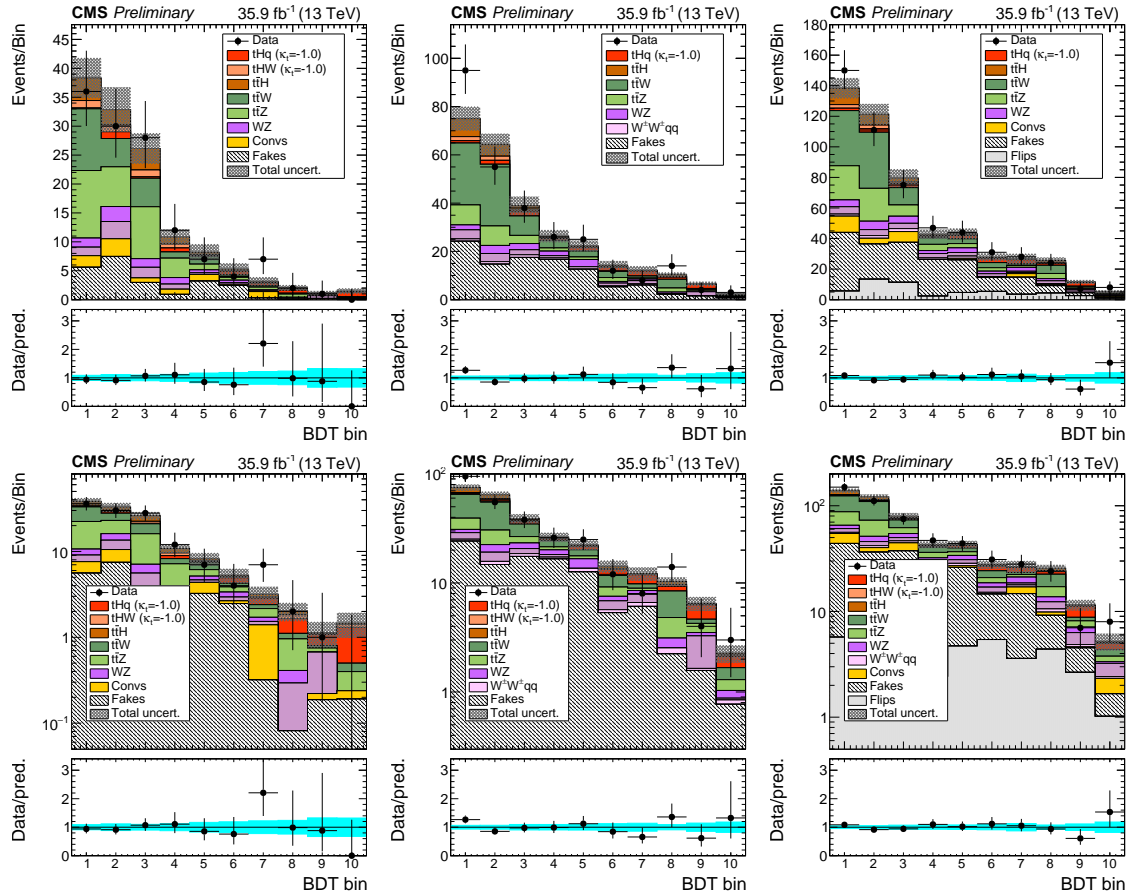


Figure 6.31: Post-fit distributions in the final binning used for the signal extraction, for (from left to right) the three lepton channel, the $\mu^\pm\mu^\pm$ channel, and the $e^\pm\mu^\pm$ channel. Linear scale (top row), and logarithmic scale (bottom row).

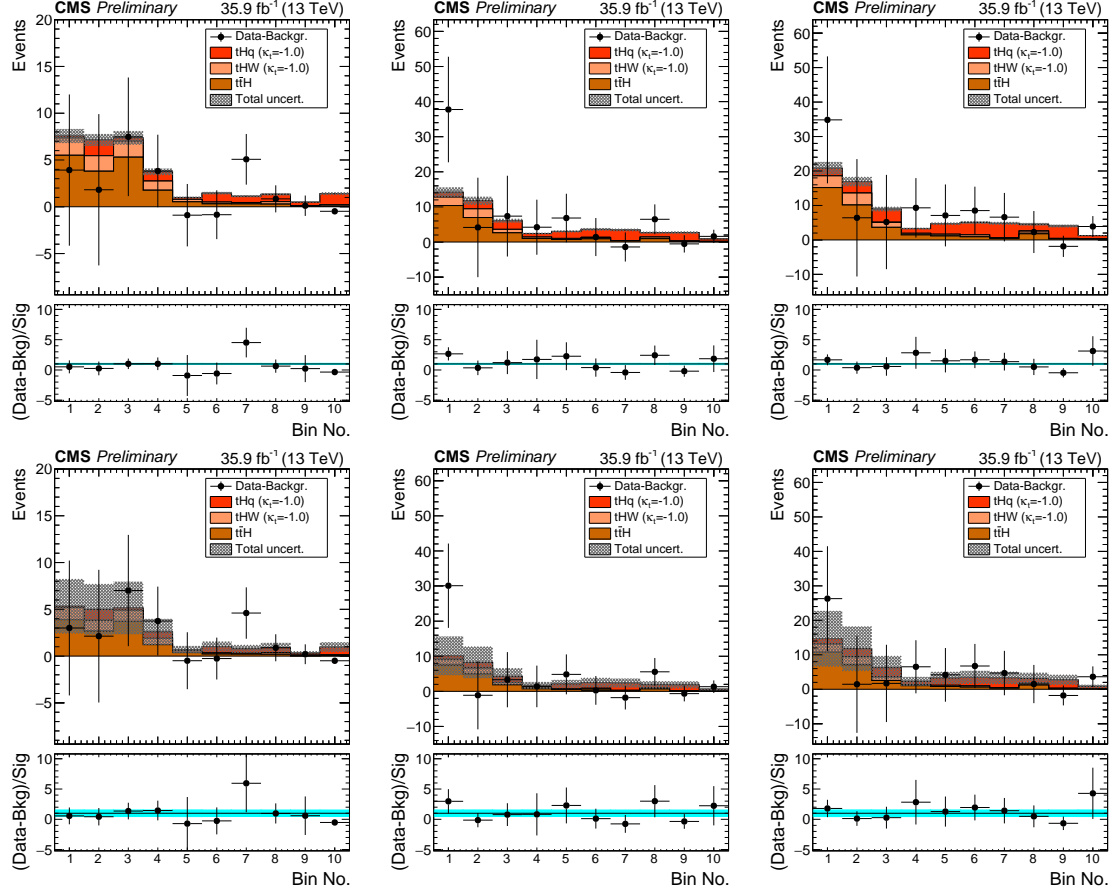


Figure 6.32: Background-subtracted pre- (top) and post-fit (bottom) distributions in the final binning used for the signal extraction, for three lepton channel (left), the $\mu^{\pm}\mu^{\pm}$ channel (center), and the $e^{\pm}e^{\pm}$ channel (right). For a fit in the inverted couplings scenario ($\kappa_V = 1, \kappa_t = -1$).

3187 As expected, the signal contribution is very small compared to the background
 3188 ground contribution; however, it is possible to see the signal contribution by subtracting
 3189 the background from the overall BDT output distributions as shown in Figure
 3190 6.32 for the inverted coupling scenario ($\kappa_V = 1, \kappa_t = -1$) and Figure 6.33 for the SM-like
 3191 scenario ($\kappa_V = 1, \kappa_t = 1$).

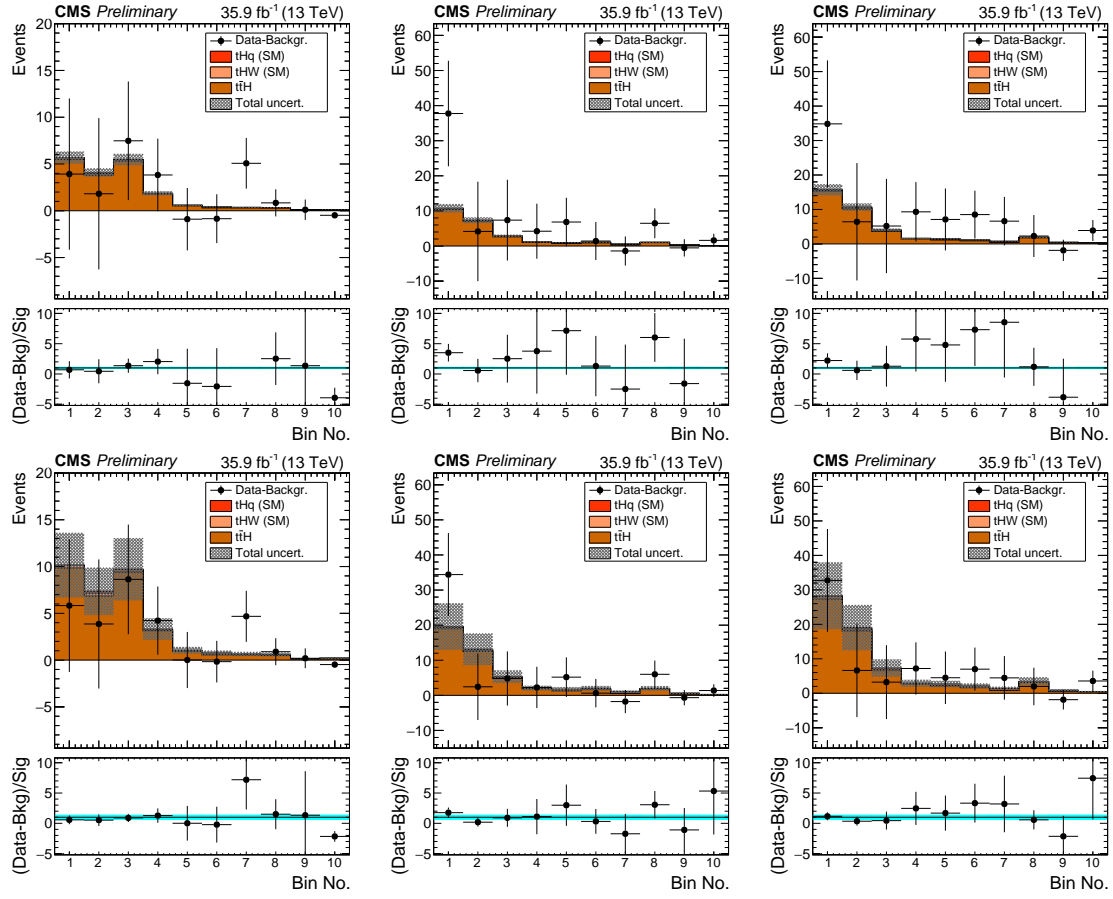


Figure 6.33: Background-subtracted pre- (top) and post-fit (bottom) distributions in the final binning used for the signal extraction, for the three lepton channel (left), the $\mu^\pm\mu^\pm$ channel (center), and the $e^\pm\mu^\pm$ channel (right). For a fit in the SM-like scenario ($\kappa_t = \kappa_V = 1$).

3192 6.13.1 CL_S and cross section limits

3193 Table 6.20 lists the expected background only, the expected SM-like Higgs signal, and
 3194 the observed 95% C.L. upper limits on the $tH + t\bar{t}H$ production cross section times
 3195 $H \rightarrow WW^* + ZZ^* + \tau\tau$ branching ratio (in pb); the corresponding plots are shown
 3196 in Figure 6.34 for $\kappa_V = 1$. The expected background-only limit is calculated on an
 3197 Asimov dataset, while the expected SM-like limit is calculated on an Asimov dataset
 3198 that includes the SM-like tH and $t\bar{t}H$ signals.

3199 An excess of more than 2σ is observed for the SM configuration ($\kappa_t/\kappa_V = 1$) for the

f_t	κ_t/κ_V	Exp. lim.	SM exp.	Obs. lim.	Best fit σ [pb]	Best fit r
-0.973	-6.000	0.328 $^{+0.136}_{-0.090}$	0.507 $^{+0.206}_{-0.158}$	0.603	0.305 $^{+0.155}_{-0.169}$	0.013 $^{+0.007}_{-0.007}$
-0.941	-4.000	0.335 $^{+0.137}_{-0.098}$	0.509 $^{+0.215}_{-0.166}$	0.627	0.322 $^{+0.157}_{-0.174}$	0.036 $^{+0.018}_{-0.020}$
-0.900	-3.000	0.335 $^{+0.138}_{-0.096}$	0.510 $^{+0.215}_{-0.172}$	0.639	0.334 $^{+0.160}_{-0.173}$	0.075 $^{+0.036}_{-0.039}$
-0.862	-2.500	0.334 $^{+0.139}_{-0.097}$	0.505 $^{+0.217}_{-0.173}$	0.649	0.341 $^{+0.160}_{-0.174}$	0.119 $^{+0.056}_{-0.061}$
-0.800	-2.000	0.330 $^{+0.141}_{-0.095}$	0.500 $^{+0.212}_{-0.176}$	0.656	0.345 $^{+0.165}_{-0.176}$	0.202 $^{+0.097}_{-0.103}$
-0.692	-1.500	0.325 $^{+0.139}_{-0.095}$	0.485 $^{+0.209}_{-0.172}$	0.660	0.340 $^{+0.164}_{-0.176}$	0.369 $^{+0.178}_{-0.191}$
-0.640	-1.333	0.325 $^{+0.139}_{-0.097}$	0.482 $^{+0.210}_{-0.173}$	0.659	0.334 $^{+0.169}_{-0.174}$	0.456 $^{+0.231}_{-0.238}$
-0.610	-1.250	0.321 $^{+0.140}_{-0.095}$	0.474 $^{+0.210}_{-0.169}$	0.653	0.328 $^{+0.164}_{-0.177}$	0.505 $^{+0.252}_{-0.272}$
-0.500	-1.000	0.315 $^{+0.142}_{-0.093}$	0.450 $^{+0.213}_{-0.160}$	0.638	0.304 $^{+0.175}_{-0.176}$	0.685 $^{+0.395}_{-0.396}$
-0.410	-0.833	0.312 $^{+0.138}_{-0.095}$	0.424 $^{+0.210}_{-0.147}$	0.615	0.276 $^{+0.168}_{-0.177}$	0.819 $^{+0.498}_{-0.526}$
-0.360	-0.750	0.307 $^{+0.138}_{-0.093}$	0.409 $^{+0.200}_{-0.136}$	0.593	0.256 $^{+0.170}_{-0.176}$	0.874 $^{+0.581}_{-0.601}$
-0.308	-0.667	0.301 $^{+0.138}_{-0.092}$	0.384 $^{+0.198}_{-0.124}$	0.566	0.231 $^{+0.165}_{-0.174}$	0.915 $^{+0.655}_{-0.689}$
-0.200	-0.500	0.292 $^{+0.136}_{-0.090}$	0.345 $^{+0.181}_{-0.109}$	0.497	0.166 $^{+0.163}_{-0.162}$	0.895 $^{+0.879}_{-0.871}$
-0.100	-0.333	0.278 $^{+0.132}_{-0.086}$	0.303 $^{+0.156}_{-0.092}$	0.409	0.092 $^{+0.157}_{-0.092}$	0.679 $^{+1.159}_{-0.679}$
-0.059	-0.250	0.268 $^{+0.129}_{-0.083}$	0.283 $^{+0.152}_{-0.085}$	0.365	0.059 $^{+0.148}_{-0.059}$	0.515 $^{+1.285}_{-0.515}$
-0.027	-0.167	0.260 $^{+0.125}_{-0.081}$	0.266 $^{+0.135}_{-0.077}$	0.328	0.029 $^{+0.142}_{-0.029}$	0.297 $^{+1.434}_{-0.297}$
0.000	0.000	0.254 $^{+0.123}_{-0.079}$	0.252 $^{+0.123}_{-0.073}$	0.294	0.000 $^{+0.132}_{-0.000}$	0.002 $^{+1.776}_{-0.002}$
0.027	0.167	0.275 $^{+0.132}_{-0.086}$	0.284 $^{+0.148}_{-0.084}$	0.357	0.040 $^{+0.154}_{-0.040}$	0.650 $^{+2.514}_{-0.650}$
0.059	0.250	0.297 $^{+0.141}_{-0.093}$	0.329 $^{+0.171}_{-0.099}$	0.458	0.119 $^{+0.183}_{-0.119}$	2.015 $^{+3.098}_{-2.015}$
0.100	0.333	0.322 $^{+0.148}_{-0.099}$	0.405 $^{+0.220}_{-0.135}$	0.611	0.246 $^{+0.166}_{-0.184}$	4.147 $^{+2.802}_{-3.103}$
0.200	0.500	0.324 $^{+0.141}_{-0.096}$	0.505 $^{+0.212}_{-0.181}$	0.730	0.413 $^{+0.150}_{-0.177}$	5.982 $^{+2.174}_{-2.559}$
0.308	0.667	0.281 $^{+0.122}_{-0.082}$	0.462 $^{+0.172}_{-0.159}$	0.651	0.382 $^{+0.136}_{-0.144}$	4.186 $^{+1.492}_{-1.574}$
0.360	0.750	0.268 $^{+0.116}_{-0.079}$	0.442 $^{+0.160}_{-0.154}$	0.620	0.364 $^{+0.130}_{-0.135}$	3.392 $^{+1.214}_{-1.253}$
0.410	0.833	0.258 $^{+0.112}_{-0.075}$	0.427 $^{+0.162}_{-0.147}$	0.599	0.351 $^{+0.127}_{-0.130}$	2.754 $^{+0.999}_{-1.022}$
0.500	1.000	0.244 $^{+0.105}_{-0.072}$	0.401 $^{+0.154}_{-0.137}$	0.562	0.328 $^{+0.118}_{-0.121}$	1.821 $^{+0.657}_{-0.671}$
0.610	1.250	0.240 $^{+0.104}_{-0.070}$	0.394 $^{+0.154}_{-0.133}$	0.545	0.315 $^{+0.118}_{-0.119}$	1.072 $^{+0.399}_{-0.403}$
0.640	1.333	0.242 $^{+0.105}_{-0.071}$	0.398 $^{+0.156}_{-0.136}$	0.547	0.316 $^{+0.122}_{-0.121}$	0.921 $^{+0.354}_{-0.352}$
0.692	1.500	0.244 $^{+0.106}_{-0.071}$	0.401 $^{+0.159}_{-0.136}$	0.543	0.312 $^{+0.120}_{-0.120}$	0.678 $^{+0.262}_{-0.261}$
0.800	2.000	0.256 $^{+0.109}_{-0.075}$	0.416 $^{+0.169}_{-0.138}$	0.552	0.311 $^{+0.121}_{-0.127}$	0.317 $^{+0.123}_{-0.129}$
0.862	2.500	0.268 $^{+0.114}_{-0.078}$	0.433 $^{+0.169}_{-0.142}$	0.558	0.310 $^{+0.127}_{-0.130}$	0.170 $^{+0.070}_{-0.072}$
0.900	3.000	0.276 $^{+0.118}_{-0.080}$	0.442 $^{+0.177}_{-0.144}$	0.563	0.308 $^{+0.128}_{-0.134}$	0.102 $^{+0.042}_{-0.044}$
0.941	4.000	0.290 $^{+0.122}_{-0.084}$	0.459 $^{+0.184}_{-0.149}$	0.566	0.304 $^{+0.134}_{-0.140}$	0.046 $^{+0.020}_{-0.021}$
0.973	6.000	0.306 $^{+0.122}_{-0.081}$	0.474 $^{+0.192}_{-0.150}$	0.571	0.300 $^{+0.131}_{-0.150}$	0.016 $^{+0.007}_{-0.008}$

Table 6.20: Expected (for background only, and for a SM-like Higgs signal) and observed 95% C.L. upper limits (in pb), and best fit signal strength r and corresponding best fit cross section for the combined $tH + t\bar{t}H$ cross section times modified branching ratio for the combination of all three channels, for different values of κ_t/κ_V or the equivalent f_t numbers.

background-only expected limit; however, the inclusion of the SM-like tH and $t\bar{t}H$ signals reveals that the excess is actually about 1σ ; furthermore, looking at $\kappa_t/\kappa_V = 0$, i.e., the $t\bar{t}H$ component in the signal is zero, it is evident that the origin of the excess is mostly due to the presence of the $t\bar{t}H$ component in the signal, given that the

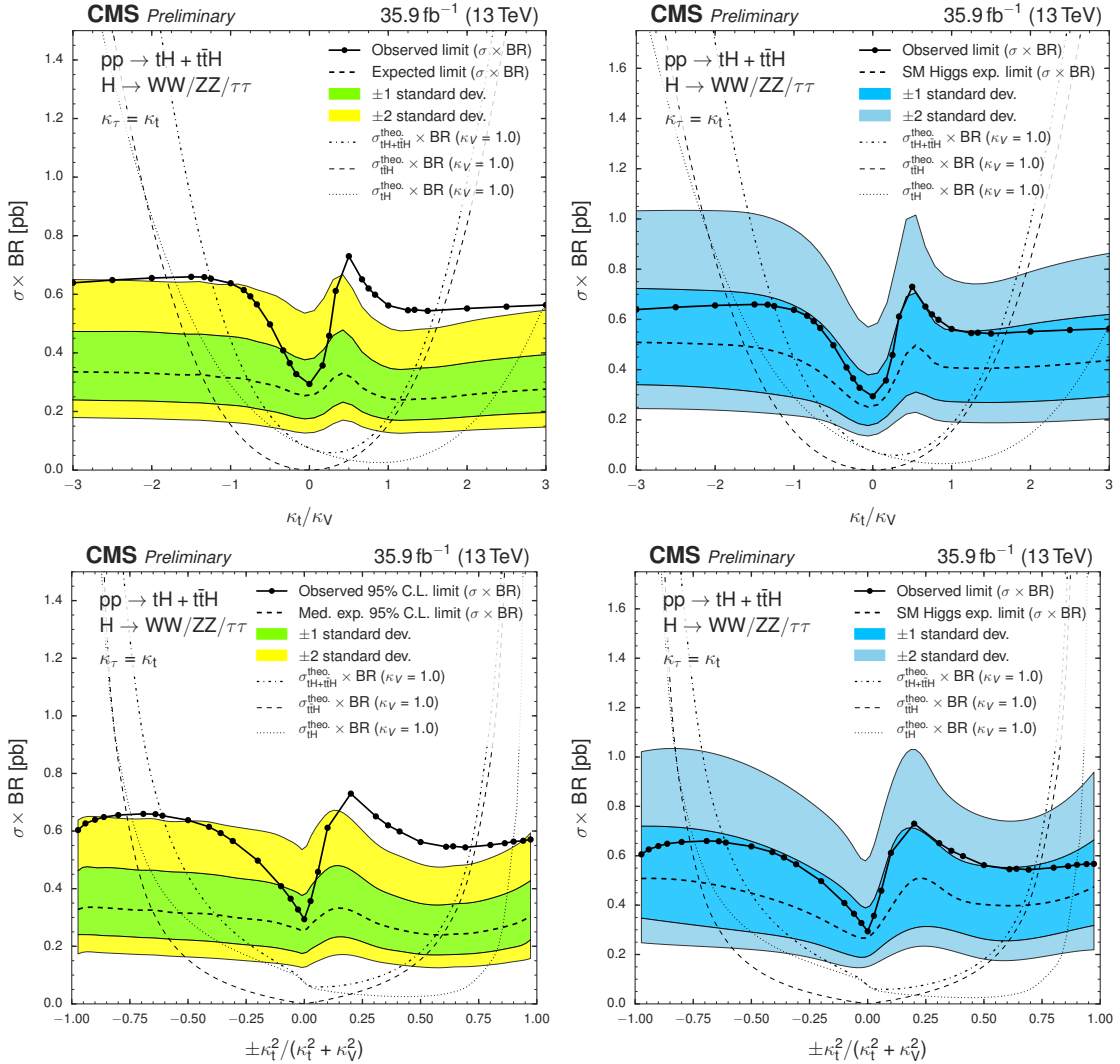


Figure 6.34: Left (Right): Expected background-only (SM-like including $t\bar{t}H$ and tH signals) and observed asymptotic limits on the combined $tH + t\bar{t}H$ cross section times modified BR as a function of κ_t/κ_V (top) and $\text{sign}(\kappa_t/\kappa_V) \times \frac{\kappa_t^2}{(\kappa_t^2 + \kappa_V^2)}$ (bottom) for the combination of three lepton channel, $\mu^\pm\mu^\pm$, and $e^\pm\mu^\pm$ channel.

3204 deviation of the observed limit from the expected one is much smaller than 1σ ; this is
 3205 consistent with the results presented in Reference [149]. It is also evident that, given
 3206 the dependence of the $t\bar{t}H$ cross section on κ_t^2 , the source of the asymmetry in both,
 3207 background-only and SM-like, limits is induced by the tH component of the signal.
 3208 Comparing the observed upper limit with the theoretical prediction of the $tH +$

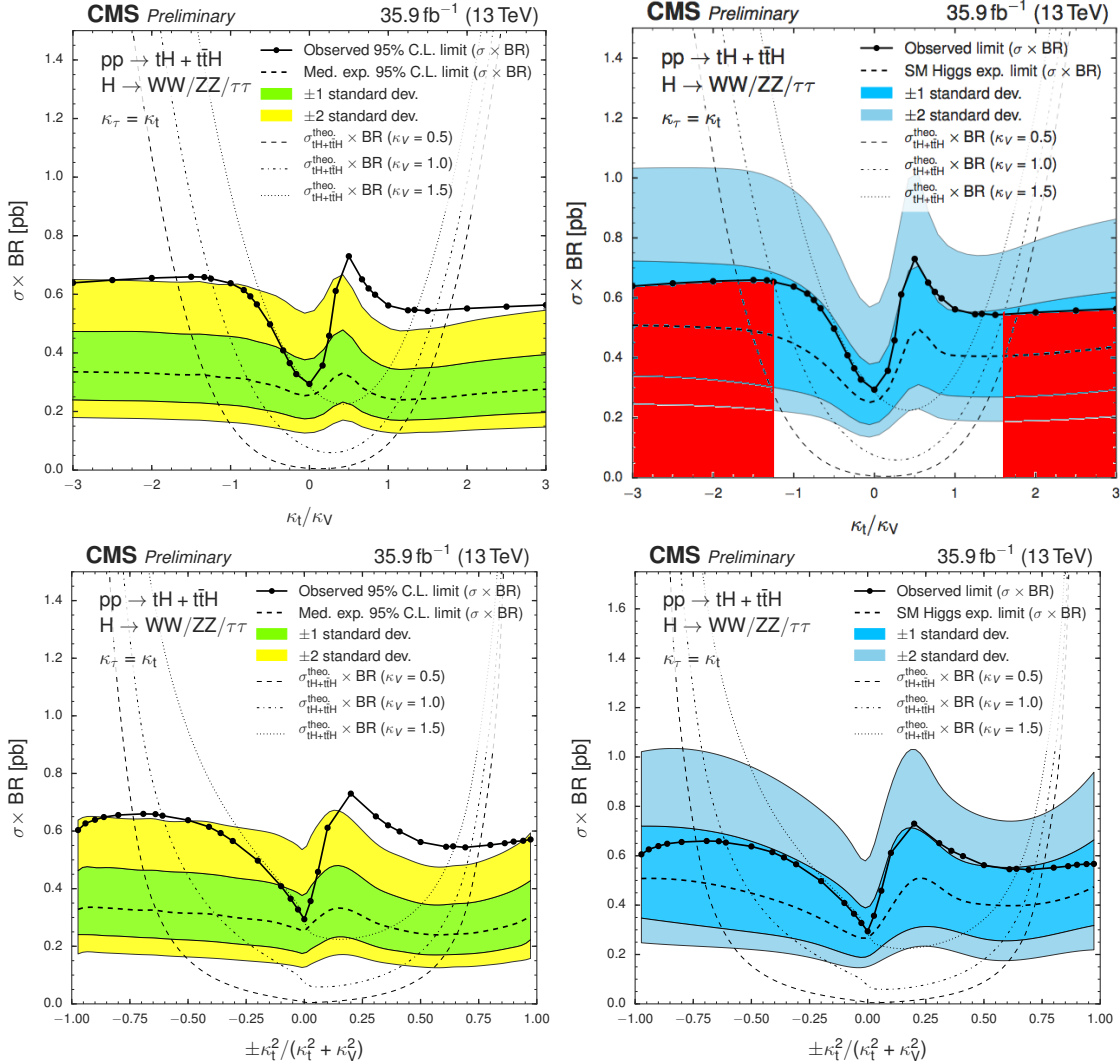


Figure 6.35: Left (Right): Expected background-only (SM-like including $t\bar{t}H$ and tH signals) and observed asymptotic limits on the combined $tH + t\bar{t}H$ cross section times modified BR as a function of κ_t/κ_V (top) and $\text{sign}(\kappa_t/\kappa_V) \times \frac{\kappa_t^2}{(\kappa_t^2 + \kappa_V^2)}$ (bottom) for the combination of three lepton channel, $\mu^\pm\mu^\pm$, and $e^\pm\mu^\pm$ channel. Theoretical $tH + t\bar{t}H$ cross section curves have been included for $\kappa_V = 0.5, 1.0, 1.5$. Red areas on the top right plot correspond to the excluded regions.

3209 $t\bar{t}H$ cross section times BR for $\kappa_V = 1.0$ constrains the allowed range of coupling
 3210 configurations κ_t/κ_V to between about -1.25 and +1.60. as shown in the top right
 3211 plot in Figure 6.35.

3212 The observed limit of about 0.64 pb on a signal shape expected for $\kappa_t/\kappa_V = -1.0$

Scenario	Channel	Obs. Limit (pb)	Exp. Limit (pb)		
			Median	$\pm 1\sigma$	$\pm 2\sigma$
$\kappa_t/\kappa_V = -1$	$\mu^\pm \mu^\pm$	1.00	0.58	[0.42, 0.83]	[0.31, 1.15]
	$e^\pm \mu^\pm$	0.84	0.54	[0.39, 0.76]	[0.29, 1.03]
	$\ell\ell\ell$	0.70	0.38	[0.26, 0.56]	[0.19, 0.79]
	Combined	0.64	0.32	[0.22, 0.46]	[0.16, 0.64]
$\kappa_t/\kappa_V = 1$ (SM-like)	$\mu^\pm \mu^\pm$	0.87	0.41	[0.29, 0.58]	[0.22, 0.82]
	$e^\pm \mu^\pm$	0.59	0.37	[0.26, 0.53]	[0.20, 0.73]
	$\ell\ell\ell$	0.54	0.31	[0.22, 0.43]	[0.16, 0.62]
	Combined	0.56	0.24	[0.17, 0.35]	[0.13, 0.49]

Table 6.21: Expected and observed 95% C.L. upper limits on the $tH + t\bar{t}H$ production cross section times $H \rightarrow WW^* + \tau\tau + ZZ^*$ branching ratio for a scenario of inverted couplings ($\kappa_t/\kappa_V = -1.0$, top rows) and for a standard-model-like signal ($\kappa_t/\kappa_V = 1.0$, bottom rows), in pb. The expected limit is calculated on a background-only Asimov dataset and quoted with $\pm 1\sigma$ and $\pm 2\sigma$ probability ranges.

Scenario	Channel	Obs. Limit	Exp. Limit				
			-2σ	-1σ	Median	$+1\sigma$	$+2\sigma$
$\kappa_V = 1.0$	$\mu^\pm \mu^\pm$	2.3	0.71	0.94	1.32	1.88	2.60
	$e^\pm \mu^\pm$	1.9	0.65	0.87	1.21	1.71	2.32
	$\ell\ell\ell$	1.6	0.43	0.59	0.86	1.26	1.78
	Combined ($\mu\mu, 3\ell$)	1.6	0.40	0.54	0.78	1.12	1.57
	Combined ($\mu\mu, e\mu, 3\ell$)	1.4	0.37	0.50	0.71	1.03	1.43
(SM)	$\mu^\pm \mu^\pm$	4.9	1.20	1.61	2.27	3.24	4.54
	$e^\pm \mu^\pm$	3.3	1.10	1.48	2.07	2.95	4.06
	$\ell\ell\ell$	3.0	0.91	1.22	1.73	2.49	3.47
	Combined ($\mu\mu, 3\ell$)	3.4	0.79	1.07	1.51	2.17	3.01
	Combined ($\mu\mu, e\mu, 3\ell$)	3.1	0.71	0.96	1.36	1.94	2.70

Table 6.22: Expected and observed CL_S limits (at 95% C.L.) on the signal strength of combined $tH + t\bar{t}H$ production in each channel, and for different combinations of them, for a scenario with inverted couplings ($\kappa_V = 1.0$, $\kappa_t = -1.0$, top section), and for the standard model ($\kappa_V = \kappa_t = 1.0$, bottom section). Numbers are for $35.9 fb^{-1}$.

and for the combination of all three channels, corresponds to 1.4 times the expected $tH + t\bar{t}H$ cross section with $\kappa_t = -1.0$, $\kappa_V = 1.0$. In the SM scenario ($\kappa_t/\kappa_V = 1.0$), the observed upper limit on the cross section times branching ratio is 0.56 pb, corresponding to 3.1 times the expected SM cross section of $tH + t\bar{t}H$. The summary of the results for the ITC and SM-like scenarios split by channel are presented in

3218 Table 6.21, whereas, the summary of the expected and observed CL_S limits (at 95%
 3219 C.L.) on the signal strength of combined $tH + t\bar{t}H$ production in each channel, and
 3220 for different combinations thereof, for the ITC and SM-like scenarios are presented in
 3221 Table 6.22.

3222 6.13.2 Best fit

3223 The best-fit results for the signal strength in all the 33 κ_t/κ_V configurations are also
 3224 listed in Table 6.20; the inverted top coupling (ITC) and the SM-like scenarios are
 3225 highlighted there and summarized in Table 6.23. The individual contributions from
 3226 all the channels to the best-fit signal strength for the SM-like Higgs signal are listed
 3227 in Table 6.24.

Scenario	Best fit signal strength	Best fit $\sigma \times BR$	Significance Obs.(exp.)
$\kappa_t/\kappa_V = -1.0$	0.68 ± 0.40	0.30 ± 0.18 pb	$1.70\sigma(2.51\sigma)$
$\kappa_t/\kappa_V = 1.0$	$1.82^{+0.66}_{-0.67}$	0.33 ± 0.12 pb	$2.73\sigma(1.50\sigma)$

Table 6.23: Best fit for signal strength r and corresponding best fit cross section for the combined $tH + t\bar{t}H$ cross section times modified branching ratio for the combination of all three channels, for the ITC and the SM-like scenarios.

$\ell\ell\ell$	$r = 1.44_{-0.84}^{+0.91}$
$e^\pm \mu^\pm$	$r = 1.42_{-1.03}^{+1.06}$
$\mu^\pm \mu^\pm$	$r = 2.75_{-1.11}^{+1.22}$
Combined	$r = 1.82_{-0.69}^{+0.76}$
Expected	$r = 1.00_{-0.65}^{+0.70}$

Table 6.24: Best-fit signal strengths for a SM-like Higgs signal for the individual channels.

3228 In the SM scenario, a signal strength of 1.82 is obtained which corresponds to a
 3229 cross section of 0.33 pb. The observed significance of the signal, in a background-
 3230 only hypothesis, is 2.7σ , with an a-priori expected significance of 1.5σ . For the
 3231 ITC scenario, the best fit signal strength is 0.68, corresponding to a significance

of 1.7σ (2.5σ expected); a scan of the observed and expected significances over the κ_t/κ_V configurations is shown in Fig. 6.36. Note that the fit favors a signal strength compatible with zero for a scenario with $\kappa_t = 0$ (where the $t\bar{t}H$ component vanishes).

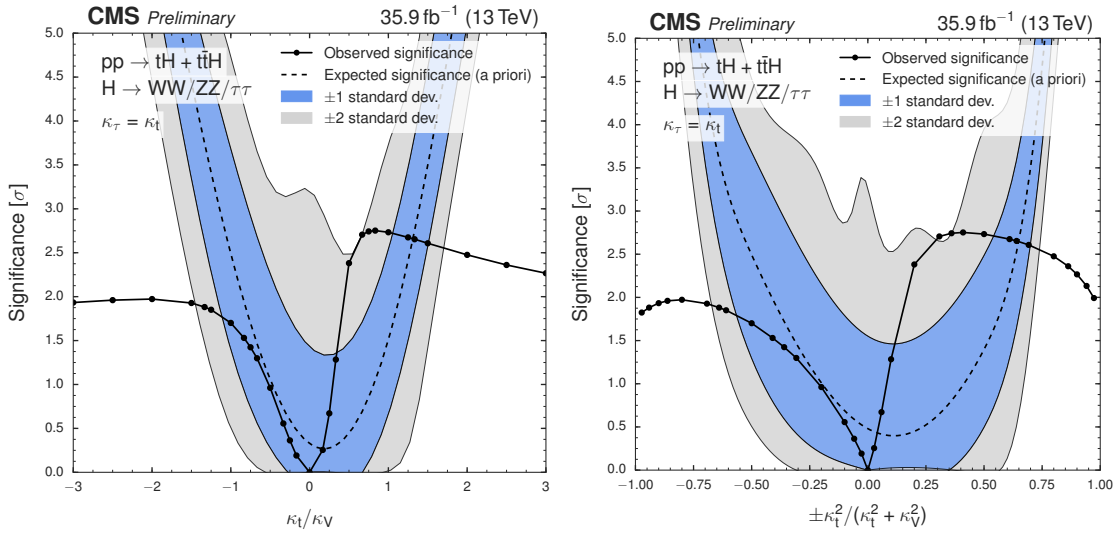


Figure 6.36: Observed and a priori expected significance of the fit result (in a background-only hypothesis) as a function of κ_t/κ_V (top) and f_t (bottom) for the combination of three lepton channel, $\mu^\pm\mu^\pm$, and $e^\pm\mu^\pm$ channel.

A scan over the best fit values of the combined cross section times modified BR is shown in Figure 6.37. The fact that the best fit signal strength at $\kappa_t = 0$, where the $t\bar{t}H$ component of the signal is zero, is compatible with zero implies that the best fit for the cross section is also compatible with zero, which again reveals that the excess in the cross section limit with respect to the expectation is not tH -like but $t\bar{t}H$ -like.

6.13.3 Effect of the nuisance parameters

The post-fit behavior of the most important nuisance parameters is presented in the pulls and impacts plots in Figures B.9, B.9 and B.9; additional pulls and impacts can be found in Appendix B.4

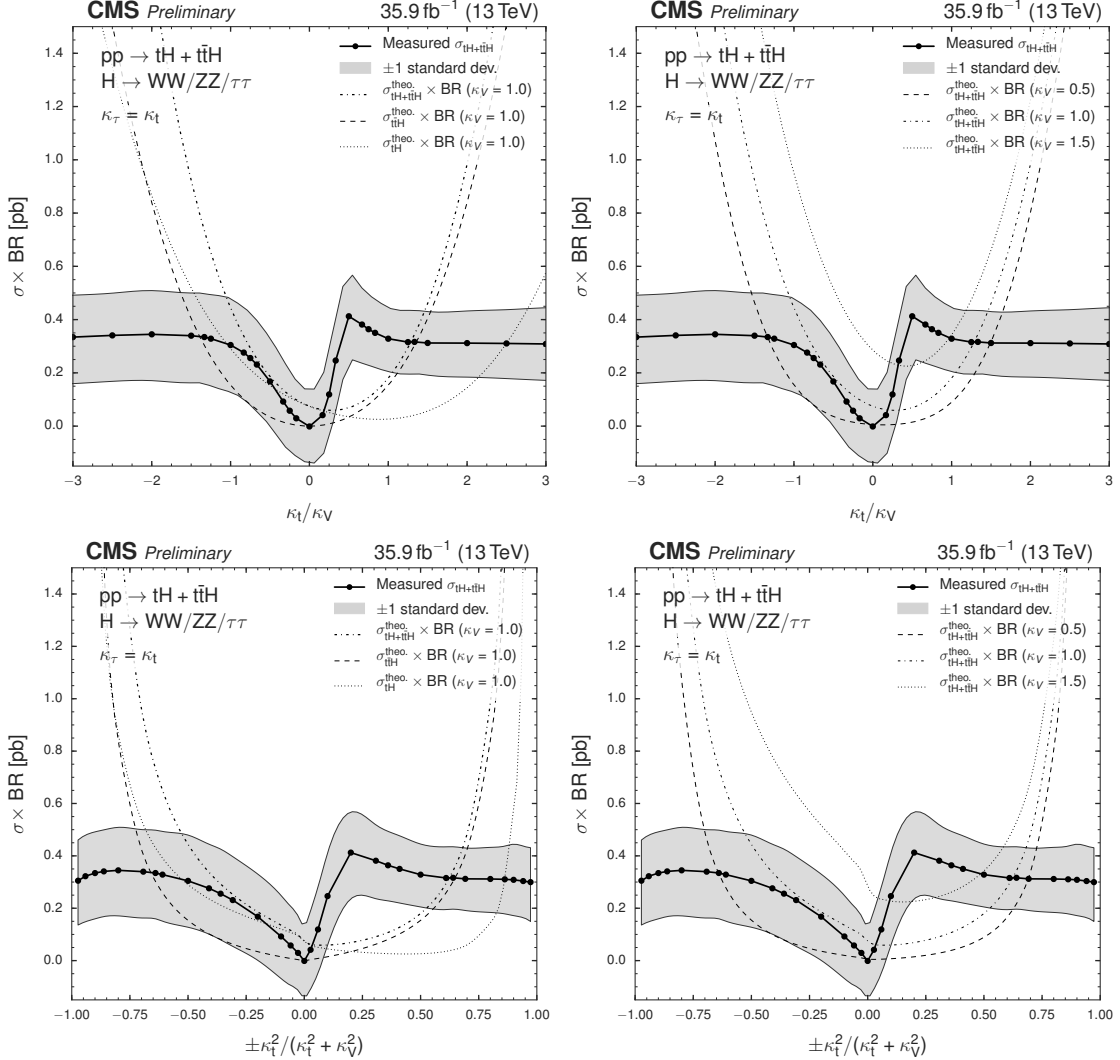


Figure 6.37: Best fit values of the combined $tH + t\bar{H}$ cross section times modified BR as a function of κ_t/κ_V (top) and $\text{sign}(\kappa_t/\kappa_V) \times \frac{\kappa_t^2}{(\kappa_t^2 + \kappa_V^2)}$ (bottom) for the combination of three lepton channel, $\mu^\pm\mu^\pm$, and $e^\pm\mu^\pm$ channel.

3244 Most of the nuisance parameters stay close to their initial values. The biggest
 3245 impact on the signal strength limits is associated to the fake rates for muons, followed
 3246 by the lepton efficiencies and nuisances associated to the QCD scales. The lower
 3247 impact in the ITC scenario is associated to the b-tag and tHq closure normalization
 3248 and shape nuisances, while in the SM scenario, nuisances associated to the forward
 3249 jet in tHq and P.D.F.s have the lower impact in the signal strength limit .

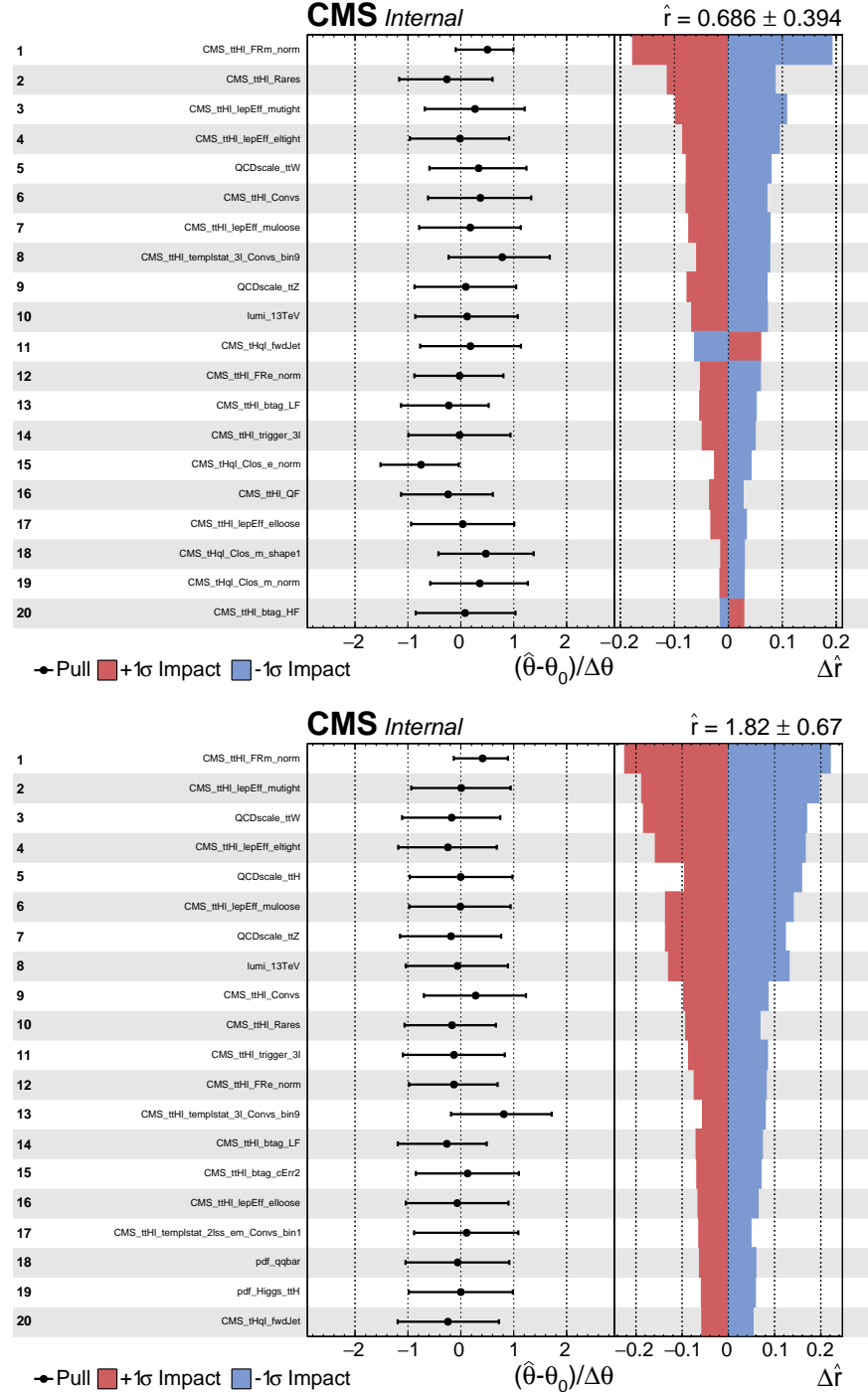


Figure 6.38: Post-fit pulls and impacts of the 20 nuisance parameters with largest impacts for the fit on the observed data, for the ITC (top) and SM (bottom) hypotheses.

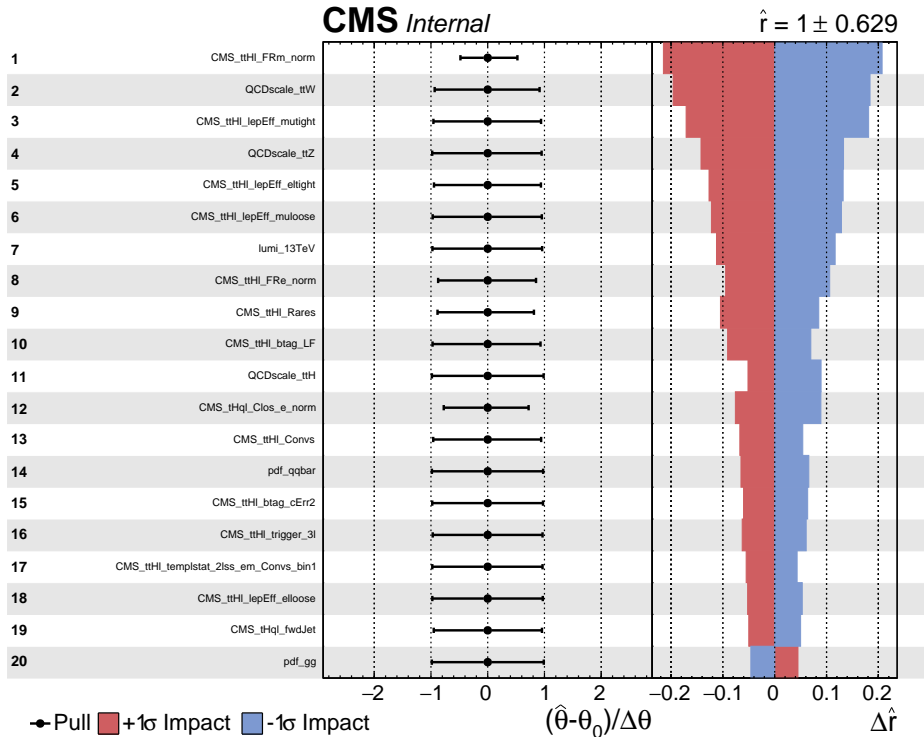


Figure 6.39: Post-fit pulls and impacts of the 20 nuisance parameters with largest impacts for a fit to the Asimov dataset with fixed signal strength, for the $\kappa_t/\kappa_V = -1.0$ hypothesis.

The sensitivity of the analysis is limited by systematic uncertainties, predominantly by those concerning the normalizations of the main background components, i.e., the non-prompt lepton estimation, the scale uncertainties for $t\bar{t}W$ and $t\bar{t}Z$, as well as by the uncertainties on the measured lepton efficiency.

3254 6.14 CP-mixing in tHq

3255 The sensitivity of the tH production process to the CP-mixing in the Higgs boson
 3256 sector was explored in Section 1.6; the theoretical model postulates the existence of a
 3257 generic spin-0 particle X_0 with CP-symmetry violating interaction with the top quark
 3258 but SM-like interaction with the W boson.

3259 The LHE reweighting procedure used in the ITC analysis is used in this CP-mixing

analysis; thus, a tX_0q simulation sample was produced, containing 21 event weights for different CP-mixing angles (α) ranging from values of $\cos\alpha = 1$ to $\cos\alpha = -1$ in steps of 0.1. The extremes of that range correspond to the previously studied points SM ($\kappa_t = 1$) and the ITC ($\kappa_t = -1$). The sample was produced at LO with MadGraph5_aMCatNLO, requiring the leptonic decay of the top quark. The cross section is scaled to its NLO prediction.

The set of BDTG input variables and training parameters are the same as for the $\kappa_t-\kappa_V$ analysis, as they already were optimized.

3268 Chapter 7

3269 Phase 1 FPix upgrade modules

3270 In chapter 2, a description of the CMS pixel detector used during the collection
3271 of the data sets used in this analysis, was presented. During the extended year-
3272 end technical stop (EYETS) 2017, the complete CMS pixel detector was replaced
3273 in order to support the full performance of the CMS experiment under the higher
3274 radiation conditions produced by the increasing instantaneous luminosities delivered
3275 by the LHC accelerator. It also was designed to address and mitigate the identified
3276 weaknesses in the previous system.

3277 In this chapter, a description of the upgraded detector will be presented, making
3278 emphasis on the contributions made by the University of Nebraska - Lincoln (UNL)
3279 HEP group, which consisted of the assembly of about 600 of the modules that make
3280 up the phase 1 upgraded forward pixel detector (FPix).

3281 7.0.1 The phase 1 FPix upgrade

3282 The previous pixel detector was designed to record efficiently and with high precision
3283 the first three space-points near the interaction region, in the range of $|\eta| < 2.5$, at
3284 a instantaneous luminosity of $1 \times 10^{34} \text{ cm}^{-2}\text{s}^{-1}$ and a bunch crossing each 25 ns.

3285 An average pileup of about 25 simultaneous overlapping events is expected. The
 3286 increasing luminosity would affects the performance of the detector reducing track
 3287 reconstruction efficiency, and increasing the data losses caused by the degradation of
 3288 the readout system; furthermore, if the LHC runs with 50 ns bunch spacing at twice
 3289 the luminosity, then the data losses would increase almost exponentially, to losses
 3290 of 50% for the innermost layer. An illustration of the foreseen reduced performance
 3291 in tracking efficiency and data loss is shown in Figure 7.1 in the case of simulated
 3292 $t\bar{t}$ events at instantaneous luminosities up to $2 \times 10^{34} \text{ cm}^{-2}\text{s}^{-1}$ with 25 ns and 50
 3293 ns bunch spacing. [?]. The increasing fake rate is also showed. In conclusion, the
 3294 previous pixel detector was not able to perform efficiently under the new luminosity,
 3295 pileup, radiation, and running conditions.

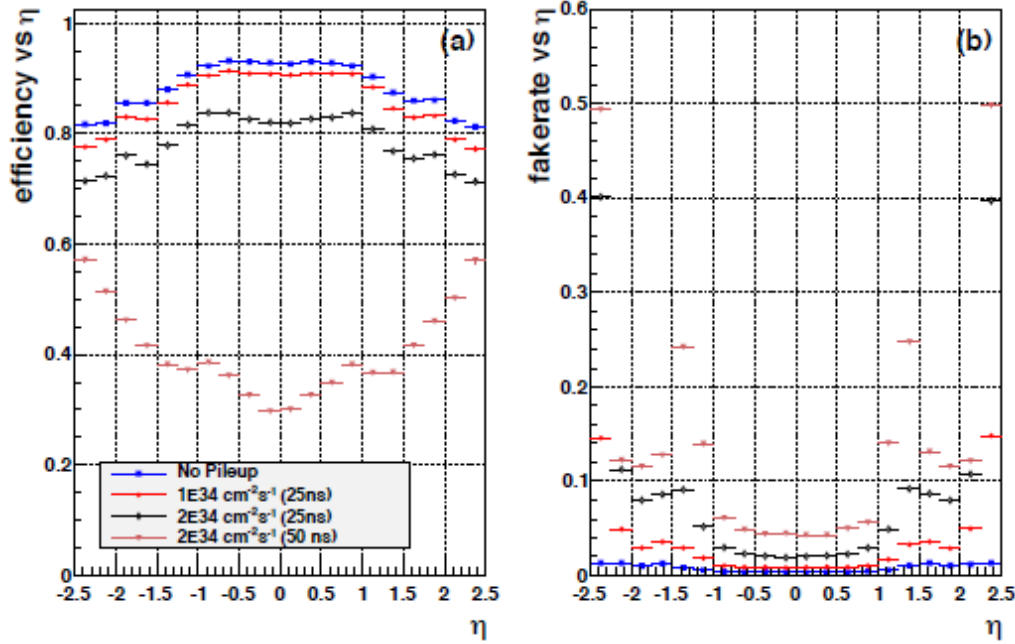


Figure 7.1: Expected performance of the previous pixel detector in simulated $t\bar{t}$ events:
 a) efficiency; b) fake rate. Conventions are the same for both plots.

3296 The present system is composed of four-layers/three-disks, low mass silicon pixel
 3297 detectors providing a high performance tracking in the high luminosity environment.

³²⁹⁸ **7.0.2 FPix module production line**

³²⁹⁹ **7.0.3 The Gluing stage**

³³⁰⁰ **7.0.4 The Encapsulation stage**

³³⁰¹ **7.0.5 The FPix module production yields**

³³⁰² **Appendix A**

³³⁰³ **Datasets and triggers**

Dataset name
/JetHT/Run2016X-23Sep2016-vY/MINIAOD
/HTMHT/Run2016X-23Sep2016-vY/MINIAOD
/MET/Run2016X-23Sep2016-vY/MINIAOD
/SingleElectron/Run2016X-23Sep2016-vY/MINIAOD
/SingleMuon/Run2016X-23Sep2016-vY/MINIAOD
/SinglePhoton/Run2016X-23Sep2016-vY/MINIAOD
/DoubleEG/Run2016X-23Sep2016-vY/MINIAOD
/MuonEG/Run2016X-23Sep2016-vY/MINIAOD
/DoubleMuon/Run2016X-23Sep2016-vY/MINIAOD
/Tau/Run2016B-23Sep2016-v3/MINIAOD
/JetHT/Run2016H-PromptReco-v3/MINIAOD
/HTMHT/Run2016H-PromptReco-v3/MINIAOD
/MET/Run2016H-PromptReco-v3/MINIAOD
/SingleElectron/Run2016H-PromptReco-v3/MINIAOD
/SingleMuon/Run2016H-PromptReco-v3/MINIAOD
/SinglePhoton/Run2016H-PromptReco-v3/MINIAOD
/DoubleEG/Run2016H-PromptReco-v3/MINIAOD
/MuonEG/Run2016H-PromptReco-v3/MINIAOD
/DoubleMuon/Run2016H-PromptReco-v3/MINIAOD

Table A.1: Full 2016 dataset used in the analysis. In the first section of the table are listed the 23Sep2016 samples; in the Run2016X-23Sep-vY label, X:B-G tag the run while Y:1,3 tag the version of the data sample. Second section list the PromptReco version of the dataset.

Same-sign dilepton (==2 muons)
HLT_Mu17_TrkIsoVVL_Mu8_TrkIsoVVL_DZ_v*
HLT_Mu17_TrkIsoVVL_TkMu8_TrkIsoVVL_DZ_v*
HLT_IsoMu22_v*
HLT_IsoTkMu22_v*
HLT_IsoMu22_eta2p1_v*
HLT_IsoTkMu22_eta2p1_v*
HLT_IsoMu24_v*
HLT_IsoTkMu24_v*
Same-sign dilepton (==2 electrons)
HLT_Ele23_Ele12_CaloIdL_TrackIdL_IsoVL_DZ_v*
HLT_Ele27_eta2p1_WP Loose_Gsf_v*
HLT_Ele27_WPTight_Gsf_v*
HLT_Ele25_eta2p1_WPTight_Gsf_v*
Same-sign dilepton (==1 muon, ==1 electron)
HLT_Mu23_TrkIsoVVL_Ele8_CaloIdL_TrackIdL_IsoVL_v*
HLT_Mu8_TrkIsoVVL_Ele23_CaloIdL_TrackIdL_IsoVL_v*
HLT_Mu23_TrkIsoVVL_Ele8_CaloIdL_TrackIdL_IsoVL_DZ_v*
HLT_Mu8_TrkIsoVVL_Ele23_CaloIdL_TrackIdL_IsoVL_DZ_v*
HLT_IsoMu22_v*
HLT_IsoTkMu22_v*
HLT_IsoMu22_eta2p1_v*
HLT_IsoTkMu22_eta2p1_v*
HLT_IsoMu24_v*
HLT_IsoTkMu24_v*
HLT_Ele27_WPTight_Gsf_v*
HLT_Ele25_eta2p1_WPTight_Gsf_v*
HLT_Ele27_eta2p1_WP Loose_Gsf_v*
Three lepton
HLT_DiMu9_Ele9_CaloIdL_TrackIdL_v*
HLT_Mu8_DiEle12_CaloIdL_TrackIdL_v*
HLT_TripleMu_12_10_5_v*
HLT_Ele16_Ele12_Ele8_CaloIdL_TrackIdL_v*
HLT_Mu23_TrkIsoVVL_Ele8_CaloIdL_TrackIdL_IsoVL_v*
HLT_Mu23_TrkIsoVVL_Ele8_CaloIdL_TrackIdL_IsoVL_DZ_v*
HLT_Mu8_TrkIsoVVL_Ele23_CaloIdL_TrackIdL_IsoVL_v*
HLT_Mu8_TrkIsoVVL_Ele23_CaloIdL_TrackIdL_IsoVL_DZ_v*
HLT_Ele23_Ele12_CaloIdL_TrackIdL_IsoVL_DZ_v*
HLT_Mu17_TrkIsoVVL_Mu8_TrkIsoVVL_DZ_v*
HLT_Mu17_TrkIsoVVL_TkMu8_TrkIsoVVL_DZ_v*
HLT_IsoMu22_v*
HLT_IsoTkMu22_v*
HLT_IsoMu22_eta2p1_v*
HLT_IsoTkMu22_eta2p1_v*
HLT_IsoMu24_v*
HLT_IsoTkMu24_v*
HLT_Ele27_WPTight_Gsf_v*
HLT_Ele25_eta2p1_WPTight_Gsf_v*
HLT_Ele27_eta2p1_WP Loose_Gsf_v*

Table A.2: Table of high-level triggers considered in the analysis.

		<i>tHq</i>		<i>tHW</i>		
κ_V	κ_t	sum of weights	cross section [pb]	sum of weights	cross section [pb]	LHE weights
1.0	-3.0	35.700022	2.991	11.030445	0.6409	LHEweight_wgt[446]
1.0	-2.0	20.124298	1.706	5.967205	0.3458	LHEweight_wgt[447]
1.0	-1.5	14.043198	1.205	4.029093	0.2353	LHEweight_wgt[448]
1.0	-1.25	11.429338	0.9869	3.208415	0.1876	LHEweight_wgt[449]
1.0	-1.0		0.7927		0.1472	
1.0	-0.75	7.054998	0.6212	1.863811	0.1102	LHEweight_wgt[450]
1.0	-0.5	5.294518	0.4723	1.339886	0.07979	LHEweight_wgt[451]
1.0	-0.25	3.818499	0.3505	0.914880	0.05518	LHEweight_wgt[452]
1.0	0.0	2.627360	0.2482	0.588902	0.03881	LHEweight_wgt[453]
1.0	0.25	1.719841	0.1694	0.361621	0.02226	LHEweight_wgt[454]
1.0	0.5	1.097202	0.1133	0.233368	0.01444	LHEweight_wgt[455]
1.0	0.75	0.759024	0.08059	0.204034	0.01222	LHEweight_wgt[456]
1.0	1.0	0.705305	0.07096	0.273617	0.01561	LHEweight_wgt[457]
1.0	1.25	0.936047	0.0839	0.442119	0.02481	LHEweight_wgt[458]
1.0	1.5	1.451249	0.1199	0.709538	0.03935	LHEweight_wgt[459]
1.0	2.0	3.335034	0.2602	1.541132	0.08605	LHEweight_wgt[460]
1.0	3.0	10.516125	0.8210	4.391335	0.2465	LHEweight_wgt[461]
1.5	-3.0	45.281492	3.845	13.426212	0.7825	LHEweight_wgt[462]
1.5	-2.0	27.606715	2.371	7.809713	0.4574	LHEweight_wgt[463]
1.5	-1.5	20.476088	1.784	5.594971	0.3290	LHEweight_wgt[464]
1.5	-1.25	17.337465	1.518	4.635978	0.2749	LHEweight_wgt[465]
1.5	-1.0	14.483302	1.287	3.775902	0.2244	LHEweight_wgt[466]
1.5	-0.75	11.913599	1.067	3.014744	0.1799	LHEweight_wgt[467]
1.5	-0.5	9.628357	0.874	2.352505	0.1410	LHEweight_wgt[468]
1.5	-0.25	7.627574	0.702	1.789184	0.1081	LHEweight_wgt[469]
1.5	0.0	5.911882	0.5577	1.324946	0.08056	LHEweight_wgt[470]
1.5	0.25	4.479390	0.4365	0.959295	0.05893	LHEweight_wgt[471]
1.5	0.5	3.331988	0.3343	0.692727	0.04277	LHEweight_wgt[472]
1.5	0.75	2.469046	0.2558	0.525078	0.03263	LHEweight_wgt[473]
1.5	1.0	1.890565	0.2003	0.456347	0.02768	LHEweight_wgt[474]
1.5	1.25	1.596544	0.1689	0.486534	0.02864	LHEweight_wgt[475]
1.5	1.5	1.586983	0.1594	0.615638	0.03509	LHEweight_wgt[476]
1.5	2.0	2.421241	0.2105	1.170602	0.06515	LHEweight_wgt[477]
1.5	3.0	7.503280	0.5889	3.467546	0.1930	LHEweight_wgt[478]
0.5	-3.0	27.432685	2.260	8.929074	0.5136	LHEweight_wgt[479]
0.5	-2.0	13.956013	1.160	4.419093	0.2547	LHEweight_wgt[480]
0.5	-1.5	8.924438	0.7478	2.757611	0.1591	LHEweight_wgt[481]
0.5	-1.25	6.835341	0.5726	2.075247	0.1204	LHEweight_wgt[482]
0.5	-1.0	5.030704	0.4273	1.491801	0.08696	LHEweight_wgt[483]
0.5	-0.75	3.510528	0.2999	1.007273	0.05885	LHEweight_wgt[484]
0.5	-0.5	2.274811	0.1982	0.621663	0.03658	LHEweight_wgt[485]
0.5	-0.25	1.323555	0.1189	0.334972	0.01996	LHEweight_wgt[486]
0.5	0.0	0.656969	0.06223	0.147253	0.008986	LHEweight_wgt[487]
0.5	0.25	0.274423	0.02830	0.058342	0.003608	LHEweight_wgt[488]
0.5	0.5	0.176548	0.01778	0.068404	0.003902	LHEweight_wgt[489]
0.5	0.75	0.363132	0.03008	0.177385	0.009854	LHEweight_wgt[490]
0.5	1.0	0.834177	0.06550	0.385283	0.02145	LHEweight_wgt[491]
0.5	1.25	1.589682	0.1241	0.692099	0.03848	LHEweight_wgt[492]
0.5	1.5	2.629647	0.2047	1.097834	0.06136	LHEweight_wgt[493]
0.5	2.0	5.562958	0.4358	2.206057	0.1246	LHEweight_wgt[494]
0.5	3.0	14.843102	1.177	5.609519	0.3172	LHEweight_wgt[495]

Table A.3: κ_V and κ_t combinations generated for the two signal samples and their NLO cross sections. The *tHq* cross section is multiplied by the branching fraction of the enforced leptonic decay of the top quark (0.324) [150].

Sample	σ [pb]	*
TTWJetsToLNu_TuneCUETP8M1_13TeV-amcatnloFXFX-madspin-pythia8	0.2043	*
TTZToLLNuNu_M-10_TuneCUETP8M1_13TeV-amcatnlo-pythia8	0.2529	*
/store/cmst3/group/susy/gpetrucc/13TeV/u/TTLL_m1to10_L0_NoMS_for76X/	0.0283	
WGToLNuG_TuneCUETP8M1_13TeV-madgraphMLM-pythia8	585.8	
ZGTo2LG_TuneCUETP8M1_13TeV-amcatnloFXFX-pythia8	131.3	
TGJets_TuneCUETP8M1_13TeV_amcatnlo_madspin_pythia8	2.967	
TGJets_TuneCUETP8M1_13TeV_amcatnlo_madspin_pythia8	2.967	
TTGJets_TuneCUETP8M1_13TeV-amcatnloFXFX-madspin-pythia8	3.697	
WpWpJJ_EWK-QCD_TuneCUETP8M1_13TeV-madgraph-pythia8	0.03711	
ZZZ_TuneCUETP8M1_13TeV-amcatnlo-pythia8	0.01398	
WWZ_TuneCUETP8M1_13TeV-amcatnlo-pythia8	0.1651	
WZZ_TuneCUETP8M1_13TeV-amcatnlo-pythia8	0.05565	
WW_DoubleScattering_13TeV-pythia8	1.64	
tZq_ll_4f_13TeV-amcatnlo-pythia8_TuneCUETP8M1	0.0758	
ST_tW1l_5f_L0_13TeV-MadGraph-pythia8	0.01123	
TTTT_TuneCUETP8M1_13TeV-amcatnlo-pythia8	0.009103	
WZTo3LNu_TuneCUETP8M1_13TeV-powheg-pythia8	4.4296	
ZZTo4L_13TeV_powheg_pythia8	1.256	
TTJets_SingleLeptFromTbar_TuneCUETP8M1_13TeV-madgraphMLM-pythia8	182.1754	*
TTJets_SingleLeptFromT_TuneCUETP8M1_13TeV-madgraphMLM-pythia8	182.1754	*
TTJets_DiLept_TuneCUETP8M1_13TeV-madgraphMLM-pythia8	87.3	*
DYJetsToLL_M-10to50_TuneCUETP8M1_13TeV-amcatnloFXFX-pythia8	18610	
DYJetsToLL_M-50_TuneCUETP8M1_13TeV-madgraphMLM-pythia8	6024	
WJetsToLNu_TuneCUETP8M1_13TeV-amcatnloFXFX-pythia8	61526.7	
ST_tW_top_5f_inclusiveDecays_13TeV-powheg-pythia8_TuneCUETP8M1	35.6	
ST_tW_antitop_5f_inclusiveDecays_13TeV-powheg-pythia8_TuneCUETP8M1	35.6	
ST_t-channel_4f_leptonDecays_13TeV-amcatnlo-pythia8_TuneCUETP8M1	70.3144	
ST_t-channel_antitop_4f_leptonDecays_13TeV-powheg-pythia8_TuneCUETP8M1	26.2278	
ST_s-channel_4f_leptonDecays_13TeV-amcatnlo-pythia8_TuneCUETP8M1	3.68064	
WWTo2L2Nu_13TeV-powheg	10.481	
ttWJets_13TeV_madgraphMLM	0.6105	
ttZJets_13TeV_madgraphMLM	0.5297/0.692	

Table A.4: List of background samples used in this analysis (CMSSW 80X). The first section of the table lists the samples used in simulation to extract the final yields and shapes; the second section lists the samples of the processes for which the yields are estimated from data. The MC simulation is used to design the data driven methods and in the derivation of the associated systematic uncertainties. The third section list the leading order $t\bar{t}W$ and $t\bar{t}Z$ samples, which in addition to the ones marked with a *, where used in the BDT training.

3304 **Appendix B**

3305 **Aditional plots**

3306 **B.1 Pre-selection kinematic variables**

3307 Figures B.1, B.2 and B.3 show the distributions of some relevant kinematic variables,
3308 normalized to the cross section of the respective processes and to the integrated
3309 luminosity.

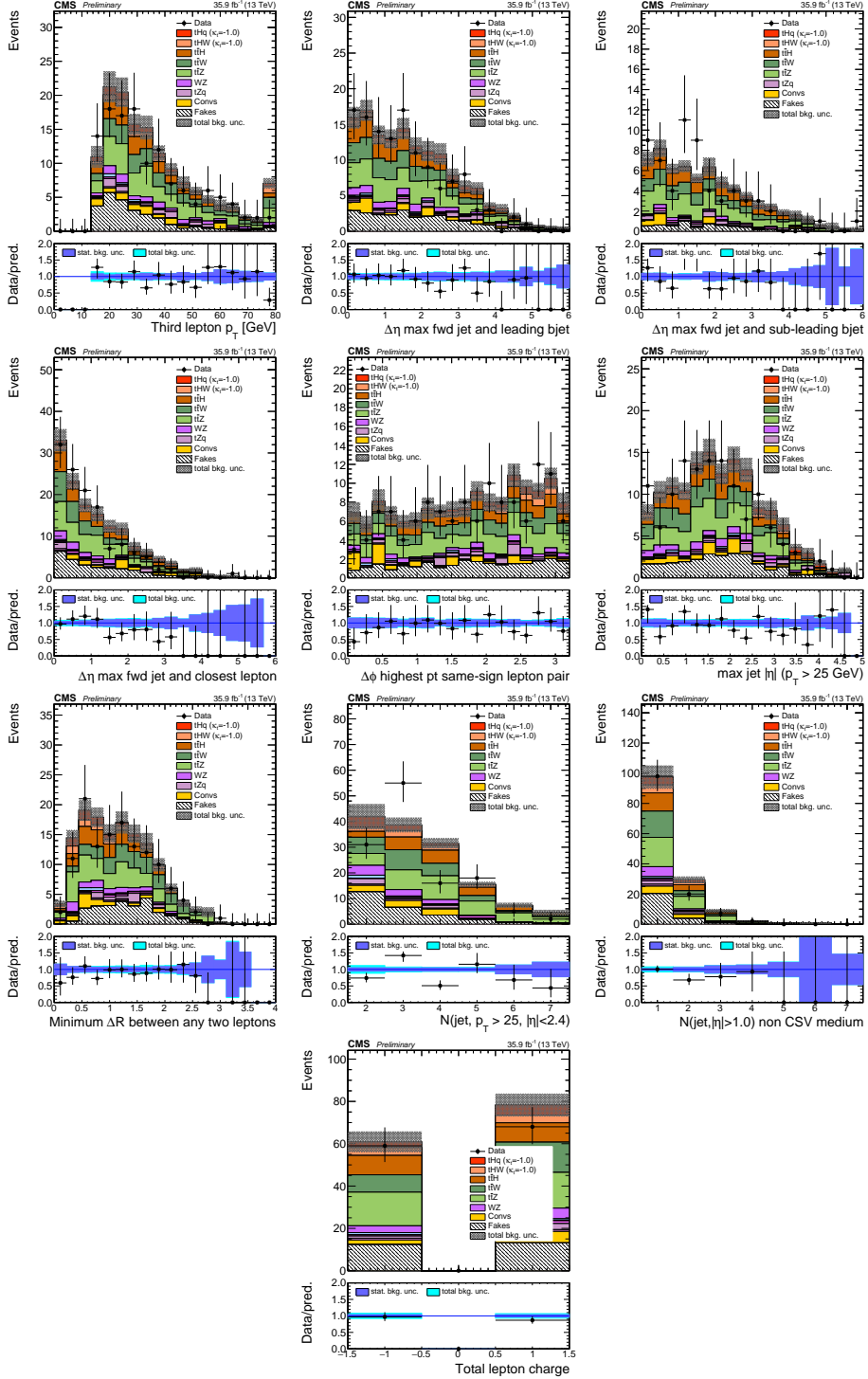


Figure B.1: Distributions of input variables to the BDT for signal discrimination, three lepton channel, normalized to their cross section and to 35.9 fb^{-1} .

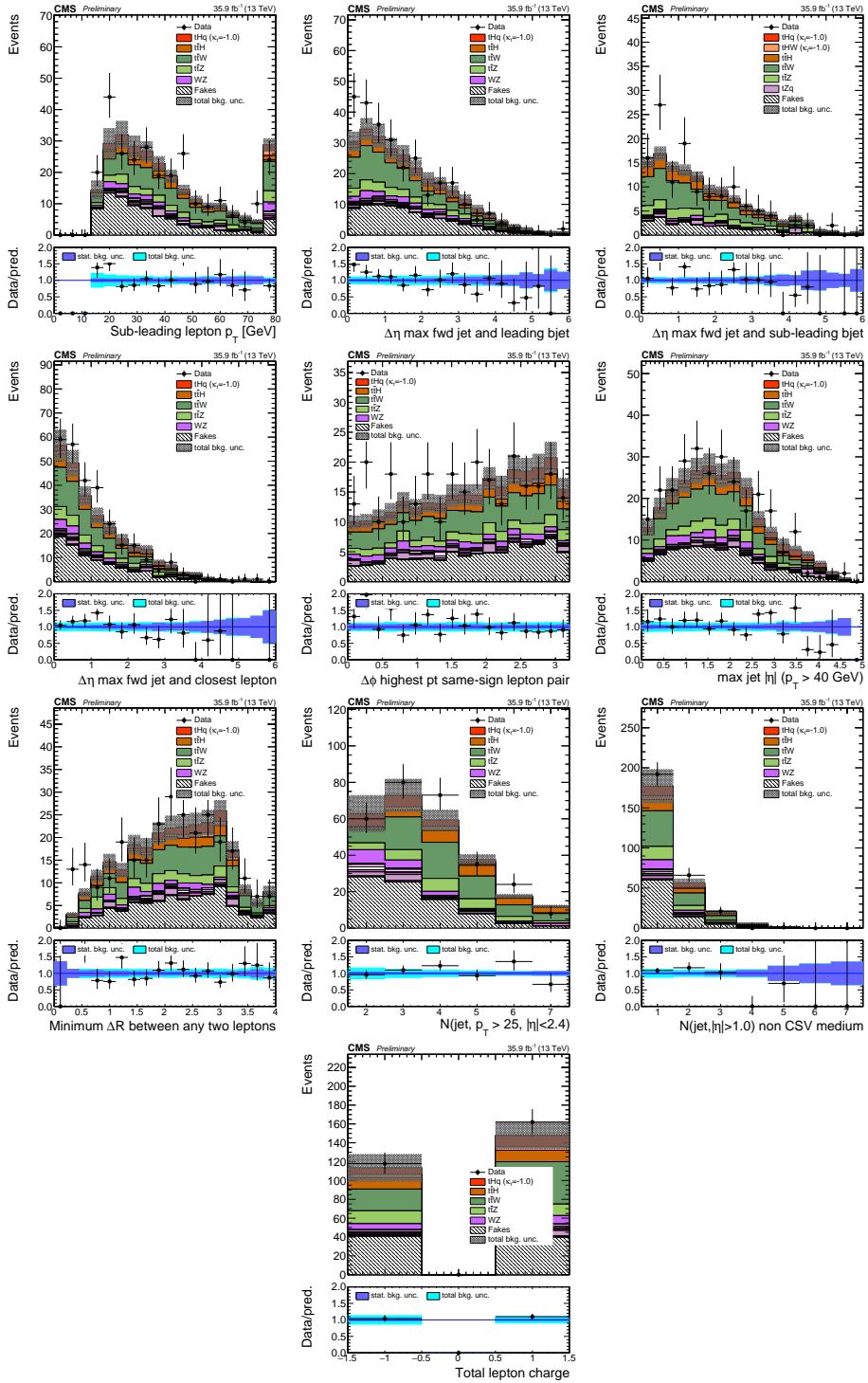


Figure B.2: Distributions of input variables to the BDT for signal discrimination, in $\mu^\pm \mu^\pm$ channel, normalized to their cross section and to 35.9fb^{-1} .

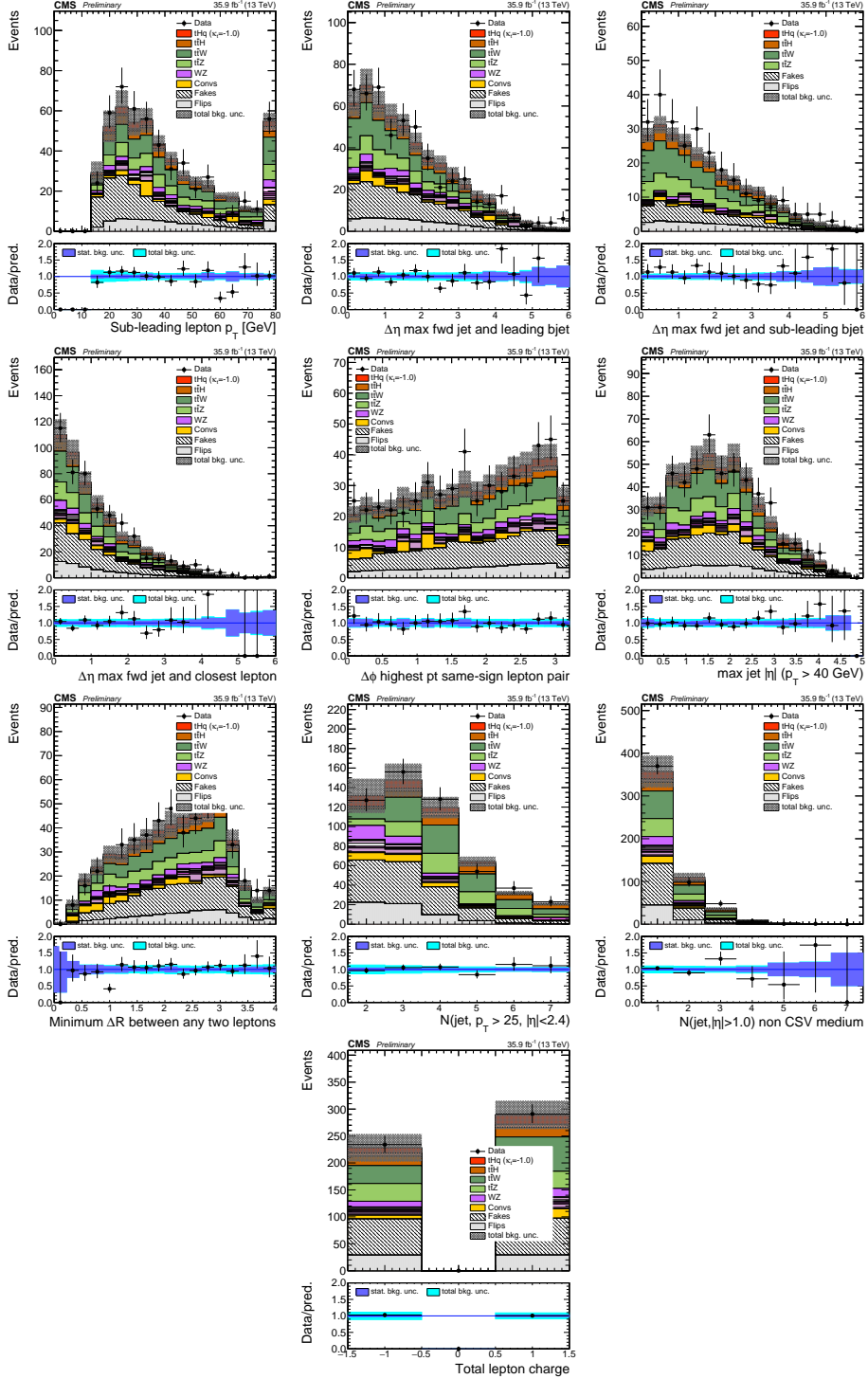


Figure B.3: Distributions of input variables to the BDT for signal discrimination, in $e^\pm\mu^\pm$ channel, normalized to their cross section and to 35.9 fb^{-1} .

3310 B.2 BDTG input variables for $2lss$ channel

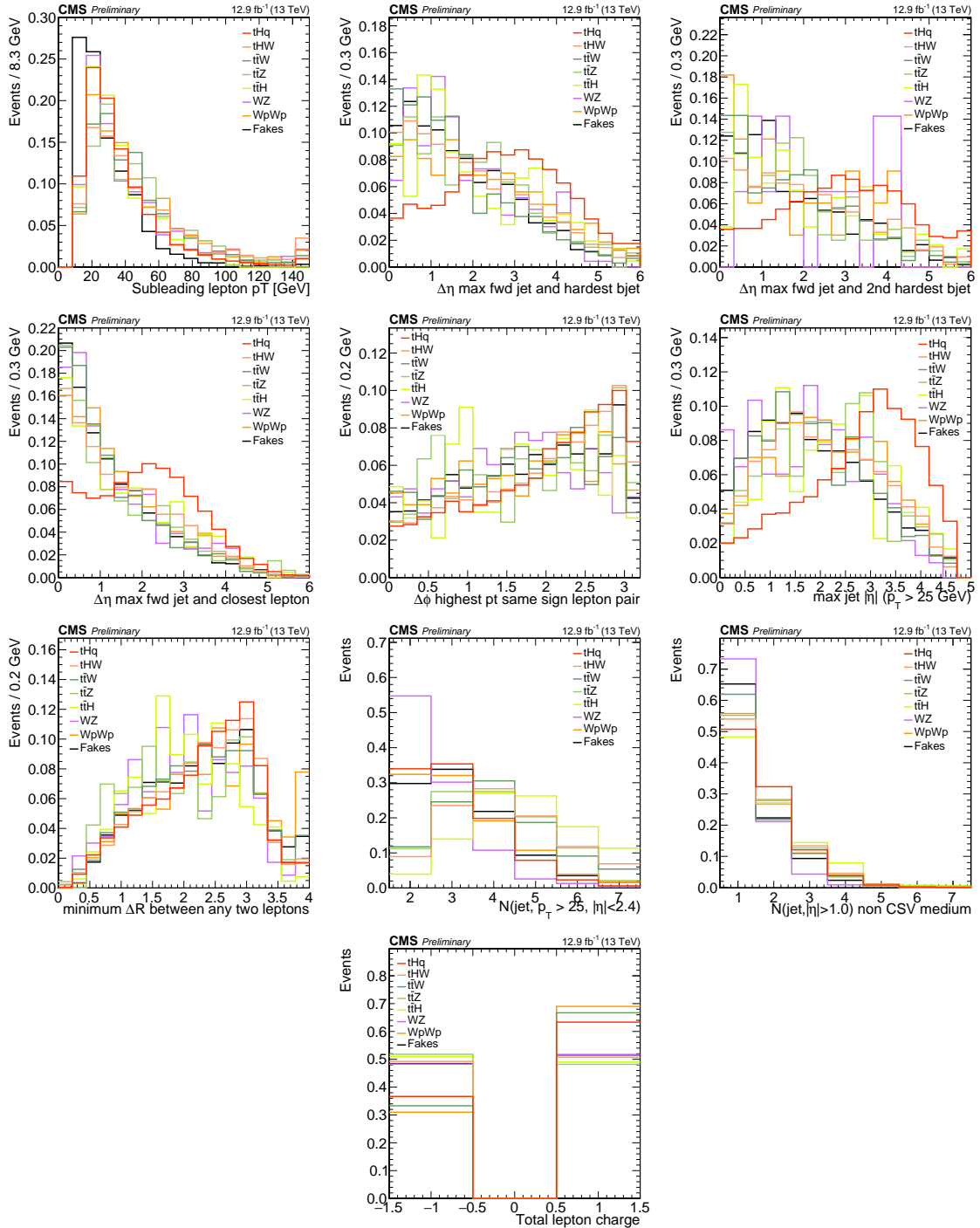


Figure B.4: Distributions of input variables to the BDT for signal discrimination, two lepton same sign channel.

3311 **B.3 Input variables distributions from BDTG**
 3312 classifiers

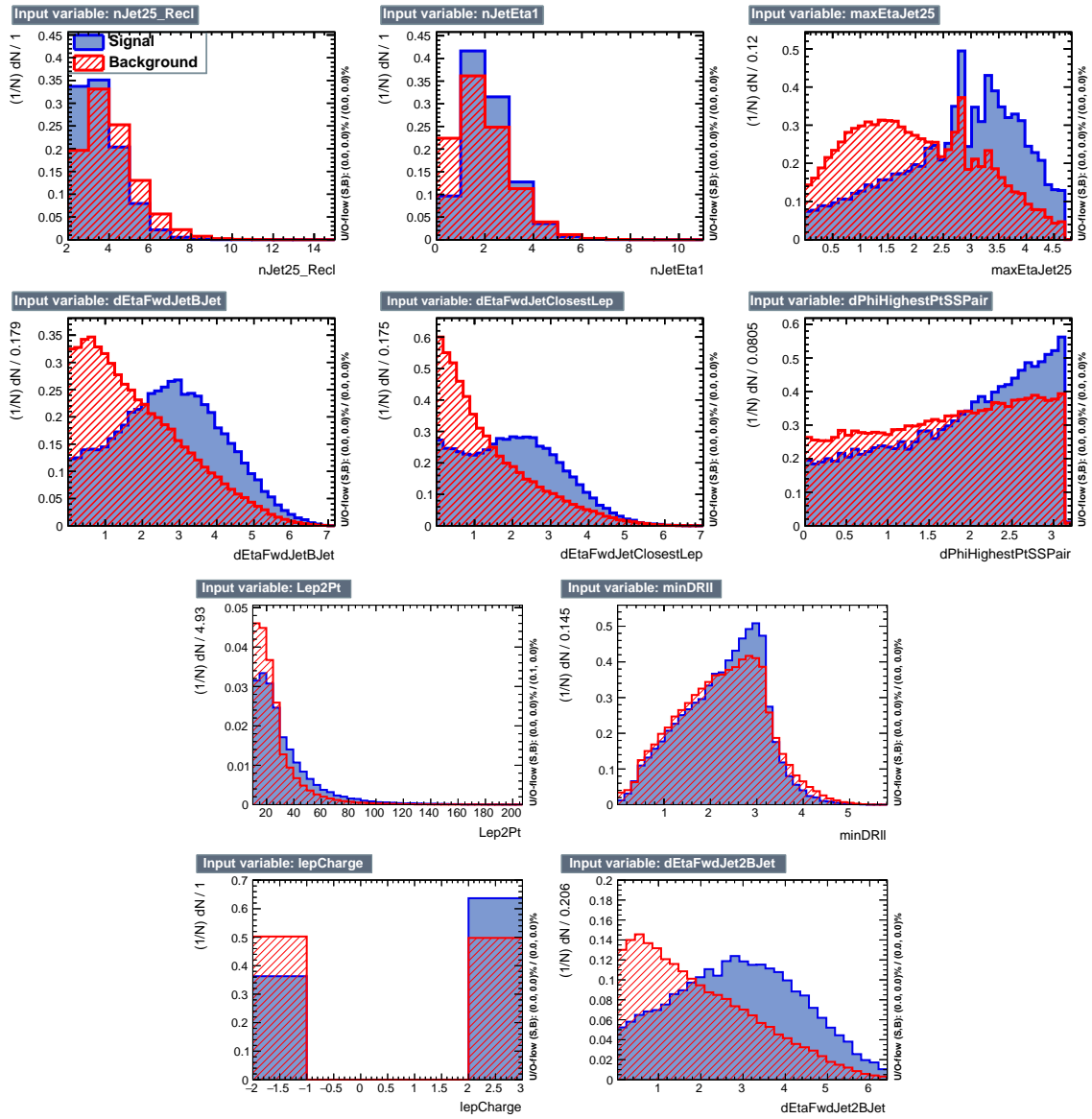


Figure B.5: BDT input variables as seen by BDTG classifier for the $2lss$ channel, tHq signal (blue) discriminated against $t\bar{t}$ background (red).

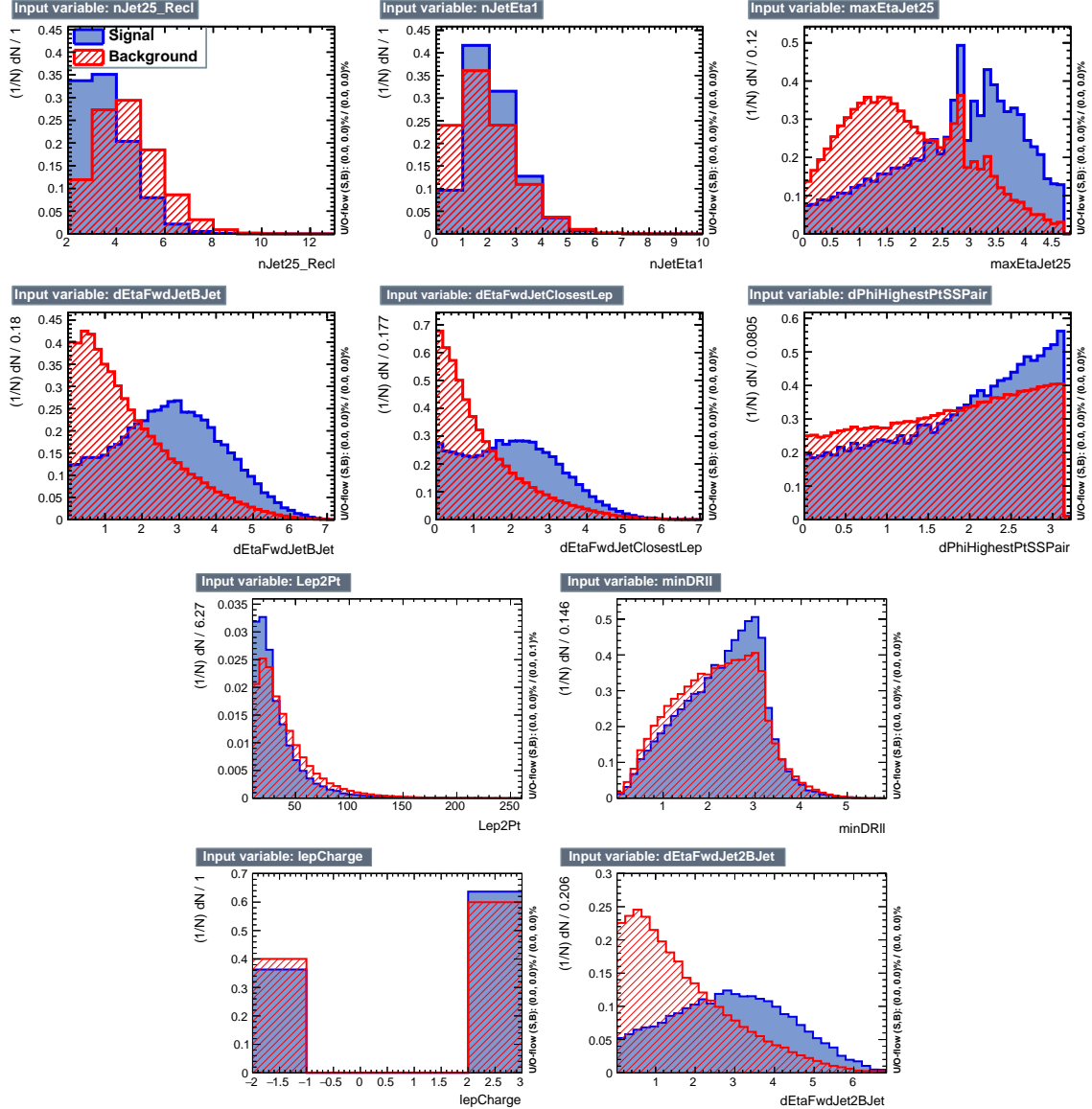


Figure B.6: BDT input variables as seen by BDTG classifier for the $2lss$ channel, tHq signal(blue) discriminated against $t\bar{t}V$ background (red).

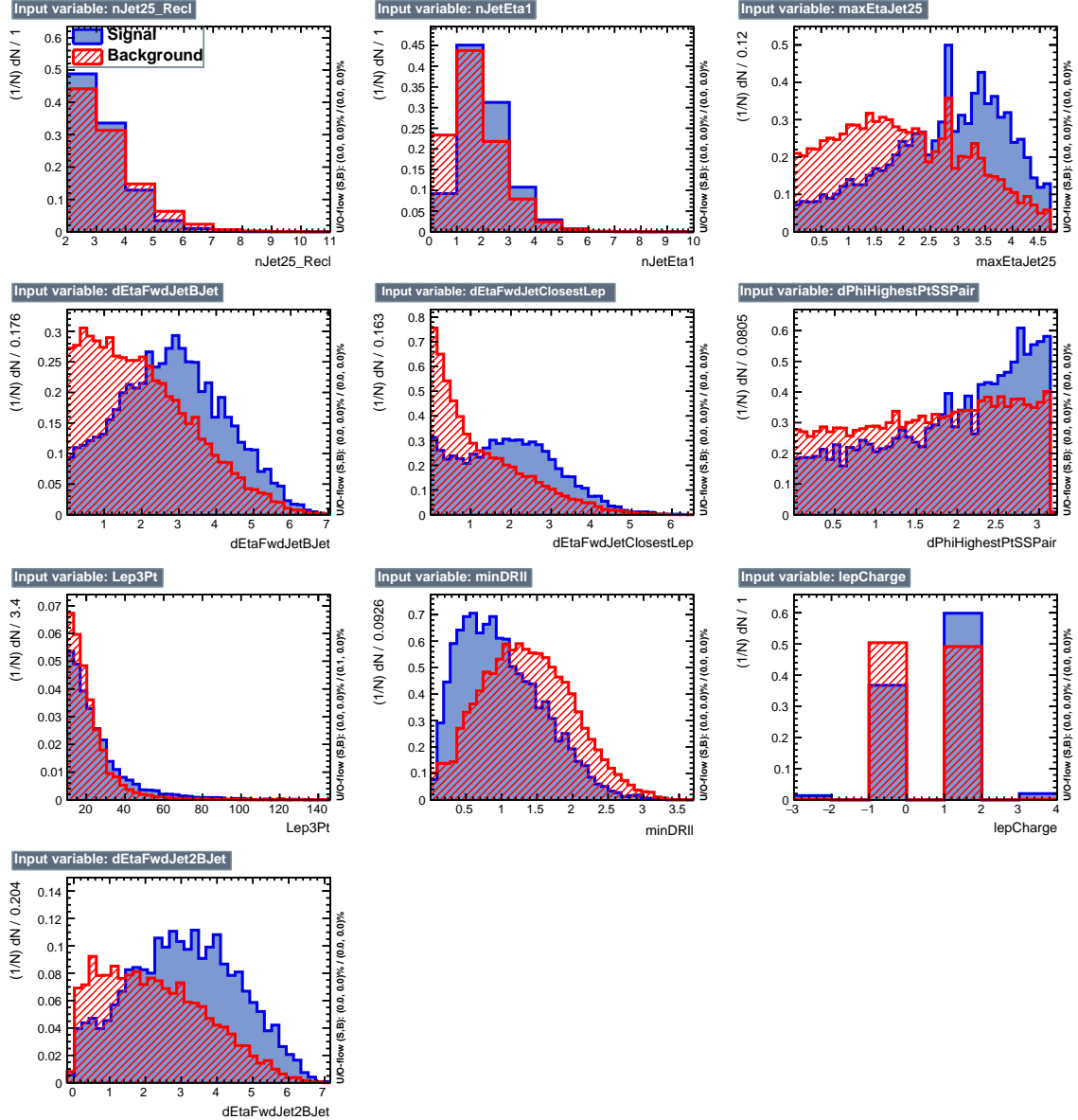


Figure B.7: BDT input variables as seen by BDTG classifier for the $3l$ channel, tHq signal (blue) discriminated against $t\bar{t}$ background (red).

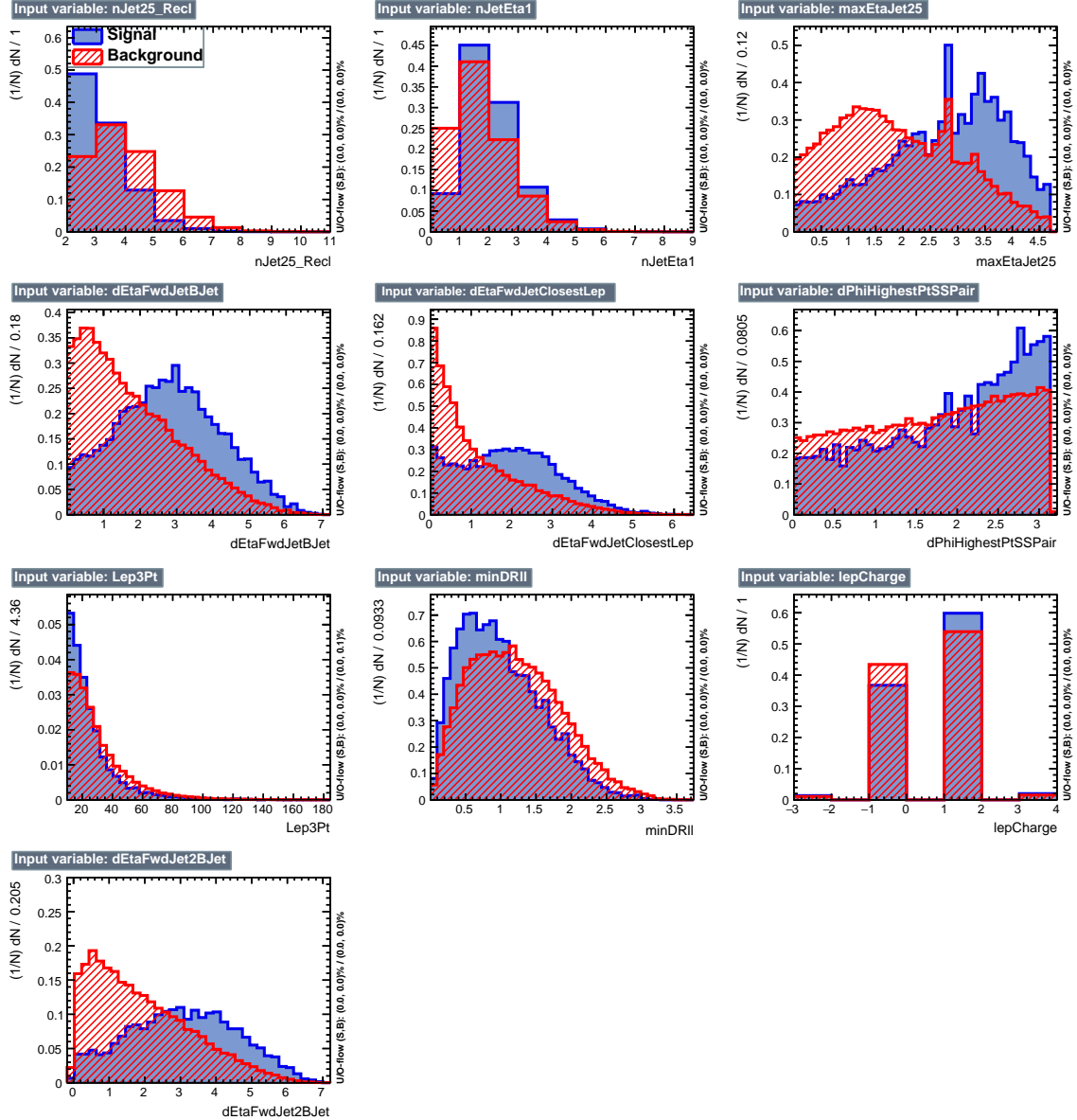


Figure B.8: BDT input variables as seen by BDTG classifier for the $3l$ channel, tHq signal (blue) discriminated against $t\bar{t}V$ background (red).

3313 B.4 Pulls and impacts

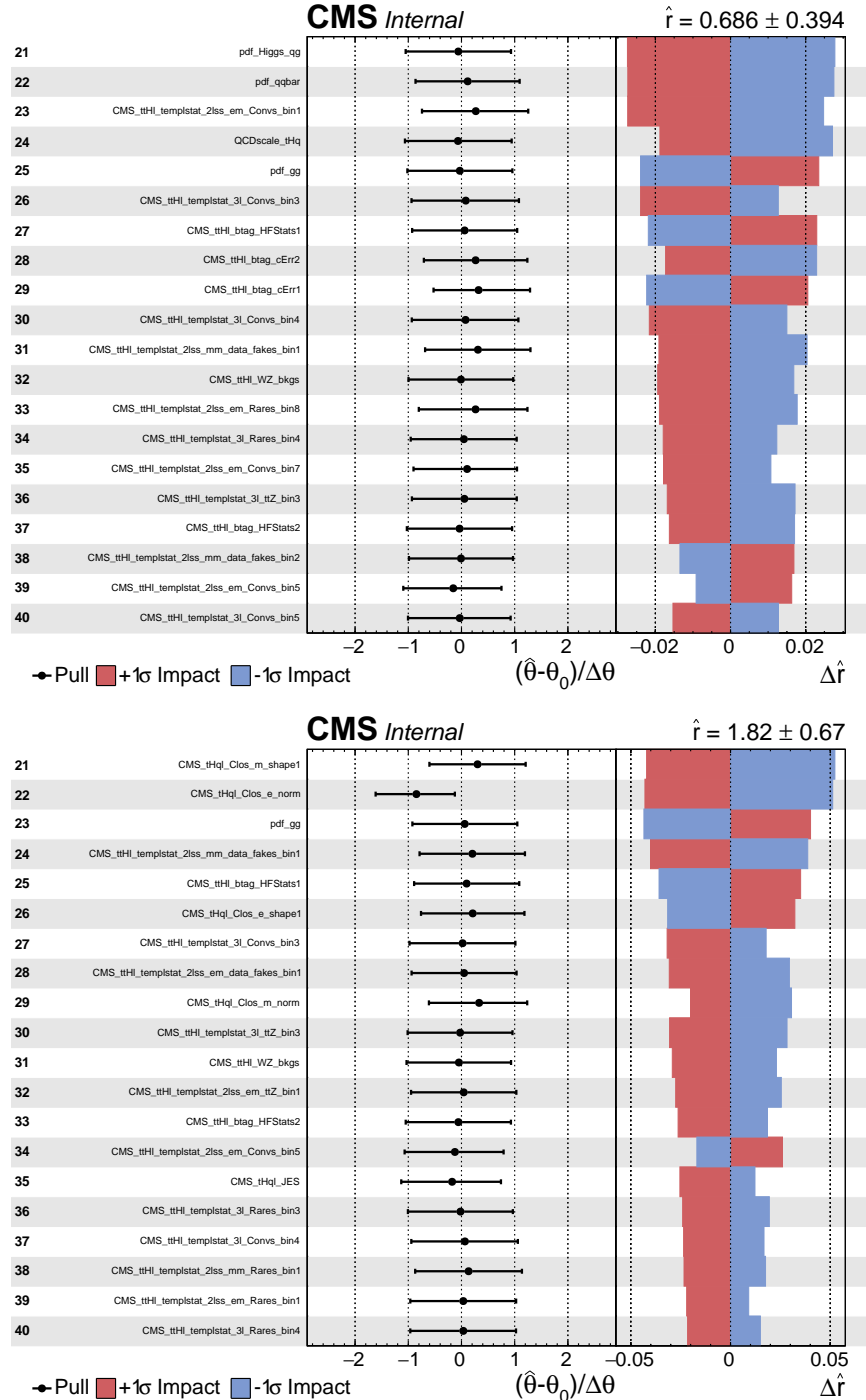


Figure B.9: Post-fit pulls and impacts of the next 20 nuisance parameters with largest impacts for the fit on the observed data, for the ITC (top) and SM (bottom) hypotheses.

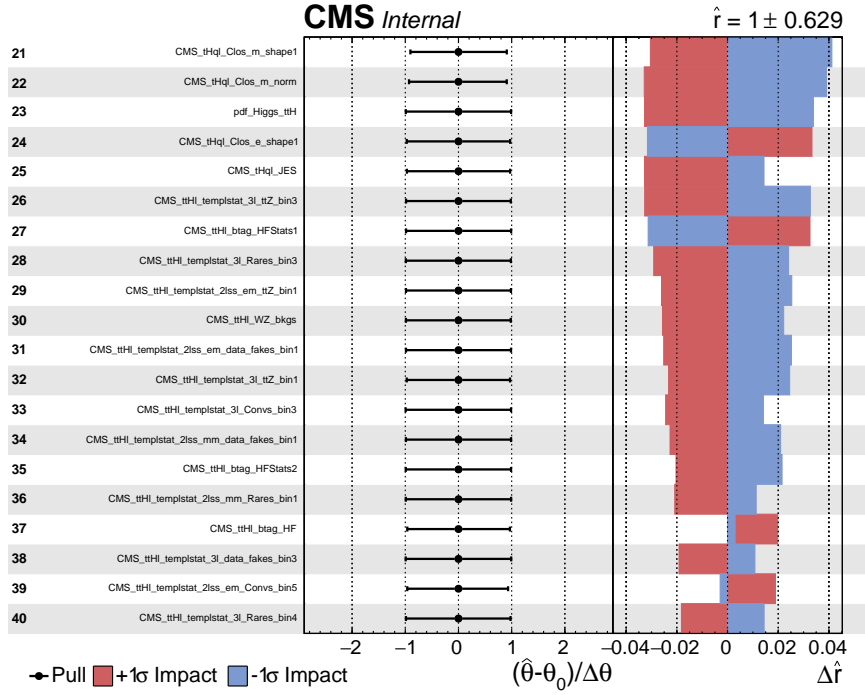


Figure B.10: Post-fit pulls and impacts of the next 20 nuisance parameters with largest impacts for a fit to the Asimov dataset with fixed signal strength, for the $\kappa_t/\kappa_V = -1.0$ hypothesis.

³³¹⁴ **Appendix C**

³³¹⁵ **Other binning strategies**

³³¹⁶ Two additional strategies of clustering regions in the 2D plane of $BDTG_{tt}$ vs $BDTG_{ttV}$
³³¹⁷ into bins were attempted, following studies done and documented in great detail in
³³¹⁸ Reference [149]. A brief description is provided in the following.

³³¹⁹ **Clustering by S/B ratio**

³³²⁰ In this method, the 2D plane is clustered into a given number of bins corresponding
³³²¹ to regions where S/B is within a certain range. The bin borders are determined
³³²² such that the number of background events in each bin is approximately equal. The
³³²³ resulting regions for $2lss$ and $3l$ events are shown in Figure C.1, while the expected
³³²⁴ distribution of signal and dominant backgrounds are shown in Figure C.2.

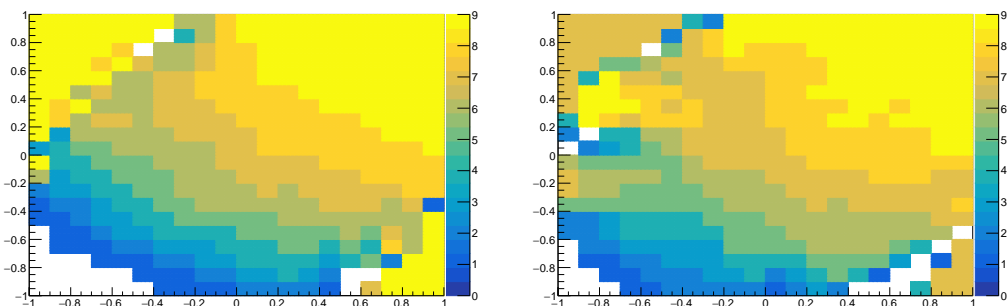


Figure C.1: Binning by S/B regions for $2lss$ (left) and $3l$ (right).

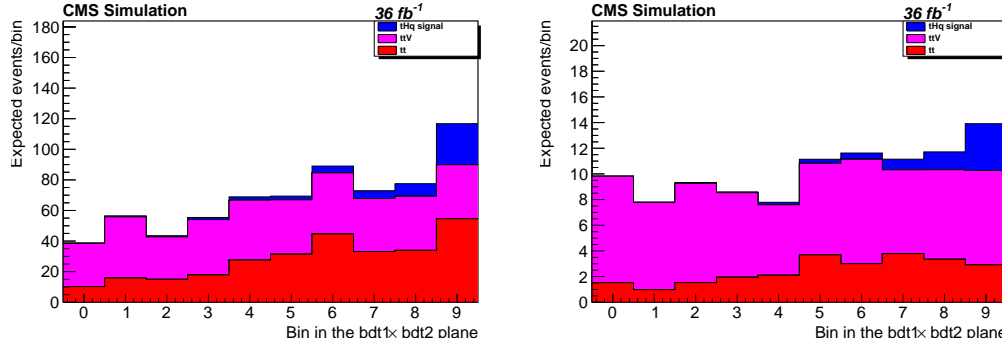


Figure C.2: Final bins (corresponding to S/B regions in the 2D plane) for $2lss$ and $3l$ (right).

Using this method, the resulting limits (for the $\kappa_t = -1, \kappa_V = 1$ scenario) are about 20% worse than with the binning in Section 6.9.6: $\mu^\pm\mu^\pm$ changed from 1.82 to 2.15, $3l$ changed from 1.52 to 1.75.

***k*-Means geometric clustering**

This method employs a recursive application of the k -means algorithm (see Appendix D in Reference [149]) to separate the 2D plane into geometric regions. The resulting clustering (using the $t\bar{t}H$ multilepton code on tHq signal and $t\bar{t}$ and $t\bar{t}V$ background events) are shown in Figure C.3. The expected distribution of events for the signal and dominant backgrounds in these bins is shown in Fig. C.4.

Similarly to the S/B ratio binning, the limits using the k -means clustering are significantly worse than those of the bins described before. In the $\mu^\pm\mu^\pm$ channel, the limit deteriorates from 1.82 to 2.05, whereas in $3l$ it changes from 1.58 to 1.78.

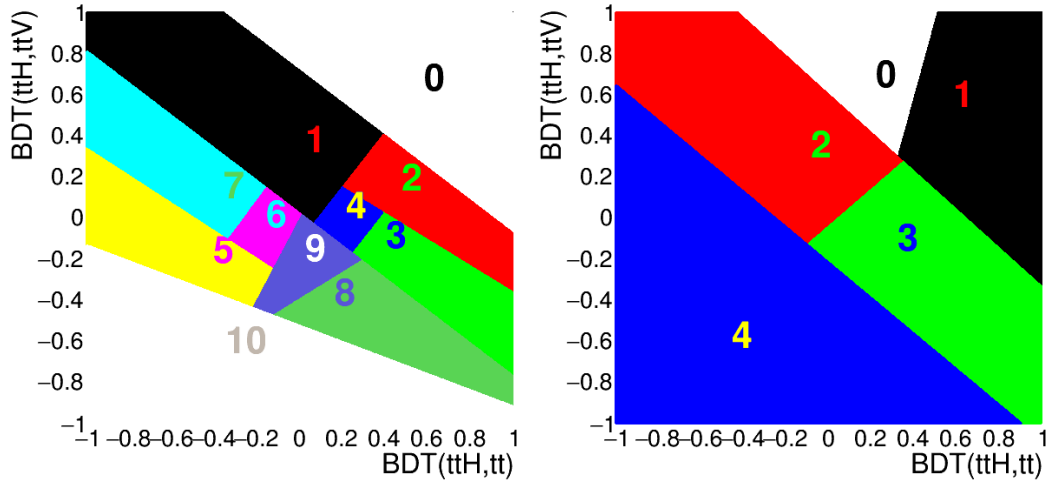


Figure C.3: Binning into geometric regions using a k -means algorithm for $2lss$ (left) and $3l$ (right).

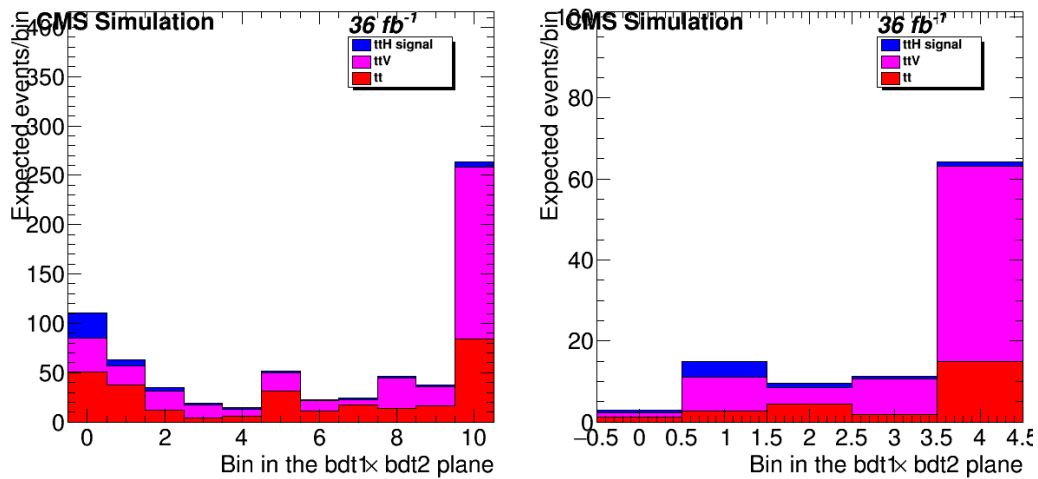


Figure C.4: Final bins using a k -means algorithm for $2lss$ (left) and $3l$ (right). Note that the bin numbering here is such that signal-like bins are lower.

³³³⁷ **Appendix D**

³³³⁸ **BDTG output variation with κ_V/κ_t**

³³³⁹ The BDTG classifier output was described in Section in the $\kappa_t = -1, \kappa_V = 1$ scenario; the
³³⁴⁰ change of BDTG classifiers output shape when varying the κ_V/κ_t coupling scenario
³³⁴¹ is shown in Figure D.1 in the $3l$ channel for five different values of κ_t , with κ_V fixed
at 1.0.

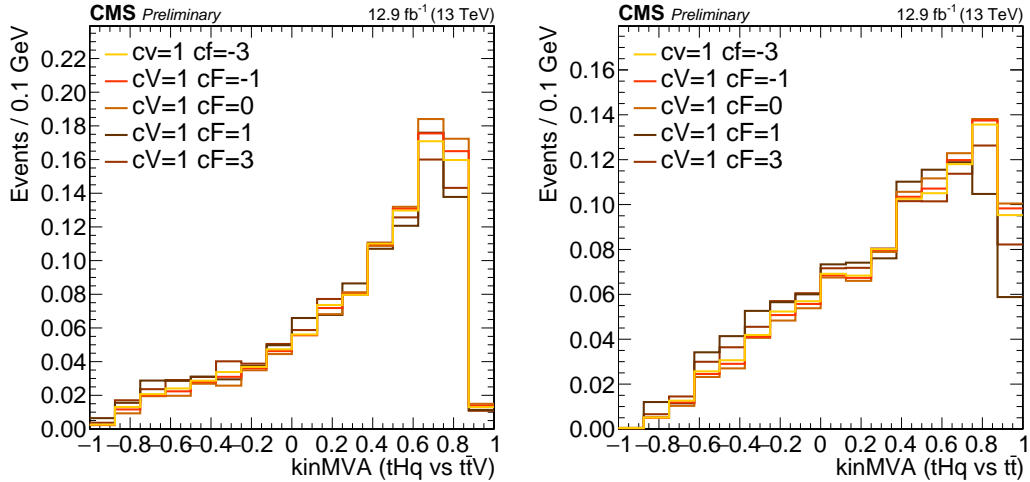


Figure D.1: Change of the BDTG classifiers output when varying κ_t coupling (κ_V is fixed at 1.0). Training vs. $t\bar{t}V$ (right) and vs. $t\bar{t}$ (left).

³³⁴²

³³⁴³ Given that the BDT classifier output shape does not change, it is enough to train
³³⁴⁴ the BDTG in one of the κ_t/κ_V points. It was chosen the SM point.

³³⁴⁵ **Appendix E**

³³⁴⁶ **tHq - $t\bar{t}H$ overlap**

³³⁴⁷ This section provides a quick overview of the differences and commonalities in event
³³⁴⁸ selections between this analysis and the $t\bar{t}H$ multilepton search [149]. The object
³³⁴⁹ selections of the two analysis are perfectly synchronized due to shared frameworks
³³⁵⁰ and samples. The only exception is the usage of forward jets ($|\eta| > 2.4, p_T > 40$ GeV)
³³⁵¹ in this analysis. Such jets are not considered in the $t\bar{t}H$ analysis.

³³⁵² Table E.1 gives an overview of the main differences in the event selections. Here,
³³⁵³ $E_T^{miss}_{LD}$ is defined as $E_T^{miss} \times 0.00397 + H_T^{miss} \times 0.00265$. Untagged jets in the tHq
³³⁵⁴ analysis are jets that do not pass the CSV loose working point and are either central
³³⁵⁵ ($|\eta| < 2.4, p_T > 25$ GeV) or forward ($|\eta| < 2.4, p_T > 40$ GeV). All jets in the $t\bar{t}H$ analysis
³³⁵⁶ are selected with $p_T > 25$ GeV. Lepton p_T cuts and the trigger selections are identical.

Channel	tHq	$t\bar{t}H$
3l	Z veto, 15bGeV $N_{jets}^{\text{b, med.}} \geq 1$ ≥ 1 un-tagged jet	Z veto, 10 GeV $N_{jets}^{\text{b, med.}} \geq 1$ OR $N_{jets}^{\text{b, loose}} \geq 2$ $E_T^{miss}_{LD} > 0.2$ OR $N_{\text{centrl.}} \geq 4$
2lss	$N_{jets}^{\text{b, med.}} \geq 1$ ≥ 1 un-tagged jet	$N_{jets}^{\text{b, med.}} \geq 1$ OR $N_{jets}^{\text{b, loose}} \geq 2$ $N_{\text{central}} \geq 4$

Table E.1: Differences in event selection between this analysis and the $t\bar{t}H$ multilepton analysis.

3357 Table E.2 shows the total events yields in the individual channels, and the yield
 3358 of shared events between each channel, for the tHq signal sample, the $t\bar{t}H$ signal
 3359 sample, and the data. In the data, for the $3l$ channel, about 80% of events passing
 3360 the tHq selection also pass the $t\bar{t}H$ selection, constituting about 70% of that channel.
 3361 In the $2lss$ channel, about 50% of data events passing the tHq selection also pass the
 3362 $t\bar{t}H$ selection, but these events constitute almost 90% of the $t\bar{t}H$ selection in those
 3363 channels. Similar overlaps are also seen in the tHq and $t\bar{t}H$ signal samples.

3364 There is no migration between different channels and different selections, i.e., no
 3365 events passing the selection of a given tHq channel pass the selection of any other
 3366 channels of $t\bar{t}H$ and vice versa.

tHq sample	tHq	$t\bar{t}H$	Common	(% tHq)	(% $t\bar{t}H$)
$\mu^\pm\mu^\pm$	7400	2353	2166	29.3	92.1
$e^\pm\mu^\pm$	11158	3600	3321	29.8	92.2
$e^\pm e^\pm$	3550	1106	1025	28.9	92.7
$\ell\ell\ell$	3115	2923	2347	75.3	80.3

$t\bar{t}H$ sample	tHq	$t\bar{t}H$	Common	(% tHq)	(% $t\bar{t}H$)
$\mu^\pm\mu^\pm$	32612	28703	26547	81.4	92.5
$e^\pm\mu^\pm$	48088	42521	39164	81.4	92.1
$e^\pm e^\pm$	15476	12869	11896	76.9	92.4
$\ell\ell\ell$	26627	30598	25288	95.0	82.6

Data	tHq	$t\bar{t}H$	Common	(% tHq)	(% $t\bar{t}H$)
$\mu^\pm\mu^\pm$	280	160	140	50.0	87.5
$e^\pm\mu^\pm$	525	280	242	46.1	86.4
$e^\pm e^\pm$	208	90	79	38.0	87.8
$\ell\ell\ell$	126	154	104	82.5	67.5

Table E.2: Individual and shared event yields between this analysis (tHq) and $t\bar{t}H$ multilepton selections.

³³⁶⁷ **Appendix F**

³³⁶⁸ **Forward jet impact plots**

³³⁶⁹ The impact of the data/MC disagreement for forward jet η is observed to reduce with
³³⁷⁰ higher p_T cuts; Figures F.1, F.2 and F.3 show this reduction in the impact of the
³³⁷¹ forward jet η nuisance in the fit.

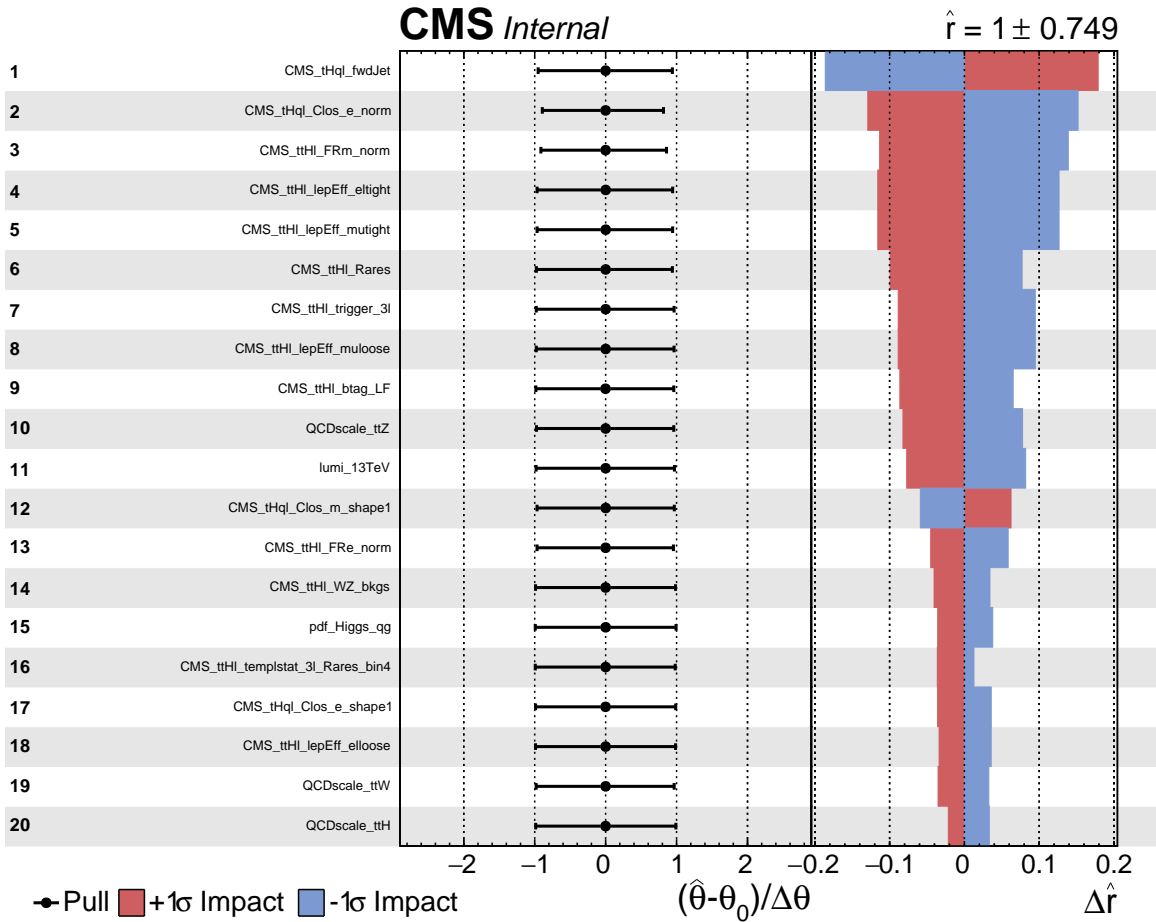


Figure F.1: Post-fit pulls and impacts of the 20 nuisance parameters with p_T cut 25 GeV for the forward jet.

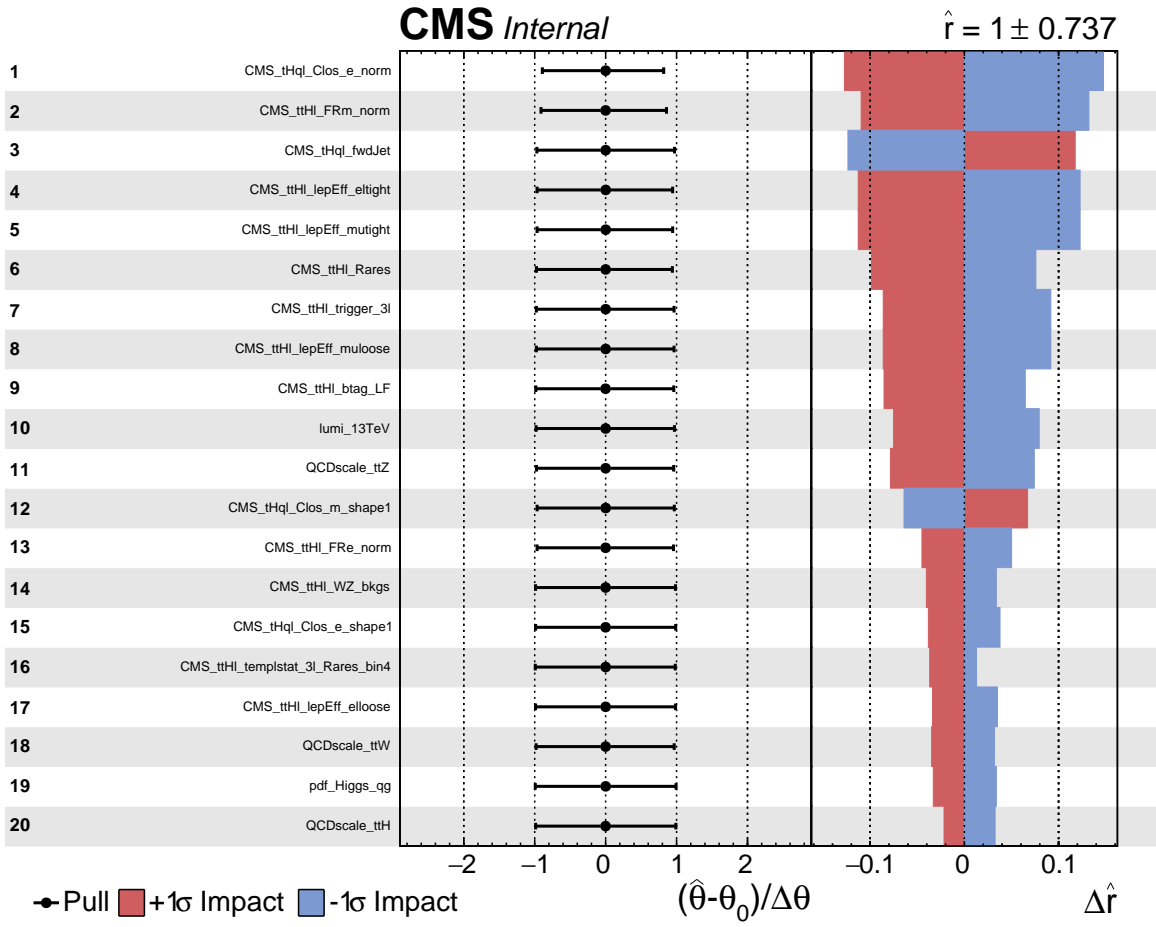


Figure F.2: Post-fit pulls and impacts of the 20 nuisance parameters with p_T cut 30 GeV for the forward jet.

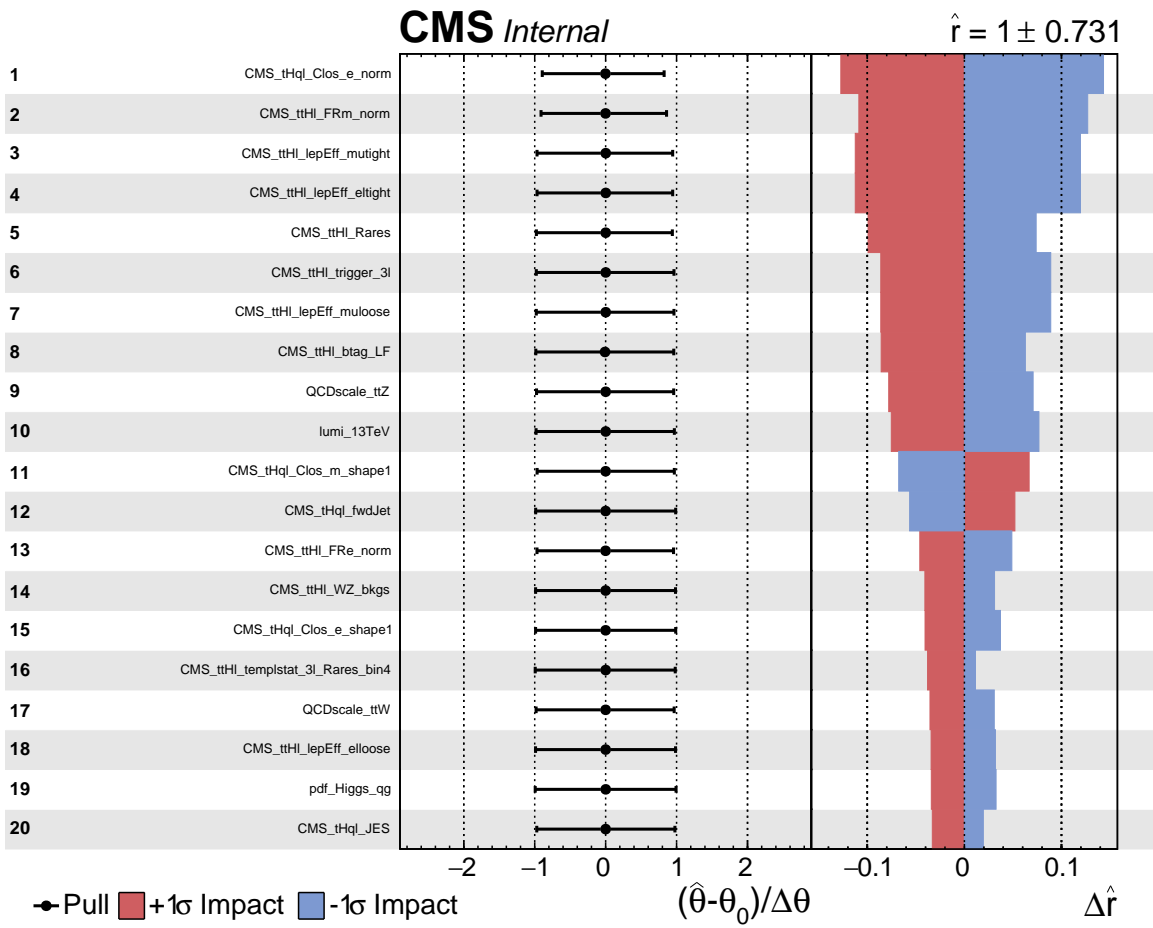


Figure F.3: Post-fit pulls and impacts of the 20 nuisance parameters with p_T cut 40 GeV for the forward jet.

³³⁷² **Appendix G**

³³⁷³ **Cross sections and Branching**

³³⁷⁴ **ratios scalings**

κ_V	κ_t	HWW	HZZ	H $\tau\tau$	H $\mu\mu$	Hbb	Hcc	H $\gamma\gamma$	HZ γ	Hgg
0.5	-6.0	0.0827	0.0827	11.9098	11.9098	0.3308	0.3308	0.3308	0.3308	0.3308
0.5	-4.0	0.1417	0.1417	9.0699	9.0699	0.5669	0.5669	0.5669	0.5669	0.5669
0.5	-3.0	0.1889	0.1889	6.7999	6.7999	0.7555	0.7555	0.7555	0.7555	0.7555
0.5	-2.5	0.2173	0.2173	5.4325	5.4325	0.8692	0.8692	0.8692	0.8692	0.8692
0.5	-2.0	0.2478	0.2478	3.9647	3.9647	0.9912	0.9912	0.9912	0.9912	0.9912
0.5	-1.5	0.2782	0.2782	2.5034	2.5034	1.1126	1.1126	1.1126	1.1126	1.1126
0.5	-1.333	0.2877	0.2877	2.0448	2.0448	1.1508	1.1508	1.1508	1.1508	1.1508
0.5	-1.25	0.2922	0.2922	1.8264	1.8264	1.1689	1.1689	1.1689	1.1689	1.1689
0.5	-1.0	0.3048	0.3048	1.2194	1.2194	1.2194	1.2194	1.2194	1.2194	1.2194
0.5	-0.833	0.3122	0.3122	0.8665	0.8665	1.2487	1.2487	1.2487	1.2487	1.2487
0.5	-0.75	0.3154	0.3154	0.7097	0.7097	1.2617	1.2617	1.2617	1.2617	1.2617
0.5	-0.667	0.3184	0.3184	0.5666	0.5666	1.2736	1.2736	1.2736	1.2736	1.2736
0.5	-0.5	0.3235	0.3235	0.3235	0.3235	1.2938	1.2938	1.2938	1.2938	1.2938
0.5	-0.333	0.3272	0.3272	0.1451	0.1451	1.3087	1.3087	1.3087	1.3087	1.3087
0.5	-0.25	0.3285	0.3285	0.0821	0.0821	1.3139	1.3139	1.3139	1.3139	1.3139
0.5	-0.167	0.3294	0.3294	0.0367	0.0367	1.3177	1.3177	1.3177	1.3177	1.3177
0.5	0.0	0.3302	0.3302	0.0000	0.0000	1.3207	1.3207	1.3207	1.3207	1.3207
0.5	0.167	0.3294	0.3294	0.0367	0.0367	1.3177	1.3177	1.3177	1.3177	1.3177
0.5	0.25	0.3285	0.3285	0.0821	0.0821	1.3139	1.3139	1.3139	1.3139	1.3139
0.5	0.333	0.3272	0.3272	0.1451	0.1451	1.3087	1.3087	1.3087	1.3087	1.3087
0.5	0.5	0.3235	0.3235	0.3235	0.3235	1.2938	1.2938	1.2938	1.2938	1.2938
0.5	0.667	0.3184	0.3184	0.5666	0.5666	1.2736	1.2736	1.2736	1.2736	1.2736
0.5	0.75	0.3154	0.3154	0.7097	0.7097	1.2617	1.2617	1.2617	1.2617	1.2617
0.5	0.833	0.3122	0.3122	0.8665	0.8665	1.2487	1.2487	1.2487	1.2487	1.2487
0.5	1.0	0.3048	0.3048	1.2194	1.2194	1.2194	1.2194	1.2194	1.2194	1.2194
0.5	1.25	0.2922	0.2922	1.8264	1.8264	1.1689	1.1689	1.1689	1.1689	1.1689
0.5	1.333	0.2877	0.2877	2.0448	2.0448	1.1508	1.1508	1.1508	1.1508	1.1508
0.5	1.5	0.2782	0.2782	2.5034	2.5034	1.1126	1.1126	1.1126	1.1126	1.1126
0.5	2.0	0.2478	0.2478	3.9647	3.9647	0.9912	0.9912	0.9912	0.9912	0.9912
0.5	2.5	0.2173	0.2173	5.4325	5.4325	0.8692	0.8692	0.8692	0.8692	0.8692
0.5	3.0	0.1889	0.1889	6.7999	6.7999	0.7555	0.7555	0.7555	0.7555	0.7555
0.5	4.0	0.1417	0.1417	9.0699	9.0699	0.5669	0.5669	0.5669	0.5669	0.5669
0.5	6.0	0.0827	0.0827	11.9098	11.9098	0.3308	0.3308	0.3308	0.3308	0.3308

Table G.1: Scalings of Higgs decay branching ratios vs. κ_t and $\kappa_V = 0.5$ for the non-resolved model.

κ_V	κ_t	HWW	HZZ	H $\tau\tau$	H $\mu\mu$	Hbb	Hcc	H $\gamma\gamma$	HZ γ	Hgg
1.0	-6.0	0.3122	0.3122	11.2408	11.2408	0.3122	0.3122	0.3122	0.3122	0.3122
1.0	-4.0	0.5144	0.5144	8.2305	8.2305	0.5144	0.5144	0.5144	0.5144	0.5144
1.0	-3.0	0.6651	0.6651	5.9862	5.9862	0.6651	0.6651	0.6651	0.6651	0.6651
1.0	-2.5	0.7517	0.7517	4.6979	4.6979	0.7517	0.7517	0.7517	0.7517	0.7517
1.0	-2.0	0.8412	0.8412	3.3647	3.3647	0.8412	0.8412	0.8412	0.8412	0.8412
1.0	-1.5	0.9271	0.9271	2.0859	2.0859	0.9271	0.9271	0.9271	0.9271	0.9271
1.0	-1.333	0.9534	0.9534	1.6941	1.6941	0.9534	0.9534	0.9534	0.9534	0.9534
1.0	-1.25	0.9658	0.9658	1.5091	1.5091	0.9658	0.9658	0.9658	0.9658	0.9658
1.0	-1.0	1.0000	1.0000	1.0000	1.0000	1.0000	1.0000	1.0000	1.0000	1.0000
1.0	-0.833	1.0196	1.0196	0.7075	0.7075	1.0196	1.0196	1.0196	1.0196	1.0196
1.0	-0.75	1.0283	1.0283	0.5784	0.5784	1.0283	1.0283	1.0283	1.0283	1.0283
1.0	-0.667	1.0362	1.0362	0.4610	0.4610	1.0362	1.0362	1.0362	1.0362	1.0362
1.0	-0.5	1.0495	1.0495	0.2624	0.2624	1.0495	1.0495	1.0495	1.0495	1.0495
1.0	-0.333	1.0593	1.0593	0.1175	0.1175	1.0593	1.0593	1.0593	1.0593	1.0593
1.0	-0.25	1.0627	1.0627	0.0664	0.0664	1.0627	1.0627	1.0627	1.0627	1.0627
1.0	-0.167	1.0652	1.0652	0.0297	0.0297	1.0652	1.0652	1.0652	1.0652	1.0652
1.0	0.0	1.0672	1.0672	0.0000	0.0000	1.0672	1.0672	1.0672	1.0672	1.0672
1.0	0.167	1.0652	1.0652	0.0297	0.0297	1.0652	1.0652	1.0652	1.0652	1.0652
1.0	0.25	1.0627	1.0627	0.0664	0.0664	1.0627	1.0627	1.0627	1.0627	1.0627
1.0	0.333	1.0593	1.0593	0.1175	0.1175	1.0593	1.0593	1.0593	1.0593	1.0593
1.0	0.5	1.0495	1.0495	0.2624	0.2624	1.0495	1.0495	1.0495	1.0495	1.0495
1.0	0.667	1.0362	1.0362	0.4610	0.4610	1.0362	1.0362	1.0362	1.0362	1.0362
1.0	0.75	1.0283	1.0283	0.5784	0.5784	1.0283	1.0283	1.0283	1.0283	1.0283
1.0	0.833	1.0196	1.0196	0.7075	0.7075	1.0196	1.0196	1.0196	1.0196	1.0196
1.0	1.0	1.0000	1.0000	1.0000	1.0000	1.0000	1.0000	1.0000	1.0000	1.0000
1.0	1.25	0.9658	0.9658	1.5091	1.5091	0.9658	0.9658	0.9658	0.9658	0.9658
1.0	1.333	0.9534	0.9534	1.6941	1.6941	0.9534	0.9534	0.9534	0.9534	0.9534
1.0	1.5	0.9271	0.9271	2.0859	2.0859	0.9271	0.9271	0.9271	0.9271	0.9271
1.0	2.0	0.8412	0.8412	3.3647	3.3647	0.8412	0.8412	0.8412	0.8412	0.8412
1.0	2.5	0.7517	0.7517	4.6979	4.6979	0.7517	0.7517	0.7517	0.7517	0.7517
1.0	3.0	0.6651	0.6651	5.9862	5.9862	0.6651	0.6651	0.6651	0.6651	0.6651
1.0	4.0	0.5144	0.5144	8.2305	8.2305	0.5144	0.5144	0.5144	0.5144	0.5144
1.0	6.0	0.3122	0.3122	11.2408	11.2408	0.3122	0.3122	0.3122	0.3122	0.3122

Table G.2: Scalings of Higgs decay branching ratios vs. κ_t and $\kappa_V = 1.0$ for the non-resolved model.

κ_V	κ_t	HWW	HZZ	H $\tau\tau$	H $\mu\mu$	Hbb	Hcc	H $\gamma\gamma$	HZ γ	Hgg
1.5	-6.0	0.6424	0.6424	10.2785	10.2785	0.2855	0.2855	0.2855	0.2855	0.2855
1.5	-4.0	1.0028	1.0028	7.1307	7.1307	0.4457	0.4457	0.4457	0.4457	0.4457
1.5	-3.0	1.2477	1.2477	4.9909	4.9909	0.5545	0.5545	0.5545	0.5545	0.5545
1.5	-2.5	1.3802	1.3802	3.8338	3.8338	0.6134	0.6134	0.6134	0.6134	0.6134
1.5	-2.0	1.5115	1.5115	2.6870	2.6870	0.6718	0.6718	0.6718	0.6718	0.6718
1.5	-1.5	1.6322	1.6322	1.6322	1.6322	0.7254	0.7254	0.7254	0.7254	0.7254
1.5	-1.333	1.6682	1.6682	1.3175	1.3175	0.7414	0.7414	0.7414	0.7414	0.7414
1.5	-1.25	1.6851	1.6851	1.1702	1.1702	0.7489	0.7489	0.7489	0.7489	0.7489
1.5	-1.0	1.7310	1.7310	0.7693	0.7693	0.7693	0.7693	0.7693	0.7693	0.7693
1.5	-0.833	1.7570	1.7570	0.5419	0.5419	0.7809	0.7809	0.7809	0.7809	0.7809
1.5	-0.75	1.7684	1.7684	0.4421	0.4421	0.7860	0.7860	0.7860	0.7860	0.7860
1.5	-0.667	1.7788	1.7788	0.3517	0.3517	0.7906	0.7906	0.7906	0.7906	0.7906
1.5	-0.5	1.7962	1.7962	0.1996	0.1996	0.7983	0.7983	0.7983	0.7983	0.7983
1.5	-0.333	1.8089	1.8089	0.0891	0.0891	0.8039	0.8039	0.8039	0.8039	0.8039
1.5	-0.25	1.8133	1.8133	0.0504	0.0504	0.8059	0.8059	0.8059	0.8059	0.8059
1.5	-0.167	1.8165	1.8165	0.0225	0.0225	0.8073	0.8073	0.8073	0.8073	0.8073
1.5	0.0	1.8191	1.8191	0.0000	0.0000	0.8085	0.8085	0.8085	0.8085	0.8085
1.5	0.167	1.8165	1.8165	0.0225	0.0225	0.8073	0.8073	0.8073	0.8073	0.8073
1.5	0.25	1.8133	1.8133	0.0504	0.0504	0.8059	0.8059	0.8059	0.8059	0.8059
1.5	0.333	1.8089	1.8089	0.0891	0.0891	0.8039	0.8039	0.8039	0.8039	0.8039
1.5	0.5	1.7962	1.7962	0.1996	0.1996	0.7983	0.7983	0.7983	0.7983	0.7983
1.5	0.667	1.7788	1.7788	0.3517	0.3517	0.7906	0.7906	0.7906	0.7906	0.7906
1.5	0.75	1.7684	1.7684	0.4421	0.4421	0.7860	0.7860	0.7860	0.7860	0.7860
1.5	0.833	1.7570	1.7570	0.5419	0.5419	0.7809	0.7809	0.7809	0.7809	0.7809
1.5	1.0	1.7310	1.7310	0.7693	0.7693	0.7693	0.7693	0.7693	0.7693	0.7693
1.5	1.25	1.6851	1.6851	1.1702	1.1702	0.7489	0.7489	0.7489	0.7489	0.7489
1.5	1.333	1.6682	1.6682	1.3175	1.3175	0.7414	0.7414	0.7414	0.7414	0.7414
1.5	1.5	1.6322	1.6322	1.6322	1.6322	0.7254	0.7254	0.7254	0.7254	0.7254
1.5	2.0	1.5115	1.5115	2.6870	2.6870	0.6718	0.6718	0.6718	0.6718	0.6718
1.5	2.5	1.3802	1.3802	3.8338	3.8338	0.6134	0.6134	0.6134	0.6134	0.6134
1.5	3.0	1.2477	1.2477	4.9909	4.9909	0.5545	0.5545	0.5545	0.5545	0.5545
1.5	4.0	1.0028	1.0028	7.1307	7.1307	0.4457	0.4457	0.4457	0.4457	0.4457
1.5	6.0	0.6424	0.6424	10.2785	10.2785	0.2855	0.2855	0.2855	0.2855	0.2855

Table G.3: Scalings of Higgs decay branching ratios vs. κ_t and $\kappa_V = 1.5$ for the non-resolved model.

κ_V	κ_t	ttHWW	ttHZZ	ttH $\tau\tau$	tHqWW	tHqZZ	tHq $\tau\tau$	tHWWW	tHWZZ	tHW $\tau\tau$
0.5	-6.0	2.9775	2.9775	428.7530	9.2066	9.2066	1325.7460	9.7660	9.7660	1406.3049
0.5	-4.0	2.2675	2.2675	145.1182	7.5740	7.5740	484.7357	7.8819	7.8819	504.4411
0.5	-3.0	1.7000	1.7000	61.1988	6.1214	6.1214	220.3702	6.2562	6.2562	225.2227
0.5	-2.5	1.3581	1.3581	33.9529	5.1857	5.1857	129.6430	5.2277	5.2277	130.6931
0.5	-2.0	0.9912	0.9912	15.8589	4.1227	4.1227	65.9633	4.0762	4.0762	65.2197
0.5	-1.5	0.6259	0.6259	5.6327	2.9838	2.9838	26.8544	2.8645	2.8645	25.7805
0.5	-1.333	0.5112	0.5112	3.6333	2.6025	2.6025	18.4974	2.4648	2.4648	17.5190
0.5	-1.25	0.4566	0.4566	2.8538	2.4154	2.4154	15.0962	2.2700	2.2700	14.1878
0.5	-1.0	0.3048	0.3048	1.2194	1.8696	1.8696	7.4784	1.7078	1.7078	6.8310
0.5	-0.833	0.2166	0.2166	0.6012	1.5271	1.5271	4.2386	1.3605	1.3605	3.7760
0.5	-0.75	0.1774	0.1774	0.3992	1.3657	1.3657	3.0729	1.1987	1.1987	2.6970
0.5	-0.667	0.1417	0.1417	0.2521	1.2111	1.2111	2.1553	1.0451	1.0451	1.8598
0.5	-0.5	0.0809	0.0809	0.0809	0.9236	0.9236	0.9236	0.7640	0.7640	0.7640
0.5	-0.333	0.0363	0.0363	0.0161	0.6720	0.6720	0.2981	0.5249	0.5249	0.2328
0.5	-0.25	0.0205	0.0205	0.0051	0.5618	0.5618	0.1405	0.4231	0.4231	0.1058
0.5	-0.167	0.0092	0.0092	0.0010	0.4622	0.4622	0.0516	0.3334	0.3334	0.0372
0.5	0.0	0.0000	0.0000	0.0000	0.2953	0.2953	0.0000	0.1909	0.1909	0.0000
0.5	0.167	0.0092	0.0092	0.0010	0.1755	0.1755	0.0196	0.1010	0.1010	0.0113
0.5	0.25	0.0205	0.0205	0.0051	0.1339	0.1339	0.0335	0.0762	0.0762	0.0191
0.5	0.333	0.0363	0.0363	0.0161	0.1043	0.1043	0.0463	0.0647	0.0647	0.0287
0.5	0.5	0.0809	0.0809	0.0809	0.0809	0.0809	0.0809	0.0809	0.0809	0.0809
0.5	0.667	0.1417	0.1417	0.2521	0.1044	0.1044	0.1859	0.1480	0.1480	0.2634
0.5	0.75	0.1774	0.1774	0.3992	0.1329	0.1329	0.2991	0.1993	0.1993	0.4485
0.5	0.833	0.2166	0.2166	0.6012	0.1720	0.1720	0.4775	0.2620	0.2620	0.7272
0.5	1.0	0.3048	0.3048	1.2194	0.2811	0.2811	1.1243	0.4200	0.4200	1.6801
0.5	1.25	0.4566	0.4566	2.8538	0.5119	0.5119	3.1993	0.7270	0.7270	4.5438
0.5	1.333	0.5112	0.5112	3.6333	0.6041	0.6041	4.2939	0.8449	0.8449	6.0051
0.5	1.5	0.6259	0.6259	5.6327	0.8096	0.8096	7.2863	1.1020	1.1020	9.9179
0.5	2.0	0.9912	0.9912	15.8589	1.5402	1.5402	24.6428	1.9827	1.9827	31.7238
0.5	2.5	1.3581	1.3581	33.9529	2.3549	2.3549	58.8716	2.9329	2.9329	73.3233
0.5	3.0	1.7000	1.7000	61.1988	3.1686	3.1686	114.0678	3.8625	3.8625	139.0502
0.5	4.0	2.2675	2.2675	145.1182	4.6200	4.6200	295.6829	5.4873	5.4873	351.1881
0.5	6.0	2.9775	2.9775	428.7530	6.6207	6.6207	953.3740	7.6698	7.6698	1104.4467

Table G.4: Scalings of cross section times BR for the non-resolved model, for the different $t\bar{t}H$, tHq , tHW signal components and $\kappa_V = 0.5$.

κ_V	κ_t	ttHWW	ttHZZ	ttH $\tau\tau$	tHqWW	tHqZZ	tHq $\tau\tau$	tHWWW	tHWZZ	tHW $\tau\tau$
1.0	-6.0	11.2408	11.2408	404.6686	40.4768	40.4768	1457.1666	41.3681	41.3681	1489.2533
1.0	-4.0	8.2305	8.2305	131.6886	34.2339	34.2339	547.7422	33.8480	33.8480	541.5676
1.0	-3.0	5.9862	5.9862	53.8759	28.5396	28.5396	256.8562	27.3983	27.3983	246.5850
1.0	-2.5	4.6979	4.6979	29.3616	24.8511	24.8511	155.3195	23.3557	23.3557	145.9734
1.0	-2.0	3.3647	3.3647	13.4590	20.6360	20.6360	82.5440	18.8497	18.8497	75.3987
1.0	-1.5	2.0859	2.0859	4.6933	16.0557	16.0557	36.1254	14.0919	14.0919	31.7068
1.0	-1.333	1.6941	1.6941	3.0102	14.4942	14.4942	25.7545	12.5059	12.5059	22.2216
1.0	-1.25	1.5091	1.5091	2.3579	13.7201	13.7201	21.4377	11.7273	11.7273	18.3239
1.0	-1.0	1.0000	1.0000	1.0000	11.4220	11.4220	11.4220	9.4484	9.4484	9.4484
1.0	-0.833	0.7075	0.7075	0.4909	9.9372	9.9372	6.8953	8.0059	8.0059	5.5552
1.0	-0.75	0.5784	0.5784	0.3254	9.2212	9.2212	5.1869	7.3200	7.3200	4.1175
1.0	-0.667	0.4610	0.4610	0.2051	8.5229	8.5229	3.7917	6.6579	6.6579	2.9620
1.0	-0.5	0.2624	0.2624	0.0656	7.1807	7.1807	1.7952	5.4076	5.4076	1.3519
1.0	-0.333	0.1175	0.1175	0.0130	5.9375	5.9375	0.6584	4.2814	4.2814	0.4748
1.0	-0.25	0.0664	0.0664	0.0042	5.3616	5.3616	0.3351	3.7730	3.7730	0.2358
1.0	-0.167	0.0297	0.0297	0.0008	4.8163	4.8163	0.1343	3.3009	3.3009	0.0921
1.0	0.0	0.0000	0.0000	0.0000	3.8183	3.8183	0.0000	2.4676	2.4676	0.0000
1.0	0.167	0.0297	0.0297	0.0008	2.9624	2.9624	0.0826	1.7981	1.7981	0.0501
1.0	0.25	0.0664	0.0664	0.0042	2.5928	2.5928	0.1620	1.5284	1.5284	0.0955
1.0	0.333	0.1175	0.1175	0.0130	2.2612	2.2612	0.2507	1.3014	1.3014	0.1443
1.0	0.5	0.2624	0.2624	0.0656	1.7115	1.7115	0.4279	0.9742	0.9742	0.2435
1.0	0.667	0.4610	0.4610	0.2051	1.3198	1.3198	0.5871	0.8188	0.8188	0.3643
1.0	0.75	0.5784	0.5784	0.3254	1.1834	1.1834	0.6657	0.8042	0.8042	0.4524
1.0	0.833	0.7075	0.7075	0.4909	1.0852	1.0852	0.7530	0.8301	0.8301	0.5760
1.0	1.0	1.0000	1.0000	1.0000	1.0000	1.0000	1.0000	1.0000	1.0000	1.0000
1.0	1.25	1.5091	1.5091	2.3579	1.1380	1.1380	1.7782	1.5278	1.5278	2.3872
1.0	1.333	1.6941	1.6941	3.0102	1.2492	1.2492	2.2197	1.7691	1.7691	3.1434
1.0	1.5	2.0859	2.0859	4.6933	1.5628	1.5628	3.5163	2.3434	2.3434	5.2727
1.0	2.0	3.3647	3.3647	13.4590	3.1023	3.1023	12.4092	4.6362	4.6362	18.5449
1.0	2.5	4.6979	4.6979	29.3616	5.2667	5.2667	32.9167	7.4799	7.4799	46.7493
1.0	3.0	5.9862	5.9862	53.8759	7.7435	7.7435	69.6914	10.5403	10.5403	94.8625
1.0	4.0	8.2305	8.2305	131.6886	12.7892	12.7892	204.6276	16.4642	16.4642	263.4266
1.0	6.0	11.2408	11.2408	404.6686	20.9516	20.9516	754.2573	25.5403	25.5403	919.4497

Table G.5: Scalings of cross section times BR for the non-resolved model, for the different $t\bar{t}H$, tHq , tHW signal components and $\kappa_V = 1.0$.

κ_V	κ_t	ttHWW	ttHZZ	ttH $\tau\tau$	tHqWW	tHqZZ	tHq $\tau\tau$	tHWWW	tHWZZ	tHW $\tau\tau$
1.5	-6.0	23.1266	23.1266	370.0260	96.1923	96.1923	1539.0768	95.1080	95.1080	1521.7272
1.5	-4.0	16.0441	16.0441	114.0913	81.6690	81.6690	580.7570	77.3512	77.3512	550.0531
1.5	-3.0	11.2295	11.2295	44.9178	68.8703	68.8703	275.4812	62.9086	62.9086	251.6344
1.5	-2.5	8.6261	8.6261	23.9614	60.7939	60.7939	168.8720	54.1622	54.1622	150.4505
1.5	-2.0	6.0458	6.0458	10.7481	51.7152	51.7152	91.9381	44.6227	44.6227	79.3293
1.5	-1.5	3.6725	3.6725	3.6725	41.9469	41.9469	41.9469	34.6991	34.6991	34.6991
1.5	-1.333	2.9643	2.9643	2.3410	38.6171	38.6171	30.4971	31.4016	31.4016	24.7987
1.5	-1.25	2.6330	2.6330	1.8284	36.9629	36.9629	25.6687	29.7807	29.7807	20.6810
1.5	-1.0	1.7310	1.7310	0.7693	32.0233	32.0233	14.2326	25.0144	25.0144	11.1175
1.5	-0.833	1.2192	1.2192	0.3760	28.7953	28.7953	8.8803	21.9653	21.9653	6.7740
1.5	-0.75	0.9948	0.9948	0.2487	27.2234	27.2234	6.8058	20.5014	20.5014	5.1254
1.5	-0.667	0.7914	0.7914	0.1565	25.6778	25.6778	5.0772	19.0767	19.0767	3.7720
1.5	-0.5	0.4491	0.4491	0.0499	22.6628	22.6628	2.5181	16.3435	16.3435	1.8159
1.5	-0.333	0.2006	0.2006	0.0099	19.7986	19.7986	0.9758	13.8117	13.8117	0.6807
1.5	-0.25	0.1133	0.1133	0.0031	18.4397	18.4397	0.5122	12.6364	12.6364	0.3510
1.5	-0.167	0.0507	0.0507	0.0006	17.1281	17.1281	0.2123	11.5203	11.5203	0.1428
1.5	0.0	0.0000	0.0000	0.0000	14.6443	14.6443	0.0000	9.4640	9.4640	0.0000
1.5	0.167	0.0507	0.0507	0.0006	12.3858	12.3858	0.1535	7.6760	7.6760	0.0951
1.5	0.25	0.1133	0.1133	0.0031	11.3529	11.3529	0.3154	6.8916	6.8916	0.1914
1.5	0.333	0.2006	0.2006	0.0099	10.3820	10.3820	0.5117	6.1783	6.1783	0.3045
1.5	0.5	0.4491	0.4491	0.0499	8.6227	8.6227	0.9581	4.9621	4.9621	0.5513
1.5	0.667	0.7914	0.7914	0.1565	7.1299	7.1299	1.4098	4.0411	4.0411	0.7990
1.5	0.75	0.9948	0.9948	0.2487	6.4888	6.4888	1.6222	3.6932	3.6932	0.9233
1.5	0.833	1.2192	1.2192	0.3760	5.9148	5.9148	1.8241	3.4176	3.4176	1.0540
1.5	1.0	1.7310	1.7310	0.7693	4.9627	4.9627	2.2057	3.0782	3.0782	1.3681
1.5	1.25	2.6330	2.6330	1.8284	4.0340	4.0340	2.8014	3.0873	3.0873	2.1440
1.5	1.333	2.9643	2.9643	2.3410	3.8531	3.8531	3.0429	3.2206	3.2206	2.5434
1.5	1.5	3.6725	3.6725	3.6725	3.6725	3.6725	3.6725	3.6725	3.6725	3.6725
1.5	2.0	6.0458	6.0458	10.7481	4.4580	4.4580	7.9254	6.3144	6.3144	11.2255
1.5	2.5	8.6261	8.6261	23.9614	6.8533	6.8533	19.0368	10.4359	10.4359	28.9887
1.5	3.0	11.2295	11.2295	44.9178	10.3536	10.3536	41.4143	15.4728	15.4728	61.8913
1.5	4.0	16.0441	16.0441	114.0913	18.9646	18.9646	134.8595	26.5208	26.5208	188.5926
1.5	6.0	23.1266	23.1266	370.0260	35.9359	35.9359	574.9741	46.2619	46.2619	740.1909

Table G.6: Scalings of cross section times BR for the non-resolved model, for the different $t\bar{t}H$, tHq , tHW signal components and $\kappa_V = 1.5$.

$\cos(\alpha_{CP})$	Cross section (pb)			95% C.L. Limits		Cross section limits (pb)	
	tHq	tHW	$t\bar{t}H$	Exp.	Obs.	Exp.	Obs.
-1.0	$0.794^{+2.8}_{-4.0}$	$0.146^{+0.2}_{-0.2}$	0.503436	$0.691^{+0.204}_{-0.299}$	1.489	$0.302^{+0.089}_{-0.131}$	0.651
-0.9	$0.728^{+2.7}_{-4.1}$	$0.135^{+0.2}_{-0.2}$	0.426117	$0.768^{+0.228}_{-0.333}$	1.632	$0.300^{+0.089}_{-0.130}$	0.637
-0.8	$0.664^{+2.7}_{-4.2}$	$0.123^{+0.2}_{-0.2}$	0.355670	$0.860^{+0.256}_{-0.374}$	1.797	$0.298^{+0.088}_{-0.130}$	0.622
-0.7	$0.601^{+2.8}_{-4.0}$	$0.112^{+0.2}_{-0.2}$	0.295533	$0.965^{+0.287}_{-0.423}$	1.984	$0.295^{+0.088}_{-0.129}$	0.606
-0.6	$0.546^{+2.9}_{-4.3}$	$0.102^{+0.2}_{-0.2}$	0.242268	$1.082^{+0.323}_{-0.476}$	2.172	$0.292^{+0.087}_{-0.128}$	0.586
-0.5	$0.497^{+3.1}_{-4.2}$	$0.092^{+0.2}_{-0.2}$	0.197595	$1.209^{+0.362}_{-0.534}$	2.362	$0.288^{+0.086}_{-0.127}$	0.563
-0.4	$0.446^{+3.1}_{-4.5}$	$0.083^{+0.2}_{-0.2}$	0.159794	$1.362^{+0.409}_{-0.605}$	2.595	$0.284^{+0.085}_{-0.126}$	0.542
-0.3	$0.398^{+3.2}_{-4.6}$	$0.074^{+0.2}_{-0.2}$	0.132302	$1.538^{+0.463}_{-0.684}$	2.870	$0.282^{+0.085}_{-0.125}$	0.526
-0.2	$0.353^{+3.5}_{-4.8}$	$0.066^{+0.2}_{-0.2}$	0.111684	$1.739^{+0.524}_{-0.776}$	3.205	$0.280^{+0.084}_{-0.125}$	0.515
-0.1	$0.314^{+3.7}_{-4.9}$	$0.059^{+0.2}_{-0.2}$	0.099656	$1.952^{+0.588}_{-0.870}$	3.597	$0.280^{+0.084}_{-0.125}$	0.515
0.0	$0.275^{+3.6}_{-5.2}$	$0.052^{+0.2}_{-0.2}$	0.094502	$2.208^{+0.664}_{-0.982}$	4.149	$0.282^{+0.085}_{-0.125}$	0.530
0.1	$0.242^{+4.0}_{-5.5}$	$0.045^{+0.2}_{-0.2}$	0.099656	$2.458^{+0.737}_{-0.889}$	4.822	$0.288^{+0.086}_{-0.128}$	0.565
0.2	$0.211^{+4.1}_{-5.8}$	$0.040^{+0.2}_{-0.2}$	0.111684	$2.690^{+0.801}_{-0.178}$	5.583	$0.296^{+0.088}_{-0.129}$	0.613
0.3	$0.182^{+4.1}_{-6.1}$	$0.035^{+0.2}_{-0.2}$	0.132302	$2.856^{+0.842}_{-0.234}$	6.242	$0.302^{+0.089}_{-0.131}$	0.661
0.4	$0.156^{+4.4}_{-6.5}$	$0.030^{+0.2}_{-0.2}$	0.159794	$2.898^{+0.845}_{-0.235}$	6.536	$0.304^{+0.089}_{-0.129}$	0.685
0.5	$0.134^{+4.5}_{-6.6}$	$0.026^{+0.2}_{-0.2}$	0.197595	$2.739^{+0.793}_{-0.157}$	6.281	$0.297^{+0.086}_{-0.125}$	0.681
0.6	$0.116^{+4.7}_{-6.9}$	$0.023^{+0.2}_{-0.2}$	0.242268	$2.460^{+0.710}_{-0.038}$	5.692	$0.284^{+0.082}_{-0.120}$	0.658
0.7	$0.100^{+5.0}_{-7.1}$	$0.020^{+0.2}_{-0.2}$	0.295533	$2.138^{+0.617}_{-0.904}$	4.971	$0.269^{+0.078}_{-0.114}$	0.626
0.8	$0.087^{+4.8}_{-7.1}$	$0.018^{+0.2}_{-0.2}$	0.357388	$1.830^{+0.528}_{-0.776}$	4.263	$0.256^{+0.074}_{-0.109}$	0.597
0.9	$0.077^{+4.7}_{-7.0}$	$0.017^{+0.2}_{-0.2}$	0.426117	$1.549^{+0.448}_{-0.658}$	3.610	$0.244^{+0.071}_{-0.104}$	0.569
1.0	$0.071^{+4.2}_{-6.7}$	$0.016^{+0.2}_{-0.2}$	0.503436	$1.322^{+0.383}_{-0.562}$	3.080	$0.236^{+0.068}_{-0.100}$	0.551

Table G.7: Production cross sections for tHq , tHW and $t\bar{t}H$ at $\sqrt{s} = 13$ TeV, as a function of $\cos(\alpha_{CP})$. The quoted uncertainties on the cross section correspond to scale variations in %. The used $t\bar{t}H$ NLO cross sections are obtained from [47] and are interpolated to the angles for which the LHE weights in the signal MC samples are available. Also listed are the expected and observed asymptotic limits at 95% C.L. for all studied CP-mixing angles. The uncertainties on the expected limit correspond to $\pm 1\sigma$.

3375 References

- 3376 [1] J. Schwinger. "Quantum Electrodynamics. I. A Covariant Formulation". Phys-
 3377 ical Review. 74 (10): 1439-61, (1948). <https://doi.org/10.1103/PhysRev.74.1439>
- 3379 [2] R. P. Feynman. "Space-Time Approach to Quantum Electrodynamics". Physical
 3380 Review. 76 (6): 769-89, (1949). <https://doi.org/10.1103/PhysRev.76.769>
- 3381 [3] S. Tomonaga. "On a Relativistically Invariant Formulation of the Quantum
 3382 Theory of Wave Fields". Progress of Theoretical Physics. 1 (2): 27-42, (1946).
 3383 <https://doi.org/10.1143/PTP.1.27>
- 3384 [4] D.J. Griffiths, "Introduction to electrodynamics". 4th ed. Pearson, (2013).
- 3385 [5] F. Mandl, G. Shaw. "Quantum field theory." Chichester, Wiley (2009).
- 3386 [6] F. Halzen, and A.D. Martin, "Quarks and leptons: An introductory course in
 3387 modern particle physics". New York: Wiley, (1984) .
- 3388 [7] File: Standard_Model_of_Elementary_Particle_dark.svg. (2017, June 12)
 3389 Wikimedia Commons, the free media repository. Retrieved November 27, 2017
 3390 from <https://www.collegiate-advanced-electricity.com/single-post/2017/04/10/The-Standard-Model-of-Particle-Physics>.

- 3392 [8] E. Noether, "Invariante Variationsprobleme", Nachrichten von der Gesellschaft
3393 der Wissenschaften zu Göttingen, mathematisch-physikalische Klasse, vol. 1918,
3394 pp. 235-257, (1918).
- 3395 [9] C. Patrignani et al. (Particle Data Group), Chin. Phys. C, 40, 100001 (2016)
3396 and 2017 update.
- 3397 [10] M. Goldhaber, L. Grodzins, A.W. Sunyar "Helicity of Neutrinos", Phys. Rev.
3398 109, 1015 (1958).
- 3399 [11] Palanque-Delabrouille N et al. "Neutrino masses and cosmology with Lyman-
3400 alpha forest power spectrum", JCAP 11 011 (2015).
- 3401 [12] M. Gell-Mann. "A Schematic Model of Baryons and Mesons". Physics Letters.
3402 8 (3): 214-215 (1964).
- 3403 [13] G. Zweig. "An SU(3) Model for Strong Interaction Symmetry and its Breaking"
3404 (PDF). CERN Report No.8182/TH.401 (1964).
- 3405 [14] G. Zweig. "An SU(3) Model for Strong Interaction Symmetry and its Breaking:
3406 II" (PDF). CERN Report No.8419/TH.412(1964).
- 3407 [15] M. Gell-Mann. "The Interpretation of the New Particles as Displaced Charged
3408 Multiplets". Il Nuovo Cimento 4: 848. (1956).
- 3409 [16] T. Nakano, K. Nishijima. "Charge Independence for V-particles". Progress of
3410 Theoretical Physics 10 (5): 581-582. (1953).
- 3411 [17] N. Cabibbo, "Unitary symmetry and leptonic decays" Physical Review Letters,
3412 vol. 10, no. 12, p. 531, (1963).

- 3413 [18] M.Kobayashi, T.Maskawa, “CP-violation in the renormalizable theory of weak
3414 interaction,” Progress of Theoretical Physics, vol. 49, no. 2, pp. 652-657, (1973).
- 3415 [19] File: Weak Decay (flipped).svg. (2017, June 12). Wikimedia Com-
3416 mons, the free media repository. Retrieved November 27, 2017
3417 from [https://commons.wikimedia.org/w/index.php?title=File:
3418 Weak_Decay_\(flipped\)\.svg&oldid=247498592](https://commons.wikimedia.org/w/index.php?title=File:Weak_Decay_(flipped)\.svg&oldid=247498592).
- 3419 [20] Georgia Tech University. Coupling Constants for the Fundamental Forces(2005).
3420 Retrieved January 10, 2018, from [http://hyperphysics.phy-astr.gsu.edu/
3421 hbase/Forces/couple.html#c2](http://hyperphysics.phy-astr.gsu.edu/hbase/Forces/couple.html#c2)
- 3422 [21] M. Strassler. (May 31, 2013).The Strengths of the Known Forces. Retrieved Jan-
3423 uary 10, 2018, from [https://profmattstrassler.com/articles-and-posts/
3424 particle-physics-basics/the-known-forces-of-nature/
3425 the-strength-of-the-known-forces/](https://profmattstrassler.com/articles-and-posts/particle-physics-basics/the-known-forces-of-nature/the-strength-of-the-known-forces/)
- 3426 [22] S.L. Glashow. “Partial symmetries of weak interactions”, Nucl. Phys. 22 579-
3427 588, (1961).
- 3428 [23] A. Salam, J.C. Ward. “Electromagnetic and weak interactions”, Physics Letters
3429 13 168-171, (1964).
- 3430 [24] S. Weinberg, “A model of leptons”, Physical Review Letters, vol. 19, no. 21, p.
3431 1264, (1967).
- 3432 [25] M. Peskin, D. Schroeder, “An introduction to quantum field theory”. Perseus
3433 Books Publishing L.L.C., (1995).
- 3434 [26] A. Pich. “The Standard Model of Electroweak Interactions” <https://arxiv.org/abs/1201.0537>
- 3435

- 3436 [27] G. Arnison et al. (UA1 Collaboration), Phys. Lett. B 122, 103 (1983).
- 3437 [28] M. Banner et al. (UA2 Collaboration), Phys. Lett. B 122, 476 (1983).
- 3438 [29] G. Arnison et al. (UA1 Collaboration), Phys. Lett. B 126, 398 (1983).
- 3439 [30] P. Bagnaia et al. (UA2 Collaboration), Phys. Lett. B 129, 130 (1983).
- 3440 [31] F.Bellaiche. (2012, 2 September). “What’s this Higgs boson anyway?”. Retrieved
3441 from: <https://www.quantum-bits.org/?p=233>
- 3442 [32] M. Endres et al. Nature 487, 454-458 (2012) doi:10.1038/nature11255
- 3443 [33] F. Englert, R. Brout. “Broken Symmetry and the Mass of Gauge
3444 Vector Mesons”. Physical Review Letters. 13 (9): 321-23.(1964)
3445 doi:10.1103/PhysRevLett.13.321
- 3446 [34] P.Higgs. “Broken Symmetries and the Masses of Gauge Bosons”. Physical Re-
3447 view Letters. 13 (16): 508-509,(1964). doi:10.1103/PhysRevLett.13.508.
- 3448 [35] G.Guralnik, C.R. Hagen and T.W.B. Kibble. “Global Conservation Laws
3449 and Massless Particles”. Physical Review Letters. 13 (20): 585-587, (1964).
3450 doi:10.1103/PhysRevLett.13.585.
- 3451 [36] CMS collaboration. “Observation of a new boson at a mass of 125 GeV with
3452 the CMS experiment at the LHC”. Physics Letters B. 716 (1): 30-61 (2012).
3453 arXiv:1207.7235. doi:10.1016/j.physletb.2012.08.021
- 3454 [37] ATLAS collaboration. “Observation of a New Particle in the Search for the Stan-
3455 dard Model Higgs Boson with the ATLAS Detector at the LHC”. Physics Letters
3456 B. 716 (1): 1-29 (2012). arXiv:1207.7214. doi:10.1016/j.physletb.2012.08.020.

- 3457 [38] ATLAS collaboration; CMS collaboration (26 March 2015). “Combined Mea-
 3458 surement of the Higgs Boson Mass in pp Collisions at $\sqrt{s} = 7$ and 8 TeV with
 3459 the ATLAS and CMS Experiments”. Physical Review Letters. 114 (19): 191803.
 3460 arXiv:1503.07589. doi:10.1103/PhysRevLett.114.191803.
- 3461 [39] LHC InternationalMasterclasses“When protons collide”. Retrieved from http://atlas.physicsmasterclasses.org/en/zpath_protoncollisions.htm
- 3463 [40] CMS Collaboration, “SM Higgs Branching Ratios and Total Decay Widths (up-
 3464 date in CERN Report4 2016)”. <https://twiki.cern.ch/twiki/bin/view/LHCPhysics/CERNYellowReportPageBR> , last accessed on 17.12.2017.
- 3466 [41] R.Grant V. “Determination of Higgs branching ratios in $H \rightarrow W^+W^- \rightarrow l\nu jj$
 3467 and $H \rightarrow ZZ \rightarrow l^+l^-jj$ channels”. Physics Department, University of Ten-
 3468 nessee (Dated: October 31, 2012). Retrieved from <http://aesop.phys.utk.edu/ph611/2012/projects/Riley.pdf>
- 3470 [42] LHC Higgs Cross Section Working Group, Denner, A., Heinemeyer, S. et al.
 3471 “Standard model Higgs-boson branching ratios with uncertainties”. Eur. Phys.
 3472 J. C (2011) 71: 1753. <https://doi.org/10.1140/epjc/s10052-011-1753-8>
- 3473 [43] D. de Florian et al., LHC Higgs Cross Section Working Group, CERN-2017-
 3474 002-M, arXiv:1610.07922[hep-ph] (2016).
- 3475 [44] ATLAS and CMS Collaborations, “Measurements of the Higgs boson produc-
 3476 tion and decay rates and constraints on its couplings from a combined ATLAS
 3477 and CMS analysis of the LHC pp collision data at $\sqrt{s} = 7$ and 8 TeV,” (2016).
 3478 CERN-EP-2016-100, ATLAS-HIGG-2015-07, CMS-HIG-15-002.

- 3479 [45] J. A. Aguilar-Saavedra, R. Benbrik, S. Heinemeyer, and M. Perez-Victoria,
 3480 “Handbook of vector-like quarks: Mixing and single production”, Phys. Rev. D
 3481 88 (2013) 094010, doi:10.1103/PhysRevD.88.094010, arXiv:1306.0572.
- 3482 [46] A. Greljo, J. F. Kamenik, and J. Kopp, “Disentangling flavor vio-
 3483 lation in the top-Higgs sector at the LHC”, JHEP 07 (2014) 046,
 3484 doi:10.1007/JHEP07(2014)046, arXiv:1404.1278.
- 3485 [47] F. Demartin, F. Maltoni, K. Mawatari, and M. Zaro, “Higgs production in
 3486 association with a single top quark at the LHC,” European Physical Journal C,
 3487 vol. 75, p. 267, (2015). doi:10.1140/epjc/s10052-015-3475-9, arXiv:1504.00611.
- 3488 [48] F. Demartin, B. Maier, F. Maltoni, K. Mawatari, and M. Zaro, “tWH associated
 3489 production at the LHC”, European Physical Journal C, vol. 77, p. 34, (2017).
 3490 arXiv:1607.05862
- 3491 [49] F. Maltoni, K. Paul, T. Stelzer, and S. Willenbrock, “Associated production
 3492 of Higgs and single top at hadron colliders”, Phys.Rev. D64 (2001) 094023,
 3493 [hep-ph/0106293].
- 3494 [50] S. Biswas, E. Gabrielli, F. Margaroli, and B. Mele, “Direct constraints on the
 3495 top-Higgs coupling from the 8 TeV LHC data,” Journal of High Energy Physics,
 3496 vol. 07, p. 073, (2013).
- 3497 [51] M. Farina, C. Grojean, F. Maltoni, E. Salvioni, and A. Thamm, “Lifting de-
 3498 generacies in Higgs couplings using single top production in association with a
 3499 Higgs boson,” Journal of High Energy Physics, vol. 05, p. 022, (2013).
- 3500 [52] T.M. Tait and C.-P. Yuan, “Single top quark production as a window to physics
 3501 beyond the standard model”, Phys. Rev. D 63 (2000) 014018 [hep-ph/0007298].

- 3502 [53] CMS Collaboration, “Modelling of the single top-quark production in associa-
3503 tion with the Higgs boson at 13 TeV.” [https://twiki.cern.ch/twiki/bin/](https://twiki.cern.ch/twiki/bin/viewauth/CMS/SingleTopHiggsGeneration13TeV)
3504 [viewauth/CMS/SingleTopHiggsGeneration13TeV](#), last accessed on 16.01.2018.
- 3505 [54] CMS Collaboration, “SM Higgs production cross sections at $\sqrt{s} =$
3506 13 TeV.” [https://twiki.cern.ch/twiki/bin/view/LHCPhysics/](https://twiki.cern.ch/twiki/bin/view/LHCPhysics/CERNYellowReportPageAt13TeV)
3507 [CERNYellowReportPageAt13TeV](#), last accessed on 16.01.2018.
- 3508 [55] S. Dawson, The effective W approximation, Nucl. Phys. B 249 (1985) 42.
- 3509 [56] S. Biswas, E. Gabrielli and B. Mele, JHEP 1301 (2013) 088 [[arXiv:1211.0499](https://arxiv.org/abs/1211.0499)
3510 [hep-ph]].
- 3511 [57] LHC Higgs Cross Section Working Group, “Handbook of LHC Higgs Cross
3512 Sections: 4.Deciphering the Nature of the Higgs Sector”, [arXiv:1610.07922](https://arxiv.org/abs/1610.07922).
- 3513 [58] J. Ellis, D. S. Hwang, K. Sakurai, and M. Takeuchi.“Disentangling Higgs-Top
3514 Couplings in Associated Production”, JHEP 1404 (2014) 004, [[arXiv:1312.5736](https://arxiv.org/abs/1312.5736)].
- 3515 [59] CMS Collaboration, V. Khachatryan et al., “Precise determination of the mass
3516 of the Higgs boson and tests of compatibility of its couplings with the standard
3517 model predictions using proton collisions at 7 and 8 TeV,” [arXiv:1412.8662](https://arxiv.org/abs/1412.8662).
- 3518 [60] ATLAS Collaboration, G. Aad et al., “Updated coupling measurements of the
3519 Higgs boson with the ATLAS detector using up to 25 fb^{-1} of proton-proton
3520 collision data”, ATLAS-CONF-2014-009.
- 3521 [61] File:Cern-accelerator-complex.svg. Wikimedia Commons, the free media repos-
3522 itory. Retrieved January, 2018 from <https://commons.wikimedia.org/wiki/>
3523 [File:Cern-accelerator-complex.svg](#)

- 3524 [62] J.L. Caron , “Layout of the LEP tunnel including future LHC infrastructures.”,
3525 (Nov, 1993). A C Collection. Legacy of AC. Pictures from 1992 to 2002. Re-
3526 trieved from <https://cds.cern.ch/record/841542>
- 3527 [63] M. Vretenar, “The radio-frequency quadrupole”. CERN Yellow Report CERN-
3528 2013-001, pp.207-223 DOI:10.5170/CERN-2013-001.207. arXiv:1303.6762
- 3529 [64] L.Evans. P. Bryant (editors). “LHC Machine”. JINST 3 S08001 (2008).
- 3530 [65] CERN Photographic Service.“Radio-frequency quadrupole, RFQ-1”, March
3531 1983, CERN-AC-8303511. Retrieved from <https://cds.cern.ch/record/615852>.
- 3533 [66] CERN Photographic Service “Animation of CERN’s accelerator network”, 14
3534 October 2013. DOI: 10.17181/cds.1610170 Retrieved from <https://videos.cern.ch/record/1610170>
- 3536 [67] C.Sutton. “Particle accelerator”.Encyclopedia Britannica. July 17,
3537 2013. Retrieved from <https://www.britannica.com/technology/particle-accelerator>.
- 3539 [68] L.Guiraud. “Installation of LHC cavity in vacuum tank.”. July 27 2000. CERN-
3540 AC-0007016. Retrieved from <https://cds.cern.ch/record/41567>.
- 3541 [69] J.L. Caron, “Magnetic field induced by the LHC dipole’s superconducting coils”.
3542 March 1998. AC Collection. Legacy of AC. Pictures from 1992 to 2002. LHC-
3543 PHO-1998-325. Retrieved from <https://cds.cern.ch/record/841511>.
- 3544 [70] AC Team. “Diagram of an LHC dipole magnet”. June 1999. CERN-DI-9906025
3545 retrieved from <https://cds.cern.ch/record/40524>.

- 3546 [71] CMS Collaboration “Public CMS Luminosity Information”. https://twiki.cern.ch/twiki/bin/view/CMSPublic/LumiPublicResults#2016__proton_proton_13_TeV_collis, last accessed 24.01.2018
- 3547
- 3548
- 3549 [72] J.L Caron. “LHC Layout” AC Collection. Legacy of AC. Pictures from 1992
- 3550 to 2002. September 1997, LHC-PHO-1997-060. Retrieved from <https://cds.cern.ch/record/841573>.
- 3551
- 3552 [73] J.A. Coarasa. “The CMS Online Cluster:Setup, Operation and Maintenance
- 3553 of an Evolving Cluster”. ISGC 2012, 26 February - 2 March 2012, Academia
- 3554 Sinica, Taipei, Taiwan.
- 3555 [74] CMS Collaboration. “The CMS experiment at the CERN LHC” JINST 3 S08004
- 3556 (2008).
- 3557 [75] CMS Collaboration. “CMS detector drawings 2012” CMS-PHO-GEN-2012-002.
- 3558 Retrieved from <http://cds.cern.ch/record/1433717>.
- 3559 [76] Davis, Siona Ruth. “Interactive Slice of the CMS detector”, Aug. 2016,
- 3560 CMS-OUTREACH-2016-027, retrieved from <https://cds.cern.ch/record/2205172>
- 3561
- 3562 [77] R. Breedon. “View through the CMS detector during the cooldown of the
- 3563 solenoid on February 2006. CMS Collection”, February 2006, CMS-PHO-
- 3564 OREACH-2005-004, Retrieved from <https://cds.cern.ch/record/930094>.
- 3565 [78] Halyo, V. and LeGresley, P. and Lujan, P. “Massively Parallel Computing and
- 3566 the Search for Jets and Black Holes at the LHC”, Nucl.Instrum.Meth. A744
- 3567 (2014) 54-60, DOI: 10.1016/j.nima.2014.01.038”

- 3568 [79] A. Dominguez et. al. “CMS Technical Design Report for the Pixel Detector
3569 Upgrade”, CERN-LHCC-2012-016. CMS-TDR-11.
- 3570 [80] CMS Collaboration. “Description and performance of track and primary-vertex
3571 reconstruction with the CMS tracker,” Journal of Instrumentation, vol. 9, no.
3572 10, p. P10009,(2014).
- 3573 [81] CMS Collaboration and M. Brice. “Images of the CMS Tracker Inner Bar-
3574 rel”, November 2008, CMS-PHO-TRACKER-2008-002. Retrieved from <https://cds.cern.ch/record/1431467>.
- 3576 [82] M. Weber. “The CMS tracker”. 6th international conference on hyperons, charm
3577 and beauty hadrons Chicago, June 28-July 3 2004.
- 3578 [83] CMS Collaboration. “Projected Performance of an Upgraded CMS Detector at
3579 the LHC and HL-LHC: Contribution to the Snowmass Process”. Jul 26, 2013.
3580 arXiv:1307.7135
- 3581 [84] L. Veillet. “End assembly of HB with EB rails and rotation inside SX ”,Jan-
3582 uary 2002. CMS-PHO-HCAL-2002-002. Retrieved from <https://cds.cern.ch/record/42594>.
- 3584 [85] J. Puerta-Pelayo.“First DT+RPC chambers installation round in the UX5 cav-
3585 ern.”. January 2007, CMS-PHO-OREACH-2007-001. Retrieved from <https://cds.cern.ch/record/1019185>
- 3587 [86] X. Cid Vidal and R. Cid Manzano. “CMS Global Muon Trigger” web site:
3588 Taking a closer look at LHC. Retrieved from https://www.lhc-closer.es/taking_a_closer_look_at_lhc/0.lhc_trigger

- 3590 [87] WLCG Project Office, “Documents & Reference - Tiers - Structure,”
 3591 (2014). <http://wlcg.web.cern.ch/documents-reference> , last accessed on
 3592 30.01.2018.
- 3593 [88] CMS Collaboration. “CMSSW Application Framework”, <https://twiki.cern.ch/twiki/bin/view/CMSPublic/WorkBookCMSSWFramework>,
 3594 last accesses 06.02.2018
 3595
- 3596 [89] A. Buckleya, J. Butterworthb, S. Giesekec, et. al. “General-purpose event gen-
 3597 erators for LHC physics”. arXiv:1101.2599v1 [hep-ph] 13 Jan 2011
- 3598 [90] A. Quadt. “Top Quark Physics at Hadron Colliders”. Advances in the Physics
 3599 of Particles and Nuclei. Springer-Verlag Berlin Heidelberg. DOI: 10.1007/978-
 3600 3-540-71060-8 (2007)
- 3601 [91] DurhamHep Data Project, “The Durham HepData Project - PDF Plotter.”
 3602 <http://hepdata.cedar.ac.uk/pdf/pdf3.html> , last accessed on 02.02.2018.
- 3603 [92] G. Altarelli and G. Parisi. “ASYMPTOTIC FREEDOM IN PARTON LAN-
 3604 GUAGE”, Nucl.Phys. B126:298 (1977).
- 3605 [93] Yu.L. Dokshitzer. Sov.Phys. JETP 46:641 (1977)
- 3606 [94] V.N. Gribov, L.N. Lipatov. “Deep inelastic e p scattering in perturbation the-
 3607 ory”, Sov.J.Nucl.Phys. 15:438 (1972)
- 3608 [95] F. Maltoni, G. Ridolfi, and M. Ubiali, “b-initiated processes at the LHC: a
 3609 reappraisal,” Journal of High Energy Physics, vol. 07, p. 022, (2012).
- 3610 [96] B. Andersson, G. Gustafson, G.Ingelman and T. Sjostrand, “Parton fragmen-
 3611 tation and string dynamics”, Physics Reports, Vol. 97, No. 2-3, pp. 31-145,
 3612 1983.

- 3613 [97] CMS Collaboration, “Event generator tunes obtained from underlying event
3614 and multiparton scattering measurements;” European Physical Journal C, vol.
3615 76, no. 3, p. 155, (2016).
- 3616 [98] J. Alwall et. al., “The automated computation of tree-level and next-to-leading
3617 order differential cross sections, and their matching to parton shower simula-
3618 tions,” Journal of High Energy Physics, vol. 07, p. 079, (2014).
- 3619 [99] T. Sjöstrand and P. Z. Skands, “Transverse-momentum-ordered showers and
3620 interleaved multiple interactions,” European Physical Journal C, vol. 39, pp.
3621 129–154, (2005).
- 3622 [100] S. Frixione, P. Nason, and C. Oleari, “Matching NLO QCD computations with
3623 Parton Shower simulations: the POWHEG method,” Journal of High Energy
3624 Physics, vol. 11, p. 070, (2007).
- 3625 [101] S. Agostinelli et al., “GEANT4: A Simulation toolkit,” Nuclear Instruments
3626 and Methods in Physics, vol. A506, pp. 250–303, (2003).
- 3627 [102] J.Allison et.al.,“Recent developments in Geant4”, Nuclear Instruments and
3628 Methods in Physics Research A 835 (2016) 186-225.
- 3629 [103] CMS Collaboration “Full Simulation Offline Guide”, <https://twiki.cern.ch/twiki/bin/view/CMSPublic/SWGuideSimulation>, last accessed 04.02.2018
- 3631 [104] A. Giammanco. “The Fast Simulation of the CMS Experiment” J. Phys.: Conf.
3632 Ser. 513 022012 (2014)
- 3633 [105] A.M. Sirunyan et. al. “Particle-flow reconstruction and global event description
3634 with the CMS detector”, JINST 12 P10003 (2017) <https://doi.org/10.1088/1748-0221/12/10/P10003>.

- 3636 [106] The CMS Collaboration. “ Description and performance of track and pri-
 3637 mary vertex reconstruction with the CMS tracker”. JINST 9 P10009 (2014).
 3638 doi:10.1088/1748-0221/9/10/P10009
- 3639 [107] J. Incandela. “Status of the CMS SM Higgs Search” July 4, 2012. Pdf slides.
 3640 Retrieved from https://indico.cern.ch/event/197461/contributions/1478917/attachments/290954/406673/CMS_4July2012_Final.pdf
- 3642 [108] P. Billoir and S. Qian, “Simultaneous pattern recognition and track fitting by
 3643 the Kalman filtering method”, Nucl. Instrum. Meth. A 294 219. (1990).
- 3644 [109] W. Adam, R. Fruhwirth, A. Strandlie and T. Todorov, “Reconstruction of
 3645 electrons with the Gaussian sum filter in the CMS tracker at LHC”, eConf
 3646 C 0303241 (2003) TULT009 [physics/0306087].
- 3647 [110] K. Rose, “Deterministic Annealing for Clustering, Compression, Classification,
 3648 Regression and related Optimisation Problems”, Proc. IEEE 86 (1998) 2210.
- 3649 [111] R. Fruhwirth, W. Waltenberger and P. Vanlaer, “ Adaptive Vertex Fitting”,
 3650 CMS Note 2007-008 (2007).
- 3651 [112] CMS collaboration, “Performance of CMS muon reconstruction in pp collision
 3652 events at $\sqrt{s} = 7 \text{ TeV}$ ”, JINST 7 P10002 2012, [arXiv:1206.4071].
- 3653 [113] Coco, Victor and Delsart, Pierre-Antoine and Rojo-Chacon, Juan and Soyez,
 3654 Gregory and Sander, Christian, “Jets and jet algorithms”, Proceedings,
 3655 HERA and the LHC Workshop Series on the implications of HERA for LHC
 3656 physics: 2006-2008, pag. 182-204. <http://inspirehep.net/record/866539/files/access.pdf>, (2009), doi:10.3204/DESY-PROC-2009-02/54

- 3658 [114] M. Cacciari, G. P. Salam, and G. Soyez, “The anti- k_t jet clustering algorithm,”
3659 Journal of High Energy Physics, vol. 04, p. 063, (2008).
- 3660 [115] S. Catani, Y. L. Dokshitzer, M. H. Seymour, and B. R. Webber, “Longitudi-
3661 nally invariant K_t clustering algorithms for hadron hadron collisions”, Nuclear
3662 Physics B, vol. 406, pp. 187–224, (1993).
- 3663 [116] Y.L. Dokshitzer, G.D. Leder, S.Moretti, and B.R. Webber, “Better jet clustering
3664 algorithms,” Journal of High Energy Physics, vol. 08, p. 001, (1997).
- 3665 [117] B. Dorney. “Anatomy of a Jet in CMS”. Quantum Diaries. June
3666 1st, 2011. Retrieved from [https://www.quantumdiaries.org/2011/06/01/
3667 anatomy-of-a-jet-in-cms/](https://www.quantumdiaries.org/2011/06/01/anatomy-of-a-jet-in-cms/)
- 3668 [118] The CMS Collaboration.“Event Displays from the high-energy collisions at 7
3669 TeV”, May 2010, CMS-PHO-EVENTS-2010-007, Retrieved from [https://cds.
3670 cern.ch/record/1429614](https://cds.cern.ch/record/1429614).
- 3671 [119] The CMS collaboration. “Determination of jet energy calibration and transverse
3672 momentum resolution in CMS”. JINST 6 P11002 (2011). [http://dx.doi.org/
3673 10.1088/1748-0221/6/11/P11002](http://dx.doi.org/10.1088/1748-0221/6/11/P11002)
- 3674 [120] The CMS Collaboration, “Introduction to Jet Energy Corrections at
3675 CMS.”. <https://twiki.cern.ch/twiki/bin/view/CMS/IntroToJEC>, last ac-
3676 cessed 10.02.2018.
- 3677 [121] CMS Collaboration Collaboration. “Identification of b quark jets at the CMS
3678 Experiment in the LHC Run 2”. Tech. rep. CMS-PAS-BTV-15-001. Geneva:
3679 CERN, (2016). <https://cds.cern.ch/record/2138504>.

- 3680 [122] CMS Collaboration Collaboration. “Performance of missing energy reconstruction
3681 in 13 TeV pp collision data using the CMS detector”. Tech. rep. CMS-PAS-
3682 JME16-004. Geneva: CERN, 2016. <https://cds.cern.ch/record/2205284>.
- 3683 [123] CMS Collaboration, “New CMS results at Moriond (Electroweak) 2013”,
3684 Retrieved from http://cms.web.cern.ch/sites/cms.web.cern.ch/files/styles/large/public/field/image/HIG13004_Event01_0.png?itok=LAWZzPHR
- 3687 [124] CMS Collaboration, “New CMS results at Moriond (Electroweak) 2013”,
3688 Retrieved from http://cms.web.cern.ch/sites/cms.web.cern.ch/files/styles/large/public/field/image/TOP12035_Event01.png?itok=uMdnSqzC
- 3691 [125] K. Skovpen. “Event displays highlighting the main properties of heavy flavour
3692 jets in the CMS Experiment”, Aug 2017, CMS-PHO-EVENTS-2017-006. Re-
3693 trieval from <https://cds.cern.ch/record/2280025>.
- 3694 [126] G. Cowan. “Topics in statistical data analysis for high-energy physics”.
3695 arXiv:1012.3589v1
- 3696 [127] A. Hoecker et al., “TMVA-Toolkit for multivariate data analysis”
3697 arXiv:physics/0703039v5 (2009)
- 3698 [128] L. Lista. “Statistical Methods for Data Analysis in Particle Physics”, 2nd
3699 ed. Springer International Publishing. (2017) <https://dx.doi.org/10.1007/978-3-319-62840-0>

- 3701 [129] I. Antcheva et al., “ROOT-A C++ framework for petabyte data storage, sta-
 3702 tistical analysis and visualization ,” Computer Physics Communications, vol.
 3703 182, no. 6, pp. 1384â€¢1385, (2011).
- 3704 [130] Y. Coadou. “Boosted decision trees”, ESIPAP, Archamps, 9 Febru-
 3705 ary 2016. Lecture. Retrieved from https://indico.cern.ch/event/472305/contributions/1982360/attachments/1224979/1792797/ESIPAP_MVA160208-BDT.pdf
- 3708 [131] J.H. Friedman. “Greedy function approximation: A gradient boosting ma-
 3709 chine”. Ann. Statist. Volume 29, Number 5 (2001), 1189-1232. https://projecteuclid.org/download/pdf_1/euclid-aos/1013203451.
- 3711 [132] W. Verkerke and D. Kirkby, “The RooFit toolkit for data modeling,” arXiv
 3712 preprint physics, (2003).
- 3713 [133] CMS Collaboration, “Documentation of the RooStats-based statistics
 3714 tools for Higgs PAG”. <https://twiki.cern.ch/twiki/bin/view/CMS/SWGuideHiggsAnalysisCombinedLimit>, last accessed on 08.04.2018.
- 3716 [134] F. James, M. Roos, “MINUIT: Function minimization and error analysis”. Cern
 3717 Computer Centre Program Library, Geneve Long Write-up No. D506, 1989
- 3718 [135] J. Neyman and E. S. Pearson, “On the problem of the most efficient tests of
 3719 statistical hypotheses”. Springer-Verlag, (1992).
- 3720 [136] A.L. Read. “Modified frequentist analysis of search results (the CL_s method),”
 3721 (2000). CERN-OPEN-2000-205.
- 3722 [137] C. Palmer. “Searches for a Light Higgs with CMS”, CMS-CR-2012-215. <https://cds.cern.ch/record/1560435>.

- 3724 [138] A. Wald, “Tests of statistical hypotheses concerning several parameters when
 3725 the number of observations is large”, Transactions of the American Mathematical
 3726 society, vol. 54, no. 3, pp. 426–482, (1943).
- 3727 [139] G. Cowan, K. Cranmer, E. Gross, and O. Vitells, “Asymptotic formulae for
 3728 likelihood-based tests of new physics”, European Physical Journal C, vol. 71,
 3729 p. 1554, (2011).
- 3730 [140] S. S. Wilks, “The Large-Sample Distribution of the Likelihood Ratio for Testing
 3731 Composite Hypotheses”, Annals of Mathematical Statistics, vol. 9, pp. 60–62,
 3732 (03, 1938).
- 3733 [141] B. Hespel, F. Maltoni, and E. Vryonidou, “Higgs and Z boson associated pro-
 3734 duction via gluon fusion in the SM and the 2HDM”, JHEP 06 (2015) 065,
 3735 [https://dx.doi.org/10.1007/JHEP06\(2015\)065](https://dx.doi.org/10.1007/JHEP06(2015)065), arXiv:1503.01656.
- 3736 [142] ATLAS Collaboration, “Measurements of Higgs boson pro-
 3737 duction and couplings in diboson final states with the AT-
 3738 LAS detector at the LHC”, Phys. Lett. B726 (2013) 88–119,
 3739 doi:10.1016/j.physletb.2014.05.011, 10.1016/j.physletb.2013.08.010,
 3740 arXiv:1307.1427. [Erratum: Phys. Lett.B734,406(2014)].
- 3741 [143] CMS Collaboration, “Search for the associated production of a Higgs boson
 3742 with a single top quark in proton-proton collisions at $\sqrt{s} = 8$ TeV”, JHEP 06
 3743 (2016) 177, doi:10.1007/JHEP06(2016)177, arXiv:1509.08159.
- 3744 [144] B. Stieger, C. Jorda Lope et al., “Search for Associated Production of a Single
 3745 Top Quark and a Higgs Boson in Leptonic Channels”, CMS Analysis Note CMS
 3746 AN-14-140, 2014.

- 3747 [145] M. Peruzzi, C. Mueller, B. Stieger et al., “Search for ttH in multilepton final
3748 states at $\sqrt{s} = 13$ TeV”, CMS Analysis Note CMS AN-16-211, 2016.
- 3749 [146] CMS Collaboration, “Search for H to bbar in association with a single top quark
3750 as a test of Higgs boson couplings at $\sqrt{s} = 13$ TeV”, CMS Physics Analysis
3751 Summary CMS-PAS-HIG-16-019, 2016.
- 3752 [147] CMS Collaboration, “Search for production of a Higgs boson and a single top
3753 quark in multilepton final states in proton collisions at $\sqrt{s} = 13$ TeV”, CMS
3754 Physics Analysis Summary CMS-PAS-HIG-17-005, 2016.
- 3755 [148] CMS Collaboration, “PdmV2016Analysis,” (2016). <https://twiki.cern.ch/twiki/bin/viewauth/CMS/PdmV2016Analysis#DATA>, last accessed 11.04.2016.
- 3757 [149] M. Peruzzi, F. Romeo, B. Stieger et al., “Search for ttH in multilepton final1
3758 states at $\sqrt{s} = 13$ TeV”, CMS Analysis Note CMS AN-17-029, 2017.
- 3759 [150] B. Maier, “SingleTopHiggProduction13TeV”, February, 2016. <https://twiki.cern.ch/twiki/bin/viewauth/CMS/SingleTopHiggsGeneration13TeV>.
- 3761 [151] B. WG, “BtagRecommendation80XReReco”, February, 2017. <https://twiki.cern.ch/twiki/bin/view/CMS/BtagRecommendation80XReReco>.
- 3763 [152] CMS Collaboration, “Identification of b quark jets at the CMS Experiment
3764 in the LHC Run 2”, CMS Physics Analysis Summary CMS-PAS-BTV-15-001,
3765 2016.
- 3766 [153] CMS Collaboration, “Baseline muon selections for Run-II.” <https://twiki.cern.ch/twiki/bin/view/CMSPublic/SWGuideMuonIdRun2>, last accessed on
3767 24.02.2018.

- 3769 [154] G. Petrucciani and C. Botta, “Two step prompt muon identification”, January,
3770 2015. [https://indico.cern.ch/event/368007/contribution/2/material/
3771 slides/0.pdf](https://indico.cern.ch/event/368007/contribution/2/material/slides/0.pdf).
- 3772 [155] H. Brun and C. Ochando, “Updated Results on MVA eID with 13 TeV samples”,
3773 October, 2014. [https://indico.cern.ch/event/298249/contribution/3/
3774 material/slides/0.pdf](https://indico.cern.ch/event/298249/contribution/3/material/slides/0.pdf).
- 3775 [156] K. Rehermann and B. Tweedie, “Efficient Identification of Boosted Semileptonic
3776 Top Quarks at the LHC”, JHEP 03 (2011) 059, [https://dx.doi:10.1007/
3777 JHEP03\(2011\)059](https://dx.doi.org/10.1007/JHEP03(2011)059), arXiv:1007.2221.
- 3778 [157] CMS Collaboration. “Tag and Probe”, [https://twiki.cern.ch/twiki/bin/
3779 view/CMS/TagAndProbe](https://twiki.cern.ch/twiki/bin/view/CMS/TagAndProbe), last accessed on 02.03.2018.
- 3780 [158] CMS Collaboration. “ \hat{t}_z coupling modifiers”, [https://twiki.cern.ch/
3781 twiki/bin/view/LHCPhysics/LHCHXSWG2KAPPA#t_ch_qbtHq](https://twiki.cern.ch/twiki/bin/view/LHCPhysics/LHCHXSWG2KAPPA#t_ch_qbtHq), last accessed on
3782 27.04.2018.